

# CHEMICAL REVIEWS

## Intriguing Optoelectronic Properties of Metal Halide Perovskites

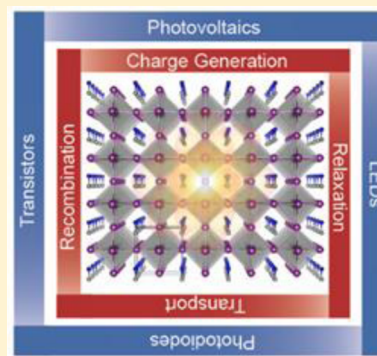
Joseph S. Manser,<sup>†‡</sup> Jeffrey A. Christians,<sup>†</sup> and Prashant V. Kamat<sup>\*,†,‡,§</sup>

<sup>†</sup>Radiation Laboratory, University of Notre Dame, Notre Dame, Indiana 46556, United States

<sup>‡</sup>Department of Chemical & Biomolecular Engineering, University of Notre Dame, Notre Dame, Indiana 46556, United States

<sup>§</sup>Department of Chemistry & Biochemistry, University of Notre Dame, Notre Dame, Indiana 46556, United States

**ABSTRACT:** A new chapter in the long and distinguished history of perovskites is being written with the breakthrough success of metal halide perovskites (MHPs) as solution-processed photovoltaic (PV) absorbers. The current surge in MHP research has largely arisen out of their rapid progress in PV devices; however, these materials are potentially suitable for a diverse array of optoelectronic applications. Like oxide perovskites, MHPs have  $ABX_3$  stoichiometry, where A and B are cations and X is a halide anion. Here, the underlying physical and photophysical properties of inorganic (A = inorganic) and hybrid organic–inorganic (A = organic) MHPs are reviewed with an eye toward their potential application in emerging optoelectronic technologies. Significant attention is given to the prototypical compound methylammonium lead iodide ( $\text{CH}_3\text{NH}_3\text{PbI}_3$ ) due to the preponderance of experimental and theoretical studies surrounding this material. We also discuss other salient MHP systems, including 2-dimensional compounds, where relevant. More specifically, this review is a critical account of the interrelation between MHP electronic structure, absorption, emission, carrier dynamics and transport, and other relevant photophysical processes that have propelled these materials to the forefront of modern optoelectronics research.



### CONTENTS

1. Introduction	12956
1.1. Structure Overview	12958
2. Electronic Structure	12960
2.1. Spin–Orbit Coupling	12963
2.2. Indirect Influence of A-Site Cations	12964
2.2.1. Structural Templating	12964
2.2.2. Dynamic Disorder	12965
3. Linear Absorption and Photoluminescence	12965
3.1. Absorption Coefficient, Optical Transitions, and Urbach Energy	12965
3.2. Chemistry and Dimensionality	12968
3.3. Amplified Spontaneous Emission and Lasing	12971
4. Photophysical Processes	12973
4.1. Interplay between Excitons and Free Carriers	12973
4.1.1. Exciton Binding Energy	12973
4.1.2. Saha Equation and Manybody Effects	12978
4.2. Optical Nonlinearity and Photoconductivity	12980
4.3. Recombination Mechanisms	12985
5. Electronic and Ionic Transport	12990
5.1. Carrier Transport	12990
5.2. Ion Transport	12995
6. Summary and Outlook	12997
Author Information	12998
Corresponding Author	12998
Notes	12998
Biographies	12998
Acknowledgments	12998
References	12998

### 1. INTRODUCTION

Perovskites are a crystallographic family with general  $ABX_3$  stoichiometry. Their discovery is credited to Gustav Rose following his report on the oxide perovskite  $\text{CaTiO}_3$  in 1839.<sup>1</sup> More than half a century after the initial identification of oxide perovskites, a series of inorganic metal trihalide perovskites, of the form  $\text{CsPbX}_3$  (X = Cl, Br, and I), was reported.<sup>2</sup> Unlike naturally occurring  $\text{CaTiO}_3$ , these synthetic perovskites were prepared by simple reaction of  $\text{PbX}_2$  and  $\text{CsX}$  salts in aqueous solutions. Their room temperature tetragonal/orthorhombic and high-temperature cubic perovskite phases were later confirmed by X-ray diffraction.<sup>3,4</sup>

Early investigations of perovskites focused on the structural and biaxial optical properties of titanate-based compounds.<sup>5</sup> Beyond their role in basic research, these materials were first applied as pigments in paints and other coatings.<sup>6</sup> It was not until the demonstration of ferroelectricity in  $\text{BaTiO}_3$  in the mid-1940s that the electronic properties of perovskites became of broad interest.<sup>7–10</sup> Shortly thereafter, the vibrant colors of  $\text{CsPbX}_3$  compounds motivated the first study of metal halide perovskite (MHP) electronic properties, which revealed a frequency-dependent photoconductive response.<sup>4</sup> Other MHPs, such as the two-dimensional (2D) family of  $\text{A}_2\text{MX}_4$ ,  $\text{A}_3\text{M}_2\text{X}_7$ , and  $\text{A}_4\text{M}_3\text{X}_{10}$  compounds that exhibit layered inorganic sheets separated by monovalent organic or inorganic A-site cations, were also under investigation during this time.<sup>11</sup>

**Special Issue:** Electronic Materials

**Received:** February 19, 2016

**Published:** June 21, 2016

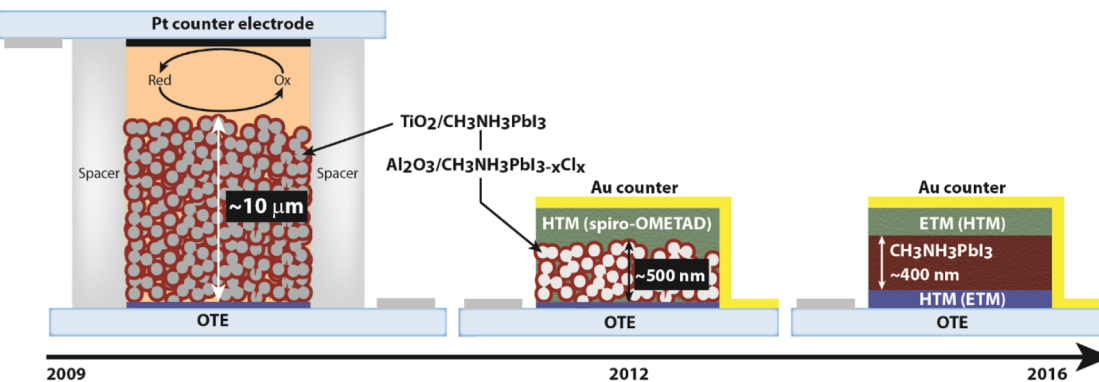


**Figure 1.** Progression of PSC architecture since the first published report in 2009 using a liquid-junction design. HTM is hole transport medium, ETM is electron transport medium, and OTE is optically transparent electrode. Device stacks are not drawn to scale. Approximate active layer thicknesses are given.

Due to the interesting ferro- and antiferromagnetic characteristics of 2D perovskites, significant efforts focused on elucidating their underlying structural properties.<sup>12–15</sup>

The transition to MHP optoelectronics began with pioneering works on hybrid organic–inorganic 2D systems. Of particular interest was the natural self-assembly of quantum well (QW) structures in  $(\text{RNH}_3)_2\text{MX}_4$  compounds.<sup>16–22</sup> The ease of fabrication and molecularly precise structural tunability of hybrid perovskites offered distinct advantages over artificial quantum well systems, in which thickness fluctuations broaden optical characteristics. Moreover, organic interlayers provide dielectric confinement effects that can drastically increase exciton binding energy, oscillator strength, and lifetime.<sup>19,23</sup> A transition from semiconducting to metallic behavior as a function of the number of adjacent inorganic layers in layered tin-based hybrid perovskites highlighted the electronic tunability of these materials.<sup>24,25</sup> As the unique optical and electronic properties of perovskites became increasingly apparent, they began finding applications as active layers in organic–inorganic light-emitting diodes (OLEDs) and as semiconducting channels in thin film field-effect transistors (TFTs).<sup>26–31</sup>

Propelling current interest in MHPs is their recent success as low-cost, tunable light absorbers in next-generation photovoltaics (PVs). The remarkable performance of perovskite solar cells (PSCs), with record laboratory-scale power conversion efficiency now certified at 22.1% (<http://www.nrel.gov/ncpv>), has thrust these materials to the forefront of cutting-edge optoelectronics research and brought their intriguing underlying properties under deeper scrutiny from chemists, physicists, engineers, and material scientists. To illustrate, the number of PSC-related publications has risen dramatically from just a single primary article in 2009 (the first) to more than 1100 publications and 28000 indexed citations in 2015.<sup>32</sup>

Because MHPs have emerged onto the larger scientific stage through the success of PSCs, and much of the fundamental research discussed herein has arisen out of this framework, it is instructive to first understand the distinctive progression of PSC architectures. Figure 1 illustrates noteworthy steps in the evolution of PSC design from the initial report in 2009 to present day. Of particular import is the modification of active layer thickness in the device stack, trending toward thinner configurations that more closely resemble traditional thin film PV architectures with each iteration of the PSC. Also of note is the diversity of device architecture in the PSC family, including

variable thickness, active layer morphology, and composition of selective contacts, ranging from semiconducting and insulating mesoporous metal oxides of various thicknesses to thin film organic and inorganic charge transport media, highlighting the flexibility and superior optoelectronic properties of MHPs. The overarching question at the time was, and to a certain extent still remains: are three-dimensional (3D) MHPs akin to conventional semiconductors, with all the long-standing models developed over the many decades of condensed matter research (like those in refs 33–36), applicable to these materials? In short, the answer to that question is a tentative yes, with some important qualifications that will be addressed throughout this review.

Despite the obvious intrigue of MHPs, early advances in PSC efficiency and design significantly outpaced complementary fundamental studies. As such, a flurry of research has since emerged seeking to better understand the multifunctional behavior and exceptional optoelectronic properties of MHPs. In addition to further development of OLEDs,<sup>37–41</sup> and to a limited extent TFTs,<sup>42</sup> the number of applications using bulk and nanoscale MHPs have correspondingly increased to include tandem PVs,<sup>43–45</sup> water splitting architectures,<sup>46–48</sup> photodetectors,<sup>49–51</sup> and optical gain media.<sup>52–57</sup> A greater appreciation for the outstanding optoelectronic properties of MHPs has evolved from the concerted global effort to characterize and understand PSC operation. This is bolstered by the fact that MHPs, unlike the current titans of the semiconductor industry, are solution and low-temperature processable. In fact, it has recently been shown that methylammonium lead halide perovskites are, in at least certain respects, on par with GaAs.<sup>58–61</sup> Various points of comparison between MHPs and conventional semiconductors are presented throughout this review.

Considering the sheer volume of recent MHP work, this review primarily covers notable fundamental research from the past five years (2012–2016), encompassing the bulk of optoelectronic studies on 3D hybrid and inorganic MHPs. Typical of a rapidly growing research field, reports on fundamental properties of MHPs, including drift/diffusion lengths, recombination mechanisms and lifetimes, the nature of the excited state (including the branching ratio between excitons and free carriers), the role and identity of defects, and operating principles of PSCs and other related devices, have been varied and in some cases drastically disparate. Discrepancies are further complicated by the complex

morphology-property relationship in perovskite thin films that, by virtue of the wide array of deposition techniques and processing conditions, many of which are still being optimized, often display dissimilar characteristics despite nominal compositional differences. We therefore outline the relevant experimental and theoretical results pertaining to these issues and, where possible and appropriate, attempt to reach consensus regarding the nature of MHPs. A brief overview of the perovskite structure, which is inextricably linked to optoelectronic properties, is provided to aid in understanding the pronounced influence of the various elemental and molecular components. This work centers primarily on Sn- and Pb-based perovskites, with much of the discussion focused on methylammonium lead halides ( $\text{CH}_3\text{NH}_3\text{PbX}_3$ ) due to their ubiquity in modern MHP research. While the focus of this review is on 3D halide perovskites, relevant reports on 2D layered materials are presented to provide insight into the impact of perovskite dimensionality on optical and electronic properties. Our goal is to provide a comprehensive picture of the underlying properties of MHPs as they relate to their use in emerging optoelectronic technologies. We hope that this review can serve as a reference for current experimentalists and theorists working in the field, as well as a convenient starting point for those interested in pursuing fundamental MHP studies.

### 1.1. Structure Overview

Though structure is not the focus of this review, it is important to understand the various perovskite motifs and extensive variety of compounds compatible with this crystallographic framework to wholly appreciate their wide-ranging optoelectronic properties. Three distinct lattice positions, referred to in general as the A, B, and X sites, comprise the perovskite structure. The ability to modify the various components in a vast number of permutations provides a useful parameter space for engineering structure-property relationships, facilitating development of multifunctional compounds with tunable physical, chemical, optical, and electronic properties.

In traditional  $\text{ABX}_3$  perovskites, the B-site element is octahedrally coordinated in a  $\text{BX}_6$  configuration. The A component is situated within the cubooctahedral cavity formed by nearest-neighbor X atoms in an  $\text{AX}_{12}$  polyhedron. MHPs in particular are typically composed of a divalent B-site metal (e.g.,  $\text{Pb}^{2+}$ ,  $\text{Sn}^{2+}$ ,  $\text{Ge}^{2+}$ ,  $\text{Cu}^{2+}$ ,  $\text{Eu}^{2+}$ , and  $\text{Ni}^{2+}$ ) and monovalent A-site cation. Trivalent MHPs are much less common but can form low-dimensionality perovskites.<sup>62</sup> Also, Bi(III) has recently been incorporated into  $\text{CH}_3\text{NH}_3\text{PbBr}_3$  as a heterovalent dopant.<sup>63</sup> A unique aspect of MHPs is the flexibility of the A component, which can range in type from a single atom to a variety of organic molecules, the size of which influences the dimensionality of the octahedral framework (vide infra).<sup>30,64</sup> Incorporation of an organic component gives rise to the series of materials known as organic–inorganic hybrid perovskites that have become archetypes in MHP optoelectronic applications. Note that the “organic–inorganic” nomenclature differentiates hybrid perovskites from related organometallic structures such as metal–organic frameworks (MOFs) due to the absence of covalent interaction between organic and inorganic species. For some of the more interesting aspects of the hybrid perovskite structure, we point the reader to a recent review by Saparov and Mitzi, as well as references therein.<sup>65</sup>

To link perovskite structure with the resulting properties, it is important to first understand the influence of the various

components on the perovskite framework. For example, use of large A-site cations disrupts the classical 3D perovskite motif, forming layered materials that can exhibit drastically altered electronic properties relative to their isotropic counterparts. A number of design rules have been established to predict formability of the general 3D MHP structure.<sup>66–69</sup> The A-site component is under size constraints dictated by cubooctahedral voids formed from the continuous array of corner-sharing  $\text{BX}_6$  octahedra. A semiempirical geometric parameter, known as the Goldschmidt tolerance factor,  $t$ , can be used to predict the stability of 3D perovskite structures given the ionic radii of components A ( $r_A$ ), B ( $r_B$ ), and X ( $r_X$ ).<sup>70</sup>

$$t = \frac{r_A + r_X}{\sqrt{2}(r_B + r_X)} \quad (1)$$

Empirically, the majority of 3D MHPs form in the approximate range  $0.81 \leq t \leq 1.0$ . Typically, hexagonal structures are formed when  $t > 1$ , and nonperovskite structures of  $\text{NH}_4\text{CdCl}_3$ -type are formed when  $t < 0.8$ .<sup>71</sup>

A second constraint known as the octahedral factor ( $\mu$ ), given by  $\mu = r_B/r_X$  and typically lying in the range of  $0.44 \leq \mu \leq 0.9$ , is a measure of octahedral stability and, together with the tolerance factor, provides a parameter space for perovskite formability.<sup>66</sup> This space is shown graphically as a 2D map of A and X ionic radii in Figure 2, with contour lines corresponding

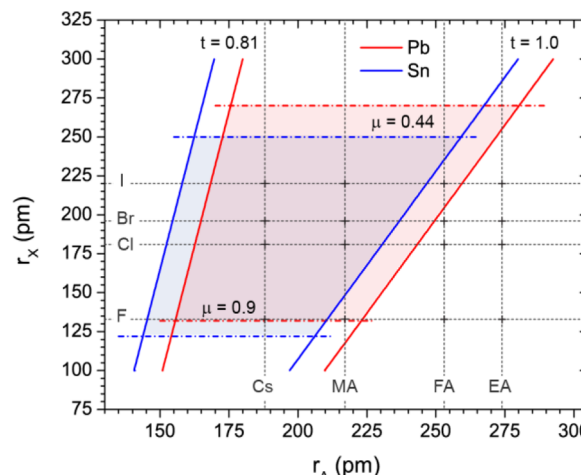


**Figure 2.** Formability of 3D lead (red) and tin (blue) halide perovskites as a function of A-site cation and halide anion radii. Solid and dashed lines mark the bounds of the tolerance and octahedral factors, respectively. The ionic radii of six-coordinate  $\text{Pb}(\text{II})$  and  $\text{Sn}(\text{II})$  are taken as 119 and 110 pm, respectively. Effective molecular cation radii, calculated using a rigid sphere model, are from ref 67.

to the general outer limits of MHP formability for the Pb and Sn family of compounds. Approximate ionic radii of  $\text{F}^-$ ,  $\text{Cl}^-$ ,  $\text{Br}^-$ , and  $\text{I}^-$ , as well as A-site cations common to Pb- and Sn-based perovskites such as  $\text{Cs}^+$ ,  $\text{CH}_3\text{NH}_3^+$  (MA),  $\text{HC}(\text{NH}_2)_2^+$  (FA), and  $\text{CH}_3\text{CH}_2\text{NH}_3^+$  (EA), are marked along the ordinate and abscissa, respectively.<sup>72,73</sup> Their intersection can be used to predict whether a perovskite is likely to result given the specified components. If the intersection lies within the limits of formation (shaded regions), the perovskite structure is favored. If it lies well outside these limits, other motifs result.

In the interest of presenting the most contemporary view of perovskite formability, we briefly cover modifications to the classical tolerance and octahedral factors that have recently

been proposed.<sup>67–69</sup> Motivation for such augmentation stems from two sources of added complexity when analyzing 3D inorganic and hybrid  $\text{ABX}_3$  ( $\text{X} = \text{Cl}$ ,  $\text{Br}$ , and  $\text{I}$ ) perovskites: (i) nonspherical molecular cations in the A-site and (ii) reduced electronegativity of heavy halides relative to oxide and fluoride anions. To address the first point, Kieslich et al. have proposed a rigid sphere model to determine effective molecular cation radii.<sup>67,68</sup> The revised A-site radius is given by  $r_{\text{A,eff}} = r_{\text{mass}} + r_{\text{ion}}$ , where  $r_{\text{mass}}$  is the distance from the molecular center of mass to the furthest nonhydrogen atom, and  $r_{\text{ion}}$  is the ionic radius of this most distant atom. The new term,  $r_{\text{A,eff}}$  can then be substituted into the standard tolerance factor expression (eq 1) for improved accuracy in predicting formation of organic–inorganic perovskites. The second modification addresses empirical observations of deviation from the standard Shannon ionic radii in  $\text{B}(\text{II})\text{X}_6$  octahedra, where  $\text{X} = \text{Cl}$ ,  $\text{Br}$ , or  $\text{I}$ .<sup>69</sup> The widely cited Shannon metal cation radii were originally calculated strictly from oxide and fluoride coordination environments.<sup>72</sup> When highly electronegative anions are replaced by less electronegative heavy halides, a larger degree of covalency results, which in general shortens the metal–halide bond relative to that expected from a rigid sphere model. To account for such deviations, Travis et al. fixed halide radii to those given by Shannon and computed modified metal cation radii from empirical bond lengths.<sup>69</sup> The result is a series of divalent B-site cations whose radius varies as a function of heavy halide chemistry. They found that deviation from Shannon radii is strongly correlated with the difference in electronegativity between the B and X components, suggesting that changes in bond ionicity are in fact responsible for the observed discrepancies. Taking both modifications into account can improve the accuracy of predictive formability models and facilitate the pursuit of new MHPs with distinct optoelectronic properties.

Favorable formability criteria do not imply that the perovskite phase is the only stable form for a given compound. In fact, a defining characteristic of the general perovskite structure is its propensity to undergo a series of phase transitions that can be modulated by temperature, pressure, and/or chemistry. The highest symmetry phase for a given inorganic MHP is the cubic ( $Pm\bar{3}m$ ) motif, with sequential transitions lowering this symmetry typically through octahedral rotations that can be described using Glazer's notation.<sup>67,71,74–76</sup> Regardless of the formability criteria, these distortions can under some circumstances be considerable enough that the perovskite structure is no longer stable, as is the case with the wide band gap nonperovskite  $\delta$ -phase of otherwise low band gap  $\text{HC}(\text{NH}_2)_2\text{PbI}_3$  and  $\text{CsPbI}_3$ .<sup>71,76,77</sup> In the prototypical material  $\text{APbI}_3$ , the cation series  $\text{CH}(\text{NH}_2)_2^+$ ,  $\text{CH}_3\text{NH}_3^+$ , and  $\text{Cs}^+$  leads to progressively larger octahedral tilting in the perovskite phase at room temperature ( $\Phi$  in Figure 3) as a result of decreasing cation size,<sup>71,78</sup> which we will see in section 2.2.1 heavily influences the electronic structure and resulting optoelectronic properties.

Beyond 3D MHPs, organic–inorganic materials with suitable octahedral factors such that the basic  $\text{BX}_6$  unit is stable, but with tolerance factors greater than one (due to the A-cation exceeding the critical size), are of particular interest for this review (Figure 4). Although not covered in depth here, all-inorganic compounds such as  $\text{Rb}_2\text{MnCl}_4$  can also exhibit layered perovskite structures.<sup>79</sup> Layered 2H-perovskites and other lower-dimensional structures, such as one-dimensional (1D) chained and zero-dimensional (0D) isolated octahedra,

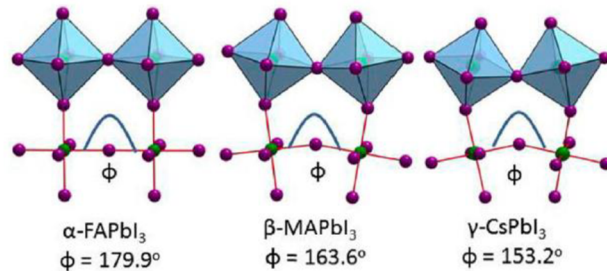


**Figure 3.** Structural deformations of the ideal  $180^\circ$   $\text{B}-\text{X}-\text{B}$  bond angle induced by the A-site cation size. The same distortions are also a function of temperature and pressure for a given compound. Reproduced from ref 71. Copyright 2015 American Chemical Society.

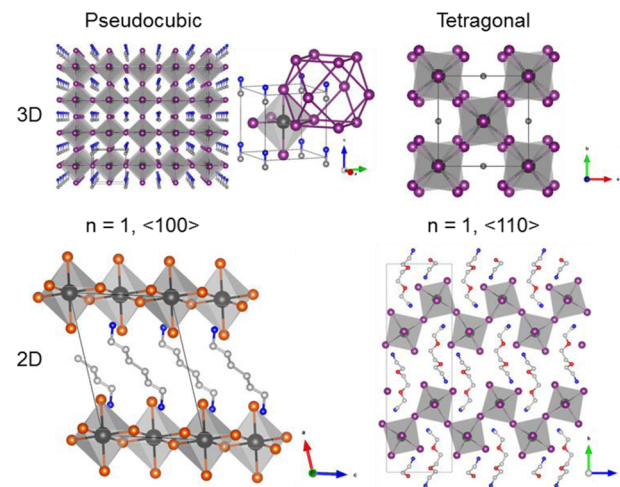


**Figure 4.** Examples of 3D and 2D hybrid MHP structure. Inorganic MHPs exhibit comparable motifs. The  $\text{AX}_{12}$  cuboctahedron in pseudocubic  $\text{CH}_3\text{NH}_3\text{PbI}_3$  is emphasized, as well as the octahedral tilting in the lower symmetry tetragonal phase examined down the  $c$  axis. 2D Layered perovskites with differing  $\text{BX}_6$  octahedral orientation are shown. Atom legend: black = Pb, purple = I, orange = Br, blue = N, gray = C, and red = O. Hydrogen has been excluded for clarity. Structures are from  $\text{CH}_3\text{NH}_3\text{PbI}_3$  (ref 76),  $\text{NH}_3(\text{CH}_2)_6\text{NH}_3\text{PbBr}_4$  (ref 96), and  $\text{C}_6\text{H}_{18}\text{N}_2\text{O}_2\text{PbI}_4$  (ref 97).

are important analogues to 3D architectures that exhibit distinctive optoelectronic properties. Subtle chemical modifications can yield materials with nearly identical composition and structure yet dramatically different properties, including disparate band gaps, exciton binding energies, and conductivities, making low-dimensional perovskites promising materials for tunable optoelectronics.<sup>30,80</sup>

A final salient point regarding the perovskite structure and its connection with optoelectronic properties is the ability to readily create solid-solutions within the three A, B, and X lattice sites. Mixed-halide perovskites of the form  $\text{ABX}_{3-x}\text{X}'_x$  have been prominent archetypes for recent PV and OLED studies. Iodide–bromide mixtures in  $\text{CH}_3\text{NH}_3\text{Pb}(\text{I}_{1-x}\text{Br}_x)_3$  ( $0 \leq x \leq 1$ ) enable modification of the band gap from 1.55 eV ( $x = 0$ ) to 2.2 eV ( $x = 1$ ).<sup>81</sup> Various solid-solutions in mixed-halide nanocrystals  $\text{CsPb}(\text{I}_{1-x}\text{Br}_x)_3$  and  $\text{CsPb}(\text{Cl}_{1-x}\text{Br}_x)_3$  exhibit tunable photoluminescence (PL) across nearly the entire visible spectrum.<sup>82</sup> As-formed MHPs also readily undergo spontaneous *in situ* exchange reactions using halide and/or molecular cation solutions or halogen gas with appropriate electrochemical potential to drive the redox reaction.<sup>83–88</sup> While I/Br

and Cl/Br alloys are isolable compounds, I and Cl do not show the same propensity for mixing (despite the ubiquitous  $\text{CH}_3\text{NH}_3\text{PbI}_{3-x}\text{Cl}_x$  nomenclature). The miscibility limits of  $\text{CH}_3\text{NH}_3\text{PbI}_3$  and  $\text{CH}_3\text{NH}_3\text{PbCl}_3$  are less than ~5% due to the lattice mismatch caused by the large size discrepancy of  $\text{I}^-/\text{Cl}^-$ .<sup>83,89–92</sup> However, the presence of Cl in the iodide precursor matrix significantly alters crystallization mechanics, resulting in improved film morphology.<sup>89,93–95</sup>

B-site alloying (e.g.,  $\text{AB}_{1-x}\text{B}'_x\text{X}_3$ ) has also been shown to provide continuous variation of material properties. Partial substitution of the B component has significant impact on the electronic properties of the material but relatively lesser effect on the lattice parameters that are influenced most heavily by the halide ion.<sup>98</sup> The near-optimal light harvesting band gap of  $\text{CH}_3\text{NH}_3(\text{Pb}_{1-x}\text{Sn}_x)\text{I}_3$  ( $E_g = 1.17\text{--}1.55$  eV) has brought recent attention to Pb/Sn mixed-metal perovskites.<sup>99–101</sup> Navas et al. recently explored material characteristics of other Pb/B(II) solid solutions, including B = Sr(II), Cd(II), and Ca(II), and found that the various dopants cause distinct alterations of the electronic structure near the band edge.<sup>102</sup>

Lastly, mixing of A-site cations (e.g.,  $\text{A}_{1-x}\text{A}'_x\text{BX}_3$ ) impacts the nature of the  $\text{BX}_6$  inorganic motif, thus influencing the optical and electronic character of the resulting materials.<sup>103</sup> While use of multiple A-site components may result in segregated phases,<sup>104</sup> it is also possible to form solid solutions of the cations. Mixed  $\text{CH}_3\text{NH}_3^+/\text{HC}(\text{NH}_2)_2^+$  Pb-based perovskites show improved PV performance over the corresponding pure phase compounds due in part to a reduction in band gap upon addition of  $\text{HC}(\text{NH}_2)_2^+$  to  $\text{CH}_3\text{NH}_3\text{PbI}_3$ .<sup>105–108</sup> Additionally,  $\text{CH}_3\text{NH}_3^+$  stabilizes the room temperature pseudocubic perovskite phase of  $\text{HC}(\text{NH}_2)_2\text{PbX}_3$ .<sup>109</sup> Similar phase stabilization has been achieved in mixed cation ( $\text{Cs}_x\text{FA}_{1-x}\text{PbX}_3$  and ( $\text{Cs}_x\text{FA}_{1-x}\text{Pb(I}_{1-x}\text{Br}_x\text{)}_3$ ) (section 3.2).<sup>43,77</sup>

A particularly interesting and less well-explored condition arises when the effective radius of one cation results in favorable 3D formability criteria with the corresponding  $\text{BX}_6$  unit, while the second cation is too large to fit within the 3D  $\text{AX}_{12}$  cuboctahedral environment. With appropriate mixed cation stoichiometry and solubility, hybrid 2D/3D perovskites can be stabilized. This situation enables control over the natural quantum well structure in 2H-layered materials. The number of adjacent inorganic layers orthogonal to the organic interlayers can then be increased from single, highly confined semiconducting sheets ( $n = 1$ , as discussed above) to motifs with  $n > 1$ .<sup>24,25</sup> Interestingly, mixed 2D/3D hybrids have been shown to exhibit improved resilience to moisture-induced degradation over pure 3D perovskites,<sup>110</sup> although the universality of this observation has yet to be determined.

## 2. ELECTRONIC STRUCTURE

Properties of particular interest for optoelectronic applications, such as excited state lifetime, recombination mechanisms, mobility, and intrinsic carrier concentration, can often be rationalized through detailed understanding of a material's band structure and density of states (DOS).<sup>111,112</sup> It is therefore useful to begin our discussion of perovskite optoelectronics here. From a fundamental standpoint, the rich variety of MHPs offers a convenient framework to systematically study the effects of dimensionality, composition, and structural disorder on underlying electronic configurations. Highlighted throughout this section are a number of unique electronic characteristics that set these perovskites, particularly Sn- and Pb-based compounds, apart from conventional semiconductors. Some

properties of interest include: (i) inverted band structures relative to typical III–V materials, (ii) pronounced relativistic effects, and (iii) dynamic electronic disorder.

Accurately determining the electronic structure and band gap ( $E_g$ ) of semiconducting MHPs, and their hybrid analogues in particular, through computational methods has proven challenging. Some of the same properties that make these compounds unique—readily disordered structures, collective orientation of polar molecular cations, and presence of high-mass elements—are also responsible for this difficulty. Since the late 1970s, a multitude of electronic models have been utilized to describe MHP frameworks with varying degrees of success. Semiempirical calculations based on the linear combination of atomic orbitals (LCAO) and extended Hückel models were used to investigate electronic structure of  $\text{CsBX}_3$  (B = Sn and Pb) and hybrid compounds, respectively, excluding A-site cation interactions.<sup>113–115</sup> Inaccuracies arise in the extended Hückel model for systems with bands composed largely of antibonding character,<sup>116</sup> as is the case for main group MHPs. Severe band gap underestimations with semiempirical LCAO approaches led to the erroneous conclusion that  $\text{CsSnBr}_3$  is a semimetal, when in fact it is a medium-gap semiconductor.<sup>115–117</sup>

Density functional theory (DFT) has more recently been applied to the MHP system but, as is typical for such methods, severely underestimates perovskite band gaps. Introduction of relativistic corrections, in particular first-order scalar relativistic (SR-DFT) and higher order spin-orbit coupling (SOC-DFT) effects, still does not provide sufficient accuracy across the family of Pb and Sn perovskites. As shown in Figure 5A, SR-DFT yields fortuitously precise  $E_g$  values for  $\text{CH}_3\text{NH}_3\text{PbI}_3$  as a result of offsetting influence of electron self-energy/many-body effects, which tend to increase  $E_g$  and relativistic interactions that reduce  $E_g$ .<sup>118</sup> However, it cannot accurately describe

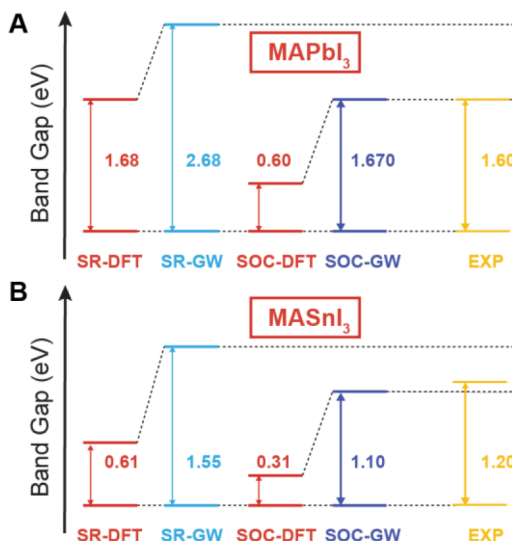


**Figure 5.** (A) Comparison of the derived  $E_g$  of  $\text{CH}_3\text{NH}_3\text{PbI}_3$  and  $\text{CH}_3\text{NH}_3\text{SnI}_3$  using various computational methods and their deviation from experimentally determined values. SR-DFT fortuitously provides a reasonable  $E_g$  for  $\text{CH}_3\text{NH}_3\text{PbI}_3$  due to cancellation of errors, but the same approach does not accurately capture the properties of the Sn analogue due to differing relativistic interactions. SOC-GW shows good agreement with the experiment in both compounds. Reprinted by permission from Macmillan Publishers Ltd.: Scientific Reports (ref 118), copyright 2014.

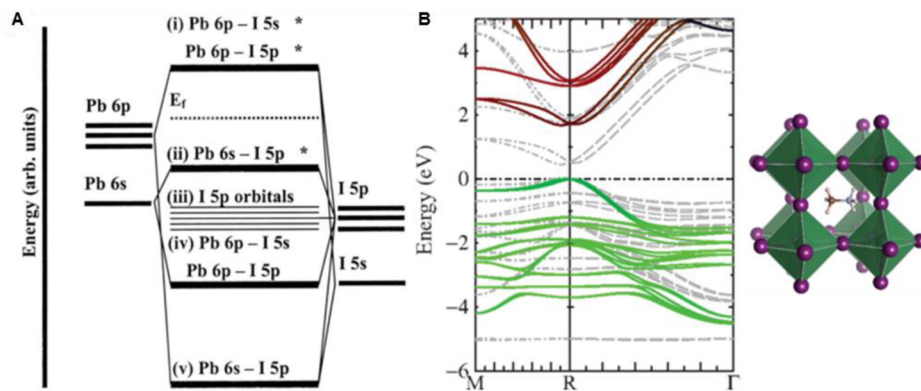


**Figure 6.** (A) Bonding diagram of isolated  $[PbI_6]^{4-}$  octahedra without considering SOC. Reprinted with permission from ref 127. Copyright 2003 by the American Physical Society. (B) Electronic band structure of  $CH_3NH_3PbI_3$  calculated using the QSGW formalism. Orbital contributions are indicated by I 5p (green), Pb 6p (red), and Pb 6s (blue). Gray dashed lines show results from LDA calculations, which severely underestimate  $E_g$  and dispersion at near VBM. Reprinted with permission from ref 119. Copyright 2014 by the American Physical Society.

dispersion of the VB in Pb perovskites, nor does it capture  $E_g$  of Sn perovskites (Figure 5B) due to milder relativistic effects with the lighter metal center. In light of the complexity of this system, state-of-the-art quasiparticle self-consistent GW with SOC corrections (SOC-QSGW) is the only approach thus far that has proven adequate in accurately determining electronic structure of inorganic and hybrid MHPs.<sup>117–120</sup> DFT can still provide structural insight and in some cases semiquantitative information sufficient for comparing electronic properties of homologous MHPs, but should be used with caution when in pursuit of quantitative results.

Halide perovskites most relevant for optoelectronics, namely those with main group metal centers, are direct gap semiconductors with strong band edge optical absorption and luminescence. That is, the valence band maximum (VBM) and conduction band minimum (CBM) lie at the same point in reciprocal space ( $k$ -space). Note that the direct gap nature of MHPs is a valid generalization, but recent calculations suggest there may be subtle yet important exceptions that arise in noncentrosymmetric hybrid compounds due to Rashba, Rashba/Dresselhaus, or Dresselhaus splitting.<sup>119,121–126</sup> Electronic structure near the band edge is primarily dictated by the basic  $BX_6$  building blocks.<sup>114,120,127–130</sup> Therefore, orbital diagrams of isolated  $[BX_6]^{4-}$  clusters, like those in the 0D perovskite analogue  $(CH_3NH_3)_4[PbI_6] \cdot 2H_2O$ ,<sup>131</sup> provide a foundation for understanding more complex band structures in higher dimensionality structures. For  $[PbI_6]^{4-}$  units in particular, a Pb 6s–I 5p  $\sigma$ -antibonding orbital comprises the highest occupied molecular orbital (HOMO), while Pb 6p–I 5p  $\pi$ -antibonding and Pb 6p–I 5s  $\sigma$ -antibonding orbitals constitute the lowest unoccupied molecular orbital (LUMO) (Figure 6A).<sup>127</sup>

Comparable electronic character is retained in the 3D perovskite  $CH_3NH_3PbI_3$ . According to quasiparticle self-consistent GW (QSGW) calculations, the VBM is approximately 3:1 I 5p to Pb 6s (Figure 6B).<sup>119</sup> The CBM is nonbonding with majority Pb 6p character along with contribution from I p states.<sup>129,132,133</sup> Hybrid Sn analogues show analogous band edge structure.<sup>118</sup> However, the direct band gap of  $CH_3NH_3SnI_3$  ( $E_g \sim 1.30$  eV) is lower than that of  $CH_3NH_3PbI_3$  ( $E_g \sim 1.6$  eV) primarily as a result of differing relativistic interactions (Section 2.1), though structural differences contribute to a lesser degree.<sup>99,118</sup> 3D Ge halide perovskites also show direct gap transitions, but their 1D

analogues are ostensibly indirect gap materials with weak, broad absorption near the band edge.<sup>134</sup> Neither  $Cs^+$  nor molecular A-site cations provide significant direct contribution to frontier orbitals, meaning hybrid and inorganic MHPs generally parallel one another in terms of the composition of their partial density of states (PDOS) in the vicinity of their lowest electronic transition.<sup>103,117,119,129,135</sup> This is not to say that the A-site plays no role in dictating electronic structure. Section 2.2 has further discussion on this point.

Another salient feature of the band structure shown in Figure 6B is the comparable parabolicity of the upper VB and lower CB near the R point. Band extrema can often be approximated using a parabolic relationship between energy ( $E$ ) and momentum ( $k$ ) according to

$$E = \frac{k^2 \hbar^2}{2m^*} \quad (2)$$

where  $\hbar$  is the reduced Planck constant and  $m^*$  is the effective mass of electrons (holes) in the CB (VB). From the time derivative of the group velocity ( $v_g$ ) (eq 3) and the relationship for an external force acting on an electron within the lattice (eq 4)

$$\frac{\partial v_g}{\partial t} = \frac{1}{\hbar} \frac{\partial^2 E}{\partial k \partial t} = a \quad (3)$$

$$F_{ext} = \hbar \frac{dk}{dt} \quad (4)$$

we arrive at the well-known parabolic approximation for effective mass as derived from band dispersion.

$$m^* = \frac{F_{ext}}{a} = \hbar^2 \left[ \frac{\partial^2 E}{\partial k^2} \right]^{-1} \quad (5)$$

It follows then that similar dispersion at the band edge of MHPs results in electrons and holes with comparable effective mass. Although parabolic approximations are generally valid, relativistic effects may cause non-negligible deviation from such estimates in Pb and Sn halide perovskites (Section 2.2). As such, theoretically calculated effective masses vary somewhat depending on the computational method employed and the level of complexity in treatment of the band dispersion (parabolic or nonparabolic), but recent calculations using SOC-GW yielded average values of  $m_e/m_0 = 0.19$  and  $m_h/m_0 =$

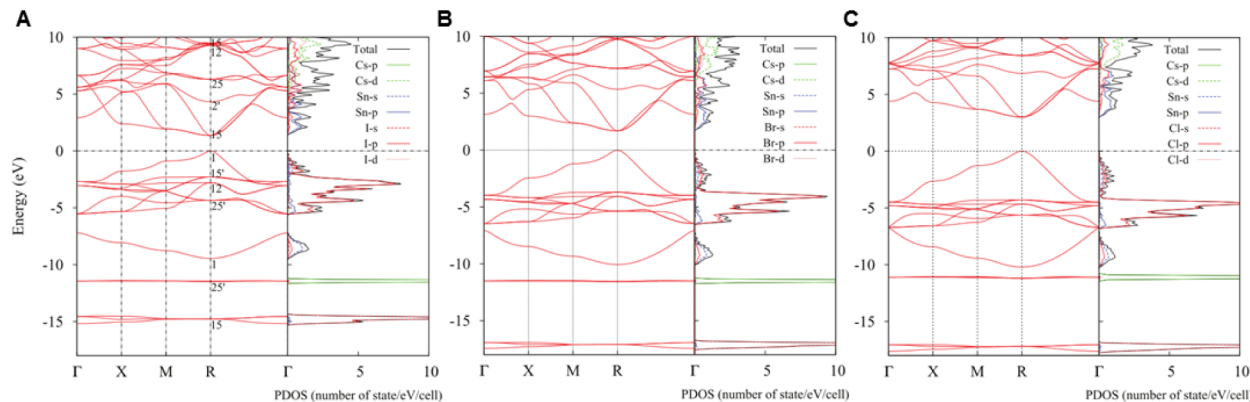


**Figure 7.** QSGW band structures (without SOC) and pDOS of cubic (A)  $\text{CsSnI}_3$ , (B)  $\text{CsSnBr}_3$ , and (C)  $\text{CsSnCl}_3$ . Lines corresponding to contributions of the various frontier orbitals to the pDOS are Cs-p (green solid), Cs-d (green dashed), Sn-s (blue dashed), Sn-p (blue solid), X-s (red dashed), X-p (red solid), and X-d (red dotted). Zero energy is set at the VBM. Reprinted with permission from ref 117. Copyright 2013 American Physical Society.

0.25 for  $\text{CH}_3\text{NH}_3\text{PbI}_3$  and  $m_e/m_0 = 0.28$  and  $m_h/m_0 = 0.13$  for  $\text{CH}_3\text{NH}_3\text{SnI}_3$ , where  $m_0$  is the free electron mass.<sup>118</sup> These are in close agreement with effective masses determined recently using high-field magnetoabsorption spectroscopy.<sup>136</sup> Contrast this with the large discrepancy in carrier effective mass in GaAs ( $m_e/m_0 = 0.07$ ,  $m_h/m_0 = 0.50$ ) and CdTe ( $m_e/m_0 = 0.11$ ,  $m_h/m_0 = 0.35$ ).<sup>33</sup> Holes in  $\text{CH}_3\text{NH}_3\text{SnI}_3$  have lower effective mass than the corresponding electrons, pointing to the high hole mobility in these compounds.<sup>76,137,138</sup> For cubic  $\text{CsSnX}_3$ , QSGW calculations predict hole effective masses decrease moving down the halogen group ( $\text{Cl} > \text{Br} > \text{I}$ ).<sup>117</sup> Considering mobility is inversely proportional to carrier effective mass ( $\mu \propto [m^*]^{-1}$ ), it is evident from the electronic structure why MHPs exhibit balanced, or ambipolar, electron and hole drift/diffusion lengths, which has been verified in a number of experimental studies.<sup>139,140</sup> Ambipolar transport has been invoked to explain the absence of photoluminescence intermittency, or blinking, in isolated  $\text{CH}_3\text{NH}_3\text{PbBr}_3$  nanoparticles with size on the order of 200 nm.<sup>141</sup> Consequently, 2D and 3D MHPs can serve as efficient intrinsic transport layers in p-i-n junctions.<sup>142–147</sup> See section 5.1 for further discussion.

MHPs can be considered a special class of sp semiconductors. Namely, they exhibit inverted electronic structure relative to conventional III–V compounds like GaAs, which has substantial As 4p character in the upper VB and Ga and As 4s character in the lower CB.<sup>113,148–151</sup> The unique electronic structure at the band edge of MHPs gives rise to a positive deformation potential ( $\alpha_v$ ),<sup>117,129,152,153</sup> described by the relation

$$\alpha_v = \frac{\partial E_g}{\partial \ln V} > 0 \quad (6)$$

where  $V$  is the unit volume. Such a relationship has been probed by monitoring changes in optical properties as a function of temperature and pressure.<sup>132,154</sup> Upon lattice contraction, covalent Pb 6s and I 5p antibonding interactions at the VBM are enhanced, causing an increase in the energy of the antibonding states. The nonbonding character of the CBM is little affected by lattice deformations. Therefore, a raised VBM and relatively constant CBM results in bathochromic absorption shifts upon lattice contraction, contrary to what is typically observed in conventional semiconductors with bonding and antibonding interactions comprising the VBM and CBM, respectively.<sup>155</sup> Previous studies of IV–VI Pb-based

compounds reveal similar positive deformation potentials relative to MHPs.<sup>33</sup> It is important to note that calculations on  $\text{CsSnX}_3$  suggest temperature-dependent absorption and PL shifts stem principally from changes in lattice dimensions rather than altered electron–phonon interactions.<sup>156</sup>

The electronic structure also has important consequences for the structural properties of perovskites. Post-transition metals display the well-known “inert-pair” effect.<sup>157,158</sup> That is, they tend to exhibit oxidation states two less than their respective valence group with general electronic configuration  $d^{10}s^2p^0$  [e.g., Pb(II) and Bi(III)]. On the basis of classical methodologies,<sup>159</sup> it is reasonable to expect the lone pair of valence electrons to actively drive stereochemistry, favoring formation of asymmetrical structures. However, compounds containing identical metal centers with identical oxidation states may or may not show signs of the stereochemically active lone pair effect. For example, Pb(II)S crystallizes in the undistorted rocksalt structure, while Pb(II)O adopts a distorted litharge motif.<sup>157</sup> Thus, electronic configuration of the metal center is only part of the picture. The anion plays a role as well. Manifestation of the lone pair behavior can be rationalized through specific orbital interactions between the two components. Increased interaction between metal s and anion p (greater metal s character in the upper VB) causes distortion to become energetically favorable through interaction with unfilled metal p orbitals.<sup>157</sup> For MHPs, such effects are important considerations in the pursuit of new compositions. The 5s and 6s levels of Sn and Pb, respectively, are energetically distant enough from halide p states due to relativistic interactions that  $(\text{Pb/Sn})\text{X}_6$  octahedra are typically only minimally distorted,<sup>138,160</sup> with some notable exceptions such as the ferroelectric distortion in  $\text{CH}_3\text{NH}_3\text{SnBr}_3$ .<sup>161</sup> Stronger orbital mixing between Ge 4s and halide states in the upper VB, and thus activation of the lone pair effect, has been invoked to explain the band edge shift observed in  $\text{AGeI}_3$  compounds upon incorporation of various A-site cations.<sup>134</sup>  $\text{AGeCl}_3$  compounds represent a rather limiting case, where low-lying Cl 3p states can effectively hybridize with Ge 4s states, giving rise to highly distorted octahedra that are better characterized as (3 + 3) trigonal-pyramidal coordination, with Ge–Cl distances ranging from 2.3 to 4.33 Å.<sup>162</sup> Such exaggerated distortion is responsible for high ionic conductivity observed in the cubic phase of  $\text{AGeCl}_3$  perovskites<sup>163</sup> (section 5.2) and ferroelectricity in the rhombohedral phase of  $\text{CsGeCl}_3$ .<sup>164,165</sup>

The band gap of MHPs is sensitive to composition of the anion. Within a homologous set of compounds, the band gap follows the trend  $\text{Cl} > \text{Br} > \text{I}$ .<sup>117,166</sup> The predominant impact of halide substitution is modulation of the upper VB as a result of the large halide  $p$  contribution at these energies. Conversely, largely nonbonding character in the lower CB makes it relatively insensitive to anion chemistry. Figure 7 shows the band structure and partial DOS (pDOS) of a series of cubic  $\text{CsSnX}_3$  compounds calculated using QSGW (excluding SOC).<sup>117</sup>  $\text{CsSnCl}_3$  exhibits the largest  $E_g$  relative to  $\text{CsSnBr}_3$  and  $\text{CsSnI}_3$  as a result of lower-lying halide  $p$  levels comprising the antibonding upper VB. The CB on the other hand shows similar character across all three compounds.

Generally, reduction in dimensionality of the 3D perovskite structure, leading to formation of layered 2H-type and other lower-dimensionality (LD) compounds (section 1.1), increases  $E_g$ .<sup>114,167,168</sup> Furthermore, considering a family of structures composed of the same metal halide octahedra, the lowest energy electronic transition follows the monotonic trend  $E_{g,3\text{D}} < E_{g,2\text{D}} < E_{g,1\text{D}} < \text{HOMO-LUMO}_{0\text{D}}$ . As the network of  $[\text{B(II)}\text{X}_6]^{4-}$  octahedra decreases in dimensionality, the bandwidth of both the CB and VB is reduced accordingly, resulting in a greater energy difference between the VB maximum and CB minimum. Reduced band dispersion is particularly evident along the vertical direction (orthogonal to the organic–inorganic interface) in the first Brillouin zone of layered 2D compounds compared to their 3D counterparts.<sup>127,149,167</sup> Anisotropy of the electronic structure is evidenced by much larger photocurrent response in the quantum well plane than along the perpendicular axis (across the organic–inorganic interface).<sup>169</sup> Inclusion of dielectric and quantum confinement effects can further increase the disparity between the optoelectronic characteristics of 3D and LD structures (sections 3 and 4.1.1).<sup>170</sup> The two extremes are therefore the relatively isotropic 3D perovskite semiconductors with highly dispersed bands and 0D octahedral  $[\text{B(II)}\text{X}_6]^{4-}$  clusters with discrete molecular-like transitions. 2D and 1D materials exhibit intermediate electronic structures that bridge the gap between the two limiting cases. For 2D layered perovskites in particular, additional degrees of electronic tunability, including tractable dielectric and quantum confinement effects, are afforded by modifying the number of adjacent inorganic sheets ( $n$ ) along the crystallographic axis perpendicular to the organic interlayer ( $n = 1, 2, 3, \dots, \infty$ ; see section 1.1) and through modification of organic cation chemistry (section 4.1.1).<sup>129,171–173</sup> These intermediary multilayer quantum well structures provide transitional properties between 2D and 3D compounds, with larger  $n$  tending more toward the properties of isotropic structures.

## 2.1. Spin–Orbit Coupling

Owing to the high atomic mass elements in main group MHPs, relativistic effects dramatically influence their electronic properties. One important consequence is stabilization of Pb(II) against oxidation due to the contracted 6s orbital. Moving up group IV, elements become more prone to losing their s electrons (and also exhibit higher lying VBM in the MHP structure), making oxidation of Sn(II) to Sn(IV) more facile than Pb(II) to Pb(IV).<sup>118,166</sup> Another important relativistic phenomenon is spin–orbit coupling (SOC), which occurs within nonspherical atomic orbitals and becomes more prevalent with increasing atomic mass. It arises due to mixing of two sources of electron angular momentum: (i) electron

motion in p, d, and f orbitals and (ii) electron spin around its own axis in a clockwise or counterclockwise fashion ( $m_s = \pm 1/2$ ). Electron orbital and spin angular momentum are thus coupled in either a partially constructive or destructive manner.<sup>174</sup> It is important to note that spin–orbit splitting is to first approximation a function of the elements themselves and not the structural properties of the solids they comprise.<sup>175</sup> Of course, the specific bonding scheme and electronic structure will dictate where SOC effects manifest.

The most apparent implication of SOC in MHPs is splitting and loss of degeneracy in states near the CBM, causing significant narrowing of the band gap.<sup>124,149,176,177</sup> A comparison of electronic structure of cubic  $\text{CsPbI}_3$  without and with SOC effects is shown in Figure 8 (panels A and B,

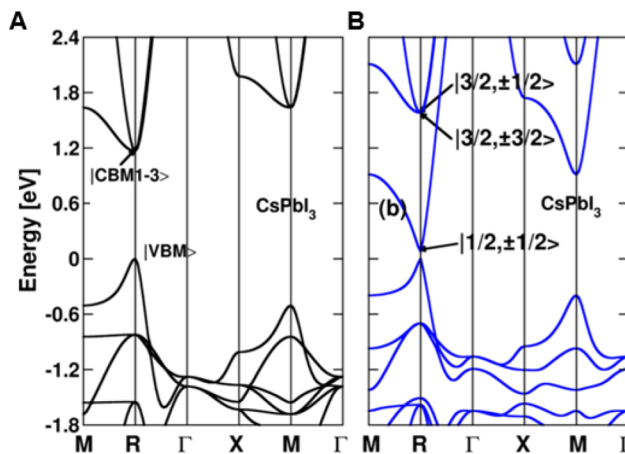


**Figure 8.** Electronic band structure of cubic  $\text{CsPbI}_3$  calculated using DFT (A) without and (B) with spin–orbit corrections. Reprinted from ref 177. Copyright 2013 American Chemical Society.

respectively).<sup>177</sup> Note that the electronic structure is derived from DFT and thus is not representative of the true  $E_g$ . However, the basic influence of SOC can still be captured at this level of calculation. SOC markedly splits the 3-fold degenerate CBM into a lower-energy 2-fold degenerate CBM and higher-energy 4-fold degenerate states at the R point. This splitting in  $\text{APbI}_3$  perovskites can be on the order of the band gap itself (~1 eV).<sup>119</sup> Because relativistic effects scale with atomic mass, SOC is enhanced roughly 3-fold in Pb perovskites compared to their Sn analogues.<sup>125</sup> As such, spin–orbit splitting of the CBM in Sn perovskites is approximately 0.4 eV.<sup>117</sup> This is a direct result of the large metal  $p$  contribution to the lower CB. Again, such behavior is inverted relative to typical sp semiconductors like GaAs, where SOC causes splitting of the upper VB due to the anion  $p$  character. SOC has also been shown to effect band dispersion. Inclusion of spin–orbit interactions in GW calculations significantly increases dispersion, resulting in lower electron and hole effective masses.<sup>118</sup> Recently it has been proposed that dispersion is altered so dramatically by SOC that the band extrema can no longer be treated with the standard parabolic approximation, yielding effective masses that vary substantially with direction in  $k$ -space.<sup>118,119</sup> However, results from experimental magneto-absorption studies appear to indicate parabolic band extrema in  $\text{CH}_3\text{NH}_3\text{PbI}_3$  (section 4.1.1).<sup>136,178</sup> Further experimental work is required to reconcile the extent of nonparabolicity near the MHP band edge.

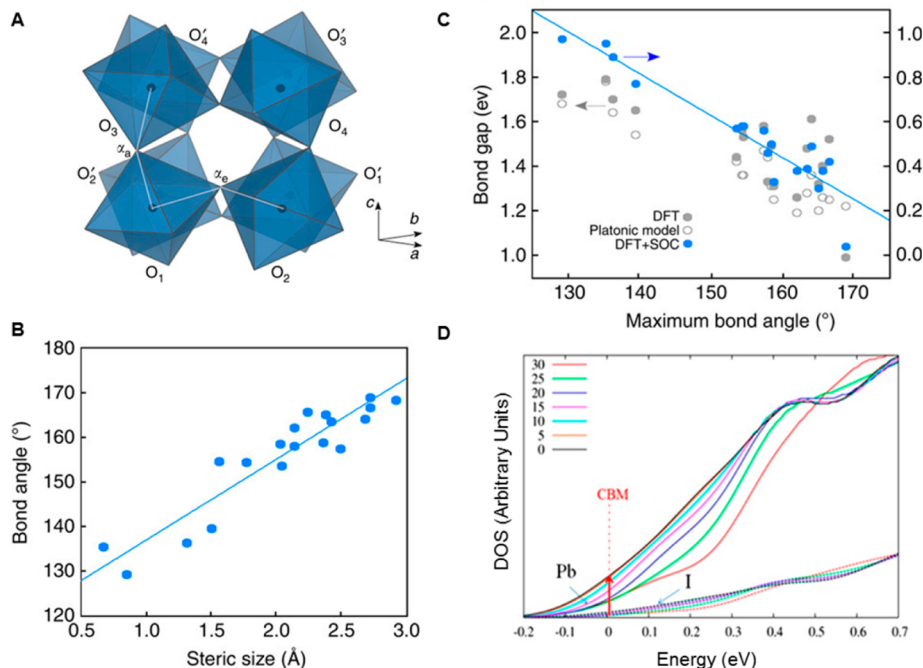


**Figure 9.** (A) Platonic model of octahedral tilting highlighting apical ( $\alpha_a$ ) and equatorial ( $\alpha_e$ ) B—X—B bond angles. (B) Effect of A-site cation steric size on the largest calculated bond angle. (C) Correlation between the largest calculated B—X—B bond angle for a given cation and the band gap. (A—C) reprinted by permission from Macmillan Publishers Ltd.: Nature Communications (ref 78), copyright 2014. (D) Pb 6p (solid lines) and I 5p (dashed lines) contributions to the CBM as a function of octahedral tilting around the *c* axis ( $0^\circ$ – $30^\circ$ ) in CsPbI<sub>3</sub>. Reprinted from ref 124. Copyright 2014 American Chemical Society.

## 2.2. Indirect Influence of A-Site Cations

**2.2.1. Structural Templating.** The A-site component serves principally as a counterion for charge balance and physical stabilization, but its influence on octahedral orientation and dimensionality leads to profound effects on electronic structure. As established at the beginning of section 2, these cations, whether inorganic or organic, generally do not directly contribute to frontier orbitals in MHPs. Cs<sup>+</sup> 5d states do contribute to the upper CB,<sup>117</sup> and a slight contribution to the CB from CH<sub>3</sub>NH<sub>3</sub><sup>+</sup> cations has been predicted by DFT.<sup>135</sup> But these minor electronic characteristics cannot account for the relatively large disparity in band gaps among homologous compounds with different A-site components. We are not concerned here with the obvious electronic changes that accompany a transition from 3D to 2D motifs upon incorporation of large cations. Instead, we focus on the subtleties associated with organic and inorganic A-site cations that yield 3D MHPs but differ in size, composition, and stereochemistry.

Based strictly on the positive deformation potential (eq 6) of MHPs as discussed above,<sup>117,152,153</sup> structures containing smaller A-site cations with reduced cell volumes should exhibit smaller band gaps. Indeed, several recent theoretical reports have come to such a conclusion.<sup>103,153</sup> While it is possible that this relationship holds in certain cases, for many MHPs the situation is more complex. For example, CsPbX<sub>3</sub> has a larger band gap relative to comparable CH<sub>3</sub>NH<sub>3</sub>PbX<sub>3</sub> and HC(NH<sub>2</sub>)<sub>2</sub>PbX<sub>3</sub> perovskites at room temperature despite a contracted lattice as a result of the smaller Cs<sup>+</sup> cation. And likewise, the larger formamidinium cation induces a narrower band gap relative to its methylammonium analogue. These seemingly contradictory observations stem from the fact that in addition to lattice dilation and contraction, the size and nature

of A-site cations drives reorientation of BX<sub>6</sub> octahedral units.<sup>133</sup> In effect, the A-site species serves as a templating agent for the inorganic motif. Therefore, because electronic properties are highly sensitive to B—X interactions, A-site cation size alone is not a sufficient predictive parameter for determining optoelectronic characteristics. Comprehensive structural elucidation is necessary to fully understand the interplay between volume, symmetry, and electronic structure.

A more robust correlation between monovalent cation and band gap can be found by closer investigation of B—X interactions in the presence of various cations. Filip et al. utilized a geometric platonic model, analogous to the original framework developed by Glazer,<sup>179</sup> to study the influence of octahedral tilting on MHP band gap.<sup>78</sup> Relevant parameters extracted from this model are the B—X—B apical and equatorial bond angles as a function of octahedral rotation (Figure 9A), which, according to this approach, play a dominant role in dictating electronic structure compared to changes in B—X bond length. As shown in Figure 9B, there is a linear correlation between size of the A-site cation and maximum bond angle in APbX<sub>3</sub>. Larger cations yield larger angles (increased B—X—B linearity). Extending this further, the band gap is then predicted to be inversely proportional to the maximum bond angle (Figure 9C). Such a relationship stems from the link between bond angle, band edge pDOS, and SOC. Calculations by Amat and co-workers suggest that structures with a lower degree of octahedral tilting exhibit greater metal p character at the CBM (Figure 9D).<sup>124</sup> Considering the discussion in section 2.1, greater metal contribution enhances SOC, which in turn leads to larger spin-orbit splitting of the CBM and a reduced band gap. It has been noted that without pronounced SOC effects, CH<sub>3</sub>NH<sub>3</sub>PbX<sub>3</sub> and HC(NH<sub>2</sub>)<sub>2</sub>PbX<sub>3</sub> would exhibit nearly

identical band gaps with incorporation of the same halide anion.<sup>124</sup>

The interplay between unit volume and octahedral distortion is apparent across phase changes in MHPs. Prior to transition to the low-temperature orthorhombic phase in  $\text{CH}_3\text{NH}_3\text{PbI}_3$ , decreasing temperature results in a red shift of the absorption onset in accord with the positive  $\alpha_v$  at the direct transition. This bathochromic shift occurs despite a concomitant decrease in average Pb—I—Pb bond angle from  $\sim 180^\circ$  at high temperature to  $\sim 165^\circ$  just before the low-temperature transition, as determined by neutron powder diffraction measurements.<sup>180</sup>

Evidently octahedral distortion is not sufficient to overcome the influence of lattice contraction over this temperature range. Besides, the platonic model correlates the maximum B—X—B angle to band gap (Figure 9C), which in this case remains  $180^\circ$  throughout the entire tetragonal temperature range. Across the tetragonal to orthorhombic transition at 161 K,<sup>181</sup> the band gap abruptly increases as a result of greater octahedral tilting in the latter.<sup>180</sup> The same temperature-induced red shift then continues within the orthorhombic phase upon further temperature reduction.<sup>182–184</sup> It is therefore imperative that computational studies aimed at elucidating electronic properties are performed with high structural accuracy for the phase of interest, especially when making direct comparison to experimental results, as recently cautioned.<sup>124</sup>

**2.2.2. Dynamic Disorder.** Templing effects of A-site cations are important but well established. Only recently have a number of more intriguing phenomena come to light. Particularly interesting effects arise with A-site cations that exhibit three distinct characteristics: (i) permanent dipole moment, (ii) dynamic reorientation within the cubooctahedral cage, and (iii) structural asymmetry. The archetypal compound for studying effects related to these qualities has been, not surprisingly, the methylammonium cation ( $\text{CH}_3\text{NH}_3^+$ ).  $\text{CH}_3\text{NH}_3^+$  is asymmetric with a sizable permanent dipole (2.3 D).<sup>153</sup> A myriad of experimental and computational studies over the last three decades have been devoted to elucidating the dynamic disorder of  $\text{CH}_3\text{NH}_3^+$  within the MHP structure.<sup>180,181,185–188</sup> Results consistently indicate these molecular cations, which interact with the inorganic framework through electrostatics and to some extent hydrogen bonding,<sup>124</sup> do in fact undergo rotation around the C—N axis and tumbling reorientation in higher temperature phases. Several possible tumbling modes of  $\text{CH}_3\text{NH}_3^+$  deduced from recent quasielastic neutron diffraction measurements are shown in Figure 10A.<sup>186</sup> Conversely,  $\text{CH}_3\text{NH}_3^+$  reorientation is inhibited in the low-temperature orthorhombic phase and such dynamic disorder is not observed.

Rotational degrees of freedom of dipoles within the perovskite structure enables molecular cations to respond to external perturbations. This has important consequences for the dielectric characteristics of these materials. A useful exercise is to examine the response of  $\text{CH}_3\text{NH}_3\text{PbI}_3$  at various temperatures. An illustration of the real part of the complex dielectric function [ $\epsilon(\omega) = \epsilon_1(\omega) + i\epsilon_2(\omega)$ ] in the low temperature (LT) orthorhombic and room temperature (RT) tetragonal phases is shown in Figure 10B,<sup>189</sup> where  $\epsilon_1(\omega)$  is related to polarizability of the medium in response to an oscillating electric field. Because polarization is frequency-dependent, it is convenient to discuss limiting cases known as the static [ $\epsilon_s = \lim_{\omega \rightarrow 0} \epsilon_1(\omega)$ ] and high-frequency or optical [ $\epsilon_\infty = \epsilon_1(\sim 10^{15} \text{ Hz})$ ] dielectric constants.  $\epsilon_s$  is associated with coupling of all polarizable

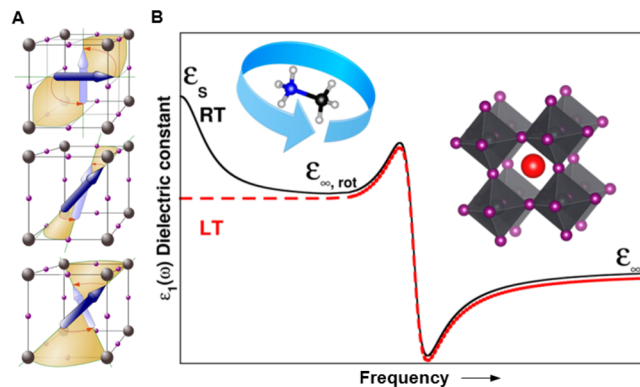


**Figure 10.** (A) High probability tumbling modes of  $\text{CH}_3\text{NH}_3^+$  in the room temperature tetragonal and high temperature cubic phases of  $\text{CH}_3\text{NH}_3\text{PbI}_3$ . Conical reorientation pathways determined using quasielastic neutron scattering are along the faces (top), edges (middle), and corners (bottom). Reproduced with permission from ref 186 under CC BY 4.0. (B) Schematic illustration of the relative enhancement in the static dielectric constant ( $\epsilon_s$ ) at room temperature due to rotational motion of  $\text{CH}_3\text{NH}_3^+$ . Contributions to the high-frequency dielectric response ( $\epsilon_\infty$ ) are from vibrational polar phonon modes associated with the inorganic lattice, thus eliminating any significant temperature dependence in this regime. Adapted from ref 189. Copyright 2014 American Chemical Society.

elements within the lattice (dipoles, ions, and electrons), while only electronic perturbations contribute to  $\epsilon_\infty$ .<sup>190</sup> For scale in Figure 10B, the plateau of  $\epsilon_\infty$  in  $\text{CH}_3\text{NH}_3\text{PbI}_3$  is 6.5 (ref 191) and  $\epsilon_s$  is 36 at LT (20 K) and 62 at RT (ref 181). In the high frequency limit, the main contributions to  $\epsilon_1$  are vibrational polar phonon modes within the inorganic lattice, thus  $\epsilon_\infty$  is comparable in the RT tetragonal and low-temperature orthorhombic phases.<sup>189</sup> However, in the static limit there is a large deviation in the response, with the tetragonal phase increasing rapidly in the vicinity of  $\epsilon_s$ . Even et al. attribute this large discrepancy to rotational motion of  $\text{CH}_3\text{NH}_3^+$ .<sup>189</sup> This same mechanism does not come into play in the orthorhombic phase where molecular cations are unable to reorient. The dielectric constant has important implications for Coulombic interactions between electrons and holes. This is discussed at length in section 4.1.

### 3. LINEAR ABSORPTION AND PHOTOLUMINESCENCE

#### 3.1. Absorption Coefficient, Optical Transitions, and Urbach Energy

Semiconductor optical absorption at a given frequency is a function of two primary factors: (i) the joint DOS (JDOS) and (ii) the transition matrix from states in the VB to states in the CB. This link between a material's electronic structure and its absorption properties can be approximated using Fermi's golden rule, which for a VB ( $v$ ) to CB ( $c$ ) transition has the form<sup>124</sup>

$$W_{\vec{k}} \cong \frac{2\pi}{\hbar} |v| |\mathcal{H}'| c^2 \delta[E_c(\vec{k}) - E_v(\vec{k}) - \hbar\omega] \quad (7)$$

where  $\mathcal{H}'$  is the dipole operator and the second term represents the JDOS. Such analysis has been used to discern the origin of disparate absorption characteristics among various MHPs and to compare optical responses of MHPs to more conventional semiconductors.<sup>124,135,192</sup> An important feature of 3D MHPs is their relatively large absorption coefficient, which in part enables high photocurrent output using submicron films

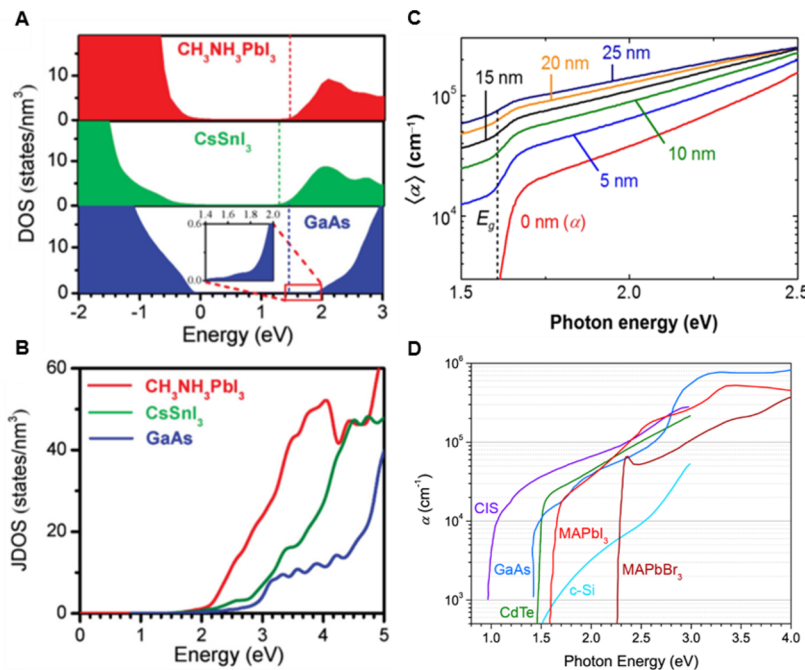


**Figure 11.** (A) Comparison of the DOS of  $\text{CH}_3\text{NH}_3\text{PbI}_3$ ,  $\text{CsSnI}_3$ , and GaAs. (B) Calculated JDOS of the compounds in (A). (A and B) reproduced with permission from ref 192. Copyright 2014 John Wiley and Sons. (C) Influence of film surface roughness on the calculated absorption coefficient. Reprinted with permission from ref 193. Copyright 2016 by the American Physical Society. (D) Experimentally determined absorption coefficients for  $\text{CH}_3\text{NH}_3\text{PbI}_3$  (MAPbI<sub>3</sub>) (ref 193),  $\text{CH}_3\text{NH}_3\text{PbBr}_3$  (MAPbBr<sub>3</sub>) (ref 198), GaAs (ref 199), and a number of other PV-relevant direct gap materials and indirect gap c-Si taken from ref 193.

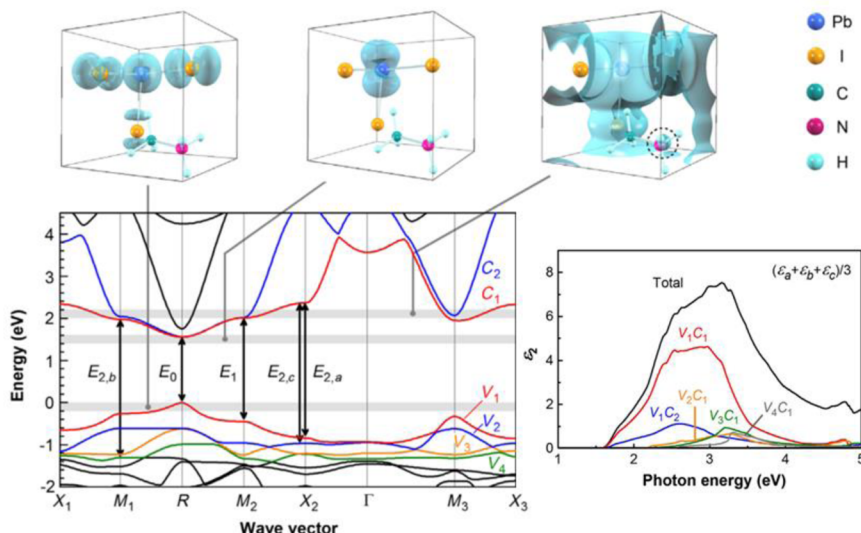


**Figure 12.** Band structure of pseudocubic  $\text{CH}_3\text{NH}_3\text{PbI}_3$  determined using DFT. High-probability optical transitions determined using polarization-dependent DFT. Contributions from these various transitions to the overall  $\epsilon_2$  spectrum are given. Reprinted with permission from ref 193. Copyright 2016 American Physical Society.

of compounds like  $\text{CH}_3\text{NH}_3\text{PbI}_3$  and  $\text{HC}(\text{NH}_2)_2\text{PbI}_3$ . In addition to the direct gap nature of most MHPs, intense optical absorption stems from the halide-*p* → metal-*p* transition at the band edge. Because *p* orbitals have inherently less dispersion than *s* orbitals, JDOS near the fundamental electronic absorption edge has been predicted to be relatively large in MHPs.<sup>192</sup> Calculations by Yin et al. suggest  $\text{CH}_3\text{NH}_3\text{PbI}_3$  and GaAs have commensurate transition matrices. However, as discussed in section 2, the CBM of GaAs is composed of cation *s* orbitals, yielding a lower DOS compared to  $\text{CH}_3\text{NH}_3\text{PbI}_3$  (and  $\text{CsSnI}_3$ ) primarily at the CBM

(Figure 11A).<sup>192</sup> The full JDOS from this analysis also indicates a substantially larger density of states in the MHPs (Figure 11B).<sup>192</sup> In accordance with eq 7, these properties should provide  $\text{CH}_3\text{NH}_3\text{PbI}_3$  and other analogous 3D MHPs with improved absorption characteristics relative to GaAs. Surveying the literature, reported band edge  $\alpha$  values for  $\text{CH}_3\text{NH}_3\text{PbI}_3$  (just above the Urbach tail) vary over nearly an order of magnitude from  $\sim 6 \times 10^3$  to  $\sim 4.5 \times 10^4 \text{ cm}^{-1}$ .<sup>139,192–197</sup>

Shirayama et al. suggest these widely varying and often overestimated  $\alpha$  values stem from two surface-related phenomena: (i) formation of a hydrate layer and (ii)

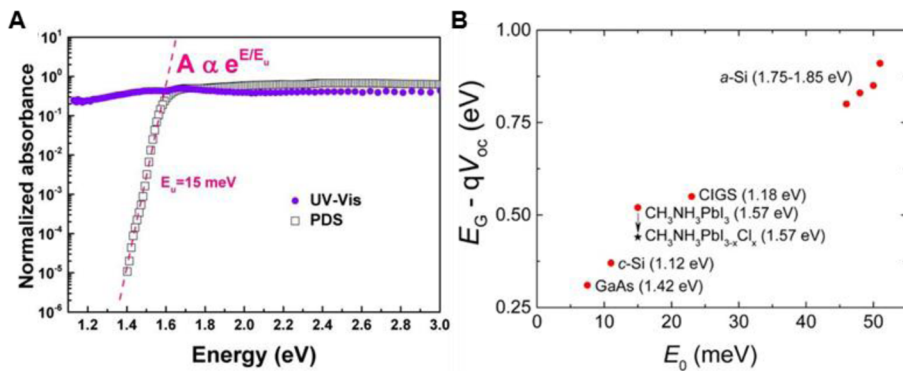


**Figure 13.** (A) UV-vis and photothermal deflection spectra (PDS) of a  $\text{CH}_3\text{NH}_3\text{PbI}_3$  thin film. The dashed line shows the linear fit used to ascertain the Urbach energy. Reproduced from ref 204. Copyright 2014 American Chemical Society. (B) Empirical relationship between the lowest reported Urbach energy ( $E_0$ ) and  $E_g - qV_{\text{oc}}$  energy differential for a number of compounds commonly used in PV applications. Reproduced from ref 205. Copyright 2014 American Chemical Society.

roughness.<sup>193</sup> The hydrated surface layer is purported to be the typical 0D compound  $(\text{CH}_3\text{NH}_3)_4[\text{PbI}_6] \cdot 2\text{H}_2\text{O}$ . However, monohydrate formation is perhaps more likely.<sup>200,201</sup> And recent calculations suggest the ready formation of a lower hydrate with 4:1  $\text{CH}_3\text{NH}_3\text{PbI}_3:\text{H}_2\text{O}$  stoichiometry.<sup>202</sup> Regardless of the precise phase, formation of this layer modifies  $\alpha$  most significantly at photon energies  $\geq 3$  eV due to the hydrate's large band gap (vide supra) and the high surface sensitivity at these frequencies resulting from shallow photon penetration depths ( $\sim 20$  nm at 3.4 eV).<sup>193</sup> While proper precautions can preclude deleterious effects of hydrate formation, typical solution-based thin film deposition methods inherently yield rough surfaces. A simulation of the apparent  $\alpha$  derived from the effective-medium approximation with a surface roughness layer thickness ranging from 0–25 nm is shown in Figure 11C.<sup>193</sup> Clearly, roughness has a marked impact, artificially enhancing apparent absorption across the entire visible spectrum, especially near the band edge. A characteristic feature that arises with increasing roughness is nonzero absorption extending well below  $E_g$ , which also hinders accurate determination of the band gap when using the Tauc method. Such effects can be difficult to address empirically or theoretically, indicating that extremely high quality thin films are necessary to accurately determine the optical properties of MHPs. The absorption coefficient of a  $\text{CH}_3\text{NH}_3\text{PbI}_3$  (MAPbI<sub>3</sub>) thin film prepared by laser evaporation is provided in Figure 11D,<sup>193</sup> along with  $\text{CH}_3\text{NH}_3\text{PbBr}_3$  (MAPbBr<sub>3</sub>) and a number of other PV-relevant semiconductors. The broadband absorption of  $\text{CH}_3\text{NH}_3\text{PbI}_3$ , with  $E_g = 1.61$  eV as determined by critical point analysis,<sup>193</sup> is on par with GaAs and CdTe, and even slightly greater at moderate energies ca. 2.5 eV. Still, the supposed order-of-magnitude larger  $\alpha$  in  $\text{CH}_3\text{NH}_3\text{PbI}_3$  versus GaAs as predicted by DFT does not hold when high quality thin films are utilized.<sup>192</sup>

$\text{CH}_3\text{NH}_3\text{PbI}_3$  shows a number of high probability transitions above its band edge. These correspond to the shoulders observed in the room-temperature absorption spectrum. Critical point analysis of the DFT-derived electronic structure has been used to determine the origin of various transitions across visible and near-UV frequencies.<sup>193</sup> This analysis is shown in Figure 12 for pseudocubic  $\text{CH}_3\text{NH}_3\text{PbI}_3$ . Also shown are the charge density profiles in the vicinity of the indicated high-intensity transitions. Note that the electronic structure here does not include relativistic effects, and thus secondary transitions resulting from spin-off bands are not encompassed

in these calculations. However, SOC-DFT reveals similar transition energies and matrix elements,<sup>189</sup> as discussed in relation to the nonlinear absorption spectrum in section 4.2. The majority of the total absorption results from direct transitions between the highest VB (V1) and lowest lying CB (C1) at the  $R$ ,  $M_2$ , and  $X_2$  high symmetry points. Other secondary contributions include transitions from V1 to a higher energy CB (C2) and various lower energy VBs (V2, V3, and V4) to C1.

In addition to general interband transitions, an important piece of information that can be garnered from linear absorption spectra is the general degree of structural disorder and distribution of subgap states. Fluctuations in electrostatic potential at the band edge caused by disorder or impurities gives rise to an exponentially increasing density of states approaching the unperturbed continuum. This phenomenological relationship near the onset of optical absorption is known as the Urbach tail and can be described by  $d(\ln \alpha)/d(h\nu) = (k_B T)^{-1}$ .<sup>33,203</sup> If, for example, we assume interband transitions occur from a parabolic VB into exponentially distributed tail states of the CB, we can arrive at the familiar expression for the Urbach energy ( $E_u$  or  $E_0$ )

$$E_u = \left[ \frac{d(\ln \alpha)}{d(h\nu)} \right]^{-1} \quad (8)$$

with the density of subgap states in the tail at a given energy proportional to  $e^{E/E_u}$ .<sup>33</sup> A smaller  $E_u$  (i.e., steeper slope on a semilog plot) indicates less disorder and a narrower distribution of states near the band edge. Several studies have utilized a sensitive technique known as photothermal deflection spectroscopy (PDS), which probes heating caused by nonradiative recombination of photogenerated carriers, to examine  $\alpha$  in the range of the Urbach tail.<sup>204,205</sup> One example of such analysis for  $\text{CH}_3\text{NH}_3\text{PbI}_3$  is given in Figure 13A, which shows  $\alpha$  as determined by highly sensitive PDS and typical UV-vis spectrophotometry.<sup>204</sup> The linear fit of the absorption tail yields  $E_u = 15$  meV. An identical value has been ascertained in a separate study.<sup>205</sup> Recent results from Fourier-transform photocurrent spectroscopy (FTPS) indicate a similar  $E_u$  of 16.4 meV in  $(\text{FA}_{0.83}\text{Cs}_{0.17})\text{Pb}(\text{I}_{0.6}\text{Br}_{0.4})_3$ ,<sup>43</sup> allowing a greater degree of generality when discussing limited formation of subgap states in MHPs. Through the compositional range of the mixed halide compound  $\text{CH}_3\text{NH}_3\text{Pb}(\text{I}_{1-x}\text{Br}_x)_3$ ,  $E_u$  is lowest for  $x = 0$ , increases monotonically to a peak value of  $\sim 90$  meV

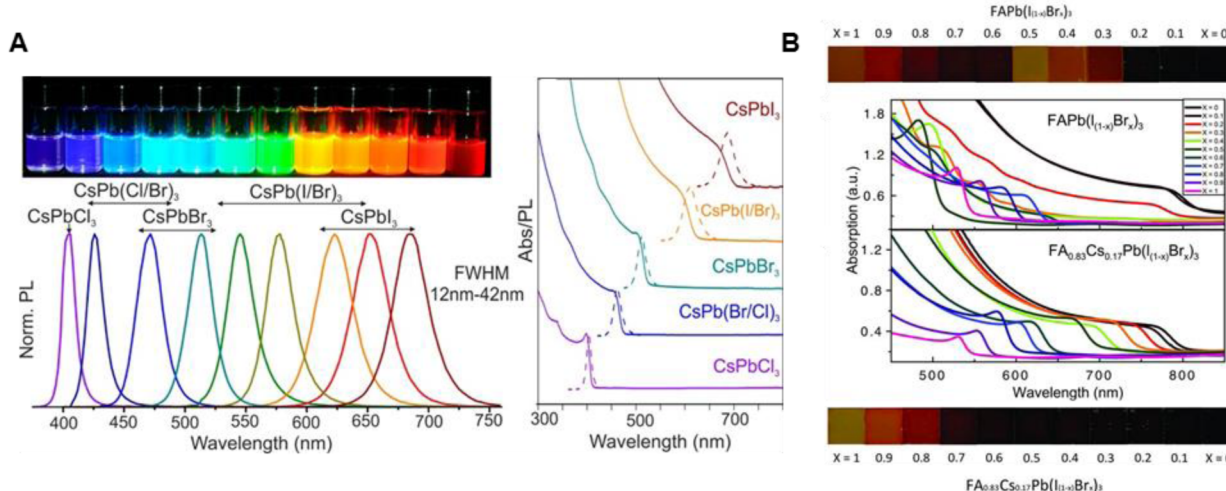


**Figure 14.** (A) Absorbance and photoluminescence of CsPbX<sub>3</sub> (X = Cl, Br, and I) nanocrystals showing their broadband tunability. Reproduced from ref 82. Copyright 2015 American Chemical Society. (B) Absorption spectra of FAPb(I<sub>1-x</sub>Br<sub>x</sub>)<sub>3</sub> and (FA<sub>0.83</sub>Cs<sub>0.17</sub>)Pb(I<sub>1-x</sub>Br<sub>x</sub>)<sub>3</sub>. Photographs of the thin films are also shown. From ref 43. Reprinted with permission from AAAS.

at  $x = 0.8$ , and then again decreases to  $\sim 25$  meV at  $x = 1$ .<sup>204</sup> Such behavior highlights the variable degrees of disorder in I:Br solid solutions, which primarily stems from phase instability due to a tetragonal  $\rightarrow$  cubic transition with increasing Br content.<sup>206</sup>

With knowledge of the characteristic CH<sub>3</sub>NH<sub>3</sub>PbI<sub>3</sub> Urbach energy, it is useful to examine how it compares with other materials. De Wolf et al. have noted a linear empirical relationship between a material's lowest reported room temperature  $E_u$  and  $(E_g - qV_{oc})$ , where  $q$  is the elementary charge and  $V_{oc}$  represents the largest reported open-circuit voltage for a given compound when serving as the active layer in a PV device (Figure 13B).<sup>205</sup> While  $V_{oc}$  is sensitive to device architecture and processing, its thermodynamic limit for a given material occurs when all recombination is radiative, otherwise known as the "radiative limit".<sup>207,208</sup> In this case, a material's intrinsic propensity for efficient energy conversion can be expressed as  $qV_{OC} = E_g - T\Delta S - k_B T \ln iPLQY$ , where  $S$  is the entropy and  $iPLQY$  is the internal photoluminescence quantum yield.<sup>209,210</sup> Because subgap states act as prominent non-radiative recombination channels, particularly at the relatively low carrier densities in PV operation (section 4.3), the general trend between  $E_u$  and  $(E_g - qV_{oc})$  is rather intuitive. Despite low-temperature processing, the fact that CH<sub>3</sub>NH<sub>3</sub>PbI<sub>3</sub> and other MHPs have Urbach energies comparable to c-Si (11 meV) and lower than that of CIGS is a testament to their high semiconducting quality and relative resilience to formation of deep electronic defects.

### 3.2. Chemistry and Dimensionality

After discussing at length the influence of chemical and structural modifications on MHP electronic structure in section 2, it is worthwhile to briefly examine how these parameters affect optical properties as well. Within a given dimensionality, optical response is most readily modified through substitution of the halide component, which primarily alters the VB position. Mixed-halide nanocrystals of CsPb(Br<sub>1-x</sub>Cl<sub>x</sub>)<sub>3</sub> together with CsPb(I<sub>1-x</sub>Br<sub>x</sub>)<sub>3</sub> provide PL tunability from  $\sim 400$ –700 nm and PLQYs of 50–90% (Figure 14A).<sup>82</sup> In contrast, (FA<sub>1-x</sub>Cs<sub>x</sub>)PbI<sub>3</sub> offers comparably less optical tractability, with  $E_g$  residing in the limited range from 1.48 eV ( $x = 0$ ) to 1.73 eV ( $x = 1$  and in the high temperature cubic phase).<sup>206</sup> Band gap

variation in mixed-metal MHPs results predominantly from modifications in SOC at the CB edge. An intriguing deviation from Vegard's law has been observed in CH<sub>3</sub>NH<sub>3</sub>(Sn<sub>1-x</sub>Pb<sub>x</sub>)I<sub>3</sub>, where the solid solution shows a lower band gap than pure CH<sub>3</sub>NH<sub>3</sub>SnI<sub>3</sub>.<sup>99</sup> A compilation of band gaps for various MHPs with disparate chemistries and dimensionalities is given in Table 1.

Recently, more complex alloys have been developed that involve partial substitutions at multiple lattice sites. One example is provided in Figure 14B for the solid solutions FAPb(I<sub>1-x</sub>Br<sub>x</sub>)<sub>3</sub> and (FA<sub>0.83</sub>Cs<sub>0.17</sub>)Pb(I<sub>1-x</sub>Br<sub>x</sub>)<sub>3</sub>.<sup>43</sup> In the former single-cation MHP, a phase instability arises for  $0.3 \leq x \leq 0.6$ , indicated by a drastic increase in the absorption edge and formation of yellow-orange colored thin films (top photograph in Figure 14B). Interestingly, the mixed-cation, mixed-halide MHP exhibits improved phase stability, affording the opportunity for continuous modification of  $E_g$  across most of the visible spectrum and notably in the ideal region for MHP-Si tandem PVs (1.7–1.8 eV).<sup>44,211</sup> An issue that has come to light recently in mixed-halide MHPs is photoinduced segregation of the solid solution, yielding separate domains that are rich in only one of the constituent halides.<sup>209,212,213</sup> This effect is particularly evident when  $0.5 \leq x < 1$  in AB(I<sub>1-x</sub>Br<sub>x</sub>)<sub>3</sub> compounds.<sup>209</sup> Initial evidence indicates the mixed-cation system protects against this photoinstability, although the mechanism has yet to be identified.

Significant changes in optical properties occur upon reduction in dimensionality. The most pronounced difference between 3D and LD perovskites is enhanced exciton binding energies in the latter (section 4.1.1), leading to intensified oscillator strength and optical nonlinearities.<sup>214</sup> An absorption spectrum representative of 2D MHPs is given in Figure 15A for the  $n = 1$  compound (C<sub>6</sub>H<sub>5</sub>C<sub>4</sub>H<sub>8</sub>NH<sub>3</sub>)<sub>2</sub>PbBr<sub>4</sub> at room temperature and at 6 K.<sup>215</sup> It is immediately apparent that unlike their 3D counterparts, 2D MHPs exhibit stable and sizable exciton resonances even at elevated temperatures, indicated here as the  $P$  band. The step-like feature at  $Q$  has been attributed to the onset of band edge absorption, with higher-energy interband transitions denoted  $R$  and  $S$ .<sup>215</sup> It is evident from these readily resolvable absorption features that natural-QW MHPs, with their substantial dielectric and

**Table 1. Band Gaps ( $E_g$ ) for Select MHPs with Variable Chemistries and Dimensionality<sup>a</sup>**

compound	$E_g$ (eV)	type	dimension	ref
$\text{CH}_3\text{NH}_3\text{PbI}_3$	1.61	direct	3D	193
$\text{CH}_3\text{NH}_3\text{Pb}(\text{I}_{1-x}\text{Br}_x)_3$	1.57 ( $x = 0$ ); 2.29 ( $x = 1$ )			81
$\text{CH}_3\text{NH}_3\text{PbCl}_3$	2.88			49
$\text{CH}_3\text{NH}_3(\text{Pb}_{1-x}\text{Sn}_x)\text{I}_3$ <sup>b</sup>	1.55 ( $x = 0$ ); 1.17 ( $x = 0.5$ ); 1.30 ( $x = 1$ )			99
$\text{HC}(\text{NH}_2)_2\text{Pb}(\text{I}_{1-x}\text{Br}_x)_3$	1.48 ( $x = 0$ ); 2.21 ( $x = 1$ )			206
$\text{CsPbI}_3$	1.73			206
$[\text{HC}(\text{NH}_2)_2]_{2,1-x}\text{Cs}_x\text{Pb}(\text{I}_{0.6}\text{Br}_{0.4})_3$	1.80 ( $x = 0.5$ ); 1.73 ( $x = 0.1$ )			43
$\text{CsGeI}_3$	1.60			134
$\text{CH}_3\text{NH}_3\text{GeI}_3$	1.90			134
$\text{HC}(\text{NH}_2)_2\text{GeI}_3$	2.20			134
$\text{CH}_3\text{C}(\text{NH}_2)_2\text{GeI}_3$	2.50			134
$\gamma\text{-CsSnI}_3$	1.30			117
$\text{Y-CsSnI}_3$	2.55			117
$\beta\text{-CsSnBr}_3$	1.80			117
$\alpha\text{-CsSnCl}_3$	2.90			117
$M\text{-CsSnCl}_3$	4.50			117
$\text{CH}_3\text{NH}_3(\text{Pb}_{1-x}\text{Bi}_x)\text{Br}_3$	2.17 ( $x = 0$ ); 1.89 ( $x \ll 0.1$ ) <sup>c</sup>			63
$(\text{Cs}_{1-x}\text{Rb}_x)\text{PbI}_3$ <sup>d</sup>	1.72 ( $x = 0$ ); 1.80 ( $x = 0.2$ )			78
$(\text{CH}_3\text{NH}_3)_3(\text{C}_9)_2\text{Pb}_4\text{I}_{13}$ ( $n = 4$ )	2.03	direct	2D	114
$(\text{CH}_3\text{NH}_3)_2(\text{C}_9)_2\text{Pb}_3\text{I}_{10}$ ( $n = 3$ )	2.17			114
$(\text{CH}_3\text{NH}_3)_2(\text{C}_9)_2\text{Pb}_2\text{I}_7$ ( $n = 2$ )	2.38			114
$(\text{C}_9)_2\text{PbI}_4$ ( $n = 1$ )	2.82			114
$(p\text{-FC}_6\text{H}_4\text{C}_2\text{H}_4\text{NH}_3)_2\text{PbI}_4$ ( $n = 1$ )	2.89			173
$(\text{C}_6\text{H}_5\text{C}_4\text{H}_8\text{NH}_3)_2\text{PbBr}_4$ ( $n = 1$ )	3.37			215
$\text{C}(\text{NH}_2)_3\text{GeI}_3$	2.70	indirect	1D	134
$(\text{NH}_2\text{Cl}=\text{NH}_2)_3\text{PbI}_5$	3.10	direct		134
$(\text{CH}_3\text{NH}_3)_4\text{PbI}_6\cdot 2\text{H}_2\text{O}$	3.87	direct	0D	114

<sup>a</sup>Some discrepancies exist for the reported  $E_g$ 's of various MHPs, as evidenced by slightly different values for  $\text{CH}_3\text{NH}_3\text{PbI}_3$  listed here. This results from variability in technique, sample type (crystal versus thin film), roughness, and/or moisture-related degradation, as indicated in the main text. <sup>b</sup>Anomalous deviation from Vegard's law. <sup>c</sup> $\text{Bi(III)}$  dopant concentration  $\sim 10^{19}$  cm<sup>-3</sup>. <sup>d</sup>Estimate based on absorption onset.

quantum confinement, provide textbook examples of excitonic resonance below the continuum edge. A series of temperature-dependent PL spectra for  $(\text{C}_6\text{H}_5\text{C}_4\text{H}_8\text{NH}_3)_2\text{PbBr}_4$  (C4) (Figure 15C) and the closely related compound  $(\text{C}_6\text{H}_5\text{C}_1\text{H}_2\text{NH}_3)_2\text{PbBr}_4$  (C1) (Figure 15B) are also shown. The small Stokes shift of only a few meV below the exciton absorption band in both compounds at room temperature suggests PL originates from radiative recombination of free excitons located in the inorganic well. Upon cooling below  $\sim 50$  K, exciton fine structure begins to manifest. Specifically, a second peak appears with larger Stokes shift and is particularly prominent in the C1 compound. This band, which has a much longer lifetime ( $\sim 10\text{--}100$  ns depending on the organic component) than the free exciton emission ( $\sim 1$  ns) (Figure 15D) has been assigned to recombination of triplet excitons formed through intersystem crossing from singlet exciton states.<sup>215–217</sup> Such typically forbidden excitonic transitions are

weakly allowed through spin-orbit interactions.<sup>217</sup> Differences in excitonic resonances between the two related compounds have been ascribed to discrepancies in the organic-inorganic interface, where triplet excitons have been reported to form.<sup>215,218</sup> Similar Stokes-shifted PL bands may also stem from bound exciton states depending on the nature of the organic component.<sup>219</sup> Strong exciton-phonon coupling has been reported for some 2D MHPs, suggesting the temperature-independent Stokes shift in  $(\text{C}_6\text{H}_5\text{C}_2\text{H}_4\text{NH}_3)_2\text{PbI}_4$  arises due to polaron formation.<sup>220</sup> Furthermore, atomically thin, free-standing single sheets of 2D MHPs show signs of PL from self-trapped excitons due to the greater structural deformability compared to the bulk.<sup>221</sup> Excitonic molecules (e.g., biexcitons) also play an important role in the PL and nonlinear response of 2D MHPs owing to their large binding energy.<sup>218,222</sup>

A direct link between highly confined 2D and bulk 3D MHPs can be found in the unique series of mixed 2D/3D compounds, whose structure was covered in section 1.1. In Figure 16A, the cryogenic absorption spectra of  $(\text{C}_6\text{H}_{13}\text{NH}_3)_2\text{PbI}_4$  ( $n = 1$ ),  $(\text{C}_6\text{H}_{13}\text{NH}_3)_2(\text{CH}_3\text{NH}_3)\text{Pb}_2\text{I}_7$  ( $n = 2$ ),  $(\text{C}_6\text{H}_{13}\text{NH}_3)_2(\text{CH}_3\text{NH}_3)_2\text{PbI}_{10}$  ( $n = 3$ ), and  $\text{CH}_3\text{NH}_3\text{PbI}_3$  ( $n = \infty$ ) demonstrate the increased  $E_g$  upon reduction in inorganic layer thickness ( $n$ ) due to decreased band dispersion and confinement (section 2), as well as the monotonic enhancement of oscillator strength from  $n = \infty \rightarrow n = 1$ .<sup>223</sup> A relatively continuous modification of optical properties in mixed-dimension MHPs was recently shown by Sichert et al. for perovskite nanoplatelets prepared using various proportions of  $\text{CH}_3\text{NH}_3\text{Br}$  and octylammonium bromide (OABr) (Figure 16B).<sup>170</sup> With increasing OABr content in the precursor solution, structures tended toward a single-layered QW, with  $n = 1$  reached in the absence of  $\text{CH}_3\text{NH}_3\text{Br}$ . Multiple peaks in the moderate OABr range indicate a mixture of compounds with variable inorganic layer thickness. The maximum PLQY reached  $\sim 30\%$  and was obtained with a 7:3 OABr: $\text{CH}_3\text{NH}_3\text{Br}$  precursor. A drastic hypsochromic shift in the absorption and PL peak wavelengths occurred at an OABr concentration of 80%, indicating the onset of the strong quantum confinement regime, in accord with a modified Kronig-Penney model.<sup>170</sup> PL tunability in mixed-structure, mixed-halide MHPs has been exploited to produce natural white light emission.<sup>40</sup>

The pronounced excitonic features in the linear absorption and PL spectra of 2D MHPs provides a convenient framework for comparison with 3D MHPs. The low binding energies and Wannier-type excitons with large Bohr radii in the latter (section 4.1.1) complicate deconvolution of continuum and excitonic absorption at room temperature. Typically, this can be overcome by recording spectra at cryogenic temperatures to minimize thermal broadening, revealing hydrogenic lines and allowing reliable determination of binding energy ( $E_b$ ) using eq 12. An example is given for GaAs measured at a lattice temperature of 1.2 K in Figure 17A.<sup>224</sup> A number of distinct features can be readily observed. These include transitions corresponding to the first, second, and third free exciton quantum states ( $n = 1, 2$ , and 3), impurity-bound excitons ( $\text{D}^0\text{-X}$ ), and the onset of continuum absorption ( $n = \infty$ ). Also shown is the expected band edge absorption in the absence of any electron-hole interactions, given in the dipole approximation as

$$\alpha(\hbar\omega) \approx (\hbar\omega - E_g)^{1/2} \quad (9)$$

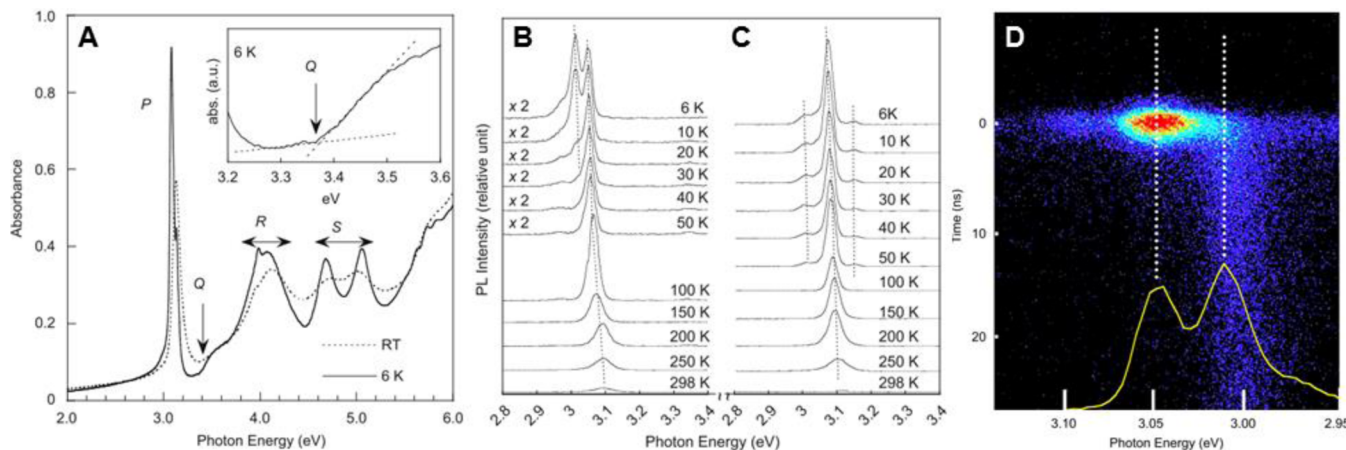


**Figure 15.** (A) Absorption spectrum of  $(C_6H_5C_4H_8NH_3)_2PbBr_4$  at RT (dotted line) and 6 K (solid line).  $P$  represents the exciton resonance,  $Q$  the continuum edge, and  $R$  and  $S$  higher energy interband transitions. Temperature-dependent PL spectra of (B)  $(C_6H_5C_1H_2NH_3)_2PbBr_4$  and (C)  $(C_6H_5C_4H_8NH_3)_2PbBr_4$ . (D) Streak camera image of  $(C_6H_5C_1H_2NH_3)_2PbBr_4$  time-resolved PL at 6 K. Note the reversal in photon energy values (i.e., the rightmost peak has a larger Stokes shift). Reprinted from ref 215, Copyright 2010, with permission from Elsevier.

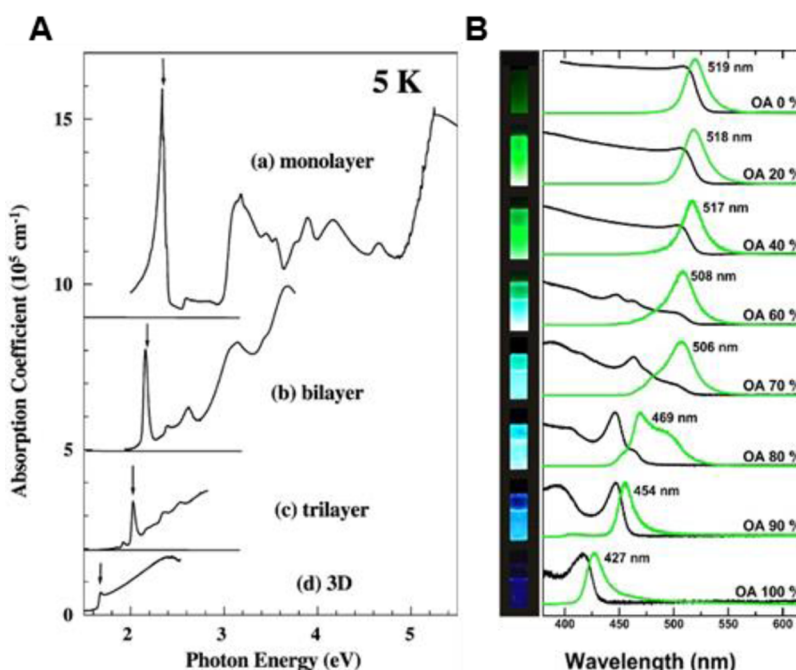


**Figure 16.** (A) Absorption coefficient (from Kramers–Kronig transformation of reflectivity) of  $(C_6H_{13}NH_3)_2PbI_4$  ( $n = 1$ ),  $(C_6H_{13}NH_3)_2(CH_3NH_3)Pb_2I_7$  ( $n = 2$ ),  $(C_6H_{13}NH_3)_2(CH_3NH_3)_2PbI_{10}$  ( $n = 3$ ), and  $CH_3NH_3PbI_3$  measure at 5 K. (A) Reprinted from ref. 223, copyright 2003, with permission from Elsevier. (B) Absorption and PL spectra of solutions prepared using various ratios of  $CH_3NH_3Br$ :OABr. Photographs of solution PL under UV irradiation are shown to the left of the spectra. Reproduced from ref 170. Copyright 2015 American Chemical Society.

for a direct gap semiconductor with parabolic bands. This square-root dependence based on the density of free electron and hole states drastically underestimates the observed absorption intensity at  $n = \infty$ . This is because continuum transitions near the band edge are also influenced by Coulombic interactions, even in GaAs where  $E_b \sim 5$  meV. The magnitude of this increased transition strength is known as the Sommerfeld enhancement factor,  $S(\hbar\omega)$ , which describes ratio of Coulomb-enhanced absorption to that predicted for noninteracting carriers. For a 3D system, it is given by<sup>36</sup>

$$S(\hbar\omega) = \frac{\pi\Delta \exp(\pi\Delta)}{\sinh(\pi\Delta)} \quad (10)$$

where  $\Delta = \sqrt{E_b/(\hbar\omega - E_g)}$ . The nature of continuum transitions is therefore also a function of exciton binding energy.

Unlike the prototypical GaAs system, low-temperature examination of device-relevant optical properties in MHPs is inhibited by the tetragonal  $\rightarrow$  orthorhombic phase transition (at  $\sim 160$  K in  $CH_3NH_3PbI_3$ ) that precludes the possibility of discerning the tetragonal or cubic phase  $E_b$  using a straightforward hydrogenic approximation. Representative  $CH_3NH_3PbI_3$  band edge absorption and PL spectra at RT and 170 K (just above the phase transition) are shown in Figure 17B.<sup>225</sup> The limited Stokes shift, which is further reduced if self-

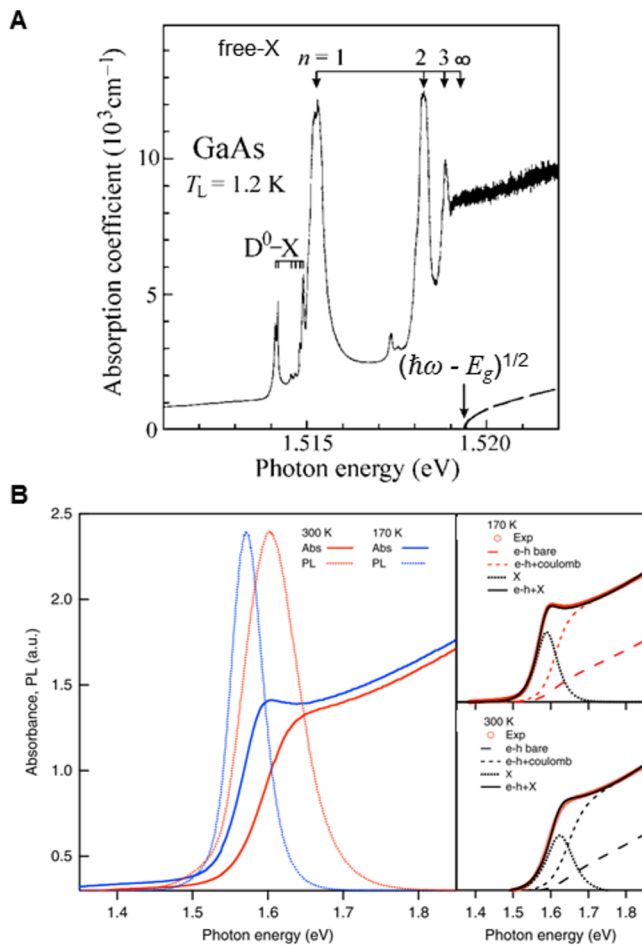


**Figure 17.** (A) Absorption coefficient of GaAs at 1.2 K showing the various excitonic and continuum contributions. Also shown is the expected continuum absorption in the absence of electron–hole interactions (dashed line). Note that the reduced intensity of the  $n = 1$  Ry line, which deviates from the typical  $1/n^3$  description of exciton oscillator strength, is a result of polariton transmittance, scattering, and fluorescence. Reprinted with permission from ref 224. Copyright 2005 Wiley VCH. (B) Band edge absorption and PL of  $\text{CH}_3\text{NH}_3\text{PbI}_3$  at RT (red) and 170 K (blue). The right-hand panels show deconvolution of the absorption spectrum into excitonic and Coulomb-enhanced contributions using eq 11 with some minor modifications. Reprinted by permission from Macmillan Publishers Ltd.: Nature Communications (ref 225), copyright 2014.

absorption is accounted for,<sup>225–227</sup> indicates that RT PL originates from intrinsic radiative processes in  $\text{CH}_3\text{NH}_3\text{PbI}_3$ .<sup>228</sup> Conversely, it has been suggested that PL in  $\text{CsSnX}_3$  compounds is extrinsic, being associated with acceptor-bound excitons at Sn vacancies.<sup>17,229</sup> And appearance of additional PL lines in the low-temperature orthorhombic phase of  $\text{CH}_3\text{NH}_3\text{PbI}_3$  has been attributed to bound-exciton or trapped-carrier emission,<sup>52,230–232</sup> the source of impurity possibly being tetragonal inclusions in the broader orthorhombic matrix.<sup>182</sup>

Comprehensive modeling of the convoluted band edge absorption in  $\text{CH}_3\text{NH}_3\text{PbX}_3$  has been carried out in a number of studies.<sup>58,59,184,189,225,233</sup> Excitonic and Coulomb-enhanced absorption are accounted for in Elliot's theory of Wannier excitons according to<sup>234</sup>

$$\alpha(\hbar\omega) = [A\theta(\hbar\omega - E_g)D_{cv}(\hbar\omega)]S(\hbar\omega) + AE_b \sum_{n=1}^{\infty} \frac{4\pi}{n^3} \delta(\hbar\omega - E_g + \frac{E_b}{n^2}) \quad (11)$$

where  $A$  is related to the transition matrix element,  $\theta$  is the step function,  $D_{cv}$  is the joint density of states,  $\delta$  is the Dirac-delta function, and  $S(\hbar\omega)$  has the same definition as given above. Examining eq 11, the first group of terms represents continuum absorption and its Coulombic enhancement through the Sommerfeld factor given in eq 10. The second set of terms denotes absorption related to discrete excitonic states with quantum number  $n$ . For analysis of the  $\text{CH}_3\text{NH}_3\text{PbI}_3$  band edge in Figure 17B, eq 11 was modified to include nonparabolic dispersion, as has been done for GaAs,<sup>235</sup> and was convoluted with a hyperbolic secant function to account for broadening.<sup>225</sup> The Sommerfeld enhancement was found to increase the continuum contribution more than 2-fold in  $\text{CH}_3\text{NH}_3\text{PbI}_3$ ,<sup>225</sup> and excitonic effects clearly augment the band edge absorption. Reported binding energies determined from modeling of the  $\text{CH}_3\text{NH}_3\text{PbI}_3$  RT absorption spectrum are  $25 \pm 3$ ,<sup>225</sup>  $9 \pm 1$ ,<sup>59</sup> and 5 meV.<sup>189</sup> Below the phase transition,  $E_b$  was reported to increase from 5 to  $\sim 15$  meV due to “freezing” of molecular cation tumbling in the orthorhombic phase (section 2.2.2).<sup>189</sup> However, more recent modeling indicates limited temperature dependence (section 4.1.1).<sup>184</sup> Similar analysis of  $\text{CH}_3\text{NH}_3\text{PbBr}_3$  and  $\text{CH}_3\text{NH}_3\text{PbCl}_3$  yields comparable results excepting increased excitonic contribution due to larger  $E_b$ .<sup>233</sup> Regardless of the true value of the highly disputed  $E_b$  in many MHPs, Coulombic effects cannot be overlooked and are in fact integral to the excellent broadband light harvesting efficiency in PSCs, particularly at frequencies near the band edge.

### 3.3. Amplified Spontaneous Emission and Lasing

Amplified spontaneous emission (ASE) and lasing have been reported for both bulk and nanostructured hybrid MHPs.<sup>52–57</sup> Favorable properties of MHPs for lasing include high PLQY at relatively large carrier densities and long excited state lifetime beneficial for achieving inversion (vide infra). Their high mobilities compared to other solution-processed materials also opens the possibility for electrically-pumped lasing.<sup>236</sup> In addition to the obvious intrigue of this behavior for potential applications, ASE provides a framework for understanding the dominant recombination pathways in MHPs. Figure 18A shows evolution of the PL spectrum of  $\text{CH}_3\text{NH}_3\text{PbI}_3$  at various excitation intensities.<sup>52</sup> At low excitation fluence, only spontaneous emission (SE), with full width at half-maximum (FWHM) of  $\sim 50$  nm, is observed. With increasing excitation intensity, a second sharp PL peak with dramatically reduced FWHM appears to the red of the SE at an excitation density of  $\sim 12 \mu\text{J}/\text{cm}^2$  under these experimental conditions (Figure 18B). This observation, together with a reduced lifetime and superlinear growth of PL intensity (Figure 18C), denotes the onset of ASE. Note that the bathochromic shift of the ASE peak is a result of parasitic self-absorption on the high-energy side of the SE,<sup>52</sup> as well as the fundamental requirement that the energy of stimulated emission must be lower than the chemical potential of the plasma (see Figure 24B).<sup>225,34</sup>

The relatively low carrier density threshold necessary to induce ASE ( $\sim 2 \times 10^{18} \text{ cm}^{-3}$ ) stems from the favorable bimolecular radiative recombination at these densities.<sup>53,225,226,237</sup> Initial speculation surrounded the source of radiative recombination, whether excitonic or free carrier in

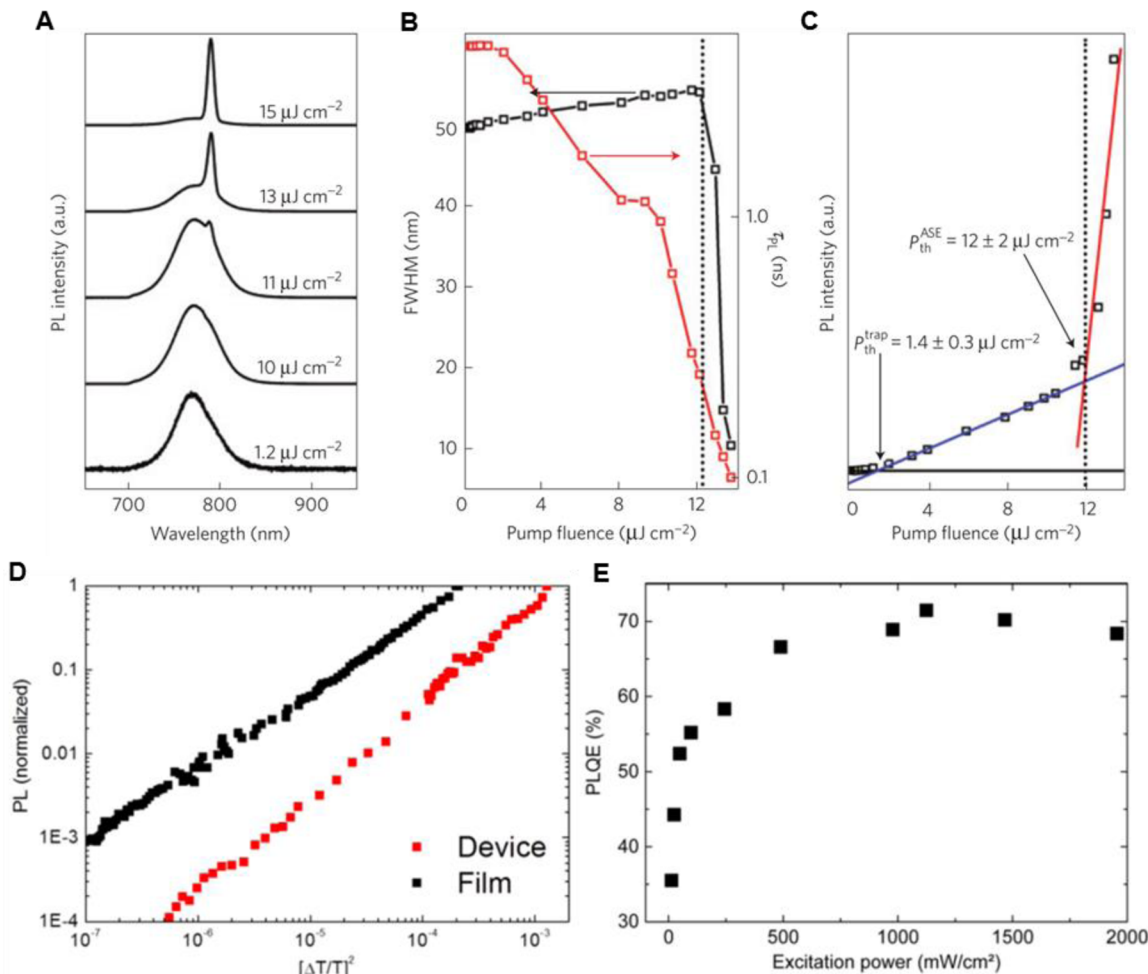


**Figure 18.** (A) PL spectra of a  $\text{CH}_3\text{NH}_3\text{PbI}_3$  thin film excited with 600 nm pulsed laser excitation (150 fs pulse width) at different intensities. The sharp peak appearing at  $\sim 11 \mu\text{J cm}^{-2}$  shows the onset of ASE. (B) PL peak FWHM and average PL lifetime as a function of excitation fluence. (C) Steady-state PL peak intensity at various fluences. Trap state saturation and ASE thresholds are indicated. (A–C) reprinted by permission from Macmillan Publishers Ltd.: Nature Materials (ref 52), copyright 2014. (D) Correlation between normalized PL intensity, integrated from 1.57 to 1.71 eV, and the square of the differential transmission signal in a  $\text{CH}_3\text{NH}_3\text{PbI}_{3-x}\text{Cl}_x$  thin film and full device architecture. (E) External PL quantum yield as a function of excitation intensity. Reproduced from ref 53. Copyright 2014 American Chemical Society.

nature.<sup>52</sup> It is important to first point out that PL coinciding with the excitonic resonance does not necessarily imply excitonic emission. A Coulombically modified electron–hole plasma can also recombine radiatively at excitonic frequencies when manybody interactions are taken into account.<sup>238,239</sup> Deschler et al. confirmed that  $\text{CH}_3\text{NH}_3\text{PbI}_3$  PL originates from recombination of free electrons and holes at carrier densities relevant for ASE.<sup>53</sup> Qualitative examination of Figure 18D indicates that PL is proportional to the square of the differential transmittance signal, which provides a measure of the total excitation density ( $n_{\text{tot}}$ ).<sup>53</sup> Because  $n_{\text{tot}}^2 = np$ , where  $n$  and  $p$  are the electron and hole density, respectively,  $\text{PL} \propto np$  and can thus be considered to result from radiative bimolecular recombination of electrons and holes. A more rigorous quantitative treatment of MHP radiative recombination is given in section 4.3. Nonradiative processes are understandably deleterious for optical gain. In addition to the density of defect states, the timescales associated with trapping and multiparticle Auger processes are important factors in dictating ASE characteristics. The interplay between radiative and nonradiative processes is inherently captured in measurement of PLQY. Results in Figure 18E demonstrate that the PLQY

increases at larger excitation densities, reaching a maximum of  $\sim 70\%$ .<sup>53</sup> Following the plateau in quantum efficiency, the PLQY will decline due to the onset of substantial Auger recombination.<sup>225,226</sup> Low-threshold ASE indicates that, following trap saturation, radiative processes outcompete Auger recombination at these excitation densities.<sup>53</sup> The fact that PLQY is maximized at approximately the same carrier densities corresponding to optical gain is beneficial for achieving efficient lasing.

Optical gain has also been explored in nanostructured MHPs.<sup>54,55</sup> Use of single-crystal nanowires (NW) of  $\text{CH}_3\text{NH}_3\text{Pb}(\text{X}_{1-x}\text{X}'_x)_3$  resulted in carrier density lasing thresholds as low as  $1.5 \times 10^{17} \text{ cm}^{-3}$ ,<sup>55</sup> an order of magnitude lower than observed in solution-processed perovskite thin films and CdS NW lasers. This is attributed to a lower defect density in the high-quality nanostructure MHP single crystals. A PL image of lasing action in a  $23.6 \mu\text{m}$  NW of  $\text{CH}_3\text{NH}_3\text{PbBr}_3$  is shown in the inset of Figure 19A. Also shown is a pseudocolor plot of the PL spectrum as a function of excitation intensity, where various lasing peaks can be discerned. Longitudinal cavity modes within the NW means that the mode spacing can be readily modified simply by changing the length of the wire.<sup>55</sup> An important

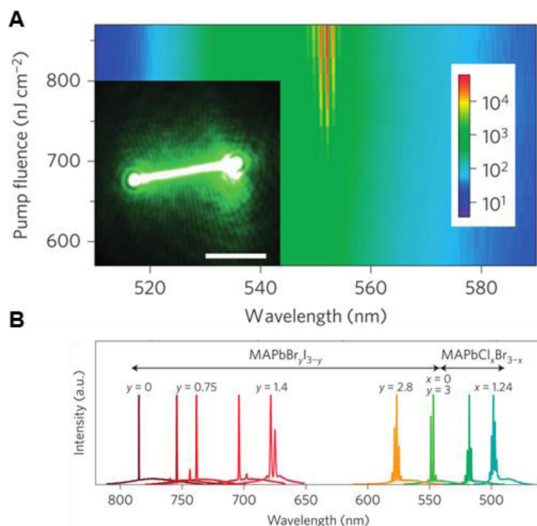


**Figure 19.** (A) PL spectrum as a function of excitation fluence for a 23.6  $\mu\text{m}$   $\text{CH}_3\text{NH}_3\text{PbBr}_3$  NW. Inset shows a PL image of a single NW above the lasing threshold, where emission is localized at the end of NW, indicating a strong waveguiding effect. (B) Wavelength tunability of optical gain in mixed halide  $\text{CH}_3\text{NH}_3\text{Pb}(\text{X}_{1-\text{x}}\text{X}'_{\text{x}})_3$  NWs. Reprinted by permission from Macmillan Publishers Ltd.: Nature Materials (ref 55), copyright 2015.

aspect of MHPs is their tunable composition and band gaps, which gives rise to a series of mixed-halide NWs that emit across the majority of the visible spectrum and into the NIR (Figure 19B).<sup>55</sup> Zhu et al. posit that lasing in the MHP single crystal NWs results from a highly excited electron–hole plasma rather than from an excitonic gas.<sup>55</sup> More discussion on this point can be found in section 4.1.2. A series of mixed-cation, mixed-halide NWs has been shown to provide more precise tunability and enhanced photostability over  $\text{CH}_3\text{NH}_3$ -based compounds.<sup>54</sup>  $\text{CsPb}(\text{X}_{1-\text{x}}\text{X}'_{\text{x}})_3$  nanocrystals have also exhibited low-threshold, tunable ASE and lasing.<sup>57</sup>

## 4. PHOTOPHYSICAL PROCESSES

### 4.1. Interplay between Excitons and Free Carriers

Captivation with the nature of excitons in MHPs stems primarily from two sources. Early on, the intriguing optical characteristics of 2D layered hybrid perovskites, resulting from the additive effects of quantum and dielectric confinement, motivated study into their excitonic properties.<sup>16,19,20,22,114,166,171,214,240,241</sup> More recently, evolution of PSC architecture (Figure 1) introduced questions as to the underlying excitonic behavior of 3D MHPs. Initial use in a conventional “excitonic” DSSC appeared to indicate that MHP sensitizers were analogous to molecular dyes. Questions regarding their photophysical properties were therefore not yet raised. Subsequent indications of their effectiveness in thin film and nonsensitized architectures spurred a flurry of photophysical studies,<sup>145,242</sup> many of them dealing at least in part with the role of excitons and free carriers in these materials.<sup>53,183,225,237</sup>

By definition, free excitons (as opposed to localized or impurity-bound excitons) in an ideal crystalline material represent the lowest excited electronic state that can freely diffuse through the lattice, propagating excitation energy without transferring electric charge.<sup>234,243</sup> The lack of net charge displacement makes exciton ionization an essential

mechanism for carrier extraction in a PV device.<sup>244</sup> For example, diffusion lengths of tightly bound electron–hole pairs in active layers of organic PVs are on the order of 10 nm. Polymeric blends or bulk heterojunctions are thus utilized to spatially separate the quasiparticles before they are lost through recombination processes. This charge separation mechanism is distinctly different from the spontaneous room temperature generation of unbound electrons and holes in conventional inorganic semiconductors like GaAs. In light-emitting applications, radiative recombination from a population of unbound electrons and holes, proportional to  $n^2$ , must outpace nonradiative trap-mediated recombination ( $\propto n$ ) to achieve high quantum yields. Optimal performance (i.e., peak quantum efficiency) of such a free-carrier device thus requires high carrier densities, on the order of  $\sim 10^{17}$ – $10^{18}$  cm<sup>-3</sup> in  $\text{CH}_3\text{NH}_3\text{PbI}_3$ .<sup>225,226,245</sup> Contrarily, if radiative recombination occurs primarily through a population of bound excitons, proportional to  $n$ , it is possible to reach peak quantum yields at lower carrier densities, making operation more efficient. In light of these disparate operating principles, spectroscopic elucidation of the nature of photogenerated species and excited state processes under various conditions is vital if the burgeoning class of MHPs is to reach their full potential in optoelectronic applications.

**4.1.1. Exciton Binding Energy.** An exciton, composed of a Coulombically bound electron–hole pair, is in many ways analogous to a hydrogen atom. As a first approximation, the electron can be imagined to orbit around the typically heavier hole “nucleus”, although the comparable masses of the two quasiparticles means they both have their own characteristic orbital radii. This is known as the hydrogenic model and can typically be used to describe the series of sharp absorption lines below the continuum transitions in semiconductors with parabolic bands. The strength of the Coulombic attraction, analogous to the hydrogen Rydberg ( $Ry(H) = 13.6$  eV), is given by the exciton binding energy ( $E_b$ ).

$$E_b = \frac{m_r e_0^4}{2\hbar^2(4\pi\epsilon\epsilon_0)^2} \frac{1}{n^2} = \frac{(m_r/m_0)}{\epsilon^2} \frac{1}{n^2} Ry(H) \quad (12)$$

The associated exciton Bohr radius ( $r_B$ ) is given by

$$r_B = \frac{\hbar^2(4\pi\epsilon\epsilon_0)}{m_r e_0^2} = \frac{\epsilon}{(m_r/m_0)} a_B \quad (13)$$

where the reduced effective mass is represented by  $m_r$  ( $\frac{1}{m_r} = \frac{1}{m_e^*} + \frac{1}{m_h^*}$ ),  $e_0$  is the elementary charge,  $\epsilon_0$  is the permittivity of free space,  $\epsilon$  is the dielectric constant of the host material,  $n \geq 1$  is the integer representation of the excitonic states ( $n = \infty$  corresponds to the continuum;  $r_B$  is given for the  $n = 1$  state), and  $a_B$  is the Bohr radius of the hydrogen  $n = 1$  state ( $\sim 0.5$  Å). The excitonic model is distinct from the atomic system in that the effective mass of the two constituent quasiparticles is nearly identical, particularly at the band edge of ambipolar MHPs, which makes  $m_r < m$ , and thus diminishes  $E_b$ . This also means the center of mass of the exciton may lie relatively far from either the electron or hole. Binding in the excitonic case is further reduced as a result of the dielectric response of its host material. A doubling of  $\epsilon$  yields a 4-fold decrease in  $E_b$ . Tightly bound excitons with small Bohr radii are known as Frenkel excitons, while low  $E_b$  excitons with large, delocalized radii much greater than the host lattice constant are known as Wannier excitons. The two types are

shown schematically in Figure 20. As a result of exciton formation, the onset of optical absorption occurs at an energy

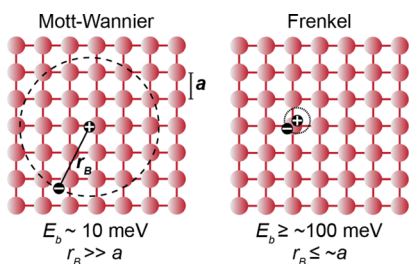


**Figure 20.** Illustration of the hydrogenic approximation for excitons in the  $n = 1$  quantum state. Excitons of the Mott-Wannier and Frenkel types in an arbitrary atomic lattice are shown. The lattice constant ( $a$ ) and Bohr radius ( $r_B$ ) are indicated.

( $E_{\text{opt}}$ ) below the electronic gap ( $E_g$ ) by an amount equivalent to the  $n = 1$  binding energy,  $E_{\text{b},1s}$ .

$$E_{\text{opt}} = E_g - E_{\text{b},1s} \quad (14)$$

A compilation of exciton binding energies in select 3D and LD MHPs, along with a number of more conventional semiconductors, is given in Table 2.

From eqs 12 and 13, it is not immediately apparent which value of the frequency-dependent  $\epsilon$  is most appropriate for a given system. Because  $E_b$  is inversely proportional to  $\epsilon^2$ , its magnitude significantly influences the calculated binding energy. This is a relatively minor point for III–V semiconductors but is particularly salient for 3D MHPs and other polar and ionic compounds. As a general rule, because large  $r_B$  Mott-Wannier excitons extend over many unit cells, the lattice acts more or less as a homogeneous dielectric, making  $\epsilon_{\text{eff}} \sim \epsilon_s$  a reasonable approximation. Furthermore, in our prototypical comparison compound GaAs,  $\epsilon_s \sim 12.9$  and  $\epsilon_{\infty} \sim 10.9$ , which makes the ambiguity in the value of the effective dielectric constant ( $\epsilon_{\text{eff}}$ ) only a minor consideration. In  $\text{CH}_3\text{NH}_3\text{PbI}_3$ , however, the difference between the limiting frequencies at room temperature is significant, with reported values of  $\epsilon_s \sim 35$  in the kHz regime (ref 197) and  $\epsilon_{\infty} \sim 6.5$  (refs 197 and 191). The large ratio  $\epsilon_s/\epsilon_{\infty} \sim 5$  suggests polaronic effects influence electron–hole interactions.<sup>178,249,250</sup> As discussed in section

**Table 2. Exciton Binding Energies ( $E_b$ ) for Select MHPs of Varying Dimensionality and a Number of Conventional Bulk Semiconductors**

compound	dimension	$E_b$ (meV) <sup>a</sup>	technique	ref
$\text{CH}_3\text{NH}_3\text{PbI}_3$	3D	29 <sup>b</sup> , 34 <sup>c</sup>	optical absorption (F-Sum)	184
		$\leq 5$ <sup>b</sup> , 16 <sup>c</sup>	high-field magnetoabsorption	136
		6 <sup>b</sup> , 30 <sup>c</sup>	optical absorption	246
		19 $\pm$ 3	temp. dep. PL	194
		55 $\pm$ 20 <sup>d</sup>	temp. dep. optical absorption	183
		2 <sup>f</sup>	IS/CELIV	197
		62.3 $\pm$ 8.9 <sup>d</sup>	temp. dep. PL	247
		50	magnetoabsorption	176
		30	optical absorption	114
		45	temp. dep. PL	241
		37	magnetoabsorption	191
$\text{CH}_3\text{NH}_3\text{PbBr}_3$	3D	25 <sup>c</sup>	high-field magnetoabsorption	178
		60	optical absorption (F-Sum)	184
		76	magnetoabsorption	176
		150	optical absorption	114
$\text{CH}_3\text{NH}_3\text{PbCl}_3$	3D	69	optical absorption	233
$\text{HC}(\text{NH}_2)_2\text{PbI}_3$	3D	$\leq 5$ <sup>b</sup> , 14 <sup>c</sup>	high-field magnetoabsorption	178
$\text{HC}(\text{NH}_2)_2\text{PbBr}_3$	3D	24 <sup>b</sup> , 22 <sup>c</sup>	high-field magnetoabsorption	178
$\text{CsSnI}_3$	3D	18	temp. dep. PL	248
$\text{GaSb}$	3D	12 <sup>e</sup> , 0.1 <sup>f</sup>	theory	117
		2.8	—	—
		4.9	—	—
		5.1	—	—
		4.2	—	—
		10.5	—	—
		15	—	—
$(\text{CH}_3\text{NH}_3)_3(\text{C}_9)_2\text{Pb}_4\text{I}_{13}$	2D ( $n = 4$ )	60	optical absorption	114
		96	optical absorption	114
		181	optical absorption	114
		$\geq 388$	optical absorption	114
		540	optical absorption	173
		$\geq 410$	optical absorption	114
		545	optical absorption	114
		—	—	—
		—	—	—
		—	—	—

<sup>a</sup>For a given compound, reported  $E_b$  values are listed in descending chronological order by year. <sup>b</sup>Tetragonal phase. <sup>c</sup>Orthorhombic phase. <sup>d</sup> $\text{CH}_3\text{NH}_3\text{PbI}_{3-x}\text{Cl}_x$ . <sup>e</sup>Calculated from the Mott-Wannier model using  $\epsilon_{\infty}$ . <sup>f</sup>Calculated from the Mott-Wannier model using  $\epsilon_s$ .

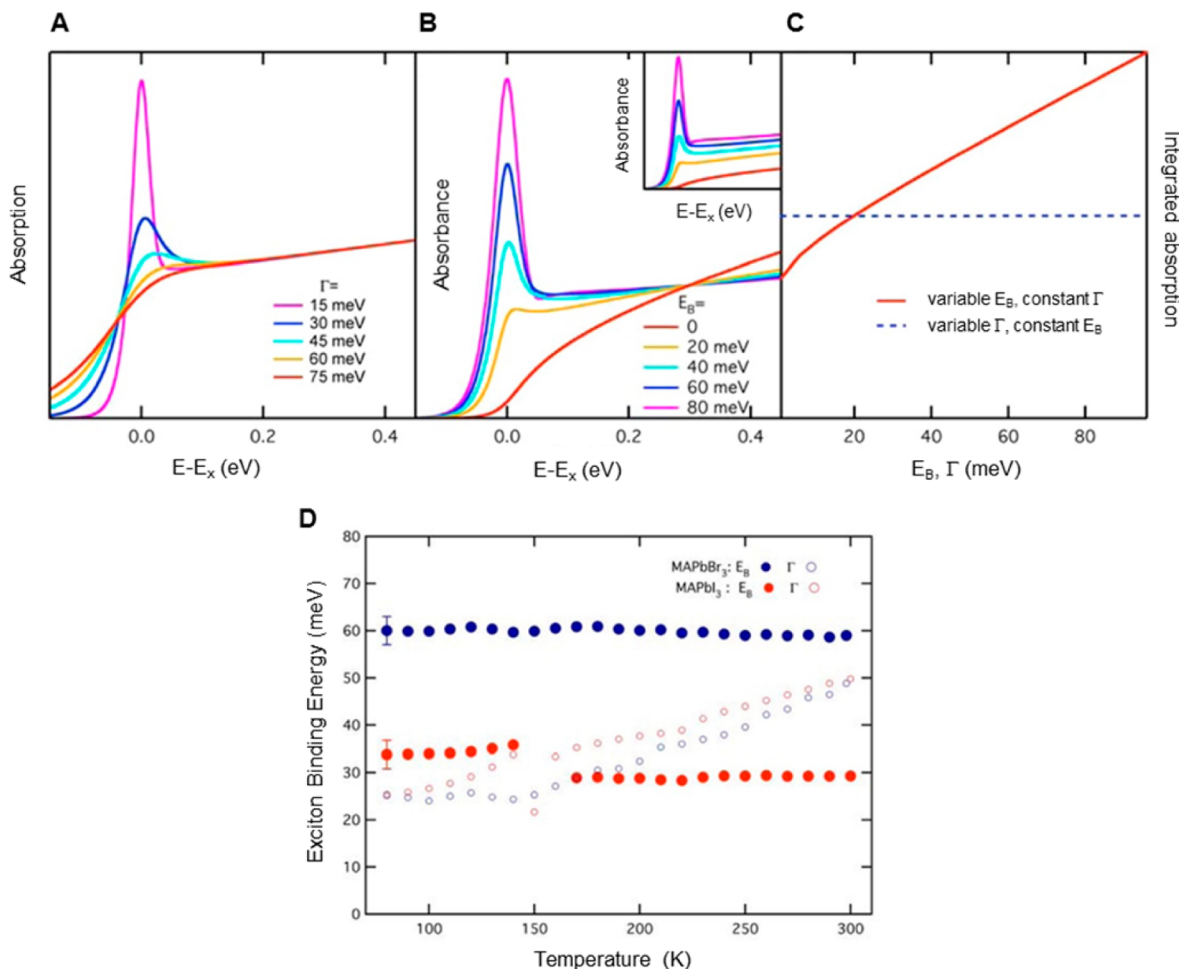


**Figure 21.** Simulation of an absorption spectrum computed using the Elliot formula (see section 3.2) illustrating the influence of (A) line width (with  $E_b = 50$  meV) and (B) binding energy (with  $\Gamma = 20$  meV) on the spectral line shape. (C) Integrated absorption with variable  $E_b$  and  $\Gamma$ , demonstrating that pure broadening does not alter the total absorption. (D)  $E_b$  and  $\Gamma$  as a function of temperature in  $\text{CH}_3\text{NH}_3\text{PbI}_3$  and  $\text{CH}_3\text{NH}_3\text{PbBr}_3$ . Reproduced from ref 184. Copyright 2015 American Chemical Society.

2.2.2, the static limit is a convolution of electron and phonon fields, while  $\epsilon_\infty$  includes only the electronic component. Thus, by taking the difference in potential energy at distance  $r$  from a point charge in the limiting dielectric regimes, it is possible to isolate the ionic/phonon contribution.<sup>34</sup>

$$\frac{e_0^2}{4\pi\epsilon_0\epsilon_\infty r} - \frac{e_0^2}{4\pi\epsilon_0\epsilon_s r} = \frac{e_0^2}{4\pi\epsilon_0 r} \left( \frac{1}{\epsilon_\infty} - \frac{1}{\epsilon_s} \right) \quad (15)$$

In cases where  $\epsilon_s/\epsilon_\infty \sim 1$ , these effects are negligible, but in MHPs, coupling between longitudinal optical (LO) phonons and photogenerated species likely plays a significant role. Menéndez-Proupin et al. utilized Haken and Pollmann-Büttner potentials, which account for polaronic effects, to modify the standard hydrogenic model in the orthorhombic phase of  $\text{CH}_3\text{NH}_3\text{PbI}_3$ .<sup>249</sup> At small and large  $r_B$ , dielectric screening in these models simplifies to  $\epsilon_\infty$  and  $\epsilon_s$ , respectively. For orthorhombic  $\text{CH}_3\text{NH}_3\text{PbI}_3$ , these models indicate that the effective dielectric constant ( $\epsilon_{\text{eff}}$ ) lies at an intermediate value between the static and optical limits in MHPs, similar to the behavior of polar compounds like TlCl ( $\epsilon_{\text{eff}} = 2.48\epsilon_\infty$ ) and in line with recent experimental and computational results.<sup>117,136,178</sup> It should be cautioned that, in addition to pure dielectric effects, determination of  $\epsilon_s$  in MHPs is complicated by ionic conduction (section 5.2),<sup>197,251</sup> which

adds further complexity to interpretation of electron–phonon interactions.

Magnetoabsorption,<sup>136,176,178,191</sup> temperature-dependent PL,<sup>194,241,248</sup> and optical absorption<sup>114,183,184,246</sup> have been employed to elucidate exciton binding energies in all-inorganic and hybrid MHPs. Because of its ubiquity in PV research, excitonic properties of  $\text{CH}_3\text{NH}_3\text{PbI}_3$  have been by far the most highly scrutinized in recent years. The wide range of disparate  $E_b$  values ( $\sim 2$ –60 meV) have been derived from an almost equally diverse set of experimental techniques, with varying degrees of assumptions inherent to each method. Of note among these approaches are recent high-field magnetoabsorption<sup>136,178</sup> and linear optical absorption modeling using the  $f$ -sum basis.<sup>184</sup> These methods are particularly salient as they allow determination of  $E_b$  without assumptions regarding the dielectric constant or the temperature-dependent interplay between homogeneous broadening ( $\Gamma_{\text{LO}}$ ), which results from exciton-LO phonon interactions, and  $E_b$ . Such assumptions can in part lead to spurious binding energy values.

Determining the binding energy from linear absorption spectra, as performed in a number of studies on MHPs,<sup>114,171,189,246</sup> requires resolving contributions from bound states and the continuum (section 3.2). Because of the large binding energy in LD MHPs, there is a clear distinction between these regimes, simplifying calculation of  $E_b$ . The same

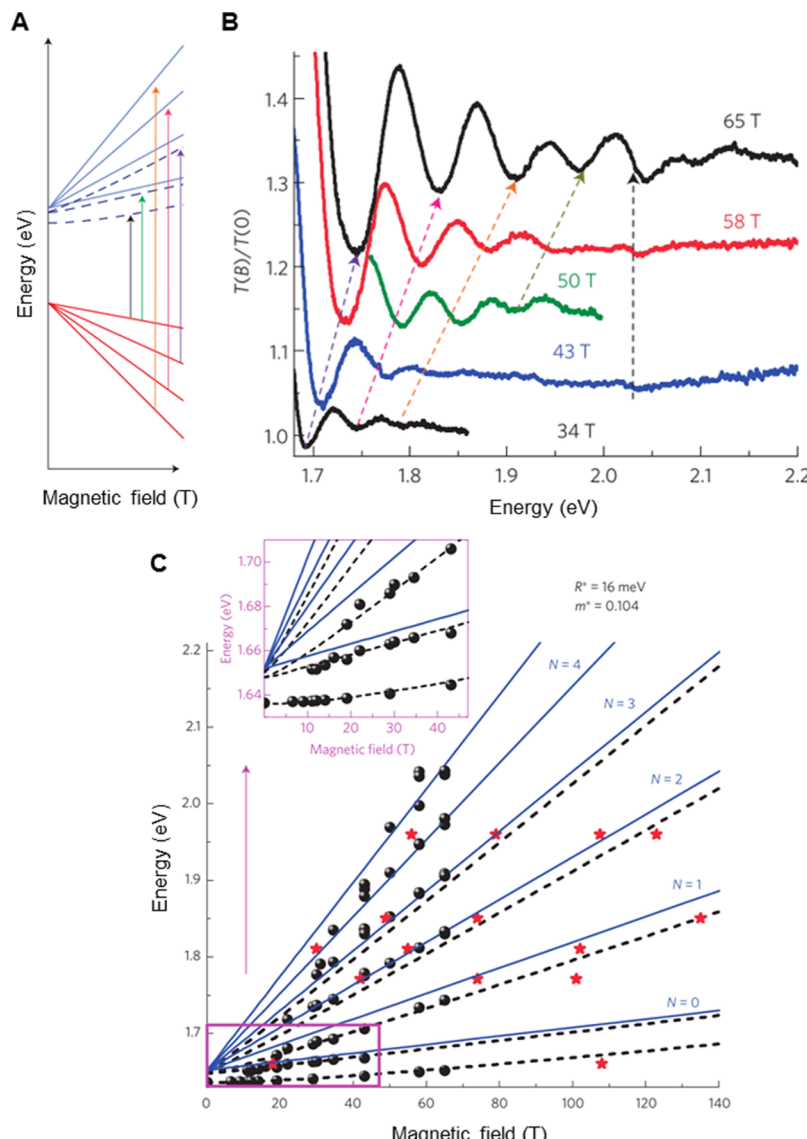


**Figure 22.** (A) Illustration of the various excitonic (dashed lines) and free carrier Landau (solid lines) levels as a function of magnetic field strength. (B) Differential magneto-transmittance spectra of  $\text{CH}_3\text{NH}_3\text{PbI}_3$  at various field strengths. (C) Fan diagram of the calculated excitonic (dashed lines) and Landau transitions (solid lines) across wide range field strengths, along with experimental data from long-pulse fixed-field spectra ( $\bullet$ ) and fixed-energy fast-field-sweep data (red  $\star$ ). Reprinted by permission from Macmillan Publishers Ltd.: Nature Physics (ref 136), copyright 2015.

does not hold for 3D MHPs and other conventional semiconductors with much lower  $E_b$ . Within the framework of Elliot theory for Wannier excitons,<sup>234</sup> when  $\Gamma_{\text{LO}}$  and  $E_b$  have similar magnitudes their deconvolution is problematic. As such, assignment of exciton, Coulomb-enhanced electron–hole, and continuum absorption is not straightforward, even at cryogenic temperatures. Reliable  $E_b$  determination by spectral analysis therefore requires more robust methods. Sestu et al. have shown that the *f*-sum rule allows for unambiguous determination of the separate influence of homogeneous broadening and  $E_b$  on the absorption line shape in  $\text{CH}_3\text{NH}_3\text{PbI}_3$ ,  $\text{CH}_3\text{NH}_3\text{PbBr}_3$ , and a control GaAs sample.<sup>184</sup> A sensitivity analysis demonstrating the effects of  $\Gamma_{\text{LO}}$ , which is the primary source of temperature-dependent homogeneous broadening in polar semiconductors,<sup>252</sup> and  $E_b$  on an example linear absorption spectrum with  $E_b \approx \Gamma_{\text{LO}}$  is given in Figure 21 (panels A and B, respectively).<sup>184</sup> With increasing  $\Gamma_{\text{LO}}$ , the exciton resonance broadens, but because the oscillator strength is unaffected, the integral of the absorption and the slope of the

continuum contribution remain constant (Figure 21C). With decreasing  $E_b$  however, the exciton resonance damps and the integrated absorption decreases, along with modification of the continuum absorption slope. Thus, by determining the integrated intensity using normalized spectra (in this case normalization was done at an energy  $E_n = E_{1s} + 0.2$  eV), a more precise  $E_b$  can be determined.

It is clear from Figure 21D that homogeneous broadening is primarily responsible for changes in spectral line shape for these samples. From this analysis, the authors calculated a relatively temperature insensitive  $E_b$  for  $\text{CH}_3\text{NH}_3\text{PbBr}_3$  of 60 meV and a slightly more temperature sensitive value of 29 meV at high temperature and 34 meV below the orthorhombic phase transition in  $\text{CH}_3\text{NH}_3\text{PbI}_3$  (Figure 21D). The fact that  $E_b$  was not found to depend significantly on phase or temperature contradicts prediction of large dielectric enhancement and increased exciton screening upon activation of  $\text{CH}_3\text{NH}_3^+$  rotation.<sup>136,189,197</sup> Back calculation of the dielectric constant using  $m_r = 0.1m_0$  revealed  $\epsilon_{\text{eff}} \sim 6$  for both compounds, in close

agreement with reported  $\epsilon_{\infty}$  values.<sup>191,197</sup> Sestu et al. argue that this may be related to the fact that molecular cation rotation in these compounds occurs at frequencies less than 1 THz according to Raman and time-resolved 2D vibrational spectroscopies,<sup>188,253</sup> yielding a relatively constant  $\epsilon$  at frequencies comparable to  $E_b$  (10–100 THz).<sup>184</sup> This will no doubt be a point of further study considering the gathering consensus that electron–phonon coupling increases  $\epsilon_{\text{eff}}$  in 3D hybrid MHPs, as discussed above.<sup>189,197,249</sup>

High-resolution magnetoabsorption spectroscopy has also recently facilitated more accurate determination of the free excitonic states in MHPs with low binding energies.<sup>136,178</sup> Because use of high fields enables unambiguous quantification of  $m_r$  and resolution of the 2s exciton transition, these measurements circumvent issues associated with early magnetoabsorption studies that required assumptions about the effective dielectric constant,<sup>176,191</sup> which, as discussed above, remains a point of contention in 3D MHPs. Figure 22A shows schematically the increased energetic splitting of conduction and valence band Landau states as well as their associated excitonic transitions as a function of field strength. At high fields, interband free carrier absorption dominates. From the energy of a series of Landau levels in  $\text{CH}_3\text{NH}_3\text{PbI}_3$  at high field,  $E(B)$  (Figure 22B),  $m_r$  can be determined through the relation<sup>136</sup>

$$E(B) = E_g + \frac{\hbar e B}{m_r} (N + 1/2) \quad (16)$$

where  $N$  is the Landau level quantum number and  $B$  is the applied magnetic field. Zeeman splitting is neglected in the presence of unpolarized light.<sup>136</sup> This analysis yields  $m_r \approx 0.1m_0$  for  $\text{CH}_3\text{NH}_3\text{PbI}_3$  in the orthorhombic phase at 2 K.<sup>136</sup> Magnetoabsorption measurements at temperatures above the orthorhombic  $\rightarrow$  tetragonal phase transition suggest a similar effective mass in the tetragonal structure.<sup>136</sup> The full set of measured transition energies (solid symbols) as a function of field strength and calculated free carrier (solid lines) and excitonic (dashed lines) transitions are given in Figure 22C. Linearity in the transitions across the entire field range suggests parabolic approximations at the band edges in MHPs are valid, contrary to theoretical predictions of severe deviation from parabolicity as discussed in section 2.1. Through global fitting,  $E_b$  is determined to be 16 meV at 2 K. Perhaps more importantly, these measurements indicate that the binding energy in  $\text{CH}_3\text{NH}_3\text{PbI}_3$  is significantly diminished at room temperature compared to cryogenic measurements. Extrapolation from the low temperature values suggests  $E_b$  is on the order of 5 meV. Because  $m_r$  was found to be constant across a wide temperature range that included the orthorhombic  $\rightarrow$  tetragonal phase transition, the only other factor that could have such a pronounced impact on  $E_b$  is a change in effective dielectric response. This is likely related to the predicted effects of cation rotation and tumbling in the high temperature phase as discussed in section 2.2.2. Back calculation from the empirical  $m_r$  and  $E_b$  values yields  $\epsilon_{\text{eff}} \sim 8–10$ .<sup>136,178</sup> Interestingly, the binding energy in  $\text{HC}(\text{NH}_2)_2\text{PbBr}_3$  shows little variance with temperature, suggesting the frequency of phonon modes in this compound are sufficiently lower than  $E_b$  such that  $\epsilon_{\text{eff}} \approx \epsilon_{\infty}$ .<sup>178</sup>

While the two most recent attempts to unambiguously resolve the  $E_b$  of hybrid 3D MHPs arrive at relatively divergent values, they do suggest the binding energy is comparable to or well below thermal energy at room temperature ( $k_b T_{298\text{ K}} =$

25.7 meV) in the triiodide family. Excitonic contributions are generally more prominent in larger band gap materials as a result of reduced background screening, thus  $\text{ABBr}_3$ ,  $\text{ABC}_3$ , and their associated solid solutions can be expected to exhibit increased excitonic behavior relative to  $\text{ABI}_3$  compounds.<sup>233</sup> After the first direct spectroscopic indication of the prominent role played by free carriers in 3D MHPs (ca. 2014),<sup>53,225,237</sup> a mass of supporting evidence has now made it clear that the majority of 3D MHPs can be considered “free carrier” semiconductors.<sup>230,233</sup> Further substantiating this claim is the analysis presented in section 4.1.2, which reveals that a substantial fraction of free carriers comprises the excited state at low and high excitation fluences, even for materials with much larger  $E_b$ . However, Coulombic interactions do certainly play a role in enhancement of absorption near the band edge (section 3.2) and at moderate excitation densities. Therefore, Coulombic effects cannot be disregarded.<sup>225</sup>

In the case of LD MHPs, which still exhibit Wannier-type excitons,<sup>217</sup> quantum and dielectric confinement dramatically alter  $E_b$ .<sup>19,114</sup> Low dielectric interlayers in natural-QW hybrid MHPs stabilize excitonic resonances through the image charge effect,<sup>254</sup> which is in large part responsible for early interest in the optoelectronic properties of MHPs. This allows for tunability of excitonic properties through simple chemical modifications of the organic interlayers. To illustrate, changing the position of fluorine in *ortho*-, *meta*-, *para*-fluorophenethylammonium A-site cations was shown to modify  $E_b$  in a 2D MHP.<sup>172</sup> For an ideal 2D system where the barrier and well have identical dielectric constants and the well thickness approaches zero, binding energy in the 2D system is related to its 3D analogue by  $E_b(2\text{D}) = 4E_b(3\text{D})$ . However, a more realistic scenario is given by the condition  $\epsilon_{\text{well}} = 3.53\epsilon_{\text{barrier}}$  as in the hybrid 2D MHP  $\text{CH}_3(\text{C}_8\text{H}_{16})\text{NH}_3\text{PbI}_4$ , which yields the relationship  $E_b(2\text{D}) = 13E_b(3\text{D})$  when  $E_b(3\text{D}) = 29$  meV and  $\epsilon_{\text{barrier}} = 1.84$ .<sup>114</sup> An empirical Hayne’s-type relationship between  $E_g$  and  $E_b$  is shown in Figure 23 for a number of 3D and LD MHPs and select conventional semiconductors. The pronounced influence of confinement in the LD systems is evidenced by the sharp increase of  $E_b$  with decreasing

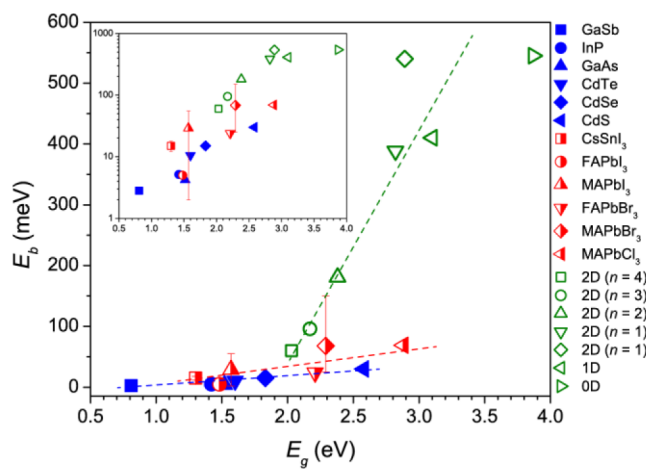
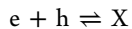


**Figure 23.** Empirical relationship between  $E_g$  and  $E_b$  in a number of 3D and LD MHPs and select conventional compounds. Lines are to guide the eye. Inset shows the same data on a semi-log plot. Data taken from Table 1 and Table 2. For materials with various reported values of  $E_b$ , the whiskers denote the highest and lowest reported values and the symbols represent the median value.

dimensionality. For 3D MHPs, Galkowski et al. showed that a similar relationship between  $m_r$  and  $E_g$  in the family of 3D MHPs  $\text{CH}_3\text{NH}_3\text{PbI}_3$ ,  $\text{CH}_3\text{NH}_3\text{PbI}_{3-x}\text{Cl}_x$ ,  $\text{CH}_3\text{NH}_3\text{PbBr}_3$ ,  $\text{HC}(\text{NH}_2)_2\text{PbI}_3$ , and  $\text{HC}(\text{NH}_2)_2\text{PbBr}_3$  can be well-described by a semiempirical two-band  $k \cdot p$  Hamiltonian approach, finding the linear relationship  $E_g/m_r = 16.6$  at 2 K.<sup>178</sup> The authors suggest that this relationship can be used to predict binding energies and reduced effective masses in other 3D MHPs.

**4.1.2. Saha Equation and Manybody Effects.** We have seen that for 3D MHPs, the 1s exciton binding energy ranges from  $E_b \leq k_B T_{298K}$  in the triiodide family to  $E_b \geq k_B T_{298K}$  in higher band gap Br- and Cl-based compounds. This range of values represents an interesting situation where excitons and free carriers can coexist in equilibrium under the appropriate circumstances. In simple reaction terms this equilibrium is given by



where e and h are free electrons and holes, and X represents a Coulombically bound pair or exciton. Equilibrium is thus reached under the familiar condition where the rate of the forward formation reaction is equivalent to the rate of the backward ionization reaction. In addition to the binding energy itself, environmental considerations that can act on this equilibrium include the lattice and carrier temperature and the density of photogenerated species, which are dictated by the energy and intensity of absorbed photons. At equilibrium, the balance between exciton and free carrier populations is determined by the well-known Saha–Langmuir equation, a distinct form of the semiconductor mass action law.<sup>255</sup> D’Innocenzo et al. were the first to examine the equilibrium branching ratio between excitons and free carriers in  $\text{CH}_3\text{NH}_3\text{PbI}_3$  using this relation.<sup>183</sup> It has since been employed in the analysis of time-resolved optical and THz spectroscopy of MHPs to estimate the quantum yield of free carrier generation, an important parameter for proper interpretation of THz photoconductivity spectra.<sup>256–258</sup> In accordance with this model, the fraction of free carriers relative to the total excitation density ( $\phi_{fc}$ ) in a 3D system is given by

$$\frac{\phi_{fc}^2}{1 - \phi_{fc}} = \frac{1}{n} \left( \frac{2\pi m_r k_B T}{h^2} \right)^{3/2} \exp \left[ -\frac{E_b}{k_B T} \right] \quad (17)$$

where  $n$  is the total excitation density (carriers/volume). Intuitively, the number of free carriers increases with increasing temperature due to enhanced phonon-induced ionization. A simulation of the Saha–Langmuir relation at room temperature is shown in Figure 24A for a range of  $E_b$  values from 5–150 meV. In accordance with this simple model, a lower total excitation density reduces the likelihood of an electron and hole coming within their mutual Coulombic capture range. In other words, the fraction of excitons increases with increasing excitation density. At low carrier densities generated under 1 sun irradiation in terrestrial PV operation ( $n \leq 10^{15} \text{ cm}^{-3}$ ,  $I_{exc} = 100 \text{ mW cm}^{-2}$ ),<sup>259</sup> the excited state population consists almost exclusively of unbound electrons and holes for  $E_b \leq \sim 100$  meV, an advantageous situation for such an application as discussed above. The majority of 3D Pb and Sn MHPs exhibit binding energies within this range (Table 2), indicating exciton ionization is not a limiting factor in these devices. Beyond the low-density regime, the fraction of free carriers begins to decrease rapidly, falling from ~95% of the population to ~25% over 2 orders of magnitude ( $10^{16}$ – $10^{18} \text{ cm}^{-3}$ ) when  $E_b = 30$

meV. At reported densities coinciding with the onset of amplified spontaneous emission in  $\text{CH}_3\text{NH}_3\text{PbI}_3$  ( $\sim 2 \times 10^{18} \text{ cm}^{-3}$ ),<sup>52</sup> Figure 24A suggests that excitons dominate the excited state at room temperature for all binding energies. Such room temperature excitonic lasing is highly unlikely in this system considering QWs with much more stable excitons generally show a transition to free-carrier lasing at high density.<sup>260</sup> In fact, Saba et al. have addressed this very issue in  $\text{CH}_3\text{NH}_3\text{PbI}_3$ .<sup>225</sup> Their analysis involved calculation of the chemical potential of charges with respect to the non-renormalized continuum band edge as a function of total excitation density using three distinct descriptions of the excited state population: (i) a pure electron–hole plasma (EHP) and an EHP/exciton gas equilibrium as predicted by (ii) the Saha relation and (iii) a Fermi–Dirac distribution for the EHP and Bose–Einstein statistics for excitons. The results are shown in Figure 24B. If free carriers and excitons were in thermal equilibrium, the onset of stimulated emission at the photon energies observed experimentally ( $E_{las}$ ) would not occur until the excitation density reached nearly an order of magnitude greater than in the pure EHP case. A population consisting primarily of free carriers at high excitation density has been further confirmed through analysis of recombination processes<sup>53,225,226,237</sup> and the nonlinear absorption signal at various excitation wavelengths.<sup>261</sup>

The Saha–Langmuir relation is therefore only generally valid at low excitation densities, as it does not account for manybody effects that begin to manifest in the high-density regime. The question then is at what carrier density does eq 17 begin to break down? With increasing density, the attractive force between an electron and hole is mitigated (i.e., the binding energy is diminished) by the presence of other carriers that screen the Coulombic interaction. In keeping with the atomic analogy, this mechanism is akin to shielding of the attraction between valence electrons and the nucleus by core electronic levels. As the density is increased further, a decreasing  $E_b$  is accompanied by band gap renormalization (BGR) that shrinks the separation between the VB → CB continuum edge. This leads to the interesting observation that exciton resonance energies (i.e., peak positions) remain largely unchanged until a critical point where exciton energy levels are absorbed into the renormalized continuum.<sup>34,262</sup> Transformation from an exciton gas to EHP, which is diametrically opposed to the excited state population predicted by the Saha equation, is one manifestation of the Mott metal–insulator transition.<sup>263</sup> Excluding exciton–exciton screening, which in most cases is a minor correction to free carrier effects,<sup>264</sup> a rigorous treatment can be carried out through the random phase approximation.<sup>265</sup> However, for illustrative purposes, the Lindhard relation that describes intraband rearrangement of carriers in  $k$ -space as a result of Coulombic interactions can be reasonably approximated using the Debye–Hückel screening length given by  $\lambda_D = [(e k_B T)/(8\pi\epsilon_0^2 n)]^{1/2}$ . The Mott transition occurs at a critical density ( $n_{crit}$ ), where the ratio  $r_B/\lambda_D$  is order one,<sup>266</sup> yielding<sup>237,266</sup>

$$n_{crit} = \frac{k_B T}{11\pi E_b r_B^3} \quad (18)$$

As indicated by the dashed line in Figure 24A, for  $E_b = 15$  meV and  $r_B = 5$  nm, the Mott transition is predicted to occur at  $n_{crit} \sim 4 \times 10^{17} \text{ cm}^{-3}$ , well below the onset of amplified spontaneous emission in  $\text{CH}_3\text{NH}_3\text{PbI}_3$ . For reference, the reported  $n_{crit}$  in bulk GaAs is  $\sim 2 \times 10^{16} \text{ cm}^{-3}$ .<sup>267</sup> The critical density for a range

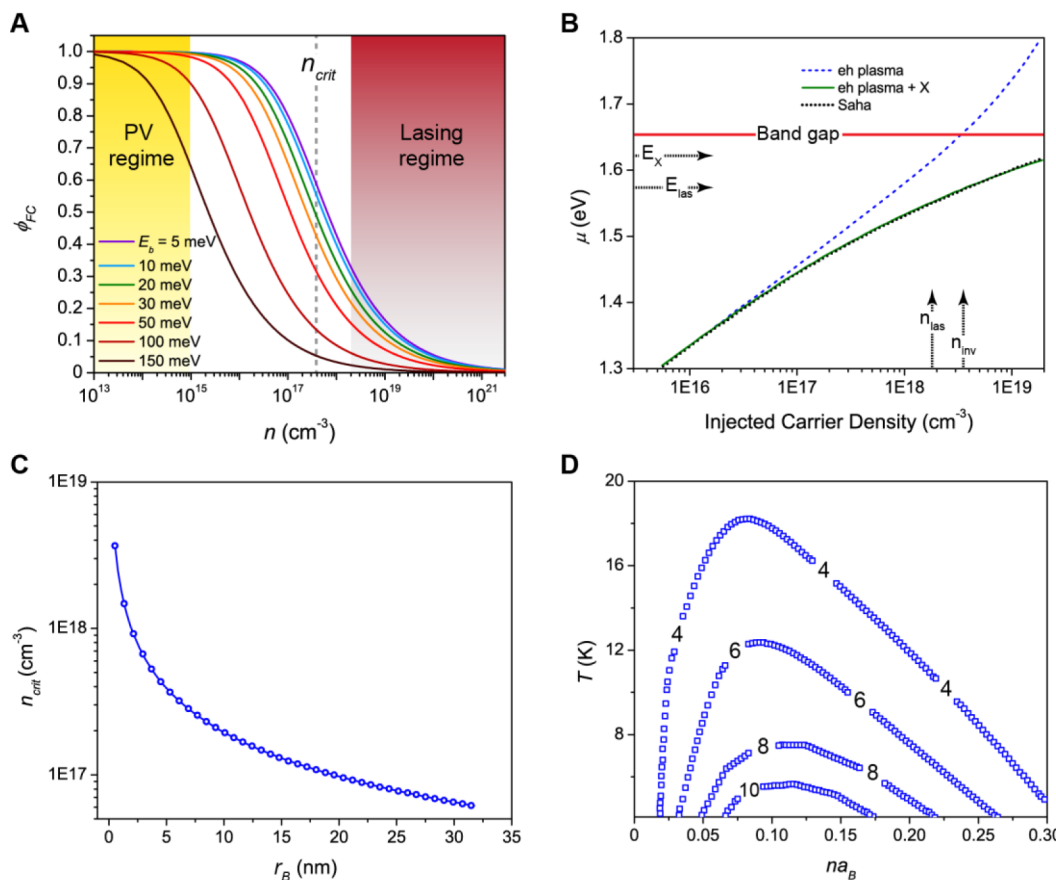


**Figure 24.** (A) Quantum yield of free carriers ( $\phi_{fc}$ ) as a function of excitation density according to the Saha eq (eq 17) for various values of  $E_b$  at room temperature, with  $m_r = 0.1m_0$ . Densities relevant for PV and lasing applications are highlighted, along with the critical carrier density,  $n_{crit}$  above which manybody effects limit exciton formation (for  $E_b = 15 \text{ meV}$ ). (B) Chemical potential of an excited state composed of a pure EHP and a population of both an EHP and excitonic species with the potential of the system determined using either the Saha equation or a combination Fermi–Dirac distribution for the EHP and Bose–Einstein statistics for excitons. Stimulated emission can only occur at photon energies where  $\hbar\omega < \mu(n)$  [i.e., below the lines indicating  $\mu(n)$  of the various populations]. (B) reprinted by permission from Macmillan Publishers Ltd.: Nature Communications (ref 225), copyright 2014. (C) Approximate critical carrier concentrations at the Mott density where excitonic species are ionized as a function of exciton Bohr radius. (D) Contour plot showing the percentage of 1s excitons formed per nanoseconds from an incoherent EHP 1.2 ns after simulated nonresonant excitation of a 1D nanostructure, with an initial carrier temperature of 60 K. Electronic parameters are roughly equivalent to a GaAs quantum well with  $E_b \sim 11 \text{ meV}$ . (D) adapted with permission from ref 269. Copyright 2003 American Physical Society.

of exciton Bohr radii is given in Figure 24C. Excitons with small  $r_B$  and large  $E_b$  require higher densities before the Mott transition induces complete dissociation. Following the initial discussion of the Mott transition in MHPs,<sup>237</sup> it has since been invoked to describe the free carrier behavior of  $\text{CH}_3\text{NH}_3\text{PbI}_3$  single crystals following resonant, high-fluence excitation above  $n_{crit}$  in time-resolved THz spectroscopic measurements.<sup>257</sup>

Realistically, the balance between bound excitons and an EHP is a complex manybody problem for any semiconductor subjected to high intensity excitation. The fraction of excitons present under low excitation density does not simply vanish at the Mott transition. Evolution of the excited state population is a continuous function of carrier density.<sup>34,263,268</sup> Decreasing  $E_b$  as a result of Coulombic screening alters the equilibrium  $\phi_{fc}$ , which in turn alters screening. A rigorous self-consistent approach is therefore required to accurately determine the nature of the excited state population at various temperatures and carrier densities. Such a microscopic manybody treatment that includes carrier–carrier and carrier–phonon interactions has been performed for nonresonantly excited 1D nanostructures. The results are given in Figure 24D.<sup>269</sup> The model parameters were chosen to reflect the properties of a GaAs

QW, with  $E_b = 11 \text{ meV}$ , on par with 3D iodide-based MHPs. Contour lines represent the percentage of incoherent, uncorrelated electrons and holes that form into Coulombically bound pairs (per nanosecond) as a function of lattice temperature. Consistent with the Saha equation, Coulombic interactions drop off sharply at low densities. And in line with our above discussion of manybody effects, exciton formation is likewise inhibited at high densities. Thus, there exists an intermediate regime where electron–hole interactions are maximized. Across all densities, temperature plays an overwhelming role, with a substantial fraction of excitons only generally stable under cryogenic conditions given the considered material parameters. The overall behavior derived from this model is expected to be applicable for higher dimensionality structures as well.<sup>269</sup>

We can therefore augment the current consensus that the majority of 3D MHPs act as free-carrier semiconductors in PV applications by asserting they are also free-carrier semiconductors at high excitation densities necessary for room temperature optical gain. Only for moderate optical or electronic excitation ( $n \sim 10^{16}\text{--}10^{17} \text{ cm}^{-3}$ ) does the situation become more muddled. Under these conditions, comprehen-

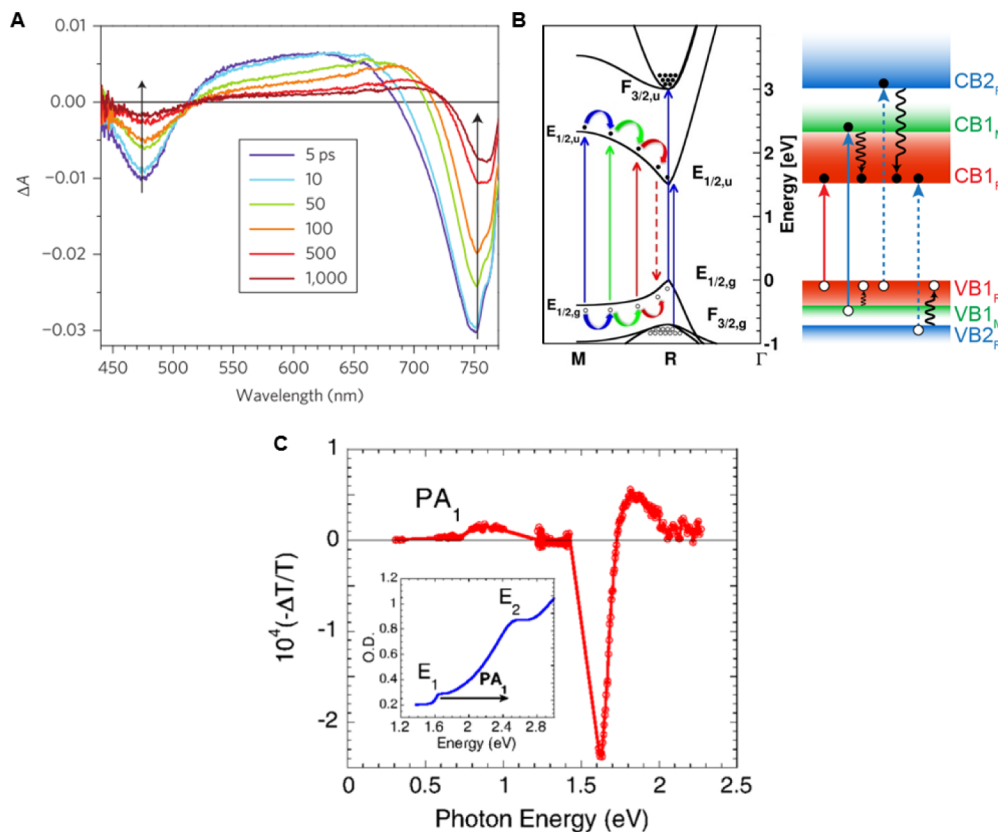


**Figure 25.** (A) Differential absorption spectrum of a mesoporous  $\text{CH}_3\text{NH}_3\text{PbI}_3$  film at various pump–probe delay times following excitation at 387 nm with an energy density of  $8 \mu\text{J cm}^{-2}$ . Reproduced with permission from Macmillan Publishers Ltd.: Nature Photonics (ref 237), copyright 2014. (B) (Left) Electronic structure of the cubic  $Pm\bar{3}m$  phase of  $\text{CH}_3\text{NH}_3\text{PbI}_3$  in the vicinity of the lowest electronic transition calculated using SOC-DFT. A correction was applied to match the experimental band gap at the R point. Upward arrows indicate allowed direct transitions. Also shown are possible carrier relaxation channels. Reproduced from ref 189. Copyright 2014 American Chemical Society. (right) Simplified band diagram according to the electronic structure in the left panel that highlights the multivalley, dual VB-dual CB nature of  $\text{CH}_3\text{NH}_3\text{PbI}_3$ . (C) Differential transmission spectrum of  $\text{CH}_3\text{NH}_3\text{PbI}_3$  across visible and into MIR frequencies immediately following excitation at 400 nm. Panel (C) reprinted with permission from ref 273. Copyright 2015 American Physical Society.

sive studies of the PL line shape in MHPs at various temperatures and excitation densities can be utilized to map out the excited state phase diagram of these compounds.<sup>268</sup> Only through such systematic investigations, which have yet to be carried out, can a more quantitative interpretation of the interplay between excitons and free carriers be realized for the family of 3D MHPs.

#### 4.2. Optical Nonlinearity and Photoconductivity

Spectroscopic studies have provided important insight into the underlying optical and electronic properties of MHPs, including details regarding exciton formation and free carrier generation, recombination pathways, and carrier transport. Following optical photoexcitation that “pumps” the material into the excited state, various processes can then be tracked either by collecting emitted photons or by probing the material using a second pulse of light. The latter experimental setup is known as pump–probe spectroscopy and forms the basis of many studies covered herein. By delaying the arrival of the probe relative to the pump, precise time-resolution can be achieved. For semiconductors, the pump has energy equal to or greater than the band gap and can be continuous, quasi-continuous, or pulsed in nature. Excitation with energies at or just below the continuum transition (i.e., at the excitonic resonance frequency) is termed resonant excitation, while use of energies above the onset of continuum absorption is said to be

nonresonant. This is an important distinction since nonresonant excitation yields hot carriers above the band edge that rapidly thermalize through emission of phonons (i.e., quanta of vibrational energy in periodic structures). This phonon emission process raises the temperature of the system and inhibits exciton formation. Because of the direct correlation between excitation fluence and the population of photo-generated species, simply varying the power density of the pump enables investigation of excited state dynamics over many orders of injected carrier concentration. This is particularly important for MHPs considering their use in low carrier-density PV and high-density lasing applications. The probe is typically a broadband source that lies in one of several relevant frequency domains depending on the species or processes of interest. Probe pulses with energy in the visible (i.e., optical), near- to mid-IR (NIR-MIR), terahertz, and gigahertz regimes have been employed in the characterization of MHPs. We begin first with a general overview of the excited state spectra of MHPs in each of the characteristic frequency domains. This will facilitate the discussion on spectral and kinetic analysis throughout this section.

A change in signal intensity as a function of time after carrier injection provides insight into the behavior of photogenerated species and the time scale of various excited state processes. In general, features in the visible and NIR regions of nonlinear pump–probe spectra originate from a number of different

electronic processes in semiconductors, including (i) attenuation of linear absorption from state or phase-space filling [photoinduced bleach (PIB)], (ii) absorption from the excited state to higher-lying energy levels [photoinduced absorption (PIA)], (iii) stimulated emission (PIB), (iv) shifts in the linear spectrum (manifesting as PIBs and/or PIAs) caused by renormalization of the band edge or electric fields established by the excited state population (e.g., electroabsorption or transient Stark effect), and (v) photoinduced modulation of the refractive index. Each of these mechanisms has been invoked in some capacity to explain optical excited state spectra of MHPs. Depending on the material and experimental conditions, these optical nonlinearities may be convoluted. Moreover, their contributions are a function of excitation density, which negates any overgeneralizations regarding the presence/relevance of these various phenomena in a given system.

In the case of MHPs, nonlinear behavior is also sensitive to thin film fabrication procedures and postprocessing. Claims regarding the validity of various techniques and interpretations without full knowledge of experimental setups and sample preparation should therefore be made lightly,<sup>270</sup> especially considering the pronounced influence of microstructure on the underlying photophysical properties of MHPs that has been evinced in recent reports.<sup>183,256,271</sup> Moreover, photo-, heat-, and moisture-induced degradation of MHPs is an ongoing issue that has been shown to impact the optical and electronic properties of these materials,<sup>168,201,212,272</sup> potentially complicating structural and spectroscopic analysis of hybrid perovskites in particular. For example, excited state transients of the degradation product PbI<sub>2</sub> can convolute the nonlinear spectral features of CH<sub>3</sub>NH<sub>3</sub>PbI<sub>3</sub> above the band edge.<sup>168</sup> Here, we make a concerted effort to focus on the intrinsic properties of MHPs, while remaining cognizant that sample quality, microstructure, and stability may influence reported results.

Figure 25A shows the basic features of the optical differential absorption spectrum of CH<sub>3</sub>NH<sub>3</sub>PbI<sub>3</sub>.<sup>237</sup> Here  $\Delta A = A_{\text{pump+probe}} - A_{\text{probe}}$ , such that reduced attenuation (increased transmittance) of the probe pulse after excitation appears as a negative feature. The main spectral features across the visible region in CH<sub>3</sub>NH<sub>3</sub>PbI<sub>3</sub> are a low-energy PIB near the band edge transition (~760 nm, 1.6 eV), a broad PIA, and a high-energy PIB (~490 nm, 2.53 eV) corresponding to the second peak in the linear spectrum.<sup>237</sup> Significant efforts have focused on determining the origin of nonlinear spectral features across the optical frequencies in hybrid MHPs.<sup>53,59,139,237,261,273</sup> Because the line shape and kinetics of nonlinear signals provide insight into the nature of the photogenerated population and charge annihilation mechanisms, the band edge photobleach of CH<sub>3</sub>NH<sub>3</sub>PbI<sub>3</sub> in particular has attracted considerable attention. It has been attributed to bleaching of both the continuum<sup>53,139,237,256</sup> and Coulombically enhanced excitonic absorption through state and phase-space filling.<sup>59</sup> The small Stokes shift in this material suggests that stimulated emission, which follows the PL line shape, also contributes on the low-energy side of the bleach.<sup>53,139,274</sup> Further complicating analysis is the change in spectral features as a function of injected carrier density.<sup>59,237</sup>

Before delving into the details of the highly scrutinized band edge bleach of CH<sub>3</sub>NH<sub>3</sub>PbI<sub>3</sub>, we first examine how the electronic structure, which has been covered in sections 2 and 3, can simplify interpretation of the optical and NIR-MIR excited state spectra. In the early stages of time-resolved spectroscopic studies of CH<sub>3</sub>NH<sub>3</sub>PbI<sub>3</sub> and related compounds,

advanced electronic structure calculations on these materials were only beginning to surface. Defining the origins of the various signals was therefore dependent on experimental analysis of their energy distribution and growth/decay kinetics. Xing et al. were the first to propose a working band structure to describe the excited state of CH<sub>3</sub>NH<sub>3</sub>PbI<sub>3</sub>.<sup>139</sup> Their model included a dual VB structure with a single CBM. Such an assignment was formed under the context of a rapid rise and subsequent subpicosecond decay in the high-energy PIB that coincided with the rise time of the band edge PIB, suggesting rapid carrier cooling from the higher energy state. It was further corroborated by charge extraction kinetics upon contact with organic electron and hole acceptors. Later, Stamplecoskie et al. proposed a VB → CB transition coupled with a separate charge transfer absorption band, essentially a four-state model, to explain the two PIBs and broad PIA in context of the underlying halometallate optical transitions present in both the precursor and final perovskite phase, as well as the differing kinetics that arise in the various signals at high carrier densities.<sup>275,272</sup>

While both of these early models provided clues to the complex multiband nature of CH<sub>3</sub>NH<sub>3</sub>PbI<sub>3</sub> across optical frequencies, utilization of sophisticated computational methods that include spin-orbit interactions have since provided a more complete picture of the electronic structure and how it relates to observed transient spectra and kinetics. Figure 25B shows the results of SOC-DFT electronic structure calculations near the band edge in the first Brillouin zone of cubic phase CH<sub>3</sub>NH<sub>3</sub>PbI<sub>3</sub>.<sup>189</sup> Also shown are possible carrier relaxation channels between high symmetry points following optically allowed direct electronic transitions in the full structure diagram and a simplified band scheme. While SOC-DFT is not the most robust method for analyzing MHP electronic structure (see section 2), similar band gaps and transition energies can be extracted from the tetragonal phase of CH<sub>3</sub>NH<sub>3</sub>PbI<sub>3</sub> using state-of-the-art SOC-GW manybody methods.<sup>124</sup> There are effectively two relevant VBM and CBMs at the R point, which we label VB1<sub>R</sub>, VB2<sub>R</sub>, CB1<sub>R</sub>, and CB2<sub>R</sub>, where 1 represents the higher (lower) lying VBM (CBM) constituting the band edge transition. There is also a related high-energy direct transition at the M point associated with the VB1 and CB1 bands, denoted VB1<sub>M</sub> and CB1<sub>M</sub>. The low-energy PIB stems from pump-induced changes (e.g., state filling, renormalization, exciton screening) at the R point ( $\Gamma$  in the tetragonal phase) corresponding to VB1<sub>R</sub> → CB1<sub>R</sub>. Primary transitions at the M point and secondary transitions at the R point comprise the high-energy PIB, partly explaining the difficulty in spectroscopic elucidation of this feature. Because M is a saddle point, carriers can readily relax down to the lower-lying R point by interaction with acoustic phonons.<sup>189</sup> However, depopulation of VB2<sub>R</sub> and CB2<sub>R</sub> requires interaction with higher frequency optical phonons. Beyond the initial relaxation, sustained bleaching of the higher-energy differential signal on the nanosecond time scale must be associated with charges at the band edge given the slow decay,<sup>139,237,275,276</sup> and most likely results from Pauli blocking of VB1<sub>R</sub> → CB2<sub>R</sub> and/or VB2<sub>R</sub> → CB1<sub>R</sub>. It is also important to note the disproportionality between the high amplitude linear absorption at ~490 nm and the comparatively diminutive differential signal at the associated PIB. This disparity is consistent with modest matrix elements associated with the secondary transitions at R and rapid recovery of the much stronger VB1<sub>M</sub> → CB1<sub>M</sub> transition as a result of thermalization to, and momentum offset from, the

band edge.<sup>189</sup> Furthermore, recovery kinetics of the high-energy PIB are enhanced relative to the band edge PIB under high injection densities.<sup>275,276</sup> A possible explanation is increased carrier–carrier scattering at high densities that leads to enhanced carrier cooling rates to the lower energy state, where carrier–phonon interactions then dominate.<sup>59,261</sup> The origin of these disparate kinetics is still an open question, but such behavior highlights the distinct behavior of the various electronic states. Understanding the distribution of states, their electronic relationships, and their transition probabilities provides a framework upon which further analysis of optical nonlinearities can be carried out. Although the most comprehensive analysis has been performed on  $\text{CH}_3\text{NH}_3\text{PbI}_3$ , the general electronic structure of other 3D MHPs share many similarities and thus their nonlinear optical properties can be rationalized in much the same manner.

Near- to mid-IR probes have also been utilized to study the photoexcitation dynamics of MHPs,<sup>273,277</sup> albeit to a much lesser extent than optical and THz frequencies. Figure 25C shows a NIR-MIR differential transmission spectra of  $\text{CH}_3\text{NH}_3\text{PbI}_3$ .<sup>273</sup> Sheng et al. attribute the relatively sharp PIA in the MIR ( $\sim 0.8$  eV, labeled PA<sub>1</sub>) to excitonic species that form within the 300 fs time resolution of their experimental setup. Specifically, 0.8 eV corresponds to an optically allowed interband transition at R from the lowest-energy excitonic state in the spin-orbit split off CB ( $\Gamma_4$ ) to higher-lying excitonic states ( $\Gamma_3$  and  $\Gamma_5$ ).<sup>273,277</sup> In accordance with our notation outlined in Figure 25B, this MIR signal is purportedly due to discrete excitonic states associated with CB1<sub>R</sub> and CB2<sub>R</sub>. While features at these energies could originate from continuum transitions corresponding to a high density of states, the authors argue that differing kinetics between the MIR PIA and band edge bleach indicate the presence of two distinct species.<sup>273</sup> In contrast, MIR and optical spectral features were shown to exhibit the same growth and decay dynamics in  $\text{CH}_3\text{NH}_3\text{PbI}_{1.1}\text{Br}_{1.9}$  and  $\text{CH}_3\text{NH}_3\text{PbI}_3(\text{Cl})$ , which has been taken as an indication of an all-excitonic photogenerated population in these compounds at room temperature.<sup>273,277</sup> Such pronounced discrepancies in the nonlinear response of  $\text{CH}_3\text{NH}_3\text{PbI}_3$  and  $\text{CH}_3\text{NH}_3\text{PbI}_3(\text{Cl})$  requires further investigation considering the generally limited compositional differences between the two materials. Overall, studies with a greater level of scrutiny are required to fully understand the origin of transient MIR spectral features in MHPs, and to reconcile the proposed significant excitonic character with the multitude of reports demonstrating their free carrier nature under typical nonresonant pulsed laser excitation.<sup>53,59,182,184,225,232,233,237,261</sup> Notably, samples utilized for MIR measurements presented here were prepared by a simple one-step deposition that yields largely inhomogeneous thin films. Similar measurements on low-defect single crystals can further support interpretation of these features. Also, examining changes in MIR signals as a function of injected carrier density and temperature could help elucidate their origin.

Before general consensus was reached regarding the room temperature free carrier nature of  $\text{CH}_3\text{NH}_3\text{PbI}_3$ , two important characteristics of its band edge bleach were discovered in early spectroscopic investigations that provided insight into the primary photoexcitations. The first was a pronounced broadening of the band edge PIB upon high intensity nonresonant excitation that was shown to increase as a function of carrier density.<sup>237</sup> This band broadening in the quasi-equilibrium regime, seen in Figure 26A, exhibited semiquantitative

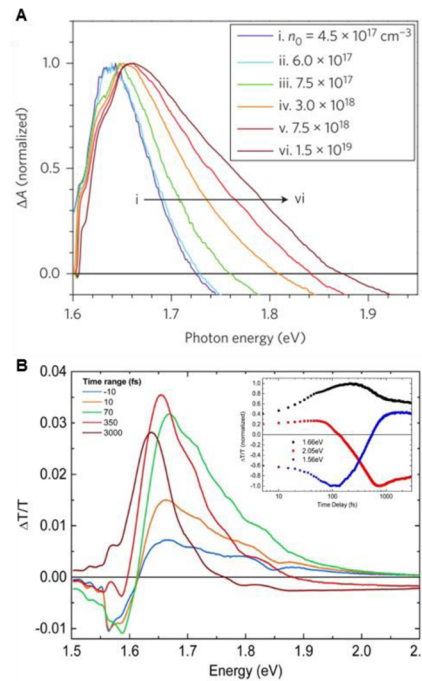


**Figure 26.** (A) Quasi-equilibrium band filling in mesoporous  $\text{CH}_3\text{NH}_3\text{PbI}_3$  at various initial injected carrier densities 5 ps after nonresonant pulsed laser excitation. Reproduced with permission from ref 237. (B) Differential transmission signal near the  $\text{CH}_3\text{NH}_3\text{PbI}_3$  band edge recorded at probe delays  $\leq 3$  ps. Both the high- and low-energy PIAs (shown here as negative signals) can be seen. Inset shows the rapid decay of the low-energy signal at 1.56 eV. Reproduced from ref 53. Copyright 2014 American Chemical Society.

agreement with the free electron Burstein–Moss band filling theory.<sup>278,279</sup> This is a well-known Pauli blocking phenomenon that is observed in conventional degenerately doped semiconductors and as a photoinduced dynamic process at high carrier densities in intrinsic compounds.<sup>252,265,267,280–282</sup> Note that the peak position does not appreciably shift due to competing manybody effects. BGR at high free carrier densities is compensated by a decrease in Coulombic interactions through enhanced screening (section 4.1.2).<sup>283</sup> However, the quasi-Fermi level of electrons and holes is proportional to  $\sim n^{2/3}$ , while BGR  $\propto \sim n^{1/3}$ , which leads to a net bleaching on the high-energy side of the transition.<sup>267</sup> The second important early observation was a small, short-lived PIA on the low-energy side of the main band edge bleach (Figure 26B).<sup>53</sup> This feature was initially attributed to the presence of a correlated electron–hole population that is rapidly ionized. More on this point below.

Since these initial observations, optical nonlinearities near the band edge have continued to attract significant attention. In particular, origins of the two PIAs on the low- and high-energy side of the ground state bleach have been widely disputed. The low-energy feature has been attributed to three possible mechanisms: (i) electroabsorption/Stark effect,<sup>53,284,285</sup> (ii) BGR,<sup>53,231,261</sup> and (iii) bleaching/broadening of the 1s excitonic transition through phase-space filling.<sup>59</sup> Proposed sources of the high-energy PIA include (i) BGR,<sup>59</sup> (ii) modulation in refractive index of the medium,<sup>53,256,261</sup> and (iii) modification of the deformation potential due to an inhomogeneous excitation profile.<sup>277</sup> Yang et al. modeled the relatively complex nonlinear spectrum of  $\text{CH}_3\text{NH}_3\text{PbI}_3$  by

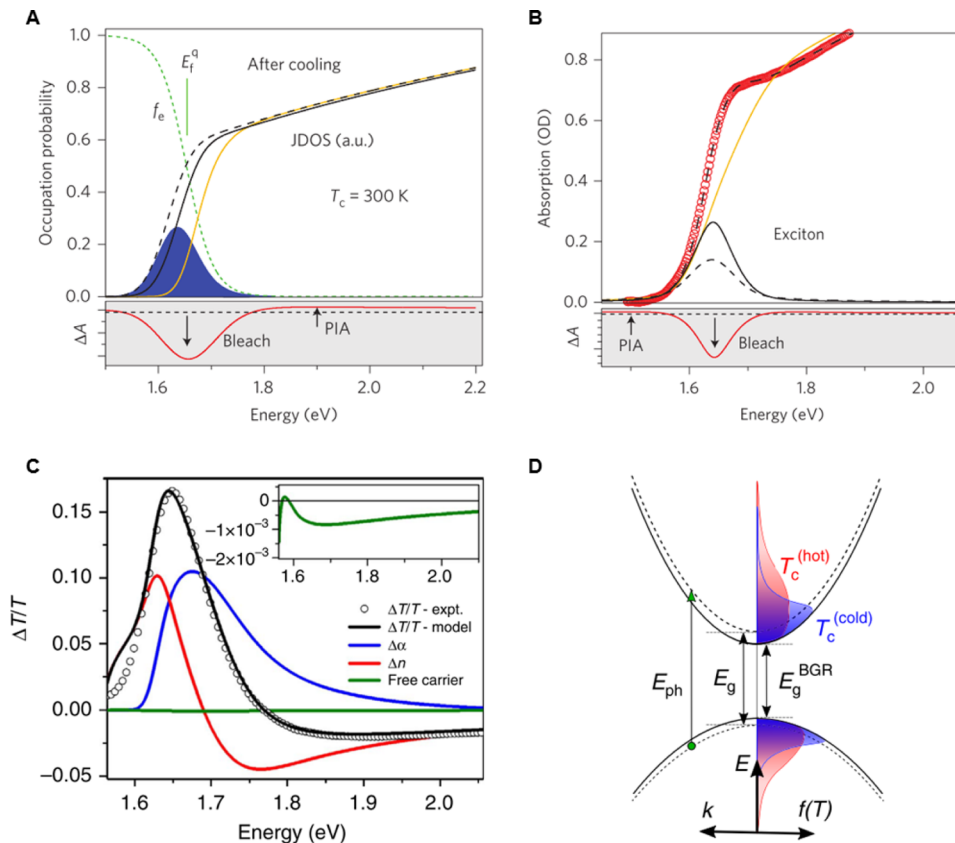


**Figure 27.** (A) Bleaching of the  $\text{CH}_3\text{NH}_3\text{PbI}_3$  continuum transitions following nonresonant pulsed laser excitation and after carrier thermalization. The differential absorption signal (red line) is taken as the difference between the unperturbed JDOS (black solid line) and the yellow line, which is a convolution of band filling (carrier distribution shown as blue shaded region) and BGR (black dashed line) effects. (B) Exciton bleaching by free carriers in  $\text{CH}_3\text{NH}_3\text{PbI}_3$ . The differential absorption (red line) is determined by subtracting the unperturbed excitonic absorption (black solid line) from the partially bleached exciton transition (black dashed line). (A and B) reprinted by permission from Macmillan Publishers Ltd.: Nature Photonics (ref 59), copyright 2015. (C) Differential transmission spectrum of  $\text{CH}_3\text{NH}_3\text{PbI}_3$  (open symbols) modeled using eq 22 (black line). Absorption (blue line), refractive index (red line), and free carrier (green line) contributions are shown. (D) Illustration of the interplay between BGR and carrier cooling upon nonresonant excitation. Hot and cold carrier distributions are shown. (C and D) reproduced with permission from ref 261 under CC BY 4.0.

taking into consideration continuum and excitonic effects as well as BGR.<sup>59</sup> Their analysis of the continuum (after carrier cooling) and excitonic contributions is shown in Figure 27 (panels A and B, respectively). The total signal is therefore a summation of the two sources of nonlinearity such that  $\Delta A(\hbar\omega) = \Delta A_{\text{fc}}(\hbar\omega) + \Delta A_{\text{ex}}(\hbar\omega)$ , where the first term denotes free carrier and the second indicates excitonic effects. The two contributions are given by eqs 19 and 20.<sup>59</sup>

$$\begin{aligned} \Delta A_{\text{fc}}(\hbar\omega) &= A_{\text{fc}}(\hbar\omega; E_g - \Delta E_g)[1 - f_e^q(\hbar\omega; E_f^q, T_e)]^2 \\ &\quad - A_{\text{fc}}(\hbar\omega; E_g) \end{aligned} \quad (19)$$

$$\Delta A_{\text{ex}}(\hbar\omega) = A_{\text{ex}}(\hbar\omega, \Gamma)f_b(n) - A_{\text{ex}}(\hbar\omega, \Gamma_0) \quad (20)$$

For the continuum,  $f_e^q(\hbar\omega; E_f^q, T_e)$  is the Fermi–Dirac distribution following photoexcitation described by a quasi-Fermi energy  $E_f^q$  and carrier temperature  $T_e$ .  $A_{\text{fc}}(\hbar\omega; E_g)$  is the nonrenormalized absorption spectrum, and  $A_{\text{fc}}(\hbar\omega; E_g - \Delta E_g)$  is the absorption spectrum after BGR. In the case of excitonic effects,  $f_b(n) = 1/(1 + n/n_c)$  represents attenuation of the exciton oscillator strength at a given free carrier concentration ( $n$ ) and is characterized by a critical density where oscillator strength is reduced by 50% ( $n_c$ ).  $A_{\text{ex}}(\hbar\omega, \Gamma_0)$  is the Voigt function with FWHM =  $\Gamma_0$ , and  $\Gamma$  is the exciton bandwidth

following photoexcitation. The yellow lines in Figure 27 (panels A and B) denote the modified absorption spectrum following photoexcitation in the continuum and excitonic regimes, respectively. Note that inclusion of excitonic effects does not imply the presence of Coulombically bound electrons and holes. Free carriers generated by nonresonant excitation can quench transitions at these energies through phase-space filling (i.e., Pauli blocking) and Coulombic interactions.<sup>286–288</sup> According to this model, the high-energy PIA results from a shift of the linear absorption spectrum due to sizable BGR, while the low-energy PIA stems from quenching of the excitonic transition.

A second recent approach to modeling  $\text{CH}_3\text{NH}_3\text{PbI}_3$  band edge nonlinearities has been proposed by Price et al.<sup>261</sup> This comprehensive method accounts for photoinduced changes in continuum and excitonic transitions as well as the refractive index. In general, photoexcitation of semiconductors leads to modulation of both components of the complex dielectric function. The imaginary extinction component has primarily been considered in analysis of MHP nonlinear spectra, but the large real component, which corresponds to reflectivity, suggests that this term must be included. Elements of a complex function are connected through the Kramers–Kronig

relations. The refractive index  $n(E)$  can thus be formulated in terms of optical absorption  $\alpha(E)$  as given by<sup>33</sup>

$$n(E) - 1 = \frac{ch}{2\pi^2} P \int_0^\infty \frac{\alpha(E')}{(E')^2 - E^2} dE' \quad (21)$$

where  $E = \hbar\omega$  is the photon energy and  $P$  is the Cauchy principle value of the integral  $P \int_0^\infty \equiv \lim_{a \rightarrow 0} (\int_0^{\omega-a} + \int_{\omega+a}^\infty)$ . The ratio between real and imaginary components dictates the extent to which refractive index changes manifest. In low dielectric organic compounds, such effects are negligible. But in conventional high dielectric semiconductors and MHPs, it is an important factor to consider when analyzing nonlinear spectra. Therefore, the differential transmittance spectrum near the band edge can be modeled using both absorption and refractive index terms<sup>261</sup>

$$\frac{\Delta T}{T} = -l\Delta\alpha(E) + \frac{2[n_g - n(E)]}{[(n(E)^2 + n(E))(n_g + n(E))]} \Delta n(E) \quad (22)$$

with  $l$  the sample thickness,  $n(E)$  the energy-dependent refractive index, and  $n_g$  the refractive index of the glass substrate. This two-reflection model is valid for a probe beam at normal incidence to the sample surface. A similar approach has also recently been taken by Yang et al.<sup>58</sup> The full fit 4 ps after nonresonant photoexcitation along with individual  $\Delta\alpha(E)$ ,  $\Delta n(E)$ , and comparatively minor free carrier contributions are given in Figure 27C. Refractive index changes clearly give rise to a high-energy PIA in the convoluted spectrum. Furthermore, separation of the various contributions allows for a more quantitative Burstein–Moss band filling analysis, yielding a reduced effective mass of  $m_r = 0.14m_0$  that is consistent with values determined by high-field magnetoabsorption spectroscopy.<sup>136,178</sup> Without considering changes in transient reflectivity, similar analysis overestimates  $m_r$  by a factor of  $\sim 2$ .<sup>237,261</sup> Price et al. also suggest that the low-energy PIA stems from two interrelated factors: rapid BGR and slow carrier cooling upon nonresonant excitation.<sup>261</sup> Following rapid renormalization ( $\leq \sim 100$  fs), states at the newly formed band edge are available for optical transitions due to an elevated carrier temperature, leading to a PIA. As the hot photoinduced carriers in a Fermi–Dirac distribution cool, band edge states become populated, reducing the PIA until it eventually becomes a PIB at longer delay times. This is shown schematically in Figure 27D. Note that the cooling of hot carriers in  $\text{CH}_3\text{NH}_3\text{PbI}_3$  [and  $\text{HC}(\text{NH}_2)_2\text{PbI}_3$ ] is anomalously slow, nearly 3 orders of magnitude slower than in GaAs under comparable excitation,<sup>59</sup> and has been attributed to a hot-phonon bottleneck at high carrier densities where reabsorption of nonequilibrium phonons reduces the rate of relaxation to the band edge.<sup>59,261</sup> The BGR-hot carrier mechanism is corroborated by: (i) slower PIA decay kinetics at high excitation densities resulting from the increased carrier cooling time and (ii) a reduced PIA magnitude upon resonant pumping.<sup>267</sup>

Spectroscopic studies employing THz and GHz probe pulses have also bolstered our understanding of the underlying photophysics of MHPs. Unlike time-resolved optical spectroscopy, low-frequency THz and GHz probes ( $\sim 10^{-2}$ – $10^2$  meV) cannot couple with high-energy electronic transitions. They can however effectively sample charge mobility within an optically excited semiconductor, probing shallow trap state and/or exciton ionization and transport mechanisms of photogenerated

species.<sup>289</sup> Such information is particularly relevant for the discussion in section 5.1. The principal experimental parameter extracted from time-resolved microwave conductivity (TRMC) and THz spectroscopy (TRTS) is a change in conductivity ( $\Delta\sigma$ ) upon photoexcitation according to<sup>290</sup>

$$\Delta\sigma = \phi_{fc}(\mu_e + \mu_h) = -\left[ \frac{\Delta E_{\text{exc}}(\omega)\epsilon_0 c}{\Delta E_{\text{gs}}(\omega)F e_0(1 - e^{-\alpha L})} \right] \quad (23)$$

where  $\phi_{fc}$  is the quantum yield of free-carrier generation and ranges from 0 to 1,  $\mu_e$  and  $\mu_h$  are the electron and hole mobility, respectively,  $\Delta E_{\text{exc}}$  and  $\Delta E_{\text{gs}}$  are the transmitted probe fields in the presence and absence of the optical pump pulse, respectively,  $\epsilon_0$  is the permittivity of free space,  $c$  is the velocity of light,  $F$  is the pump fluence,  $e_0$  is the elementary charge,  $\alpha$  is the absorption coefficient at the pump frequency, and  $L$  is the sample thickness. Evolution of the photoconductivity spectrum with time can arise from changes in carrier population and/or mobility. Precise knowledge of the exciton/free carrier branching ratio as a function of time is therefore vital for proper analysis of these spectra. It is often estimated using known parameters such as the dielectric constant, effective mass, and injected carrier density through the Saha relation (section 4.1.2). It can also be deduced by fitting  $\Delta\sigma$  with an appropriate model (e.g., Drude or Drude-Smith) across a broad frequency range.<sup>257,291</sup> Consequences of these assumptions as they pertain to determination of carrier mobility in MHPs are discussed in section 5.1. It is important to note that recent high-energy broadband TRTS measurements appear to directly probe exciton ionization, which occurs within  $\sim 1$  ps, using THz pulses ranging from 8 to 100 meV.<sup>257</sup> Time-resolved spectra in the MIR seem to suggest a similar rapid ionization in  $\text{CH}_3\text{NH}_3\text{PbI}_3$  thin films.

TRTS and TRMC enable direct measurement of the real ( $\Delta\sigma_1$ ) and imaginary ( $\Delta\sigma_2$ ) components (amplitude and phase) of the photoinduced complex conductivity without Kramers–Kronig transformation. In the case of band-like charge mobility, both the real and imaginary conductivities are positive, with  $\Delta\sigma_1$  maximized and  $\Delta\sigma_2 = 0$  in the DC limit. Localized charges within disordered systems exhibit a negative imaginary component, while the real component follows non-Drudian behavior signified by decreasing magnitude at low frequencies.<sup>292,293</sup> The solid points in Figure 28 (panels A and B) show  $\Delta\sigma_1$  and  $\Delta\sigma_2$ , respectively, for a room temperature  $\text{CH}_3\text{NH}_3\text{PbI}_3$  thin film as measured by broadband TRTS.<sup>291</sup> The data clearly show characteristics of non-Drudian disordered transport. Fits to  $\Delta\sigma_1$  and  $\Delta\sigma_2$  (dashed lines) are therefore derived from a more general Drude-Smith model that accounts for carrier scattering, with contributions from Drude (yellow) and Smith (red) terms indicated.<sup>291</sup> Note that such disordered transport is not unexpected considering these films were prepared by a simple stoichiometric one-step deposition technique known to yield inhomogeneous films.<sup>93,201,276</sup> Commensurate non-Drudian photoconductivity spectra were obtained in a separate study utilizing similarly prepared films<sup>294</sup> and in high-quality thin films at low temperatures (<80 K) where carrier localization is enhanced.<sup>230</sup> Conversely, recent TRTS measurements on  $\text{CH}_3\text{NH}_3\text{PbI}_3$  single crystals and vapor-deposited thin films at room temperature indicate that broadband  $\Delta\sigma$  spectra can be well-described by the standard Drude model, suggesting increased long-range order under these conditions (Figure 28C).<sup>257,295</sup>

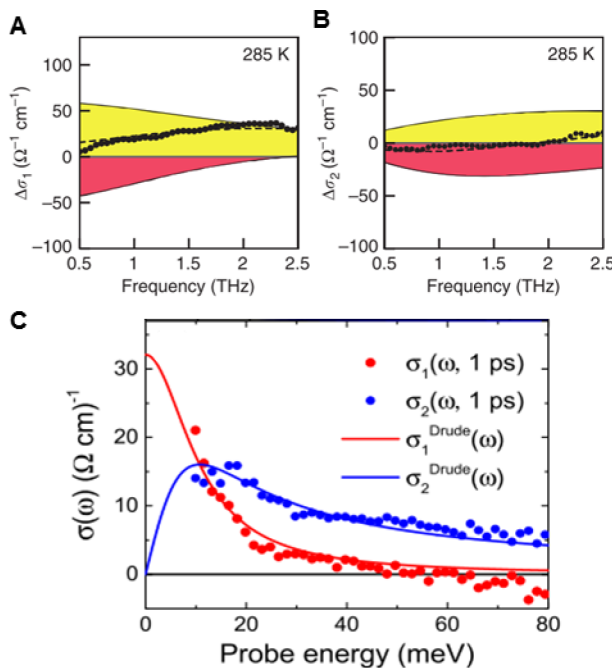


**Figure 28.** (A) Real and (B) imaginary THz photoconductivity spectra of a  $\text{CH}_3\text{NH}_3\text{PbI}_3$  sample recorded at room temperature 4.5 ps after 400 nm excitation. Drude (yellow), Smith (red), and total (dashed line) contributions are given. Reproduced with permission from ref 291 under CC BY 4.0. (C) Complex photoconductivity spectrum of a  $\text{CH}_3\text{NH}_3\text{PbI}_3$  single crystal 1 ps after resonant photoexcitation at 795 nm. Fits to the standard Drude model are shown as solid lines. Reproduced from ref 257 with permission of The Royal Society of Chemistry.

### 4.3. Recombination Mechanisms

The second important piece of information that can be conveniently derived from time-resolved spectroscopy is a kinetic description of photoinduced processes. Generally, after rapid dephasing and cooling of photogenerated species immediately following photoexcitation, additional loss of energy out of this nonequilibrium state over much longer time scales occurs radiatively through emission of light and/or nonradiatively through vibrational or carrier–carrier interactions. Appropriate modeling of time-resolved decay kinetics and steady-state PL intensity over a wide range of excitation intensities can provide physical insight into the processes that return an excited semiconductor to the ground state. Understanding the prevailing energy loss pathways at various carrier densities is vital to optimizing optoelectronic device configurations and operating conditions.<sup>244</sup> This is especially pertinent for the wide range of possible applications, from PVs to LEDs to optical gain media, on the horizon for MHPs.

Transient absorption/reflectance (TAS) (refs 53, 58, 59, 168, 228, 231, 237, 273, 275–277, 284, 285, 294, and 296–298) and time-resolved photoluminescence (TRPL) (refs 52, 53, 109, 140, 206, 209, 225, 226, 228, 232, 236, 258, 259, 284, 296, and 299–304), THz (TRTS), (refs 43, 213, 230, 257, 291, 294, 295, 301, 305, and 306) and microwave (TRMC)<sup>294,305,307</sup> spectroscopies have been used to probe recombination dynamics in hybrid MHPs. Steady-state PL measurements performed over a wide range of excitation intensities have also provided useful insight into the dominant recombination mechanisms through judicious choice of kinetic models.<sup>209,225,226</sup>

**Figure 29** provides a blueprint for possible generation and recombination channels. These can be separated into three

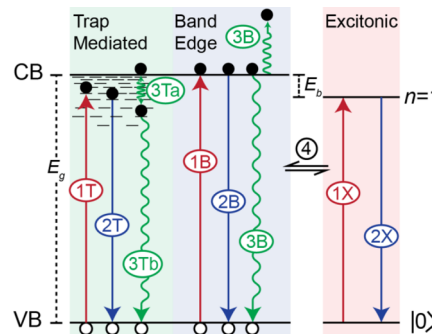


**Figure 29.** Blueprint of the various charge generation and recombination pathways in a bulk semiconductor. The ground state of the crystal is indicated by  $|0\rangle$ .

distinct classes: (i) trap mediated (T), (ii) band edge (B), and (iii) excitonic (X). For simplicity, hole-trapping mechanisms are neglected. As we will see, this is a fair assumption in  $\text{CH}_3\text{NH}_3\text{PbI}_3$ . Processes involving photons, whether a quantum excitation (1) or recombination event (2), are depicted by solid lines in the various regimes. Nonradiative interactions (3) are denoted by curved lines. The formation-ionization equilibrium between free carriers and excitonic species, which is a function of binding energy, temperature, and carrier density (section 4.1.2), is represented by 4. It is important to note that the excitonic ground state is not well-defined with respect to the continuum band edges as derived from the one-electron approximation. It is only possible to define an overall ground state of the crystal  $|0\rangle$  and excited-state energy levels relative to the CBM for Coulombically bound electron–hole pairs.<sup>34</sup> Subgap states in the trap-mediated regime can be directly populated by excitation into a semiconductor's Urbach tail (1T) (section 3.1).<sup>273,277</sup> However, these transitions have nominal absorption coefficients ( $\alpha \sim 10\text{--}1000 \text{ cm}^{-1}$ ) relative to above-gap excitations.<sup>33,205,308</sup> A more commonly considered population pathway is through nonradiative localization of band edge carriers (3Ta). Trapped carriers can recombine both radiatively (2T) and/or through phonon-assisted nonradiative processes (3Tb), although the latter is most commonly considered. Population of the band edge occurs through direct nonresonant excitation (1B), ionization of excitons (4), or thermally induced detrapping from shallow subgap states (3Ta). Bimolecular radiative recombination (2B) or three-carrier nonradiative Auger processes (3B) can then commence. Note that radiative recombination of hot carriers above the band edge has also been observed in  $\text{CH}_3\text{NH}_3\text{PbI}_3$ .<sup>284</sup> The excitonic regime is generally more complicated than the case of free carriers, and certainly more so than the simple diagrammatic representation in Figure 29. Coulombically bound pairs can be generated directly through resonant excitation (1X) or indirectly through free carrier emission of optical and acoustic phonons (4). Hot excitons with excess energy, given by  $E(K) = E_g - E_b + \hbar K^2/2(m_e^* + m_h^*)$ , where  $K$  is the center-of-mass momentum, can thus be generated, and their cooling mechanisms resemble those of hot carriers aside from increased involvement of lower-energy acoustic phonons.<sup>36</sup> Radiative recombination of excitons (2X) can proceed via a number of different mechanisms, including through polariton, self-trapped, and defect-bound states, and by phonon

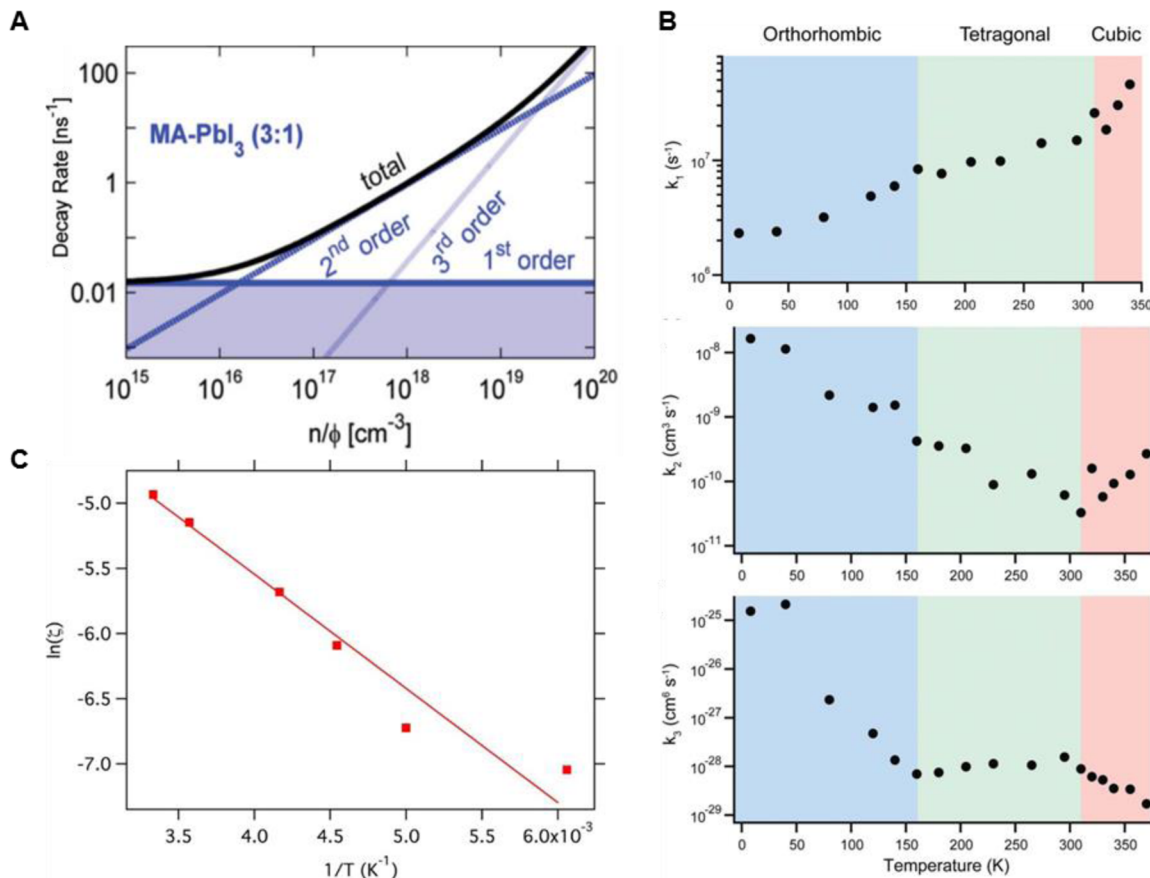


**Figure 30.** (A) Detailed interplay between trap-mediated (1st order), bimolecular (2nd order), and Auger (3rd order) recombination as a function of injected carrier density. Reproduced with permission from ref 301 under CC BY 4.0. (B) Temperature-dependence of the various recombination rate constants in  $\text{CH}_3\text{NH}_3\text{PbI}_3$ . Adapted with permission from ref 230 under CC BY 4.0. (C) Arrhenius analysis of recombination in mesoporous  $\text{CH}_3\text{NH}_3\text{PbI}_3$ , where  $\zeta$  is a coefficient that relates the observed bimolecular recombination rate to that predicted by Langevin theory. Reproduced from ref 307. Copyright 2014 American Chemical Society.

assistance.<sup>34</sup> The downward arrow from the  $n = 1$  state, while not physically meaningful, is meant to be simultaneously representative of one or all of these mechanisms. Nonradiative recombination is also possible in defect-bound excitons and through two-body exciton–exciton Auger processes but will not be discussed here in detail.<sup>34</sup>

Though somewhat oversimplified relative to true photochemical mechanics, Figure 29 does at least provide a framework from which we can build useful kinetic models. Complicating interpretation of recombination dynamics is the fact that the above-mentioned mechanisms are not mutually exclusive and are indeed often coincident. Furthermore, at elevated temperatures and low  $E_b$  and/or defect energy, spectral signatures representative of the various states involved become smeared into a single band. As a first approximation, carrier generation and annihilation can be modeled in parallel using

$$\frac{dn}{dt} = G - k_1 n - k_2 n^2 - k_3 n^3 \quad (24)$$

where  $n$  is the total carrier concentration as a function of time,  $G$  is the generation term and is related to the intensity of excitation by  $G = \alpha I_{\text{ex}}$  and  $k_1$  ( $\text{s}^{-1}$ ),  $k_2$  ( $\text{cm}^3 \text{s}^{-1}$ ), and  $k_3$  ( $\text{cm}^6 \text{s}^{-1}$ ) are the monomolecular, bimolecular, and three-body Auger recombination rate constants, respectively. The monomolecular term is associated with trap-mediated or geminate/excitonic recombination, the bimolecular term with nongeminate or exciton–exciton annihilation, and the third-order term with

nonradiative three-carrier interactions in direct gap materials.  $G$  can be eliminated through use of ultrashort femtosecond laser pulses where concurrent recombination and generation is negligible or by tracking the ensuing kinetics post-excitation. The universal kinetic model in eq 24 has been used extensively in the study of MHPs.<sup>43,53,59,225,237,291,298,301</sup>

To improve the fidelity of eq 24, kinetic data is typically acquired over a broad range of excitation intensities (i.e., initial photogenerated carrier densities) and a global fitting analysis is then performed across the entire data set. Low densities are required to isolate monomolecular processes. As such,  $k_1$  is typically determined through TRPL and used as a fixed parameter in determination of higher-order terms. See Table 3 for PL lifetimes of various MHPs. Rate constants derived from such analysis vary somewhat for  $\text{CH}_3\text{NH}_3\text{PbI}_3$  depending on sample quality and measurement conditions, but are approximately  $k_1 \approx 1.5 \times 10^7 \text{ s}^{-1}$ ,  $k_2 \approx 1-9 \times 10^{-10} \text{ cm}^3 \text{s}^{-1}$ , and  $k_3 \approx 1.5 \times 10^{-28} \text{ cm}^6 \text{s}^{-1}$ .<sup>245</sup>  $\text{HC}(\text{NH}_2)_2\text{PbI}_3$  exhibits comparable values, with  $k_2$  and  $k_3$  increasing an order of magnitude in the Br-based analogue, signifying the marked influence of the halide on intrinsic recombination rates.<sup>213</sup> Bimolecular and Auger recombination rate constants in  $\text{CH}_3\text{NH}_3\text{PbBr}_3$  are also larger than in the triiodide isomorph,<sup>298</sup> suggesting that these mechanisms generally play a more prominent role in Br-based materials. Because the radiative recombination rate is proportional to  $E_g |P_{cv}|^2$ , where  $|P_{cv}|^2$  is the transition matrix element and is related to the absorption coefficient,<sup>298,309</sup> larger

band gap Br compounds should in fact exhibit larger values for  $k_2$ . However, based simply on fundamental optical properties, hybrid MHPs show larger Auger constants than expected.<sup>245,298</sup> The value of  $k_3$  is typically inversely related to  $E_g$  in bulk semiconductors.<sup>310,311</sup> Comparing  $\text{CH}_3\text{NH}_3\text{PbI}_3$  and GaAs ( $k_3 \sim 10^{-30} \text{ cm}^6 \text{ s}^{-1}$ ), which have comparable band gaps and near edge absorption coefficients (section 3), Auger rates are enhanced nearly 2 orders of magnitude in the MHP.<sup>298</sup> Commensurate behavior is also observed in examining  $k_3$  between I and Br compounds.<sup>213,298</sup> Yang et al. point out that this anomalous behavior could arise from either (i) carrier localization or (ii) enhanced Coulombic interactions between carriers.<sup>298</sup> In accordance with the Heisenberg uncertainty principle,  $\Delta x \Delta k \geq 1/2$ , strong localization in real space imposes delocalization of the wave function in  $k$ -space, relaxing momentum conservation requirements and enhancing  $k_3$ . However, without direct empirical evidence for such localization, the increased  $k_3$  in Br compounds relative to I isomorphs, and  $\text{CH}_3\text{NH}_3\text{PbI}_3$  relative to GaAs, is attributed to enhanced Coulombic interactions, which increase the probability of spatial overlap between carriers.<sup>298,312</sup>

Note that bimolecular and Auger rate constants are largely intrinsic properties of a given material that cannot be readily “engineered” or manipulated. In contrast, monomolecular processes associated with trap-assisted energy loss are extrinsic, which makes their minimization a key target in materials processing. For example, the ready oxidation of Sn(II) to Sn(IV) (section 2.1) creates a large concentration of self-doped holes that significantly increases the monomolecular rate constant in  $\text{CH}_3\text{NH}_3\text{SnI}_3$  ( $k_1 = 8.08 \times 10^9 \text{ s}^{-1}$ ).<sup>306</sup> Distinction between intrinsic and extrinsic recombination is necessary for analyzing the theoretical limits of MHP optoelectronics, where recombination and carrier transport are inextricably linked.<sup>245,301,306,313</sup> See section 5.1 for further details.

Manifestation of higher-order recombination mechanisms is a strong function injected carrier density. Thorough understanding of the contribution from each process in different excitation regimes aids both fundamental and application-focused studies. It informs simplifying assumptions in kinetic modeling and determines the primary loss mechanisms under device operation. However, tempting as it may be, kinetic analysis alone is insufficient to distinguish between excitonic and free carrier effects. For example, CdSe nanowires, with 1D excitons stabilized by dielectric confinement, exhibit comparable  $k_2$  values ( $\sim 2 \times 10^{-10} \text{ cm}^3 \text{ s}^{-1}$ ) relative to hybrid 3D MHPs resulting not from bimolecular band edge recombination but rather exciton–exciton Auger annihilation.<sup>314</sup> We stress that assignment of the excited state population at a given temperature and carrier density comes only through self-consistent examination of the binding energy, linear and nonlinear optical properties, transport mechanisms, and photogeneration/recombination kinetics. Figure 30A shows the contribution of monomolecular, bimolecular, and Auger components as a function of excitation density over 5 orders of magnitude in  $\text{CH}_3\text{NH}_3\text{PbI}_3$ .<sup>301</sup> Three regimes are apparent. Monomolecular processes dominate for  $n \leq \sim 10^{16} \text{ cm}^{-3}$ , prominent bimolecular effects can be expected in the range of  $\sim 10^{17} \leq n \leq \sim 10^{19} \text{ cm}^{-3}$ , and Auger processes begin to play a significant role at  $n > \sim 10^{19} \text{ cm}^{-3}$ . The influence of higher-order recombination events grows monotonically with increasing carrier density in bulk  $\text{CH}_3\text{NH}_3\text{PbI}_3$ . This is rather intuitive considering second- and third-order processes are proportional to  $n^2$  and  $n^3$ , respectively. Such behavior

corroborates initial reports of predominant bimolecular recombination at moderate excitation densities.<sup>53,225,237</sup> It also has important consequences for PLQY. Excluding monomolecular exciton recombination as a significant source of PL in  $\text{CH}_3\text{NH}_3\text{PbI}_3$ , PL intensity is proportional to  $k_2 np$  and thus a greater contribution from band edge bimolecular recombination enhances the QY. This is covered in further detail below.

Characteristics charge densities in  $\text{CH}_3\text{NH}_3\text{PbI}_3$  PV and lasing applications are  $\leq \sim 10^{15} \text{ cm}^{-3}$  and  $n \geq \sim 10^{18} \text{ cm}^{-3}$ , respectively, suggesting disparate performance-limiting mechanics in each case. As a first approximation for PV-relevant carrier densities, interference effects can be ignored and reflection from the back metal contact can be assumed to provide two-pass excitation. Thus, the carrier density ( $N$ ) under typical  $\text{CH}_3\text{NH}_3\text{PbI}_3$  PV operation can be estimated by<sup>259</sup>

$$N = \frac{[\sum_{\lambda} E_{\lambda} \lambda (1 - 10^{-2OD_{\lambda}})] \langle \tau \rangle}{hcD} \quad (25)$$

where  $E_{\lambda}$  and  $OD_{\lambda}$  are the solar irradiance and active layer optical density, respectively, at wavelength  $\lambda$ ,  $\langle \tau \rangle$  is the average PL lifetime,  $D$  is the active layer thickness, and  $c$  is the speed of light. At  $J_{sc} \langle \tau \rangle$  is taken as the lifetime upon contact with a selective carrier extraction medium like PCBM ( $\sim 5 \text{ ns}$ ), and at  $V_{oc}$ ,  $\langle \tau \rangle$  is approximated as the intrinsic lifetime at one sun intensity, yielding  $\sim 10^{13} \text{ cm}^{-3}$  ( $J_{sc} \leq N \leq \sim 10^{15} \text{ cm}^{-3}$  ( $V_{oc}$ )).

Examination of  $\text{CH}_3\text{NH}_3\text{PbI}_3$  recombination kinetics using TRTS and TRPL has been carried out by Milot et al. across a broad range of temperatures and carrier densities.<sup>230</sup> Temperature-dependence of the rate constants can provide insight into trapping and transport characteristics. Figure 30B illustrates changes in  $k_1$ ,  $k_2$ , and  $k_3$  in the low-temperature orthorhombic and higher-temperature tetragonal and cubic phases of  $\text{CH}_3\text{NH}_3\text{PbI}_3$ . The rising  $k_1$  as a function of temperature suggests that ionized impurities act as monomolecular recombination channels. A greater fraction of these centers are ionized with increasing thermal energy, enhancing their activity in the recombination process. Arrhenius analysis based on the  $k_1$  behavior yielded effective defect energies of 20 and 200 meV below the band edge in the tetragonal and cubic phases, respectively. The origin of such a dramatic difference in activation energy is ostensibly caused by modification of the electronic structure upon transition to the cubic phase.<sup>230</sup> The lower bimolecular constant with increasing temperature reflects a decrease in mobility, in accord with the general principles of Langevin theory (vide infra).<sup>230,315</sup> The slight uptick in  $k_2$  upon transition to the cubic phase may stem from an increase of the B–X–B bond angle in the high-temperature phase (section 2). This type of structural modification has been linked to increased mobility in MHPs (section 5.1),<sup>99,316,317</sup> and, as expected from Langevin theory,  $k_2$  should increase. However, the mobility measured by TRTS does not show appreciable increase in the cubic phase.<sup>230</sup> Auger recombination is highly phase specific in  $\text{CH}_3\text{NH}_3\text{PbI}_3$ .<sup>230</sup> Energy and momentum conservation requirements render many-body interactions sensitive to electronic structure, and involvement of phonons means  $k_3$  is also heavily dependent on temperature. Further computational studies are required to better understand the influence of these parameters on Auger recombination in MHPs, especially considering the many open questions regarding carrier-phonon interactions in these materials.

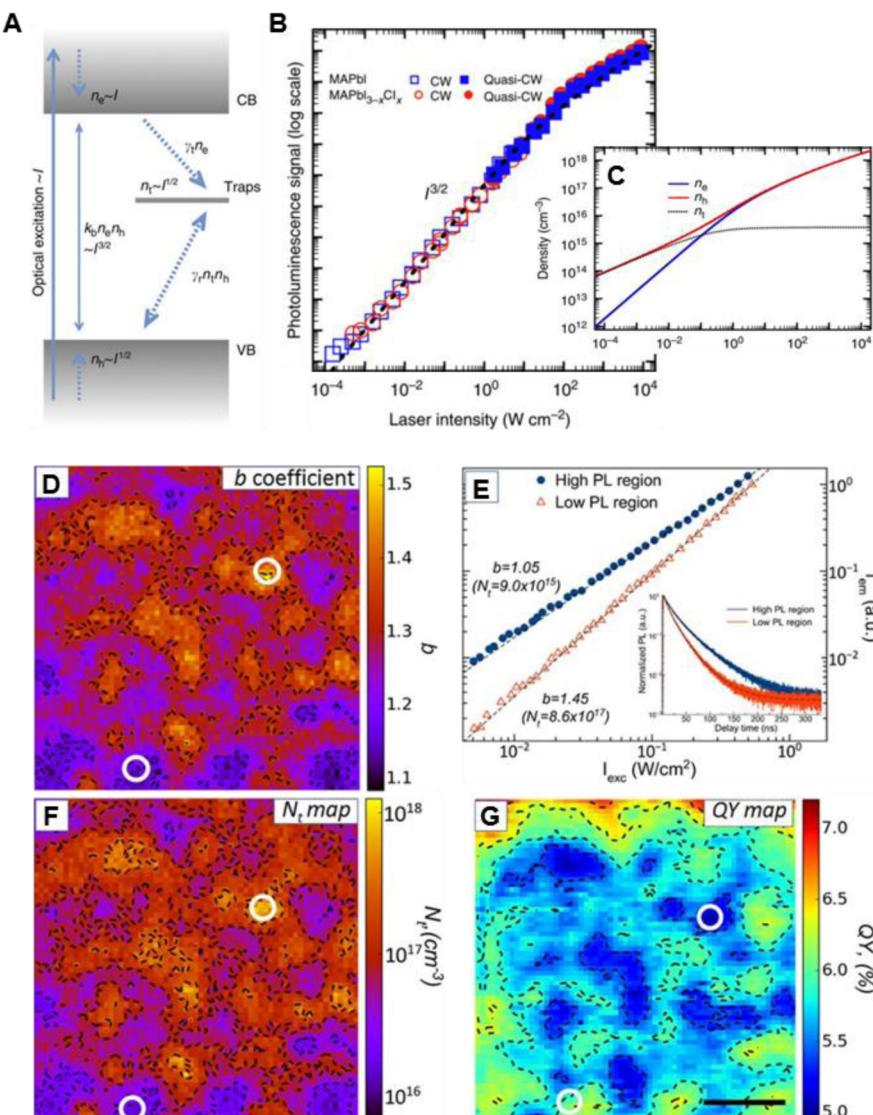


**Figure 31.** (A) Three-state model outlining the dependence of emission intensity on excitation intensity during steady-state and quasi-steady state PL measurements. (B) PL intensity as a function of laser intensity over 8 orders of magnitude in  $\text{CH}_3\text{NH}_3\text{PbI}_3$  and  $\text{CH}_3\text{NH}_3\text{PbI}_{3-x}\text{Cl}_x$ . (C) Modeled VB hole, CB electron, and trapped carrier densities (presumably electrons) as a function of excitation intensity. At high intensities, trap saturation occurs. (A–C) reprinted by permission from Macmillan Publishers Ltd.: Nature Communications (ref 225), copyright 2014. (D) Spatially resolved map of  $b$ -coefficients in a  $\text{CH}_3\text{NH}_3\text{PbI}_3$  thin film, where  $I_{\text{em}} \propto I_{\text{exc}}^b$ . (E) Data extracted at the locations indicated by the white circles in (D). Inset shows the TRPL traces at the denoted locations, with high- $b$  regions exhibiting a shorter decay time. Spatially resolved trap densities ( $N_t$ ) and absolute external QY calculated using eq 28 are shown in (F and G), respectively. The scale bar in (G) is 10  $\mu\text{m}$ . (D–G) reproduced from ref 226. Copyright 2016 American Chemical Society.

A testament to the exceptional optoelectronic properties of solution-processed hybrid MHP films is their low intrinsic bimolecular recombination rate and significant deviation from simple Langevin kinetics.<sup>225,237,258,295,307</sup> The bimolecular Langevin rate constant ( $k_{2L}$ ) is a function of carrier mobility (in the cases discussed here, individual electron and hole mobilities cannot be distinguished, thus  $\mu = \mu_e + \mu_h$ ) and the dielectric properties of the host material, as given by  $k_{2L} = \mu e_0(\epsilon_0\epsilon_{\text{eff}})^{-1}$ .<sup>295,315</sup> Mobility dictates the likelihood that an electron and hole move within their mutual Coulomb capture radius, while the dielectric constant determines the effective capture cross section. Increasing mobility thus raises  $k_{2L}$ , while a larger  $\epsilon_{\text{eff}}$  screens the electron–hole interaction and decreases  $k_{2L}$ . By comparing the empirically determined ratio  $k_2/\mu$  with that predicted by  $e_0(\epsilon_0\epsilon_{\text{eff}})^{-1}$ , Wehrenfennig et al. were the first to discover that the bimolecular recombination rate in

$\text{CH}_3\text{NH}_3\text{PbI}_3$  is approximately 4 orders of magnitude below that predicted by Langevin theory.<sup>301</sup> Such deviation has in the past been ascribed to spatial localization of carriers in disordered materials and polymer blends.<sup>318,319</sup> In particular, random electrostatic fluctuations in a-Si lead to similar divergence from Langevin kinetics.<sup>318</sup> Such a situation is in line with energetic fluctuations and spatial segregation of electrons and holes recently predicted to result from randomly oriented  $\text{CH}_3\text{NH}_3^+$  dipoles in tetragonal and cubic phase hybrid MHPs.<sup>320</sup> As an illustrative exercise, we can consider a simple sinusoidal representation of electrostatic fluctuation around the band edge to arrive at a rough approximation for the effective bimolecular rate constant ( $k_{2,\text{eff}}$ ), given by<sup>318</sup>

$$k_{2,\text{eff}} = k_{2L} \left( \frac{2\pi\Delta_{\text{es}}}{kT} \right) \exp\left(-\frac{2\Delta_{\text{es}}}{kT}\right) \quad (26)$$

where  $\Delta_{\text{es}}$  is the amplitude of the oscillating potential. From this relation, we expect  $k_2$  to be sensitive to the thermal environment, decreasing at lower temperatures. While this is contrary to the above-mentioned temperature dependence of  $k_2$ ,<sup>230</sup> Savenije et al. observed just such behavior in mesoporous  $\text{CH}_3\text{NH}_3\text{PbI}_3$ , reporting a decrease in  $k_{2,\text{eff}}/k_{2L}$  from  $\sim 10^{-2}$  at 300 K to  $\sim 10^{-3}$  at 165 K.<sup>307</sup> This implies  $\Delta_{\text{es}} \sim 100$  meV in the simplified model, on par with bimolecular activation energies empirically derived from the Arrhenius analysis in Figure 30C ( $\sim 75$  meV).<sup>307</sup> Interestingly, both Milot et al. and Savenije et al. reported a drop in  $\mu$  with increasing temperature.<sup>230,307</sup> The stark contrast between these two results, in one case  $\text{CH}_3\text{NH}_3\text{PbI}_3$  follows the general principles of Langevin kinetics, albeit with sharp deviation in  $k_2$  values, while in the other,  $\mu$  and  $k_2$  are inversely related, indicating total breakdown of Langevin theory, is likely to be a significant point of interest moving forward. Whether spatial localization,<sup>320</sup> polaron formation,<sup>236,250</sup> or simply the electronic structure of hybrid MHPs gives rise to non-Langevinian bimolecular recombination remains an open question. With respect to the latter, recent calculations predict slight indirect gap character due to the combination of SOC and noncentrosymmetric space groups in  $\text{CH}_3\text{NH}_3\text{PbX}_3$  and  $\text{HC}(\text{NH}_2)_2\text{SnI}_3$ , giving rise to Rashba/Dresselhaus effects.<sup>119,121–126</sup> Also, sample morphology may play a role, considering the larger degree of disorder and strain inherent to thin films, particularly those with mesostructured morphologies.<sup>256,271,321</sup>

In reality, more comprehensive models beyond the universal rate law (eq 24) can be developed that enable extraction of relevant parameters such as defect density and exciton-free carrier branching ratio. Indeed, a number of more sophisticated approaches to the problem of MHP photodynamics have been utilized.<sup>225,226,228,258,259</sup> One such model proposed by Saba et al. is given in Figure 31A.<sup>225</sup> Its principal assumption is that trapping of one species (presumably electrons) directly competes with radiative bimolecular recombination of free carriers. The various processes at steady state can be quantitatively described by the following set of coupled expressions.<sup>225</sup>

$$\begin{aligned}\frac{dn}{dt} &= 0 = \alpha I_{\text{exc}} - k_t n(N_t - n_t) - k_2 np - k_3 np^2 \\ \frac{dp}{dt} &= 0 = \alpha I_{\text{exc}} - k_h n_t p - k_2 np - k_3 np^2 \\ \frac{dn_t}{dt} &= 0 = k_t n(N_t - n_t) - k_h n_t p\end{aligned}\quad (27)$$

Here,  $n$ ,  $p$ , and  $n_t$  are the CB electron, VB hole, and trapped electron concentrations, respectively,  $N_t$  is the total trap density,  $k_t$  is the electron trapping rate constant, and  $k_h$  is the trapped electron-VB hole recombination rate constant. Note that Auger processes here are assumed to occur between one electron and two holes. The qualitative framework laid out in Figure 29 becomes particularly useful here for understanding the origin of the various terms. To assess the fidelity of the rate equations above, steady-state emission intensity ( $I_{\text{em}}$ ) was correlated with excitation intensity ( $I_{\text{exc}}$ ) over 8 orders of magnitude.<sup>225</sup> This is a well-established approach for characterizing complex, multiprocess recombination dynamics in bulk and nanostructured materials.<sup>34,322,323</sup> Experimental  $I_{\text{em}}$  versus  $I_{\text{exc}}$  along with results from the fitting routine are shown in Figure 31B. Individual trapped electron and continuum carrier

concentrations at various  $I_{\text{exc}}$  are displayed in Figure 31C. In the broad range of  $10^{-4} \leq I_{\text{exc}} \leq 10 \text{ W cm}^{-2}$ ,  $I_{\text{em}} \propto I_{\text{exc}}^{3/2}$ , yielding a slope of 3/2 in the double-log plot. Above this regime,  $I_{\text{em}} \propto \sim I_{\text{exc}}$  with a corresponding log–log slope of 1. This behavior can be rationalized by examining limiting regimes, keeping in mind that  $I_{\text{em}} \propto np$ . At low carrier densities, recombination through trap states dominates, thus the bimolecular and Auger terms in eq 27 can be eliminated, yielding  $n = \alpha I_{\text{exc}}/k_t N_t$ ,  $p = (\alpha I_{\text{exc}}/k_h)^{1/2}$ , and  $I_{\text{em}} \propto np \propto I_{\text{exc}}^{3/2}$  (assuming  $n_t \sim p$  under these conditions).<sup>226</sup> Note that the inclusion of both electron and hole traps would yield a slope of 2,<sup>322</sup> verifying the assumption of substantial trapping of only one type of carrier. At higher intensities, the rate of bimolecular recombination surpasses that of carrier trapping, as indicated by the saturation of  $n_t$  above  $\sim 1 \text{ W cm}^{-2}$  in Figure 31C. Because trapping processes are no longer dominant in this regime,  $n = (\alpha I_{\text{exc}}/k_2)^{1/2}$ ,  $p = (\alpha I_{\text{exc}}/k_2)^{1/2}$ , and  $I_{\text{em}} \propto np \propto I_{\text{exc}}$  (when  $n = p$ ) prior to the onset of Auger recombination. Upon activation of Auger processes at even higher densities,  $I_{\text{em}}$  grows sublinearly.<sup>225</sup>

It has become increasingly apparent that substantial heterogeneities exist in device-quality, solution-processed MHP thin films, resulting in spatial variation of the PL response.<sup>259,324</sup> Recently, Draguta et al. performed spatially resolved  $I_{\text{em}}$  versus  $I_{\text{exc}}$  analysis on  $\text{CH}_3\text{NH}_3\text{PbI}_3$  thin films.<sup>226</sup> The resulting contour map of  $b$  coefficients over a  $\sim 30 \times 30 \mu\text{m}$  area and excitation range from  $10^{-2}$  to  $1 \text{ W cm}^{-2}$ , where  $b$  describes the power law  $I_{\text{em}} \propto I_{\text{exc}}^b$ , is shown in Figure 31D. Each pixel represents an area of  $\sim 0.36 \mu\text{m}^2$ . This map reveals a significant variation in  $b$ , ranging from  $\sim 1$  to  $\sim 1.5$  (Figure 31E). Such behavior highlights the nonuniformity of trap states in these films. Note that heterogeneities are larger than the characteristic grains, suggesting grain boundaries are not the sole nonradiative recombination channels. Correlation between  $b$  and the total trap density ( $N_t$ ) permits generation of a similar contour map outlining the trap densities over the same region of interest (Figure 31F).  $N_t$  was found to fluctuate over 2 orders of magnitude ( $10^{16} – 10^{18} \text{ cm}^{-3}$ ). Furthermore, a spatially resolved absolute external quantum yield ( $\eta_{\text{ext}}^{\text{opt}}$ ) was also determined using an all-optical model given by<sup>226,325</sup>

$$\frac{I_{\text{em}}}{I_{\text{exc}}} = \beta \left[ 1 - (1 - \eta_{\text{ext}}^{\text{opt}}) \frac{1 + \overline{I}_{\text{exc}}}{2(\overline{I}_{\text{exc}})^{1/2}} \right] \quad (28)$$

where  $\overline{I}_{\text{exc}} = I_{\text{exc}}/I_{\text{exc}}^{\text{max}}$  is the normalized excitation intensity, with the denominator indicating the excitation intensity at maximum QY, and  $\beta$  is a constant of proportionality. The contour map in Figure 31G emphasizes the link between trap density and external QY, with lower QY directly correlated with trap-rich regions. Note that the low  $\eta_{\text{ext}}^{\text{opt}} \approx 5–7\%$  near one sun excitation intensity again reflects extensive trapping at these carrier densities. On the other hand,  $\eta_{\text{ext}}^{\text{opt}} \approx 70\%$  at  $I_{\text{exc}} = 30 \text{ W cm}^{-2}$  in these samples is in good agreement with previously reported maximum QYs<sup>53</sup> without the need for artificial scaling as used previously,<sup>225</sup> confirming the validity of eq 28. Considering the reciprocity between  $V_{\text{oc}}$  and external PLQY (section 3.1),<sup>209,210</sup> spatially resolved characterization of external QY, and in particular the influence of passivating layers, can facilitate fabrication of MHP device stacks with lower fundamental losses and improved power conversion efficiency.

Table 3. Measured Ranges for  $L_D$  and  $\mu$  for Various Metal Halide Perovskites

compound	sample type	$\mu$ ( $\text{cm}^2 \text{V}^{-1} \text{s}^{-1}$ )	$L_D$ ( $\mu\text{m}$ )	$\tau$ (ns)	technique(s)	ref
$\text{CH}_3\text{NH}_3\text{PbI}_3$	thin film (solution)	1.4 <sup>b</sup>	0.13 <sup>b</sup>	4.5	PLQ	139
		0.9 <sup>c</sup>	0.09 <sup>c</sup>			
		0.66 <sup>b</sup>	0.13 <sup>b</sup>	9.6	PLQ	140
		0.43 <sup>c</sup>	0.11 <sup>c</sup>			
		8.2 <sup>b,c</sup>	1.2	67	TRTS	301
		12.5 <sup>b</sup>	—	—	TRTS	294
		7.5 <sup>c</sup>				
		2 <sup>b</sup>	2.3 <sup>b</sup>	1000 <sup>a</sup>	TRMC	294
		1 <sup>c</sup>	1.6 <sup>c</sup>			
		11 <sup>b,c</sup>	~ 1 <sup>b,c</sup>	~ 40	TRTS	291
PV device		3.1 <sup>b,c</sup>	1.27 <sup>b,c</sup>	50	TAM	296
		33 <sup>b,c</sup>	2.5 <sup>b,c</sup>	~ 70	TRTS	230
		—	~ 1 <sup>b,c</sup>	—	EBIC	142
		—	~ 1 <sup>b,c</sup>	—	IS	329
pellet	single crystal	66 <sup>b</sup>	—	—	resistivity, Hall	76
		2.5 <sup>b,c</sup>	2–8 <sup>b,c</sup>	1032	PL, SCLC	60
		67 <sup>b,c</sup>	9.7	570	SCLC, TA	330
		25 <sup>b</sup>	175	90,000	SCLC, TOF, Hall, TPV, IS	331
$\text{CH}_3\text{NH}_3\text{Pb}(\text{I}_{1-x}\text{Cl}_x)_3$	thin film (solution)	160 <sup>c</sup>				
		1.6 <sup>b</sup>	1.07 <sup>b</sup>	273	PLQ	140
		2.1 <sup>c</sup>	1.21 <sup>c</sup>			
		11.6 <sup>b,c</sup>	2.4 <sup>b,c</sup>	200	TRTS	301
		33 <sup>b,c</sup>	2.66 <sup>b,c</sup>	83	TRTS	301
		—	1.2 <sup>b</sup>	—	EBIC	142
		—	1.9 <sup>c</sup>			
		—	~ 1.4 <sup>b,c</sup>	—	EBIC	332
		—	—	—	IS	329
	PV device	—	0.15–0.45 <sup>b</sup>	—	EBIC	332
$\text{CH}_3\text{NH}_3\text{PbBr}_3$	thin film (vapor assisted)	8.9 <sup>b</sup>	1.06 <sup>b</sup>	51	PLQ	333
		9.4 <sup>c</sup>	1.08 <sup>c</sup>			
		20–115 <sup>b,c</sup>	3–17 <sup>b,c</sup>	357–978	PL, TOF, Hall, SCLC, TA	60
		24	4.2	300	SCLC, TA	330
$\text{CH}_3\text{NH}_3\text{PbCl}_3$	single crystal	42 <sup>b,c</sup>	3–8.5 <sup>b,c</sup>	83–662	SCLC, TA	49
	thin film	0.16 <sup>b</sup>	0.18 <sup>b</sup>	~ 75	PLQ	206
$\text{CH}(\text{NH}_2)_2\text{PbBr}_3$	thin film	3.5 <sup>c</sup>	0.82 <sup>c</sup>			
		27 <sup>b,c</sup>	3.1	~ 140	TRTS	213
		14 <sup>b,c</sup>	1.3	~ 50	TRTS	213
		200 <sup>c</sup>	—	—	Hall	137
$\text{CH}_3\text{NH}_3\text{SnI}_3$	single crystal	1.6 <sup>b,c</sup>	0.03 <sup>b,c</sup>	~ 0.2	TRTS	306
		~ 60 <sup>c</sup>	—	—	Hall	138
		2320 <sup>b</sup>	—	—	resistivity, Hall	76
		322 <sup>c</sup>	—	—	resistivity, Hall	76
$\text{CsSnI}_3$	thin film	585 <sup>c</sup>	—	—	Hall	334, 229
	pellet	536 <sup>b</sup>	—	—	resistivity, Hall	76
$\text{CH}(\text{NH}_2)_2\text{SnI}_3$	pellet	103 <sup>b</sup>	—	—	resistivity, Hall	76

<sup>a</sup> $L_D$  value calculated using the reported diffusivity and relevant time scale of the experimental setup through the relation  $L_D = (D\tau)^{1/2}$ . <sup>b</sup>Electron. <sup>c</sup>Hole.

## 5. ELECTRONIC AND IONIC TRANSPORT

### 5.1. Carrier Transport

Determining how charges move in these materials and how changes in material processing and component substitutions influence this process is of critical importance for improving their charge transport properties. Diffusion of charges occurs in any semiconductor, even when no electric field is present, due to thermal energy,  $k_B T$ . The diffusion length of a charge is simply the average distance that charge is able to travel because of diffusion before recombination occurs.<sup>326</sup> Diffusion length,

$L_D$ , can be calculated from the diffusion coefficient,  $D$ , and charge carrier lifetime,  $\tau$ , using

$$L_D = \sqrt{D\tau} \quad (29)$$

$L_D$  is a critical parameter for solar cell operation because it directly influences the efficiency of charge collection in a solar cell film.

Field-free diffusion can be directly related to the mobility (carrier transport under the influence of an electric field) by the Einstein relation

$$\mu = Dq/k_B T \quad (30)$$

where  $\mu$  is the mobility,  $q$  the electronic charge,  $k_B$  is Boltzmann's constant, and  $T$  is temperature. This equivalence between carrier transport with and without an electric field is due to the fact that in each case transport is limited by carrier scattering and carrier effective mass.<sup>35</sup> Because of this,  $L_D$  can be calculated via eq 29 by determining the charge lifetime,  $\tau_s$ , and either  $D$  or  $\mu$ .

The Drude model is a useful simplification of charge transport in metals or semiconductors. This model treats electrons semiclassically as particles moving through the lattice and scattering off sources such as phonons, defects, and impurities. From this model, the mobility of a charge (either electron or hole) can be determined from the scattering time,  $\tau_s$  (or mean free path,  $\lambda_s$ ) and effective mass of the charge carrier,  $m^*$ .<sup>35</sup>

$$\mu = \frac{q\tau_s}{m^*} = \frac{q\lambda_s}{\sqrt{3kTm^*}} \quad (31)$$

A key consequence of this picture of charge transport is that high carrier mobility is a result of low scattering and low effective masses. Deviations from the simple Drude model can arise from high charge densities where electron–hole scattering is non-negligible, where strong electron–phonon interactions (small polarons) are present, or charge hopping occurs, among others.<sup>289</sup> The consequences of this with respect to MHPs will be discussed in detail subsequently but can be clearly seen in the decrease in mobility that doping induces (i.e., more scattering centers).<sup>327</sup>

While a detailed discussion of all experimental methods and their theory is beyond the scope of this manuscript, the fact that methods for extracting diffusion/mobility are indirect necessitates the use of specific assumptions with varying validity based on the system interrogated. Thus, it is critical that the assumptions underlying these diverse methods be covered in part in the subsequent discussion to facilitate broader comparison between different measurement techniques which can yield different results even on identical samples.<sup>328</sup> With this in mind, we will also briefly highlight some of the most relevant assumptions for measurement techniques which have, to date, been employed in the characterization of MHPs. A concise summary of the charge carrier mobility and  $L_D$  measurements conducted on MHP samples is provided in Table 3.

For the case of excited charge carriers acting only under the influence of isotropic diffusion, the time distribution of charge carriers in a semiconductor can be described by the following time-dependent partial differential equation.

$$\frac{\partial n}{\partial t} = D\nabla^2 n - k_1 n - k_2 n^2 - k_3 n^3 \quad (32)$$

Here,  $n$  is the carrier population as a function of position and time,  $D$  is the diffusion coefficient,  $\nabla$  is the Laplace operator, and  $k_1$ ,  $k_2$ , and  $k_3$  reflect the various recombination processes discussed at length in section 4.3. In general, the carrier population depends on all three spatial coordinates as well as on time, yet experiments are typically designed such that diffusion is only considered in one or two of the spatial coordinates. The commonality between eqs 32 and 24 highlights the interplay between recombination and diffusion of photogenerated charges.

Utilizing this model, Xing et al. and Stranks et al. first demonstrated the ambipolar nature of  $\text{CH}_3\text{NH}_3\text{PbI}_3$  by

measuring a diffusion length of  $\sim 100$  nm for both electrons and holes from photoluminescence (PL) quenching experiments.<sup>139,140</sup> Stranks et al. also showed that  $\text{CH}_3\text{NH}_3\text{PbCl}_{x}\text{I}_{3-x}$  films prepared using a 3:1 MAI:PbCl<sub>2</sub> mole ratio precursor solution yielded over 1  $\mu\text{m}$  electron and hole diffusion lengths (Figure 32).<sup>140</sup> In this case, the calculated diffusion coefficient/

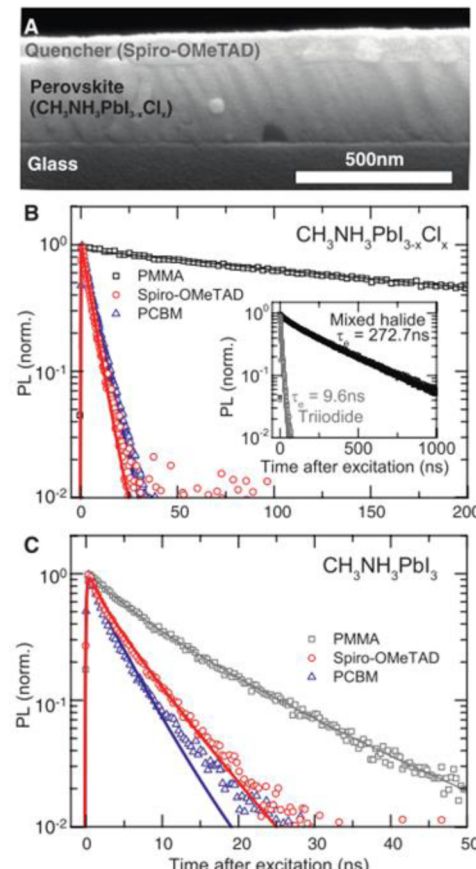


**Figure 32.** (A) Cross-sectional SEM image of perovskite film with spiro-OMeTAD quenching layer. Time-resolved PL measurements of (B)  $\text{CH}_3\text{NH}_3\text{PbCl}_{x}\text{I}_{3-x}$  and (C)  $\text{CH}_3\text{NH}_3\text{PbI}_3$  films with insulating PMMA (black) or either a hole (spiro-OMeTAD, red) or an electron (PCBM, blue) quenching layer. Panels (A–C) from ref 140. Reprinted with permission from AAAS.

diffusion length rests on the boundary condition at the selective contact (e.g.,  $\text{CH}_3\text{NH}_3\text{PbI}_3$ /spiro-OMeTAD or  $\text{CH}_3\text{NH}_3\text{PbI}_3$ /PCBM) where it is assumed that carriers are completely quenched (concentration = 0). Because any barrier to charge transfer across this interface will lead to a systematic underestimation in  $L_D$ ,<sup>313</sup> these relatively high diffusion lengths represent a lower bound for the true diffusion length of the material, and their accuracy is directly linked to the effectiveness of the quencher.

The nearly order of magnitude difference in  $L_D$  between the  $\text{CH}_3\text{NH}_3\text{PbCl}_{x}\text{I}_{3-x}$  and  $\text{CH}_3\text{NH}_3\text{PbI}_3$  films as determined by PL quenching spurred further study. While Cl concentration in fully annealed  $\text{CH}_3\text{NH}_3\text{PbCl}_{x}\text{I}_{3-x}$  films is low,<sup>335</sup> Cl does induce significant morphological changes on the perovskite film which may contribute to the longer diffusion lengths seen when Cl is added.<sup>93</sup> Processing  $\text{CH}_3\text{NH}_3\text{PbI}_3$  films in I-poor conditions using lead acetate as a Cl-free precursor revealed diffusion lengths of  $600 \pm 40$  nm.<sup>336</sup> This implies that the benefit of Cl in  $\text{CH}_3\text{NH}_3\text{PbCl}_{x}\text{I}_{3-x}$  films may be a combination

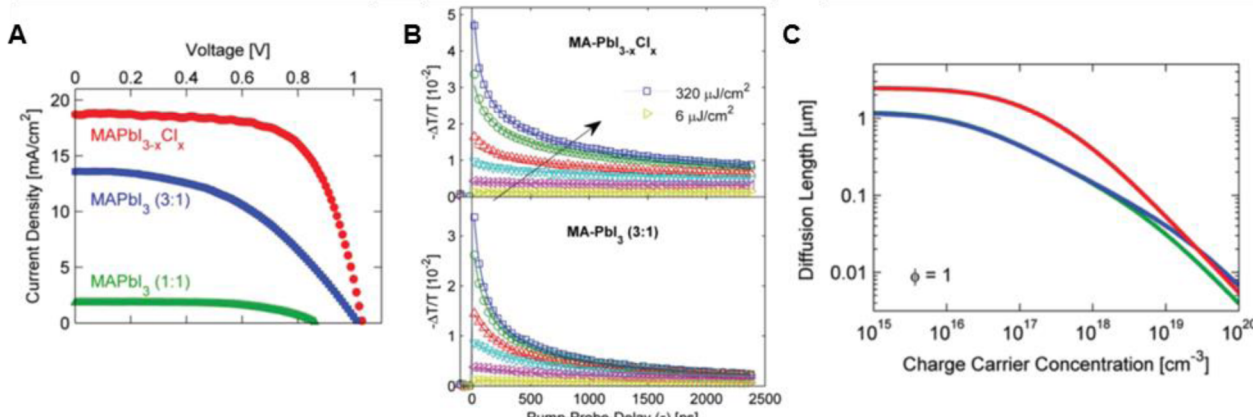


**Figure 33.** (A) Photovoltaic performance of  $\text{Al}_2\text{O}_3$ /perovskite/spiro-OMeTAD solar cells with different perovskite active layers. (B) THz photoinduced absorption transient of  $\text{CH}_3\text{NH}_3\text{PbI}_{3-x}\text{Cl}_x$  and  $\text{CH}_3\text{NH}_3\text{PbI}_3$  (3:1) after excitation at 550 nm for fluences between 6 and 320  $\mu\text{J cm}^{-2}$ . Solid lines are fits based on second- and third-order charge recombination. (C) Charge-carrier diffusion lengths  $L_D = [(\mu k_B T)/(eR_{\text{total}})]^{1/2}$  for  $\text{CH}_3\text{NH}_3\text{PbI}_{3-x}\text{Cl}_x$  (red),  $\text{CH}_3\text{NH}_3\text{PbI}_3$  (3:1) (blue), and  $\text{CH}_3\text{NH}_3\text{PbI}_3$  (1:1) (green) as a function of charge-carrier concentration. (A–C) reproduced with permission from ref 301 under CC BY 4.0.

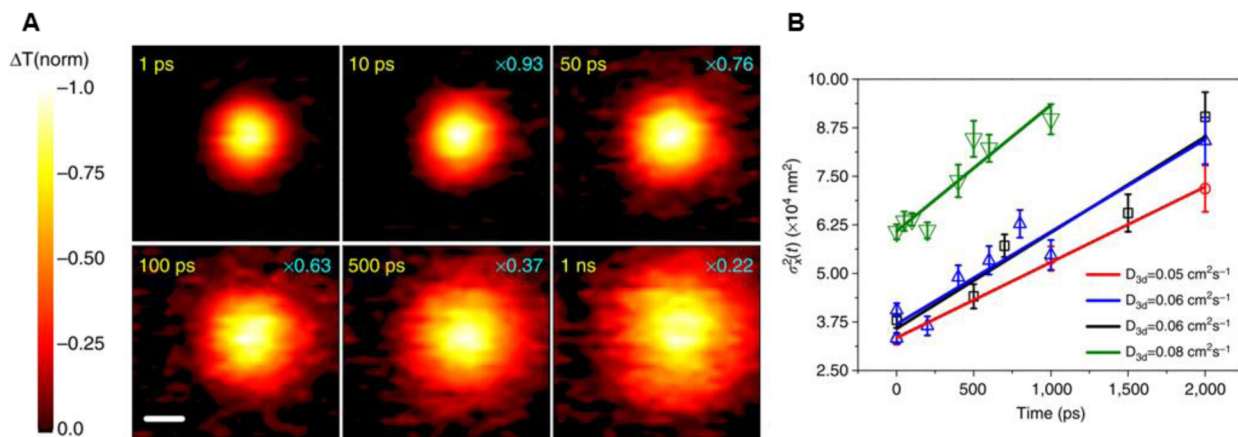


**Figure 34.** (A) 2D transient absorption microscopy imaging of the carrier density profile in  $\text{CH}_3\text{NH}_3\text{PbI}_3$  at different pump–probe delay times. The initial carrier density was  $4 \times 10^{18} \text{ cm}^{-3}$  at zero delay time. For delay time  $> 1 \text{ ps}$ , the signal maximum in each image was normalized to the signal maximum at 1 ps. The scale bar in the figure is 300 nm. (B) Diffusion coefficients obtained through fitting the variances of Gaussian profiles at four different sample spots. (A and B) reproduced with permission from ref 296 under CC BY 4.0.

of superior morphology and I-poor growth conditions. On the other hand, Cl content may correlate with increased photoluminescence lifetime compared to pure  $\text{CH}_3\text{NH}_3\text{PbI}_3$ , which would lead to longer carrier diffusion lengths and indicate that the effect of Cl may go beyond morphology and I-poor growth conditions.<sup>259,337</sup>

Time-resolved THz spectroscopy (TRTS) has also been employed by Wehrenfennig et al. on both  $\text{CH}_3\text{NH}_3\text{PbI}_3$  and  $\text{CH}_3\text{NH}_3\text{PbCl}_x\text{I}_{3-x}$  films to further elucidate carrier transport and recombination.<sup>301</sup> As discussed previously, TRTS measures changes in conductivity ( $\Delta\sigma$ ) by variations in the transmittance in the THz regime (Equation 23). Because TRTS is sensitive to free charge carriers only, the calculated mobility is the summation of contributions from electrons and holes and does not include any excitonic contributions ( $\phi_{\text{fc}}$  is the fraction of free carriers). This assumption of complete excitonic dissociation appears to hold quite well for the typical materials used in photovoltaics (e.g.,  $\text{CH}_3\text{NH}_3\text{PbI}_3$ ,  $\text{CH}_3\text{NH}_3\text{PbI}_{3-x}\text{Cl}_x$ ,  $\text{CH}_3\text{NH}_3\text{PbBr}_3$ ,  $\text{CH}(\text{NH}_2)_2\text{PbI}_3$  and  $\text{CH}(\text{NH}_2)_2\text{PbBr}_3$ ), as discussed in section 4.1.2, but is not applicable for all MHPs, particularly 2D perovskite materials where excitons are

dominant (section 3.2). Because TRTS experiments do not rely on charge extraction to measure diffusion, they can probe material properties without introducing contact artifacts. On the other hand, the high frequency of THz radiation means TRTS does not probe carrier transport through the entire thickness of device-sized perovskite films and is therefore more sensitive to intrinsic material properties than large scale morphological features.<sup>245</sup>

From the combination of mobility and lifetime measurements obtained by TRTS,  $L_D$  was calculated across 5 orders of magnitude in carrier concentration, as shown in Figure 33.<sup>301</sup>  $L_D$  is clearly strongly dependent on charge carrier concentration at high concentrations, but saturates at lower concentrations where first order recombination predominates. It was found that  $\text{CH}_3\text{NH}_3\text{PbCl}_x\text{I}_{3-x}$  films had a factor of  $\sim 2$  longer  $L_D$  than  $\text{CH}_3\text{NH}_3\text{PbI}_3$ . This difference in  $L_D$  pushes the photovoltaic performance of the  $\text{CH}_3\text{NH}_3\text{PbCl}_x\text{I}_{3-x}$  films significantly higher than pure  $\text{CH}_3\text{NH}_3\text{PbI}_3$  samples, although some of the improvement can be attributed to morphological effects as  $\text{CH}_3\text{NH}_3\text{PbI}_3$  made from a 1:1 and 3:1 MAI:PbI<sub>2</sub> solutions showed nearly identical  $L_D$ , but the 3:1 sample showed

significantly better film coverage and thus had higher PCE (0.9% vs 8.5%) (Figure 33A).

Ensemble measurements for determination of  $L_D$  are not able to capture important aspects of local morphology. By combining high spatial resolution microscopy with high time resolution spectroscopy, transient absorption microscopy (TAM) yields information with  $\sim 50$  nm spatial and femtosecond time resolution. Guo et al. utilized TAM to study carrier transport in polycrystalline  $\text{CH}_3\text{NH}_3\text{PbI}_3$ .<sup>296</sup> Following initial spot excitation by the pump beam, the distribution of charge carriers grows while maintaining its Gaussian character. This directly shows diffusion of photogenerated charges in  $\text{CH}_3\text{NH}_3\text{PbI}_3$  (Figure 34A). Over the 2 ns probe delay window, diffusion of 220 nm could be directly visualized. Extrapolation over a 50 ns PL lifetime, and assuming  $D$  does not change appreciably at low carrier densities, yields an estimated diffusion length of  $\sim 1.2 \mu\text{m}$ . Probing diffusion at 4 unique points in the perovskite film revealed nearly a factor of 2 difference in the diffusion coefficient for different areas of the same film (Figure 34B). This highlights the strong effects which local morphology can have on  $L_D$ . Heterogeneity of comparable magnitude has also been observed in electron beam induced current (EBIC) measurements on  $\text{CH}_3\text{NH}_3\text{PbBr}_{3-x}\text{Cl}_x$ .<sup>332</sup>

The long diffusion lengths seen in  $\text{CH}_3\text{NH}_3\text{PbI}_3$  and  $\text{CH}_3\text{NH}_3\text{PbCl}_{3-x}\text{I}_{3-x}$  have been corroborated in working perovskite solar cells as well. Various methods exist to probe charge transport in working devices, but such techniques invariably introduce contact-induced field effects, thus yielding effective diffusion lengths that include a combination of diffusion and drift. Edri et al. measured an effective  $L_D$  of  $1.9 \pm 0.2 \mu\text{m}$  for electrons and  $1.5 \pm 0.1 \mu\text{m}$  for holes in complete  $\text{TiO}_2/\text{CH}_3\text{NH}_3\text{PbI}_{3-x}\text{Cl}_x/\text{spiro-OMeTAD}$  devices by electron beam induced current (EBIC).<sup>142,143</sup> Similarly, the appearance of transmission line (TL) behavior in the impedance spectra of nanostructured  $\text{CH}_3\text{NH}_3\text{PbI}_3$  and planar thin film  $\text{CH}_3\text{NH}_3\text{PbI}_{3-x}\text{Cl}_x$  devices is a feature of transport-recombination.<sup>329</sup> Fitting of the TL feature allowed Gonzalez-Pedro et al. to determine that the effective  $L_D$  of both nanostructure and planar thin film devices is  $> 1 \mu\text{m}$  when the cells are operating at low voltage, with the planar structures showing slightly higher  $L_D$ .<sup>329</sup>

While one of the remarkable aspects of MHPs is their ability to form high-quality semiconductor films from solution, morphological effects hinder transport in these films. In fact, for thin films of the prototypical material  $\text{CH}_3\text{NH}_3\text{PbI}_3$ , a factor of  $\sim 4$  increase in mobility ( $8$  to  $35 \text{ cm}^2 \text{ V}^{-1} \text{ s}^{-1}$ ) has been observed by TRTS which can be attributed to better deposition techniques.<sup>230,301</sup> Similar effects have been seen in  $\text{CH}_3\text{NH}_3\text{PbI}_3$  films derived from  $\text{PbI}_2$  or  $\text{PbAc}$  ( $L_D = 200 \text{ nm}$  vs  $600 \text{ nm}$ , respectively).<sup>336</sup> A better picture of the intrinsic material properties should thus be realizable through studies on single crystals. Pioneering work on  $\text{CH}_3\text{NH}_3\text{PbI}_3$  crystals by Shi et al. and Dong et al. has lent a greater understanding of the limits and promise of  $\text{CH}_3\text{NH}_3\text{PbI}_3$  and of MHPs more generally.<sup>60,331</sup> Space-charge-limited current (SCLC) was used in both cases to probe carrier mobility, which was found to be  $2.5 \text{ cm}^2 \text{ V}^{-1} \text{ s}^{-1}$  for both electrons and holes,<sup>60</sup> and approximately  $160 \text{ cm}^2 \text{ V}^{-1} \text{ s}^{-1}$  and  $25 \text{ cm}^2 \text{ V}^{-1} \text{ s}^{-1}$  for holes and electrons, respectively, in the sample prepared by Dong et al., although in both cases confirmation using other techniques gave somewhat varied values.<sup>331</sup> The large difference in the mobility of these single crystals may be due to differences in

crystal quality, but could also arise due to contact effects which complicate the SCLC measurements.

From their measurements of charge carrier mobility and the charge carrier lifetime of 1032 ns by TRPL, Shi et al. estimated  $L_D$  to be  $2\text{--}8 \mu\text{m}$ .<sup>60</sup> Similarly, Dong et al. estimated  $L_D$  to be  $175 \pm 25 \mu\text{m}$  under 1 sun illumination based on a charge carrier lifetime of  $80\text{--}100 \mu\text{s}$  as measured by transient photovoltaic and impedance spectroscopy (IS).<sup>331</sup> The very large discrepancy in  $L_D$  in these two reports primarily arises due to the 2 orders of magnitude difference in the reported carrier lifetimes. While the lifetime measured by TRPL is characteristic of regions of the semiconductor with both electrons and holes present, it is not reflective of the true lifetime in the bulk material because it does not account for surface recombination effects.<sup>58</sup> On the other hand, transient photovoltaic measurements and IS may be more characteristic of a single charge carrier lifetime, as either the electron or hole can be extracted at the contacts.<sup>338</sup>

In an effort to determine the limits of  $L_D$  in  $\text{CH}_3\text{NH}_3\text{PbI}_3$ , Johnston and Herz modeled  $L_D$  with charge-carrier density based on a mobility of  $30 \text{ cm}^2 \text{ V}^{-1} \text{ s}^{-1}$  and measurements of the bimolecular and Auger recombination rate constant (Figure 35), which are for the most part intrinsic material properties

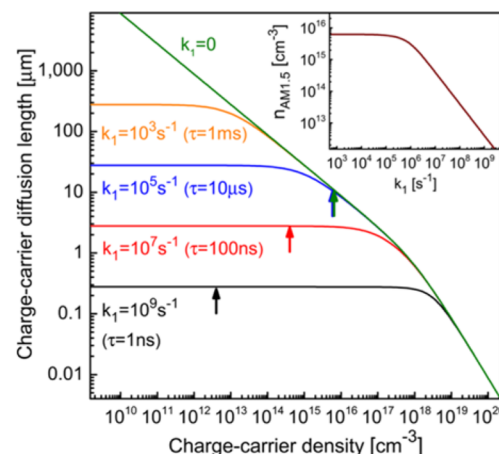


**Figure 35.** Calculated  $L_D$  for  $\text{CH}_3\text{NH}_3\text{PbI}_3$  (with the absence of charge extraction) over a range of monomolecular recombination rate constants,  $k_1$ . Calculations are based on  $\mu = 30 \text{ cm}^2 \text{ V}^{-1} \text{ s}^{-1}$ , a bimolecular recombination rate constant of  $k_2 = 10^{-10} \text{ cm}^3 \text{ s}^{-1}$  and an Auger rate constant of  $k_3 = 10^{-28} \text{ cm}^6 \text{ s}^{-1}$ . The inset shows the charge carrier density under steady-state AM 1.5G illumination as a function of  $k_1$  in the absence of charge extraction. Reproduced from ref 245. Copyright 2016 American Chemical Society.

(section 4.3).<sup>245</sup> This analysis revealed that  $L_D$  is unlikely to much exceed  $\sim 10 \mu\text{m}$  under 1 sun conditions even were all trap-mediated recombination eliminated because of the contributions of second- and third-order mechanisms at high charge-carrier densities. Furthermore, mobilities of  $\sim 120 \text{ cm}^2 \text{ V}^{-1} \text{ s}^{-1}$  would only raise the maximum achievable  $L_D$  by a factor of 2, showing the difficulty inherent in achieving  $L_D$  in  $\text{CH}_3\text{NH}_3\text{PbI}_3$  significantly higher than  $10\text{--}20 \mu\text{m}$  under 1 sun conditions without dramatically increased mobility.

The extremely efficient charge collection witnessed in lead-based perovskite solar cells is directly linked to these long and balanced charge carrier diffusion lengths. Ambipolar charge carrier diffusion is a direct result of the unique electronic structure of MHPs (section 2).<sup>148</sup> In addition, the bimolecular

recombination rate deviates from the Langevin model by 4–5 orders of magnitude (section 4.3). Electrostatic fluctuations caused by random orientation of  $\text{CH}_3\text{NH}_3^+$  molecular dipoles may facilitate formation of spatially localized electron and hole potential wells on the order of 5 nm, which could explain the significant deviation.<sup>320</sup> Another possibility is splitting of the band edge states in reciprocal space due to momentum selection rules.<sup>339</sup>

Nevertheless, an interesting aspect of  $\text{CH}_3\text{NH}_3\text{PbI}_3$  is that, while the mobility of  $\text{CH}_3\text{NH}_3\text{PbI}_3$  is high when compared to other solution-processed materials, such as organic semiconductors,<sup>340,341</sup> it has a relatively modest mobility compared to other PV-relevant inorganic semiconductors which display similar effective masses. In fact, the mobility of other PV-relevant semiconductors is typically 1 to 2 orders of magnitude higher than has been observed in the two most widely used PSC materials,  $\text{CH}_3\text{NH}_3\text{PbX}_3$  and  $\text{CH}(\text{NH}_2)_2\text{PbX}_3$ .<sup>61</sup> This is somewhat surprising because the measured effective masses of carriers in  $\text{APbX}_3$  semiconductors is generally similar to those of Si and GaAs.<sup>61</sup> In addition, surface potential measurements on well-performing perovskite solar cells indicate that the device efficiency of solar cells with thick active layers is limited by this low charge carrier mobility,<sup>342</sup> prompting further study into the underlying reasons for this discrepancy.

Analysis of trap states in  $\text{CH}_3\text{NH}_3\text{PbX}_3$  has revealed trap densities as low as  $10^9$ – $10^{10}$  cm<sup>-3</sup> in single crystals,<sup>49,60,144,330,331,343</sup> on par with monocrystalline Si.<sup>344</sup> In addition, the traps that are formed are largely shallow, making  $\text{CH}_3\text{NH}_3\text{PbI}_3$  unusually defect tolerant.<sup>231,336,345–347</sup> It has therefore been concluded that the mobility of carriers in  $\text{CH}_3\text{NH}_3\text{PbI}_3$  is significantly limited by scattering (eq 32) but that the primary scattering centers must not be recombination centers.<sup>61</sup> This is supported by the  $\sim T^{-3/2}$  temperature dependence of the mobility, which implies that there is only limited impurity scattering. Transport is therefore primarily slowed by acoustic phonons (Figure 36).<sup>230,250,307,345</sup> Slow carrier cooling in  $\text{CH}_3\text{NH}_3\text{PbI}_3$ , a result of a hot phonon bottleneck (section 4.2), lends further evidence for limited phonon impurity scattering.<sup>261</sup> Conversely, Sn-based MHPs made by current fabrication methods do appear to suffer significantly from reduced mobility as a result of impurity scattering arising from the facile Sn(II) to Sn(IV) oxidation.<sup>306</sup>

The B—X bond angle is also important in charge transport. With octahedral tilting, orbital overlap, and thus conductivity, decreases.<sup>99</sup> This effect was observed by Yamada et al. in the decreasing conductivity of the series  $\text{CsSnBr}_3$ ,  $\text{CH}_3\text{NH}_3\text{SnBr}_3$ ,  $\text{CH}_3\text{NH}_3\text{Sn}_{1-x}\text{Pb}_x\text{Br}_3$ , and  $\text{CH}_3\text{NH}_3\text{PbBr}_3$ .<sup>316</sup> Hao et al. observed the same effect in  $\text{CH}_3\text{NH}_3\text{Sn}_{1-x}\text{Pb}_x\text{I}_3$  alloys where the conductivity is at a maximum in pure  $\text{CH}_3\text{NH}_3\text{SnI}_3$ . In  $\text{CH}_3\text{NH}_3\text{SnI}_3$ , the Sn—I—Sn bond angles are close to 180°, but this angle decreases with increasing Pb as the B—I—B bond distorts, leading to a decrease in conductivity (Figure 37).<sup>99</sup> Conductivity increase coinciding with temperature-induced phase changes, such as have been observed in  $\text{CsSnI}_3$ , further support that the conductivity of the perovskite phase is closely linked with the linear X—B—X—B chain.<sup>317</sup> Thus, all other effects being equal, conductivity is highest in the cubic ( $Pm\bar{3}m$ ) phase where the B—X—B bond angle is 180°.<sup>99</sup>

Theoretical work shows that a somewhat similar trend exists between  $\text{CH}_3\text{NH}_3\text{PbI}_3$  and  $\text{CH}(\text{NH}_2)_2\text{PbI}_3$ . Stronger  $\text{CH}(\text{NH}_2)_2\text{—I}$  bonds compared to  $\text{CH}_3\text{NH}_3\text{—I}$  stabilize the more ionic Pb—I bonds (with more partial negative charge on iodide anions) of pseudocubic  $\text{CH}(\text{NH}_2)_2\text{PbI}_3$ .<sup>348</sup> This reduced

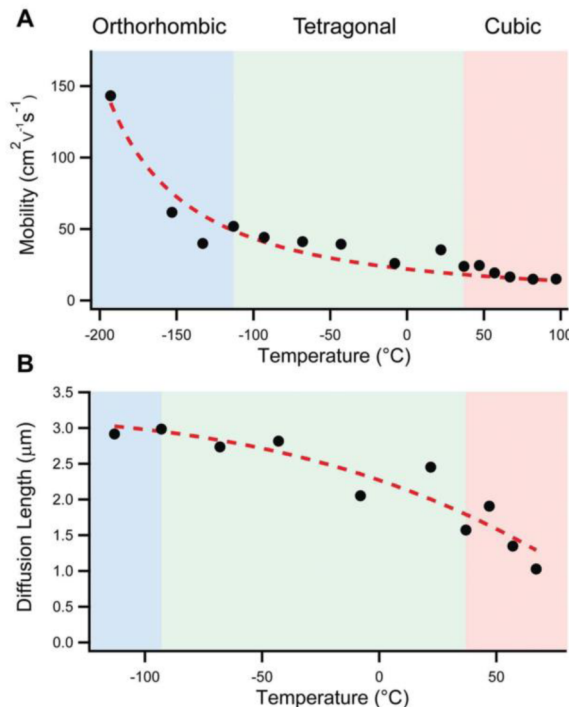


**Figure 36.** (A) Temperature dependence of the mobility showing (●) a  $\sim T^{-3/2}$  dependence (red dashed line) as predicted for band-like transport. (B) Diffusion lengths (●) at possible cell working temperatures. (A and B) reproduced with permission from ref 230 under CC BY 4.0.

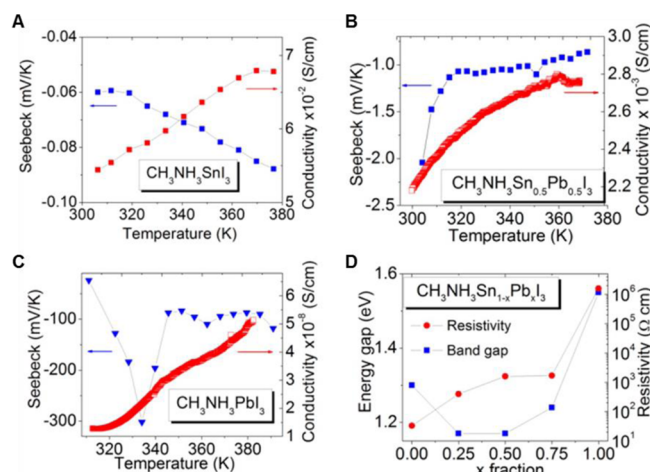


**Figure 37.** Conductivity and Seebeck measurements as a function of temperature for (A)  $\text{CH}_3\text{NH}_3\text{SnI}_3$ , (B)  $\text{CH}_3\text{NH}_3\text{Sn}_{0.5}\text{Pb}_{0.5}\text{I}_3$ , and (C)  $\text{CH}_3\text{NH}_3\text{SnI}_3$  samples prepared from solution. (D) Resistivity and optical band gap as a function of composition ( $x$ ) in  $\text{CH}_3\text{NH}_3\text{Sn}_{1-x}\text{Pb}_x\text{I}_3$  solid solutions. (A–D) reproduced from ref 99. Copyright 2014 American Chemical Society.

octahedral tilting increases the Pb character of the conduction band minimum and promotes increased spin-orbit splitting (section 2.2.1), explaining the reduced band gap of  $\text{CH}(\text{NH}_2)_2\text{PbI}_3$  compared to  $\text{CH}_3\text{NH}_3\text{PbI}_3$  and ultimately resulting in superior transport properties.<sup>124</sup> Recent work by Kedem et al. showed a several-fold increase in the  $L_D$ , as measured by EBIC, in  $\text{CH}_3\text{NH}_3\text{PbBr}_3(\text{Cl})$  devices when illuminated, an effect which may arise from analogous light-induced structural changes in the material.<sup>332</sup> On the other hand, the similar PV

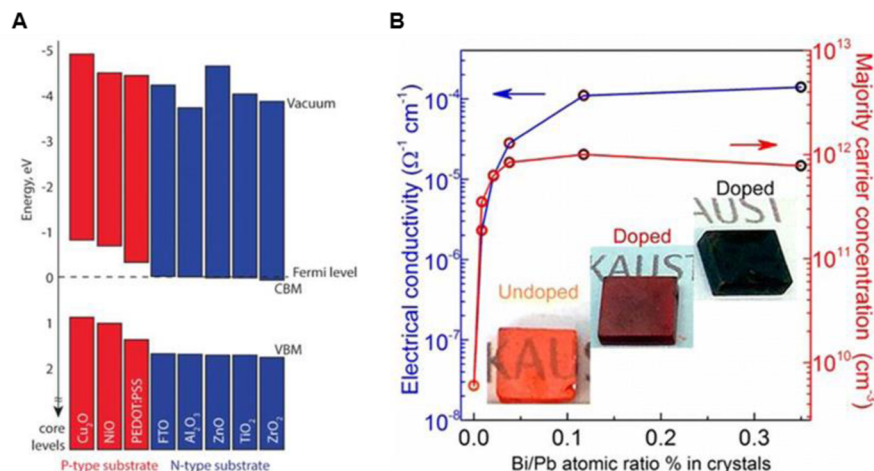


**Figure 38.** (A) Summary of photoelectron spectroscopy results of  $\text{CH}_3\text{NH}_3\text{PbI}_3$  deposited on various p-type and n-type substrates revealing substrate-controlled band shifts. The conduction band minimum is determined by adding the transport gap (1.7 eV) to the experimentally determined valence band minimum. Reproduced from ref 351 with permission of The Royal Society of Chemistry. (B) Change in electrical conductivity and carrier concentration upon heterovalent doping of  $\text{CH}_3\text{NH}_3\text{PbBr}_3$  single crystals with  $\text{Bi}^{3+}$ . Reproduced from ref 63. Copyright 2016 American Chemical Society.

performance of  $\text{CH}_3\text{NH}_3\text{PbBr}_3$  and  $\text{CsPbBr}_3$  demonstrates the amenability of these materials to A-site substitutions.<sup>349</sup> A-site substitution is a promising way of improving mobility considering Cs-based materials have shown significantly increased mobility compared to  $\text{CH}_3\text{NH}_3$  and  $\text{CH}(\text{NH}_2)_2$  (Table 3). This indicates that carrier scattering may be tied to the A-site dipole, although more evidence is required to verify this hypothesis. It has also been recently hypothesized that large polarons may form in some  $\text{ABX}_3$  perovskites due to the polarizability of the A-site cation.<sup>249,250,350</sup> This would cause localization of carriers, dramatically raising the carrier effective mass while still allowing for long-range transport and good mobility; however, direct experimental evidence to support this hypothesis is still lacking, and current data on low carrier effective mass would need to be reconciled with this hypothesis.<sup>178</sup>

Further insight into the charge transport aspects of Sn- and Pb-based MHPs has been gained through the investigation of majority carrier type. Very low carrier concentrations, particularly in Pb-based materials, give rise to large Seebeck coefficients and near-intrinsic behavior as deduced from the ambipolar nature of charge transport in these materials (see Table 3).<sup>76</sup> However, a UPS and XPS study of the valence band position by Miller et al. revealed that carrier type and band position in  $\text{CH}_3\text{NH}_3\text{PbI}_3$  are sensitive to deposition conditions and substrate (Figure 38A).<sup>351</sup>

The admittedly limited existing evidence suggests that deposition conditions affect Sn-based materials even more radically than their Pb-containing counterparts. This arises primarily from the facile oxidation of Sn(II) to Sn(IV); Pb(IV) is not known to exist in these systems due to stabilization of the  $s^2$  electronic configuration through relativistic effects (section 2.1). Sn(IV) can act as a p-type dopant, and its presence is highly dependent on synthetic conditions. Partial oxidation of the B-site in Sn perovskites gives rise to significantly higher carrier concentrations than typically observed in similarly prepared Pb-based samples.<sup>76,99,229</sup>

While the p- or n-type nature of MHPs is dependent on fabrication conditions, a deliberate tuning of the majority carrier type is a potential method for achieving all-hybrid-

perovskite p–n junction solar cells. Toward this end, Abdelhady et al. recently showed that the doping of  $\text{CH}_3\text{NH}_3\text{PbBr}_3$  crystals with Bi(III) decreases the band gap of the material and leads to a 4 orders of magnitude increase in electrical conductivity (Figure 38B).<sup>63</sup> This heterovalent doping also led to a change in sign of the majority carriers from p-type to n-type along with the conversion from intrinsic to extrinsic semiconductor. Both heterovalent and isoivalent doping of MHPs still remain largely unexplored,<sup>102</sup> as do the full implications of synthesis conditions on carrier type and concentration. As with Si, GaAs, and other semiconductors, controlling carrier type and concentration through synthetic means and deliberate doping will likely be a critical aspect in further developing MHP optoelectronic technology.

## 5.2. Ion Transport

Early work on MHPs provided the first evidence for ionic conduction.<sup>163,352</sup> Busmundrud and Feder demonstrated anomalies in the temperature-dependent conductivity of  $\text{CsPbCl}_3$  occurring at the phase transitions which they ascribed to ionic conductivity.<sup>352</sup> Pioneering work by Yamada et al. demonstrated Cl conduction in  $\text{AGeCl}_3$  [ $\text{A} = \text{CH}_3\text{NH}_3$  and  $(\text{CH}_3)_4\text{N}$ ]. These materials adopt a dynamic-disordered cubic ( $Pm\bar{3}m$ ) perovskite structure where the Cl atoms occupy the 6f sites (instead of the typical 3c sites) with 50% probability.<sup>163</sup> It was proposed that Cl conduction in these materials arises from a dynamic switching of the bonds,  $\text{Cl}-\text{Ge}\cdots\text{Cl}$  and  $\text{Cl}\cdots\text{Ge}-\text{Cl}$  (hopping of Cl between adjacent 6f sites), followed by reorientation of the  $\text{GeCl}_3^-$  units about the  $C_3$  axis. Earlier work carried out by Mizusaki et al. investigated the ionic conduction of  $\text{CsPbCl}_3$ ,  $\text{CsPbBr}_3$ , and  $\text{KMnCl}_3$  and determined that, in each case, the perovskite materials were halide conductors. Halide conduction was considered to arise from vacancy migration with activation energies of approximately 0.25–0.4 eV.<sup>353</sup>

More recently, the advent of MHP photovoltaics has spurred further interest in ion transport in these materials. Specifically, beginning with the initial reports of hysteresis in the current–voltage measurements of perovskite PVs by Snaith et al.,<sup>354</sup> great effort has been devoted to determining the fundamental causes of hysteresis in the devices. Snaith and co-workers first

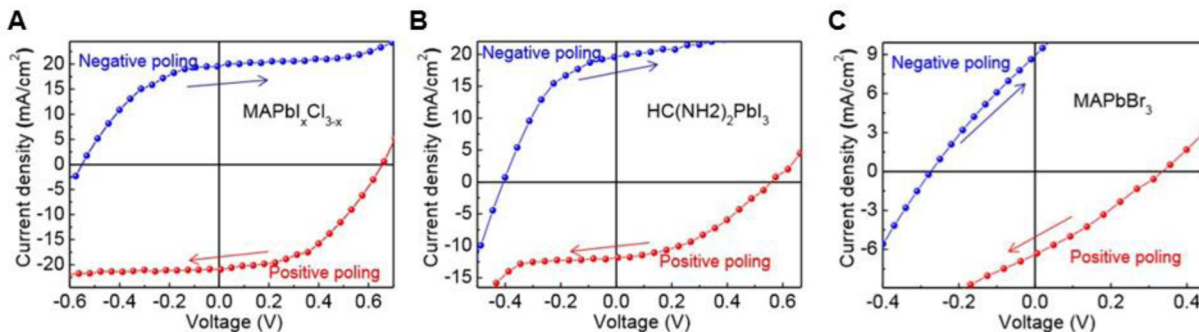


**Figure 39.** Switchable photovoltaic effect of ITO/PEDOT:PSS/Perovskite (300 nm)/Au vertical architecture devices with (A)  $\text{CH}_3\text{NH}_3\text{PbI}_{3-x}\text{Cl}_x$ , (B)  $\text{HC}(\text{NH}_2)_2\text{PbI}_3$ , and (C)  $\text{CH}_3\text{NH}_3\text{PbBr}_3$  active layers. Reprinted by permission from Macmillan Publishers Ltd.: Nature Materials (ref 367), copyright 2014.

investigated the hysteresis in detail and proposed three likely root causes: (i) interfacial traps which are filled/emptied depending on bias, (ii) ferroelectric polarization, and (iii) screening of the built-in electric field by mobile ions in the film.<sup>354</sup> Subsequently, many reports have sought to fully explain the origins of the hysteresis. While a complete treatment of hysteresis in perovskite solar cells is beyond the scope of the present work, current evidence is strong that ion migration plays a major role,<sup>251,355–360</sup> although device architecture and interfaces are also of great importance.<sup>361,362</sup>

Theoretical studies of ionic conduction on the photovoltaically relevant perovskite  $\text{CH}_3\text{NH}_3\text{PbI}_3$  have differed in details but reach the consensus that the mobility of ions follows the trend  $\text{I}^- > \text{CH}_3\text{NH}_3^+ > \text{Pb}^{2+}$ .<sup>363–365</sup> Eames et al. predicted that  $\text{I}^-$  is the dominant mobile ion with only limited mobility of  $\text{CH}_3\text{NH}_3^+$ .<sup>363</sup> Their theoretical activation energies for  $\text{I}^-$  migration matched well with the activation energy inferred from temperature-dependent chronoamperometry measurements (0.58 eV vs 0.60–0.68 eV). Migration activation energies of a similar magnitude (~0.45 eV) were calculated by Haruyama et al. for  $\text{I}^-$  conduction in  $\text{CH}_3\text{NH}_3\text{PbI}_3$  and  $\text{CH}(\text{NH}_2)_2\text{PbI}_3$ .<sup>365</sup> However, they also predicted the relatively facile migration of both  $\text{CH}_3\text{NH}_3^+$  and  $\text{CH}(\text{NH}_2)_2^+$  cations. On the other hand, Aziproz et al. calculated very low migration activation energies for  $\text{I}^-$  on the order of ~0.1 eV, which would imply very fast (<1  $\mu\text{s}$ ) migration, much more rapid than the time scales of device hysteresis (seconds–minutes).<sup>364</sup> Theoretical work by Egger et al. has further proposed that protons can migrate through the perovskite lattice under device-relevant conditions.<sup>366</sup>

Indirect experimental evidence for ion migration in organic–inorganic lead halide perovskites was shown by Xiao et al. by investigating lateral and vertical device architectures with symmetric electrodes.<sup>367</sup> Electrically poling the symmetric device transformed the film from neutral to a p-i-n junction with significant open circuit voltage and photocurrent. This switchable device polarity was attributed to mobile ions and was found in  $\text{CH}_3\text{NH}_3\text{PbI}_3$ ,  $\text{CH}_3\text{NH}_3\text{PbBr}_3$ , and  $\text{CH}(\text{NH}_2)_2\text{PbI}_3$  perovskites (Figure 39) and with different electrode materials.

Yuan et al. extended this study and provided more direct evidence of ion migration by investigating a lateral device architecture (continuous, thin perovskite film deposited on top of micrometer-spaced Au contacts).<sup>368</sup> Kelvin probe force microscopy (KPFM) measurements of the surface potential showed that the device transformed from a neutral planar film to a p-i-n junction when electrically poled (Figure 40).

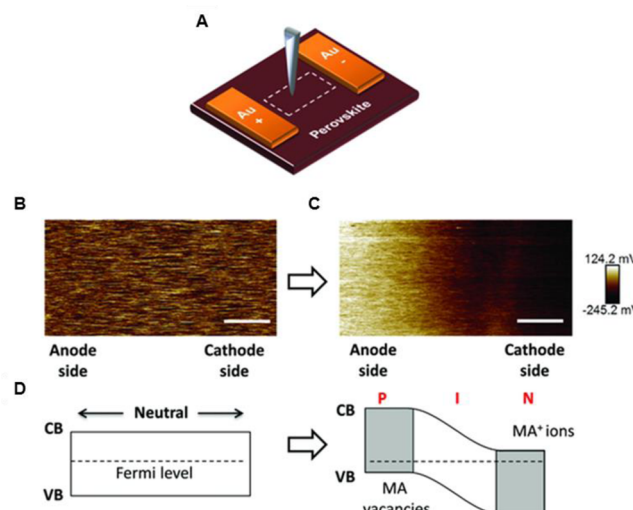


**Figure 40.** (A) Schematic KPFM measurements on lateral structure  $\text{CH}_3\text{NH}_3\text{PbI}_3$  devices. Dashed white box indicates scanning region. KPFM potential of the scanning region (B) before and (C) after electrical poling at  $1.2 \text{ V}/\mu\text{m}$  for 100s. Au electrode spacing is  $50 \mu\text{m}$  and the scale bar in (B) and (C) is  $6 \mu\text{m}$ . (D) Energy diagram of the  $\text{CH}_3\text{NH}_3\text{PbI}_3$  devices before and after poling. Reproduced with permission from ref 368. Copyright 2015 John Wiley and Sons.

Photothermal-induced resistance (PTIR) measurements revealed that the transformation from neutral to p-i-n junction was caused by a buildup of  $\text{CH}_3\text{NH}_3^+$  ions at the cathode, demonstrating that the mobility of  $\text{CH}_3\text{NH}_3^+$  can dramatically affect the field in a device. Varying the electric field strength showed that  $\text{CH}_3\text{NH}_3^+$  migration can occur under an applied field as small as  $\sim 0.3 \text{ V}/\mu\text{m}$  (fields can be  $\sim 3 \text{ V}/\mu\text{m}$  in  $\text{CH}_3\text{NH}_3\text{PbI}_3$  solar cells) with an activation energy of  $\sim 0.36 \text{ eV}$  and an ion mobility of  $\mu = 1.5 \times 10^{-9} \pm 0.5 \text{ cm}^2 \text{ V}^{-1} \text{ s}^{-1}$ .<sup>368</sup> From the similarity in the activation energy of  $\text{CH}_3\text{NH}_3^+$  migration and the formation energy of  $\text{CH}_3\text{NH}_3^+$  substitutions in I-rich  $\text{CH}_3\text{NH}_3\text{PbI}_3$  or  $\text{CH}_3\text{NH}_3^+$  interstitials in I-poor  $\text{CH}_3\text{NH}_3\text{PbI}_3$ ,<sup>347</sup> Yuan et al. hypothesized that  $\text{CH}_3\text{NH}_3^+$  may migrate by substituting Pb or via  $\text{CH}_3\text{NH}_3^+$  interstitial sites.<sup>368</sup> In a similar study, Li et al. provided direct evidence for  $\text{I}^-$  migration.<sup>369</sup> In a lateral device architecture, the I/Pb ratio was found, using XPS, to change from  $\sim 3.03$  initially to  $5.65 \pm 0.93$  at the positive electrode and  $2.29 \pm 0.04$  at the negative electrode after extended biasing of the perovskite film.

Similar conclusions have been drawn from temperature-dependent electrochemical impedance spectroscopy by fitting

of the Warburg ion diffusion component in thin film measurements.<sup>370</sup> Calculated migration activation energies of  $\text{CH}_3\text{NH}_3^+$  and  $\text{CH}(\text{NH}_2)_2^+$  match well with other experimental and theoretical predictions and demonstrate that  $\text{CH}_3\text{NH}_3^+$  is somewhat more mobile than  $\text{CH}(\text{NH}_2)_2^+$ .

The full implications of ion migration on optoelectronic device performance remain somewhat elusive. In perovskite solar cells, the buildup of ions at the contacts screens the internal electric field in the perovskite layer, leading to hysteretic behavior.<sup>371</sup> Mobile ions also appear to be responsible for the poor performance of organic–inorganic MHP field-effect transistors, considering that “freezing” of the mobile ions by reducing the temperature below 200 K resulted in a near 2 orders of magnitude increase in the field-effect carrier mobility.<sup>42</sup>

Significant further experimental and theoretical work is required to fully characterize the ion migration in MHPs. Even before recent attempts to characterize ion migration in MHPs, early reports of halide migration in such various materials as  $\text{CsPbCl}_3$ ,  $\text{CsPbBr}_3$ ,  $\text{KMnCl}_3$ ,  $\text{CH}_3\text{NH}_3\text{GeCl}_3$ , and  $(\text{CH}_3)_4\text{N}-\text{GeCl}_3$ ,<sup>163,352,353</sup> particularly when combined with the current theoretical understanding of ion migration in MHPs, makes halide migration in  $\text{CH}_3\text{NH}_3\text{PbX}_3$  and  $\text{CH}(\text{NH}_2)_2\text{PbX}_3$  semiconductors likely.<sup>363–365</sup> The facile halide exchange in  $\text{CH}_3\text{NH}_3\text{PbX}_3$  supports this.<sup>85</sup> Similarly, cation exchange from  $\text{CH}_3\text{NH}_3\text{PbI}_3$  to  $\text{CH}(\text{NH}_2)_2\text{PbX}_3$  provides evidence of cation mobility and highlights the complexity of this system.<sup>88</sup>

Current state-of-the-art device-grade perovskite films are highly heterogeneous with varied structural and optical properties and relatively small domains (ca. 100 nm–1  $\mu\text{m}$ ).<sup>226,259,321,372</sup> It is anticipated that the large degree of disorder in polycrystalline perovskite films will greatly affect the mechanistic details of ion migration, but it is yet unclear how ion migration can be tuned via control of perovskite stoichiometry/crystallinity/composition or even to what degree it is present in high-performance devices which exhibit little hysteresis.<sup>373</sup> Detailed studies on single crystals will likely prove valuable in this regard. Also, while device aging may give rise to new/more mobile ions which can decrease steady-state device performance,<sup>168,371,374</sup> it is still unclear if ion migration will prove detrimental to the long-term stability of optoelectronic devices that utilize MHPs.

## 6. SUMMARY AND OUTLOOK

Drawing from all the various optoelectronic characteristics discussed herein, it is apparent that MHPs can be regarded as close cousins to conventional III–V semiconductors. But that is not to say their unique properties can be overlooked. An important distinguishing feature of MHPs is their relatively high ionicity and large discrepancy between static and high frequency dielectric constants compared to III–V materials, suggesting carrier-phonon and polaronic effects may play a more prominent role in the former. Such polaronic interactions are indeed common among main group halometallates and can substantially impact carrier transport, cooling, and recombination.

Elucidating the underlying excited state properties of MHPs is a particularly challenging problem. One major obstacle is the low-temperature tetragonal → orthorhombic phase transition that dramatically alters the dielectric properties of hybrid compounds like  $\text{CH}_3\text{NH}_3\text{PbI}_3$  and may also alter phase-specific properties such as Auger recombination and trap-state energies. This inhibits study of device-relevant phases and characteristics

at cryogenic temperatures, as is often done with conventional semiconductors to more accurately elucidate electronic properties such as excitation binding energy and the nature of defects. The absence of a low-temperature phase transition in  $(\text{C}_4\text{H}_9\text{NH}_3)_2\text{PbBr}_4$  has indeed facilitated understanding of its fundamental electronic properties.<sup>217</sup> However, this lack of transition is the exception rather than the rule. As such, complex models and tenuous assumptions must often be invoked to describe properties of the high-temperature tetragonal and cubic phases of most MHPs. Concerted efforts using a variety of experimental and computational techniques are therefore required to define the essential optoelectronic characteristics of MHPs in a self-consistent manner. Further investigations into the MIR nonlinear spectrum of MHPs could help elucidate the role of excitons in these materials.

Intricacies regarding the microstructure–property relationship in MHP thin films deserve continued attention. From heterogeneous trap densities and PLQY to variable excitonic stability, microstructure and morphology clearly have a marked impact on the excited state properties of MHPs. Highly disordered or amorphous regions are known to constitute a large fractional volume of mesostructured perovskite films,<sup>321</sup> and it is not improbable that some degree of amorphyticity is present in device-quality planar thin films. Differences in microstructure are likely one major cause of the wide variability in optoelectronic properties (e.g., mobility, lifetime, diffusion length, etc.) reported for nominally identical materials. Addressing these issues will likely remain a challenge for the community. Closer investigation of high-quality MHP single crystals can aid in teasing out the inherent properties of bulk perovskites. Rapid formation of MHP crystals (on the order of hours),<sup>49,330,375</sup> should facilitate advancement in the fundamental study and application of perovskite single crystals. However, hybrid MHPs at room temperature are in a sense highly disordered even in the bulk due to the rotational degrees of freedom of the molecular cation. Because thin films are currently the most probable candidates for large scale PV production, microstructural effects must be adequately characterized and addressed. One technique that may help in this regard is fluorescence microscopy. It has only recently been employed in the study of MHPs at both the diffraction and subdiffraction limits but has already revealed a number of interesting phenomena, including shape-correlated synchronous photoluminescence intermittency at the single particle level,<sup>376</sup> light-induced enhancement of PL,<sup>227</sup> and observation of photon antibunching in MHP quantum dots.<sup>377</sup> Such studies can reveal details regarding the nature of defects in bulk and quantum confined MHPs, as well as provide insight into processes such as ion diffusion.

A growing number of studies are beginning to shift focus from bulk perovskites to MHP nanocrystals. The photophysical properties of these nanoparticles, including their high PLQY and propensity for optical gain, will no doubt come under increased scrutiny moving forward. Nanocrystals offer an intriguing system for understanding the surface chemistry of MHPs while also opening up the possibility of harnessing quantum size effects. Toward this end, the development of robust, well-controlled synthetic protocols, akin to those successfully employed in metal chalcogenide systems, will be an important step toward fully utilizing these nanoscale materials.

Most studies to date have focused on the photovoltaically relevant compound  $\text{CH}_3\text{NH}_3\text{PbI}_3$ , providing a wealth of

information about this material. Yet due to the compositional instability of materials which incorporate the  $\text{CH}_3\text{NH}_3^+$  cation,<sup>95,168,201,374</sup> recent work has shifted to other systems that may offer improved resilience toward heat and moisture, most notably  $\text{CsPbI}_3$  and  $\text{CH}(\text{NH}_2)_2\text{PbI}_3$ . This transition has highlighted a gap in the understanding of how the A-site cation influences material properties. Further complicating matters, recent success achieved with perovskite photovoltaics has been enabled by complex alloys featuring multiple A-site and/or X-site species. It is surprising that these alloys, specifically X-site alloys, consistently outperform pure materials in photovoltaic devices given the increased disorder of the metal-halide network which is so crucial for charge transport. A challenge for the community will be to understand the effect of such alloying, namely to what degree improved device metrics can be attributed to improved film microstructure or modulation of inherent material properties.

Though we have learned much in recent years regarding the prominent recombination pathways in MHPs, the origin of low bimolecular recombination rates has yet to be unambiguously assigned. They have thus far been attributed to a variety of phenomena, including spatial localization of carriers as a result of electrostatic fluctuations from randomized molecular dipoles, molecular ferroelectric domains, polaron formation, the charge transfer nature of the halometallate electronic transitions, and indirect transitions at the band edge resulting from symmetry breaking. Reconciling these propositions will constitute an important step toward a more complete understanding of these intriguing compounds.

## AUTHOR INFORMATION

### Corresponding Author

\*E-mail: pkamat@nd.edu.

### Notes

The authors declare no competing financial interest.

### Biographies

Joseph S. Manser received his B.S. in Chemistry from Catawba College in 2011 and his Ph.D. in Chemical and Biomolecular Engineering from the University of Notre Dame in 2016. At Notre Dame, he worked under Prof. Prashant V. Kamat to characterize the excited state properties of metal halide perovskites, as well as to develop new applications for perovskite solar cells. Joe has been involved in a number of collaborations focused on spatially resolved measurements to elucidate charge transport and trapping mechanisms in perovskite thin films. He has also taken an interest in the solution-based growth and subsequent moisture-induced degradation of perovskites. His broader research interests include understanding the underlying material and device properties that govern performance of next-generation photovoltaics.

Jeffrey A. Christians earned his B.S.E. in Chemical Engineering with a second major in Chemistry from Calvin College in 2010 while performing research on quantum dot biosensors under the direction of Prof. David E. Benson. Following this, he joined the Department of Chemical and Biomolecular Engineering at the University of Notre Dame, where he worked under the guidance of Prof. Prashant V. Kamat performing research on hole transfer processes in  $\text{Sb}_2\text{S}_3$  solar cells and the stability of perovskite solar cells. In 2015, Jeff earned his Ph.D. from Notre Dame and was awarded the Shaheen Graduate School Award for the College of Engineering. He currently works as a postdoctoral researcher with Prof. Joseph M. Luther at the National

Renewable Energy Laboratory in Golden, Colorado, where he is continuing his research on perovskite solar cells.

Prashant V. Kamat is a Rev. John A. Zahm, C.S.C., Professor of Science in the Department of Chemistry and Biochemistry and Radiation Laboratory at the University of Notre Dame. He is also a Concurrent Professor in the Department of Chemical and Biomolecular Engineering. He earned his doctoral degree (1979) in Physical Chemistry from Bombay University and performed postdoctoral research at Boston University (1979–1981) and the University of Texas at Austin (1981–1983). He joined Notre Dame in 1983. Professor Kamat has for nearly three decades worked to build bridges between physical chemistry and material science to develop advanced nanomaterials that promise cleaner and more efficient light energy conversion. He is currently serving as the Editor-in-Chief of *ACS Energy Letters*. He has also served as the deputy editor of the *Journal of Physical Chemistry Letters*. He is a member of the advisory board of several scientific journals.

## ACKNOWLEDGMENTS

We thank O. Sharia for offering his expertise regarding electronic properties of MHPs. This work was supported by the Division of Chemical Sciences, Geosciences, and Biosciences, Office of Basic Energy Sciences of the U.S. Department of Energy, through awards DE-FC02-04ER15533 and DE-SC0014334. This work was supported in part by ND Energy, University of Notre Dame. J.S.M. acknowledges the support of King Abdullah University of Science and Technology (KAUST) through Award OCRF-2014-CRG3-2268. This is contribution number NDRL no. 5108 from the Notre Dame Radiation Laboratory.

## REFERENCES

- (1) Rose, G. De Perowskite, Fossili Novo. In *De Novis Quibusdam Fossilibus Quae In Montibus Uraliis Inveniuntur*; AG Schade: Berlin, 1839; pp 3–5.
- (2) Wells, H. L. Über Die Cäsium- Und Kalium-Bleihalogenide. *Zeitschrift für Anorg. Chemie* **1893**, *3*, 195–210.
- (3) Møller, C. K. A Phase Transition in Cæsium Plumbochloride. *Nature* **1957**, *180*, 981–982.
- (4) Møller, C. K. Crystal Structure and Photoconductivity of Cæsium Plumbohalides. *Nature* **1958**, *182*, 1436–1436.
- (5) Bowman, H. L. On the Structure of Perovskite from the Burgumer Alp, Pfitschthal, Tyrol. *Mineral. Mag.* **1908**, *15*, 156–176.
- (6) Goldschmidt, V. M. Titanium Pigment and Process of Producing the Same. US1436164 A, 1922.
- (7) Wainer, E. High Titania Dielectrics. *Trans. Electrochem. Soc.* **1946**, *89*, 331.
- (8) Miyake, S.; Ueda, R. On Polymorphic Change of  $\text{BaTiO}_3$ . *J. Phys. Soc. Jpn.* **1946**, *1*, 32–33.
- (9) Gray, R. B. Transducer and Method of Making the Same. US2486560 A, 1946.
- (10) Cross, L. E.; Newnham, R. E. History of Ferroelectrics. *Ceram. Civiliz.* **1987**, *III*, 289–305.
- (11) Balz, D. Über Die Struktur Des  $\text{K}_2\text{NiF}_4$ . *Naturwissenschaften* **1953**, *40*, 241–241.
- (12) de Jongh, L. J.; Miedema, A. R. Experiments on Simple Magnetic Model Systems. *Adv. Phys.* **1974**, *23*, 1–260.
- (13) Willett, R.; Place, H.; Middleton, M. Crystal Structures of Three New Copper(II) Halide Layered Perovskites: Structural, Crystallographic, and Magnetic Correlations. *J. Am. Chem. Soc.* **1988**, *110*, 8639–8650.
- (14) Mostafa, M.; Willett, R. Magnetic Properties of Ferrous Chloride Complexes with Two-Dimensional Structures. *Phys. Rev. B* **1971**, *4*, 2213–2215.

- (15) Geick, R.; Strobel, K. Phonons in Perovskite-Type Layer Structures. *J. Phys. C: Solid State Phys.* **1979**, *12*, 27–39.
- (16) Ishihara, T.; Takahashi, J.; Goto, T. Exciton State in Two-Dimensional Perovskite Semiconductor  $(C_{10}H_{21}NH_3)_2PbI_4$ . *Solid State Commun.* **1989**, *69*, 933–936.
- (17) Xu, C.-Q.; Fukuta, S.; Sakakura, H.; Kondo, T.; Ito, R.; Takahashi, Y.; Kumata, K. Anomalous Electro-Absorption in the Low-Temperature Phase of  $(C_{10}H_{21}NH_3)_2PbI_4$ . *Solid State Commun.* **1991**, *77*, 923–926.
- (18) Xu, C.; Kondo, T.; Sakakura, H.; Kumata, K.; Takahashi, Y.; Ito, R. Optical Third-Harmonic Generation in Layered Perovskite-Type Material  $(C_{10}H_{21}NH_3)_2PbI_4$ . *Solid State Commun.* **1991**, *79*, 245–248.
- (19) Hong, X.; Ishihara, T.; Nurmikko, A. Dielectric Confinement Effect on Excitons in  $PbI_4$ -Based Layered Semiconductors. *Phys. Rev. B: Condens. Matter Mater. Phys.* **1992**, *45*, 6961–6964.
- (20) Hirasawa, M.; Ishihara, T.; Goto, T.; Sasaki, S.; Uchida, K.; Miura, N. Magnetoreflection of the Lowest Exciton in a Layered Perovskite-Type Compound  $(C_{10}H_{21}NH_3)_2PbI_4$ . *Solid State Commun.* **1993**, *86*, 479–483.
- (21) Papavassiliou, G. C.; Koutselas, I. B.; Terzis, A.; Whangbo, M.-H. Structural and Electronic Properties of the Natural Quantum-Well System  $(C_6H_5CH_2CH_2NH_3)_2SnI_4$ . *Solid State Commun.* **1994**, *91*, 695–698.
- (22) Ishihara, T.; Hong, X.; Ding, J.; Nurmikko, A. V. Dielectric Confinement Effect for Exciton and Biexciton States in  $PbI_4$ -Based Two-Dimensional Semiconductor Structures. *Surf. Sci.* **1992**, *267*, 323–326.
- (23) Hanamura, E.; Nagaosa, N.; Kumagai, M.; Takagahara, T. Quantum Wells with Enhanced Exciton Effects and Optical Non-Linearity. *Mater. Sci. Eng., B* **1988**, *1*, 255–258.
- (24) Mitzi, D. B.; Feild, C. A.; Harrison, W. T. A.; Guloy, A. M. Conducting Tin Halides with a Layered Organic-Based Perovskite Structure. *Nature* **1994**, *369*, 467–469.
- (25) Mitzi, D. B.; Wang, S.; Feild, C. A.; Chess, C. A.; Guloy, A. M. Conducting Layered Organic-Inorganic Halides Containing <110>-Oriented Perovskite Sheets. *Science* **1995**, *267*, 1473–1476.
- (26) Era, M.; Tsutsui, T.; Saito, S.; Morimoto, S. Electroluminescent Device Using Two Dimensional Semiconductor  $(C_6H_5C_2H_4NH_3)_2PbI_4$  as an Emitter. *Synth. Met.* **1995**, *71*, 2013–2014.
- (27) Hattori, T.; Taira, T.; Era, M.; Tsutsui, T.; Saito, S. Highly Efficient Electroluminescence from a Heterostructure Device Combined with Emissive Layered-Perovskite and an Electron-Transporting Organic Compound. *Chem. Phys. Lett.* **1996**, *254*, 103–108.
- (28) Chondroudis, K.; Mitzi, D. B. Electroluminescence from an Organic–Inorganic Perovskite Incorporating a Quaterthiophene Dye within Lead Halide Perovskite Layers. *Chem. Mater.* **1999**, *11*, 3028–3030.
- (29) Kagan, C. R.; Mitzi, D. B.; Dimitrakopoulos, C. D. Organic–Inorganic Hybrid Materials as Semiconducting Channels in Thin-Film Field-Effect Transistors. *Science* **1999**, *286*, 945–947.
- (30) Mitzi, D. B.; Dimitrakopoulos, C. D.; Kosbar, L. L. Structurally Tailored Organic–Inorganic Perovskites: Optical Properties and Solution-Processed Channel Materials for Thin-Film Transistors. *Chem. Mater.* **2001**, *13*, 3728–3740.
- (31) Mitzi, D. B.; Dimitrakopoulos, C. D.; Rosner, J.; Medeiros, D. R.; Xu, Z.; Noyan, C. Hybrid Field-Effect Transistor Based on a Low-Temperature Melt-Processed Channel Layer. *Adv. Mater.* **2002**, *14*, 1772–1776.
- (32) Web of Science, Accessed 27 April 2016. Search Query: TS = (perovskite solar cell OR perovskite\* NEAR sensitiz\* OR perovskite\* NEAR photovoltaic\* OR "organometal halide") NOT TS = (Er3\*) NOT TS = (Yb3\*) NOT TS = (SrT\*) NOT AU = Neelgund NOT TS = (calcium) NOT TS = (Manganite) NOT TS = (hydroxystannate) NOT TS = (titannate) NOT TS = (stanninate) NOT TS = (ceramic) NOT TS = (oxide\*) NOT TS = (stannate) NOT TS = (Bi2\*) NOT TS = (titania) Refined by: [excluding] DOCUMENT TYPES: (NEWS ITEM OR MEETING ABSTRACT OR CORRECTION)
- (33) Pankove, J. I. *Optical Processes in Semiconductors*; Dover Publications, Inc.: New York, 1971.
- (34) Pelant, I.; Valenta, J. *Luminescence Spectroscopy of Semiconductors*; Oxford University Press: New York, 2012.
- (35) Sze, S. M.; Ng, K. K. *Physics of Semiconductor Devices*, 3rd ed.; Wiley-Interscience: Hoboken, 2007.
- (36) Shah, J. *Ultrafast Spectroscopy of Semiconductors and Semiconductor Nanostructures*; Springer: Heidelberg, 1996.
- (37) Lin, C. C.; Meijerink, A.; Liu, R.-S. Critical Red Components for Next-Generation White LEDs. *J. Phys. Chem. Lett.* **2016**, *7*, 495–503.
- (38) Zhang, X.; Lin, H.; Huang, H.; Reckmeier, C.; Zhang, Y.; Choy, W. C. H.; Rogach, A. L. Enhancing the Brightness of Cesium Lead Halide Perovskite Nanocrystal Based Green Light-Emitting Devices through the Interface Engineering with Perfluorinated Ionomer. *Nano Lett.* **2016**, *16*, 1415–1420.
- (39) Ling, Y.; Yuan, Z.; Tian, Y.; Wang, X.; Wang, J. C.; Xin, Y.; Hanson, K.; Ma, B.; Gao, H. Bright Light-Emitting Diodes Based on Organometal Halide Perovskite Nanoplatelets. *Adv. Mater.* **2016**, *28*, 305–311.
- (40) Pathak, S.; Sakai, N.; Wisnivesky Rocca Rivarola, F.; Stranks, S. D.; Liu, J.; Eperon, G. E.; Ducati, C.; Wojciechowski, K.; Griffiths, J. T.; Haghshirad, A. A.; et al. Perovskite Crystals for Tunable White Light Emission. *Chem. Mater.* **2015**, *27*, 8066–8075.
- (41) Tan, Z.-K.; Moghaddam, R. S.; Lai, M. L.; Docampo, P.; Higler, R.; Deschler, F.; Price, M.; Sadhanala, A.; Pazos, L. M.; Credgington, D.; et al. Bright Light-Emitting Diodes Based on Organometal Halide Perovskite. *Nat. Nanotechnol.* **2014**, *9*, 687–692.
- (42) Chin, X. Y.; Cortecchia, D.; Yin, J.; Bruno, A.; Soci, C. Lead Iodide Perovskite Light-Emitting Field-Effect Transistor. *Nat. Commun.* **2015**, *6*, 7383.
- (43) McMeekin, D. P.; Sadoughi, G.; Rehman, W.; Eperon, G. E.; Saliba, M.; Horantner, M. T.; Haghshirad, A.; Sakai, N.; Korte, L.; Rech, B.; et al. A Mixed-Cation Lead Mixed-Halide Perovskite Absorber for Tandem Solar Cells. *Science* **2016**, *351*, 151–155.
- (44) Bailie, C. D.; Christoforo, M. G.; Mailoa, J. P.; Bowring, A. R.; Unger, E. L.; Nguyen, W. H.; Burschka, J.; Pellet, N.; Lee, J. Z.; Grätzel, M.; et al. Semi-Transparent Perovskite Solar Cells for Tandems with Silicon and CIGS. *Energy Environ. Sci.* **2015**, *8*, 956–963.
- (45) Werner, J.; Weng, C.-H.; Walter, A.; Fesquet, L.; Seif, J. P.; De Wolf, S.; Niesen, B.; Ballif, C. Efficient Monolithic Perovskite/Silicon Tandem Solar Cell with Cell Area > 1 cm<sup>2</sup>. *J. Phys. Chem. Lett.* **2016**, *7*, 161–166.
- (46) Chen, Y.-S.; Manser, J. S.; Kamat, P. V. All Solution-Processed Lead Halide Perovskite-BiVO<sub>4</sub> Tandem Assembly for Photolytic Solar Fuels Production. *J. Am. Chem. Soc.* **2015**, *137*, 974–981.
- (47) Luo, J.; Im, J.-H.; Mayer, M. T.; Schreier, M.; Nazeeruddin, M. K.; Park, N.-G.; Tilley, S. D.; Fan, H. J.; Grätzel, M. Water Photolysis at 12.3% Efficiency via Perovskite Photovoltaics and Earth-Abundant Catalysts. *Science* **2014**, *345*, 1593–1596.
- (48) Gurudayal; Sabba, D.; Kumar, M. H.; Wong, L. H.; Barber, J.; Grätzel, M.; Mathews, N. Perovskite–Hematite Tandem Cells for Efficient Overall Solar Driven Water Splitting. *Nano Lett.* **2015**, *15*, 3833–3839.
- (49) Maculan, G.; Sheikh, A. D.; Abdelhady, A. L.; Saidaminov, M. I.; Haque, M. A.; Murali, B.; Alarousu, E.; Mohammed, O. F.; Wu, T.; Bakr, O. M.  $CH_3NH_3PbCl_3$  Single Crystals: Inverse Temperature Crystallization and Visible-Blind UV-Photodetector. *J. Phys. Chem. Lett.* **2015**, *6*, 3781–3786.
- (50) Lin, Q.; Armin, A.; Burn, P. L.; Meredith, P. Filterless Narrowband Visible Photodetectors. *Nat. Photonics* **2015**, *9*, 687–694.
- (51) Moehl, T.; Im, J. H.; Lee, Y. H.; Domanski, K.; Giordano, F.; Zakeeruddin, S. M.; Dar, M. I.; Heiniger, L.; Nazeeruddin, M. K.; Park, N.; et al. Strong Photocurrent Amplification in Perovskite Solar Cells with a Porous TiO<sub>2</sub> Blocking Layer under Reverse Bias. *J. Phys. Chem. Lett.* **2014**, *5*, 3931–3936.

- (52) Xing, G.; Mathews, N.; Lim, S. S.; Yantara, N.; Liu, X.; Sabba, D.; Grätzel, M.; Mhaisalkar, S.; Sum, T. C. Low-Temperature Solution-Processed Wavelength-Tunable Perovskites for Lasing. *Nat. Mater.* **2014**, *13*, 476–480.
- (53) Deschler, F.; Price, M.; Pathak, S.; Klintberg, L. E.; Jarausch, D. D.; Higler, R.; Hüttner, S.; Leijtens, T.; Stranks, S. D.; Snaith, H. J.; et al. High Photoluminescence Efficiency and Optically Pumped Lasing in Solution-Processed Mixed Halide Perovskite Semiconductors. *J. Phys. Chem. Lett.* **2014**, *5*, 1421–1426.
- (54) Fu, Y.; Zhu, H.; Schrader, A. W.; Liang, D.; Ding, Q.; Joshi, P.; Hwang, L.; Zhu, X.-Y.; Jin, S. Nanowire Lasers of Formamidinium Lead Halide Perovskites and Their Stabilized Alloys with Improved Stability. *Nano Lett.* **2016**, *16*, 1000–1008.
- (55) Zhu, H.; Fu, Y.; Meng, F.; Wu, X.; Gong, Z.; Ding, Q.; Gustafsson, M. V.; Trinh, M. T.; Jin, S.; Zhu, X.-Y. Lead Halide Perovskite Nanowire Lasers with Low Lasing Thresholds and High Quality Factors. *Nat. Mater.* **2015**, *14*, 636–642.
- (56) Sutherland, B. R.; Hoogland, S.; Adachi, M. M.; Wong, C. T. O.; Sargent, E. H. Conformal Organohalide Perovskites Enable Lasing on Spherical Resonators. *ACS Nano* **2014**, *8*, 10947–10952.
- (57) Yakunin, S.; Protesescu, L.; Krieg, F.; Bodnarchuk, M. I.; Nedelcu, G.; Humer, M.; De Luca, G.; Fiebig, M.; Heiss, W.; Kovalenko, M. V. Low-Threshold Amplified Spontaneous Emission and Lasing from Colloidal Nanocrystals of Caesium Lead Halide Perovskites. *Nat. Commun.* **2015**, *6*, 8056.
- (58) Yang, Y.; Yan, Y.; Yang, M.; Choi, S.; Zhu, K.; Luther, J. M.; Beard, M. C. Low Surface Recombination Velocity in Solution-Grown  $\text{CH}_3\text{NH}_3\text{PbBr}_3$  Perovskite Single Crystal. *Nat. Commun.* **2015**, *6*, 7961.
- (59) Yang, Y.; Ostrowski, D. P.; France, R. M.; Zhu, K.; van de Lagemaat, J.; Luther, J. M.; Beard, M. C. Observation of a Hot-Phonon Bottleneck in Lead-Iodide Perovskites. *Nat. Photonics* **2015**, *10*, 53–59.
- (60) Shi, D.; Adinolfi, V.; Comin, R.; Yuan, M.; Alarousu, E.; Buin, A.; Chen, Y.; Hoogland, S.; Rothenberger, A.; Katsiev, K.; et al. Low Trap-State Density and Long Carrier Diffusion in Organolead Trihalide Perovskite Single Crystals. *Science* **2015**, *347*, 519–522.
- (61) Brenner, T. M.; Egger, D. A.; Kronik, L.; Hodes, G.; Cahen, D. Hybrid Organic–Inorganic Perovskites: Low-Cost Semiconductors with Intriguing Charge-Transport Properties. *Nat. Rev. Mater.* **2016**, *1*, 15007.
- (62) Mitzi, D. B. Templating and Structural Engineering in Organic–Inorganic Perovskites. *J. Chem. Soc. Dalton Trans.* **2001**, 1–12.
- (63) Abdelhady, A. L.; Saidaminov, M. I.; Murali, B.; Adinolfi, V.; Voznyy, O.; Katsiev, K.; Alarousu, E.; Comin, R.; Dursun, I.; Sinatra, L.; et al. Heterovalent Dopant Incorporation for Bandgap and Type Engineering of Perovskite Crystals. *J. Phys. Chem. Lett.* **2016**, *7*, 295–301.
- (64) Mei, A.; Li, X.; Liu, L.; Ku, Z.; Liu, T.; Rong, Y.; Xu, M.; Hu, M.; Chen, J.; Yang, Y.; et al. A Hole-Conductor-Free, Fully Printable Mesoscopic Perovskite Solar Cell with High Stability. *Science* **2014**, *345*, 295–298.
- (65) Saparov, B.; Mitzi, D. B. Organic–Inorganic Perovskites: Structural Versatility for Functional Materials Design. *Chem. Rev.* **2016**, *116*, 4558–4596.
- (66) Li, C.; Lu, X.; Ding, W.; Feng, L.; Gao, Y.; Guo, Z. Formability of  $\text{ABX}_3$  ( $\text{X} = \text{F}, \text{Cl}, \text{Br}, \text{I}$ ) Halide Perovskites. *Acta Crystallogr., Sect. B: Struct. Sci.* **2008**, *64*, 702–707.
- (67) Kieslich, G.; Sun, S.; Cheetham, T. Solid-State Principles Applied to Organic–Inorganic Perovskites: New Tricks for an Old Dog. *Chem. Sci.* **2014**, *5*, 4712–4715.
- (68) Kieslich, G.; Sun, S.; Cheetham, T. An Extended Tolerance Factor Approach for Organic–Inorganic Perovskites. *Chem. Sci.* **2015**, *6*, 3430–3433.
- (69) Travis, W.; Glover, E. N. K.; Bronstein, H.; Scanlon, D. O.; Palgrave, R. G. On the Application of the Tolerance Factor to Inorganic and Hybrid Halide Perovskites: A Revised System. *Chem. Sci.* **2016**, DOI: [10.1039/C5SC04845A](https://doi.org/10.1039/C5SC04845A).
- (70) Goldschmidt, V. M. Die Gesetze Der Krystallochemie. *Naturwissenschaften* **1926**, *14*, 477–485.
- (71) Stoumpos, C. C.; Kanatzidis, M. G. The Renaissance of Halide Perovskites and Their Evolution as Emerging Semiconductors. *Acc. Chem. Res.* **2015**, *48*, 2791–2802.
- (72) Shannon, R. D. Revised Effective Ionic Radii and Systematic Studies of Interatomic Distances in Halides and Chalcogenides. *Acta Crystallogr., Sect. A: Cryst. Phys., Diffraction, Theor. Gen. Crystallogr.* **1976**, *32*, 751–767.
- (73) Cohen, B. N.; Labarca, C.; Davidson, N.; Lester, H. A. Mutations in M2 Alter the Selectivity of the Mouse Nicotinic Acetylcholine Receptor for Organic and Alkali Metal Cations. *J. Gen. Physiol.* **1992**, *100*, 373–400.
- (74) Salje, E. Characteristics of Perovskite-Related Materials [and Discussion]. *Philos. Trans. R. Soc., A* **1989**, *328*, 409–416.
- (75) Glazer, A. M. Simple Ways of Determining Perovskite Structures. *Acta Crystallogr., Sect. A: Cryst. Phys., Diffraction, Theor. Gen. Crystallogr.* **1975**, *31*, 756–762.
- (76) Stoumpos, C. C.; Malliakas, C. D.; Kanatzidis, M. G. Semiconducting Tin and Lead Iodide Perovskites with Organic Cations: Phase Transitions, High Mobilities, and Near-Infrared Photoluminescent Properties. *Inorg. Chem.* **2013**, *S2*, 9019–9038.
- (77) Li, Z.; Yang, M.; Park, J.-S.; Wei, S.-H.; Berry, J. J.; Zhu, K. Stabilizing Perovskite Structures by Tuning Tolerance Factor: Formation of Formamidinium and Cesium Lead Iodide Solid-State Alloys. *Chem. Mater.* **2016**, *28*, 284–292.
- (78) Filip, M. R.; Eperon, G. E.; Snaith, H. J.; Giustino, F. Steric Engineering of Metal–Halide Perovskites with Tunable Optical Band Gaps. *Nat. Commun.* **2014**, *5*, 5757.
- (79) Goodyear, J.; Ali, E. M.; Steigmann, G. A. Rubidium Tetrachloromanganate. *Acta Crystallogr., Sect. B: Struct. Crystallogr. Cryst. Chem.* **1977**, *33*, 2932–2933.
- (80) Mitzi, D. B.; Chondroudis, K.; Kagan, C. R. Organic–Inorganic Electronics. *IBM J. Res. Dev.* **2001**, *45*, 29–45.
- (81) Noh, J. H.; Im, S. H.; Heo, J. H.; Mandal, T. N.; Seok, S. Il. Chemical Management for Colorful, Efficient, and Stable Inorganic–Organic Hybrid Nanostructured Solar Cells. *Nano Lett.* **2013**, *13*, 1764–1769.
- (82) Protesescu, L.; Yakunin, S.; Bodnarchuk, M. I.; Krieg, F.; Caputo, R.; Hendon, C. H.; Yang, R. X.; Walsh, A.; Kovalenko, M. V. Nanocrystals of Cesium Lead Halide Perovskites ( $\text{CsPbX}_3$ ,  $\text{X} = \text{Cl}, \text{Br}$ , and  $\text{I}$ ): Novel Optoelectronic Materials Showing Bright Emission with Wide Color Gamut. *Nano Lett.* **2015**, *15*, 3692–3696.
- (83) Nedelcu, G.; Protesescu, L.; Yakunin, S.; Bodnarchuk, M. I.; Grotevent, M. J.; Kovalenko, M. V. Fast Anion-Exchange in Highly Luminescent Nanocrystals of Cesium Lead Halide Perovskites ( $\text{CsPbX}_3$ ,  $\text{X} = \text{Cl}, \text{Br}, \text{I}$ ). *Nano Lett.* **2015**, *15*, 5635–5640.
- (84) Li, G.; Ho, J. Y.-L.; Wong, M.; Kwok, H. S. Reversible Anion Exchange Reaction in Solid Halide Perovskites and Its Implication in Photovoltaics. *J. Phys. Chem. C* **2015**, *119*, 26883–26888.
- (85) Pellet, N.; Teuscher, J.; Maier, J.; Grätzel, M. Transforming Hybrid Organic–Inorganic Perovskites by Rapid Halide Exchange. *Chem. Mater.* **2015**, *27*, 2181–2188.
- (86) Akkerman, Q. a.; D’Innocenzo, V.; Accornero, S.; Scarpellini, A.; Petrozza, A.; Prato, M.; Manna, L. Tuning the Optical Properties of Cesium Lead Halide Perovskite Nanocrystals by Anion Exchange Reactions. *J. Am. Chem. Soc.* **2015**, *137*, 10276–10281.
- (87) Solis-Ibarra, D.; Smith, I. C.; Karunadasa, H. I. Post-Synthetic Halide Conversion and Selective Halogen Capture in Hybrid Perovskites. *Chem. Sci.* **2015**, *6*, 4054–4059.
- (88) Eperon, G. E.; Beck, C. E.; Snaith, H. J. Cation Exchange for Thin Film Lead Iodide Perovskite Interconversion. *Mater. Horiz.* **2016**, *3*, 63–71.
- (89) Yu, H.; Wang, F.; Xie, F.; Li, W.; Chen, J.; Zhao, N. The Role of Chlorine in the Formation Process of “ $\text{CH}_3\text{NH}_3\text{PbI}_{3-x}\text{Cl}_x$ ” Perovskite. *Adv. Funct. Mater.* **2014**, *24*, 7102–7108.
- (90) Colella, S.; Mosconi, E.; Fedeli, P.; Listorti, A.; Gazza, F.; Orlandi, F.; Ferro, P.; Besagni, T.; Rizzo, A.; Calestani, G.; et al.  $\text{MAPbI}_{3-x}\text{Cl}_x$  Mixed Halide Perovskite for Hybrid Solar Cells: The

- Role of Chloride as Dopant on the Transport and Structural Properties. *Chem. Mater.* **2013**, *25*, 4613–4618.
- (91) Unger, E. L.; Bowring, A. R.; Tassone, C. J.; Pool, V. L.; Gold-Parker, A.; Cheacharoen, R.; Stone, K. H.; Hoke, E. T.; Toney, M. F.; McGehee, M. D. Chloride in Lead Chloride-Derived Organo-Metal Halides for Perovskite-Absorber Solar Cells. *Chem. Mater.* **2014**, *26*, 7158–7165.
- (92) Pistor, P.; Borchert, J.; Fränzel, W.; Csuk, R.; Scheer, R. Monitoring the Phase Formation of Coevaporated Lead Halide Perovskite Thin Films by in Situ X-Ray Diffraction. *J. Phys. Chem. Lett.* **2014**, *5*, 3308–3312.
- (93) Williams, S. T.; Zuo, F.; Chueh, C.-C.; Liao, C.-Y.; Liang, P.-W.; Jen, A. K.-Y. Role of Chloride in the Morphological Evolution of Organo-Lead Halide Perovskite Thin Films. *ACS Nano* **2014**, *8*, 10640–10654.
- (94) Williams, S. T.; Chueh, C.; Jen, A. K.-Y. Navigating Organo-Lead Halide Perovskite Phase Space via Nucleation Kinetics toward a Deeper Understanding of Perovskite Phase Transformations and Structure-Property Relationships. *Small* **2015**, *11*, 3088–3096.
- (95) Nenon, D. P.; Christians, J. A.; Wheeler, L. M.; Blackburn, J. L.; Sanehira, E. M.; Dou, B.; Olsen, M. L.; Zhu, K.; Berry, J. J.; Luther, J. M. Structural and Chemical Evolution of Methylammonium Lead Halide Perovskites during Thermal Processing from Solution. *Energy Environ. Sci.* **2016**, DOI: 10.1039/C6EE01047D.
- (96) Mousdis, G. A.; Papavassiliou, G. C.; Raptopoulou, C. P.; Terzis, A. Preparation and Characterization of  $[H_3N(CH_2)_6NH_3]PbI_4$  and Similar Compounds with a Layered Perovskite Structure. *J. Mater. Chem.* **2000**, *10*, 515–518.
- (97) Dohner, E. R.; Jaffe, A.; Bradshaw, L. R.; Karunadasa, H. I. Intrinsic White-Light Emission from Layered Hybrid Perovskites. *J. Am. Chem. Soc.* **2014**, *136*, 13154–13157.
- (98) Clark, S. J.; Donaldson, J. D.; Harvey, J. A. Evidence for the Direct Population of Solid-State Bands by Non-Bonding Electron Pairs in Compounds of the Type  $CsM^{II}X_3$  ( $M^{II}$  = Ge, Sn, Pb; X = Cl, Br, I). *J. Mater. Chem.* **1995**, *5*, 1813–1818.
- (99) Hao, F.; Stoumpos, C. C.; Chang, R. P. H.; Kanatzidis, M. G. Anomalous Band Gap Behavior in Mixed Sn and Pb Perovskites Enables Broadening of Absorption Spectrum in Solar Cells. *J. Am. Chem. Soc.* **2014**, *136*, 8094–8099.
- (100) Ogomi, Y.; Morita, A.; Tsukamoto, S.; Saitho, T.; Fujikawa, N.; Shen, Q.; Toyoda, T.; Yoshino, K.; Pandey, S. S.; Ma, T.; et al.  $CH_3NH_3Sn_xPb_{(1-x)}I_3$  Perovskite Solar Cells Covering up to 1060 nm. *J. Phys. Chem. Lett.* **2014**, *5*, 1004–1011.
- (101) Kanhere, P.; Chakraborty, S.; Rupp, C. J.; Ahuja, R.; Chen, Z. Substitution Induced Band Structure Shape Tuning in Hybrid Perovskites ( $CH_3NH_3Pb_{1-x}Sn_xI_3$ ) for Efficient Solar Cell Applications. *RSC Adv.* **2015**, *5*, 107497–107502.
- (102) Navas, J.; Sánchez-Coronilla, A.; Gallardo, J. J.; Cruz Hernández, N.; Piñero, J. C.; Alcántara, R.; Fernández-Lorenzo, C.; De los Santos, D. M.; Aguilar, T.; Martín-Calleja, J. New Insights into Organic-Inorganic Hybrid Perovskite  $CH_3NH_3PbI_3$  Nanoparticles. An Experimental and Theoretical Study of Doping in  $Pb^{2+}$  Sites with  $Sn^{2+}$ ,  $Sr^{2+}$ ,  $Cd^{2+}$  and  $Ca^{2+}$ . *Nanoscale* **2015**, *7*, 6216–6229.
- (103) Giorgi, G.; Fujisawa, J.; Segawa, H.; Yamashita, K. The Cation Role in Structural and Electronic Properties of 3D Organic-Inorganic Perovskite Halides: A DFT Analysis. *J. Phys. Chem. C* **2014**, *118*, 12176–12183.
- (104) Choi, H.; Jeong, J.; Kim, H.-B.; Kim, S.; Walker, B.; Kim, G.-H.; Kim, J. Y. Cesium-Doped Methylammonium Lead Iodide Perovskite Light Absorber for Hybrid Solar Cells. *Nano Energy* **2014**, *7*, 80–85.
- (105) Pellet, N.; Gao, P.; Gregori, G.; Yang, T.-Y.; Nazeeruddin, M. K.; Maier, J.; Grätzel, M. Mixed-Organic-Cation Perovskite Photovoltaics for Enhanced Solar-Light Harvesting. *Angew. Chem., Int. Ed.* **2014**, *53*, 3151–3157.
- (106) Jeon, N. J.; Noh, J. H.; Yang, W. S.; Kim, Y. C.; Ryu, S.; Seo, J.; Seok, S. I. Compositional Engineering of Perovskite Materials for High-Performance Solar Cells. *Nature* **2015**, *517*, 476–480.
- (107) Yang, W. S.; Noh, J. H.; Jeon, N. J.; Kim, Y. C.; Ryu, S.; Seo, J.; Seok, S. I. High-Performance Photovoltaic Perovskite Layers Fabricated through Intramolecular Exchange. *Science* **2015**, *348*, 1234–1237.
- (108) Lee, J. W.; Seol, D. J.; Cho, A. N.; Park, N. G. High-Efficiency Perovskite Solar Cells Based on the Black Polymorph of  $H-(NH_2)_2PbI_3$ . *Adv. Mater.* **2014**, *26*, 4991–4998.
- (109) Binek, A.; Hanusch, F. C.; Docampo, P.; Bein, T. Stabilization of the Trigonal High-Temperature Phase of Formamidinium Lead Iodide. *J. Phys. Chem. Lett.* **2015**, *6*, 1249–1253.
- (110) Smith, I. C.; Hoke, E. T.; Solis-Ibarra, D.; McGehee, M. D.; Karunadasa, H. I. A Layered Hybrid Perovskite Solar-Cell Absorber with Enhanced Moisture Stability. *Angew. Chem.* **2014**, *126*, 11414–11417.
- (111) Hachmann, J.; Olivares-Amaya, R.; Atahan-Evrenk, S.; Amador-Bedolla, C.; Sánchez-Carrera, R. S.; Gold-Parker, A.; Vogt, L.; Brockway, A. M.; Aspuru-Guzik, A. The Harvard Clean Energy Project: Large-Scale Computational Screening and Design of Organic Photovoltaics on the World Community Grid. *J. Phys. Chem. Lett.* **2011**, *2*, 2241–2251.
- (112) Ungersboeck, E.; Dhar, S.; Karlowatz, G.; Sverdlov, V.; Kosina, H.; Selberherr, S. The Effect of General Strain on the Band Structure and Electron Mobility of Silicon. *IEEE Trans. Electron Devices* **2007**, *54*, 2183–2190.
- (113) Fröhlich, D.; Heidrich, K.; Künzel, H.; Trendel, G.; Treusch, J. Cesium-Trihalogen-Plumbates a New Class of Ionic Semiconductors. *J. Lumin.* **1979**, *18*–19, 385–388.
- (114) Koutselas, I. B.; Ducasse, L.; Papavassiliou, G. C. Electronic Properties of Three- and Low-Dimensional Semiconducting Materials with Pb Halide and Sn Halide Units. *J. Phys.: Condens. Matter* **1996**, *8*, 1217–1227.
- (115) Parry, D. E.; Tricker, M. J.; Donaldson, J. D. The Electronic Structure of  $CsSnBr_3$  and Related Trihalides; Studies Using XPS and Band Theory. *J. Solid State Chem.* **1979**, *28*, 401–408.
- (116) Lefebvre, I.; Lippens, P. E.; Lannoo, M.; Allan, G. Band Structure of  $CsSnBr_3$ . *Phys. Rev. B: Condens. Matter Mater. Phys.* **1990**, *42*, 9174–9177.
- (117) Huang, L. Y.; Lambrecht, W. R. L. Electronic Band Structure, Phonons, and Exciton Binding Energies of Halide Perovskites  $CsSnCl_3$ ,  $CsSnBr_3$ , and  $CsSnI_3$ . *Phys. Rev. B: Condens. Matter Mater. Phys.* **2013**, *88*, 165203.
- (118) Umari, P.; Mosconi, E.; De Angelis, F. Relativistic GW Calculations on  $CH_3NH_3PbI_3$  and  $CH_3NH_3SnI_3$  Perovskites for Solar Cell Applications. *Sci. Rep.* **2014**, *4*, 4467.
- (119) Brivio, F.; Butler, K. T.; Walsh, A.; van Schilfgaarde, M. Relativistic Quasiparticle Self-Consistent Electronic Structure of Hybrid Halide Perovskite Photovoltaic Absorbers. *Phys. Rev. B: Condens. Matter Mater. Phys.* **2014**, *89*, 155204.
- (120) Chiarella, F.; Zappettini, A.; Licci, F.; Borriello, I.; Cantele, G.; Ninno, D.; Cassinese, A.; Vaglio, R. Combined Experimental and Theoretical Investigation of Optical, Structural, and Electronic Properties of  $CH_3NH_3SnX_3$  Thin Films (X = Cl, Br). *Phys. Rev. B: Condens. Matter Mater. Phys.* **2008**, *77*, 045129.
- (121) Kepenekian, M.; Robles, R.; Katan, C.; Saporì, D.; Pedesseau, L.; Even, J. Rashba and Dresselhaus Effects in Hybrid Organic-Inorganic Perovskites: From Basics to Devices. *ACS Nano* **2015**, *9*, 11557–11567.
- (122) Kim, M.; Im, J.; Freeman, A. J.; Ihm, J.; Jin, H. Switchable  $S = 1/2$  and  $J = 1/2$  Rashba Bands in Ferroelectric Halide Perovskites. *Proc. Natl. Acad. Sci. U. S. A.* **2014**, *111*, 6900–6904.
- (123) Even, J. Pedestrian Guide to Symmetry Properties of the Reference Cubic Structure of 3D All-Inorganic and Hybrid Perovskites. *J. Phys. Chem. Lett.* **2015**, *6*, 2238–2242.
- (124) Amat, A.; Mosconi, E.; Ronca, E.; Quartì, C.; Umari, P.; Nazeeruddin, M. K.; Grätzel, M.; De Angelis, F. Cation-Induced Band-Gap Tuning in Organohalide Perovskites: Interplay of Spin-Orbit Coupling and Octahedra Tilting. *Nano Lett.* **2014**, *14*, 3608–3616.
- (125) Even, J.; Pedesseau, L.; Jancu, J. M.; Katan, C. DFT and k-p Modelling of the Phase Transitions of Lead and Tin Halide

- Perovskites for Photovoltaic Cells. *Phys. Status Solidi RRL* **2014**, *8*, 31–35.
- (126) Stroppa, A.; Di Sante, D.; Barone, P.; Bokdam, M.; Kresse, G.; Franchini, C.; Whangbo, M.-H.; Picozzi, S. Tunable Ferroelectric Polarization and Its Interplay with Spin–orbit Coupling in Tin Iodide Perovskites. *Nat. Commun.* **2014**, *5*, 5900.
- (127) Umebayashi, T.; Asai, K.; Kondo, T.; Nakao, A. Electronic Structures of Lead Iodide Based Low-Dimensional Crystals. *Phys. Rev. B: Condens. Matter Mater. Phys.* **2003**, *67*, 155405.
- (128) Brivio, F.; Walker, A. B.; Walsh, A. Structural and Electronic Properties of Hybrid Perovskites for High-Efficiency Thin-Film Photovoltaics from First-Principles. *APL Mater.* **2013**, *1*, 042111.
- (129) Chang, Y. H.; Park, C. H.; Matsuishi, K. First-Principles Study of the Structural and the Electronic Properties of the Lead-Halide-Based Inorganic-Organic Perovskites  $(\text{CH}_3\text{NH}_3)\text{PbX}_3$  and  $\text{CsPbX}_3$  ( $X = \text{Cl}, \text{Br}, \text{I}$ ). *J. Korean Phys. Soc.* **2004**, *44*, 889–893.
- (130) Borriello, I.; Cantele, G.; Ninno, D. Ab Initio Investigation of Hybrid Organic-Inorganic Perovskites Based on Tin Halides. *Phys. Rev. B: Condens. Matter Mater. Phys.* **2008**, *77*, 235214.
- (131) Vincent, B. R.; Robertson, K. N.; Cameron, T. S.; Knop, O. Alkylammonium Lead Halides. Part 1. Isolated  $\text{PbI}_6^{4-}$  Ions in  $(\text{CH}_3\text{NH}_3)_4\text{PbI}_6 \bullet 2\text{H}_2\text{O}$ . *Can. J. Chem.* **1987**, *65*, 1042–1046.
- (132) Matsuishi, K.; Ishihara, T.; Onari, S.; Chang, Y. H.; Park, C. H. Optical Properties and Structural Phase Transitions of Lead-Halide Based Inorganic-Organic 3D and 2D Perovskite Semiconductors under High Pressure. *Phys. Status Solidi B* **2004**, *241*, 3328–3333.
- (133) Knutson, J. L.; Martin, J. D.; Mitzi, D. B. Tuning the Band Gap in Hybrid Tin Iodide Perovskite Semiconductors Using Structural Templating. *Inorg. Chem.* **2005**, *44*, 4699–4705.
- (134) Stoumpos, C. C.; Frazer, L.; Clark, D. J.; Kim, Y. S.; Rhim, S. H.; Freeman, A. J.; Ketterson, J. B.; Jang, J. I.; Kanatzidis, M. G. Hybrid Germanium Iodide Perovskite Semiconductors: Active Lone Pairs, Structural Distortions, Direct and Indirect Energy Gaps, and Strong Nonlinear Optical Properties. *J. Am. Chem. Soc.* **2015**, *137*, 6804–6819.
- (135) Motta, C.; El-Mellouhi, F.; Kais, S.; Tabet, N.; Alharbi, F.; Sanvito, S. Revealing the Role of Organic Cations in Hybrid Halide Perovskite  $\text{CH}_3\text{NH}_3\text{PbI}_3$ . *Nat. Commun.* **2015**, *6*, 7026.
- (136) Miyata, A.; Mitioglu, A.; Plochocka, P.; Portugall, O.; Wang, J. T.-W.; Stranks, S. D.; Snaith, H. J.; Nicholas, R. J. Direct Measurement of the Exciton Binding Energy and Effective Masses for Charge Carriers in Organic-Inorganic Tri-Halide Perovskites. *Nat. Phys.* **2015**, *11*, 582–587.
- (137) Takahashi, Y.; Hasegawa, H.; Takahashi, Y.; Inabe, T. Hall Mobility in Tin Iodide Perovskite  $\text{CH}_3\text{NH}_3\text{SnI}_3$ : Evidence for a Doped Semiconductor. *J. Solid State Chem.* **2013**, *205*, 39–43.
- (138) Mitzi, D. B.; Feild, C. A.; Schlesinger, Z.; Laibowitz, R. B. Transport, Optical, and Magnetic Properties of the Conducting Halide Perovskite  $\text{CH}_3\text{NH}_3\text{SnI}_3$ . *J. Solid State Chem.* **1995**, *114*, 159–163.
- (139) Xing, G.; Mathews, N.; Sun, S.; Lim, S. S.; Lam, Y. M.; Mhaisalkar, S.; Sum, T. C.; Grätzel, M.; Mhaisalkar, S.; Sum, T. C. Long-Range Balanced Electron- and Hole-Transport Lengths in Organic-Inorganic  $\text{CH}_3\text{NH}_3\text{PbI}_3$ . *Science* **2013**, *342*, 344–347.
- (140) Stranks, S. D.; Eperon, G. E.; Grancini, G.; Menelaou, C.; Alcocer, M. J. P.; Leijtens, T.; Herz, L. M.; Petrozza, A.; Snaith, H. J. Electron-Hole Diffusion Lengths Exceeding 1 Micrometer in an Organometal Trihalide Perovskite Absorber. *Science* **2013**, *342*, 341–344.
- (141) Wen, X.; Ho-Baillie, A.; Huang, S.; Sheng, R.; Chen, S.; Ko, H.; Green, M. A. Mobile Charge-Induced Fluorescence Intermittency in Methylammonium Lead Bromide Perovskite. *Nano Lett.* **2015**, *15*, 4644–4649.
- (142) Edri, E.; Kirmayer, S.; Henning, A.; Mukhopadhyay, S.; Gartsman, K.; Rosenwaks, Y.; Hodes, G.; Cahen, D. Why Lead Methylammonium Tri-Iodide Perovskite-Based Solar Cells Require a Mesoporous Electron Transporting Scaffold (but Not Necessarily a Hole Conductor). *Nano Lett.* **2014**, *14*, 1000–1004.
- (143) Edri, E.; Kirmayer, S.; Mukhopadhyay, S.; Gartsman, K.; Hodes, G.; Cahen, D. Elucidating the Charge Carrier Separation and Working Mechanism of  $\text{CH}_3\text{NH}_3\text{PbI}_{(3-x)}\text{Cl}_x$  Perovskite Solar Cells. *Nat. Commun.* **2014**, *5*, 3461.
- (144) Samiee, M.; Konduri, S.; Ganapathy, B.; Kottokkaran, R.; Abbas, H. A.; Kitahara, A.; Joshi, P.; Zhang, L.; Noack, M.; Dalal, V. Defect Density and Dielectric Constant in Perovskite Solar Cells. *Appl. Phys. Lett.* **2014**, *105*, 153502.
- (145) Lee, M. M.; Teuscher, J.; Miyasaka, T.; Murakami, T. N.; Snaith, H. J. Efficient Hybrid Solar Cells Based on Meso-Superstructured Organometal Halide Perovskites. *Science* **2012**, *338*, 643–647.
- (146) Ke, W.; Fang, G.; Wan, J.; Tao, H.; Liu, Q.; Xiong, L.; Qin, P.; Wang, J.; Lei, H.; Yang, G.; et al. Efficient Hole-Blocking Layer-Free Planar Halide Perovskite Thin-Film Solar Cells. *Nat. Commun.* **2015**, *6*, 6700.
- (147) Seo, J.; Park, S.; Chan Kim, Y.; Jeon, N. J.; Noh, J. H.; Yoon, S. C.; Seok, S. Il. Benefits of Very Thin PCBM and LiF Layers for Solution-Processed p-i-n Perovskite Solar Cells. *Energy Environ. Sci.* **2014**, *7*, 2642–2646.
- (148) Yin, W.-J.; Yang, J.-H.; Kang, J.; Yan, Y.; Wei, S.-H. Halide Perovskite Materials for Solar Cells: A Theoretical Review. *J. Mater. Chem. A* **2015**, *3*, 8926–8942.
- (149) Even, J.; Pedesseau, L.; Dupertuis, M.-A.; Jancu, J.-M.; Katan, C. Electronic Model for Self-Assembled Hybrid Organic/perovskite Semiconductors: Reverse Band Edge Electronic States Ordering and Spin-Orbit Coupling. *Phys. Rev. B: Condens. Matter Mater. Phys.* **2012**, *86*, 205301.
- (150) Gray, A. X.; Papp, C.; Ueda, S.; Balke, B.; Yamashita, Y.; Plucinski, L.; Minár, J.; Braun, J.; Ylvisaker, E. R.; Schneider, C. M.; et al. Probing Bulk Electronic Structure with Hard X-Ray Angle-Resolved Photoemission. *Nat. Mater.* **2011**, *10*, 759–764.
- (151) Yan, Y.; Wang, Q.; Shu, W.; Jia, Z.; Ren, X.; Zhang, X.; Huang, Y. First-Principle Study of the Electronic and Optical Properties of  $\text{BiInGaAs}$  Quaternary Alloy Lattice-Matched to GaAs. *Phys. B* **2012**, *407*, 4570–4573.
- (152) Bardeen, J.; Shockley, W. Deformation Potentials and Mobilities in Non-Polar Crystals. *Phys. Rev.* **1950**, *80*, 72–80.
- (153) Frost, J. M.; Butler, K. T.; Brivio, F.; Hendon, C. H.; van Schilfgaarde, M.; Walsh, A. Atomistic Origins of High-Performance in Hybrid Halide Perovskite Solar Cells. *Nano Lett.* **2014**, *14*, 2584–2590.
- (154) Dittrich, T.; Awino, C.; Prajontgat, P.; Rech, B.; Lux-Steiner, M. C. Temperature Dependence of the Band Gap of  $\text{CH}_3\text{NH}_3\text{PbI}_3$  Stabilized with PMMA: A Modulated Surface Photovoltage Study. *J. Phys. Chem. C* **2015**, *119*, 23968–23972.
- (155) Maintz, S.; Deringer, V. L.; Tchougréeff, A. L.; Dronkowski, R. Analytic Projection from Plane-Wave and PAW Wavefunctions and Application to Chemical-Bonding Analysis in Solids. *J. Comput. Chem.* **2013**, *34*, 2557–2567.
- (156) Yu, C.; Chen, Z.; Wang, J. J.; Pfenninger, W.; Vockic, N.; Kenney, J. T.; Shum, K. Temperature Dependence of the Band Gap of Perovskite Semiconductor Compound  $\text{CsSnI}_3$ . *J. Appl. Phys.* **2011**, *110*, 063526.
- (157) Walsh, A.; Payne, D. J.; Egddell, R. G.; Watson, G. W. Stereochemistry of Post-Transition Metal Oxides: Revision of the Classical Lone Pair Model. *Chem. Soc. Rev.* **2011**, *40*, 4455–4463.
- (158) Pyykko, P. Relativistic Effects in Structural Chemistry. *Chem. Rev.* **1988**, *88*, 563–594.
- (159) Gillespie, R. J.; Nyholm, R. S. Inorganic Stereochemistry. *Q. Rev., Chem. Soc.* **1957**, *11*, 339–380.
- (160) Wang, S.; Mitzi, D. B.; Feild, C. A.; Guloy, A. Synthesis and Characterization of  $[\text{NH}_2\text{C}(=\text{O})\text{NH}_2]_3\text{MI}_5$  ( $\text{M} = \text{Sn}, \text{Pb}$ ): Stereocchemical Activity in Divalent Tin and Lead Halides Containing Single [110] Perovskite Sheets. *J. Am. Chem. Soc.* **1995**, *117*, 5297–5302.
- (161) Swainson, I.; Chi, L.; Her, J. H.; Cranswick, L.; Stephens, P.; Winkler, B.; Wilson, D. J.; Milman, V. Orientational Ordering, Tilting and Lone-Pair Activity in the Perovskite Methylammonium Tin Bromide,  $\text{CH}_3\text{NH}_3\text{SnBr}_3$ . *Acta Crystallogr., Sect. B: Struct. Sci.* **2010**, *66*, 422–429.

- (162) Fütterer, K.; Depmeier, W.; Petříček, V. The Low-Temperature Phase Transition Sequence of the Halide Perovskite Tetramethylammonium Trichlorogermanate(II) and the Structure of Its Incommensurately Modulated  $\delta$ -Phase. *Acta Crystallogr., Sect. B: Struct. Sci.* **1995**, *51*, 768–779.
- (163) Yamada, K. Chloride Ion Conductor  $\text{CH}_3\text{NH}_3\text{GeCl}_3$  Studied by Rietveld Analysis of X-Ray Diffraction and  $^{35}\text{Cl}$  NMR. *Solid State Ionics* **1995**, *79*, 152–157.
- (164) Winkler, B.; Milman, V.; Lee, M.-H. Pressure-Induced Change of the Stereochemical Activity of a Lone Electron Pair. *J. Chem. Phys.* **1998**, *108*, 5506–5509.
- (165) Christensen, A. N.; Rasmussen, S. E.; Karvonen, P.; Kjær, A.; Shapiro, R. H.; Westerdahl, A. A Ferroelectric Chloride of Perowskite Type. Crystal Structure of  $\text{CsGeCl}_3$ . *Acta Chem. Scand.* **1965**, *19*, 421–428.
- (166) Papavassiliou, G. C.; Koutselas, I. B. Structural, Optical and Related Properties of Some Natural Three- and Lower-Dimensional Semiconductor Systems. *Synth. Met.* **1995**, *71*, 1713–1714.
- (167) Mosconi, E.; Amat, A.; Nazeeruddin, K.; Angelis, F. De; Nazeeruddin, M. K.; Grätzel, M.; De Angelis, F. First-Principles Modeling of Mixed Halide Organometal Perovskites for Photovoltaic Applications. *J. Phys. Chem. C* **2013**, *117*, 13902–13913.
- (168) Christians, J. A.; Miranda Herrera, P. A.; Kamat, P. V. Transformation of the Excited State and Photovoltaic Efficiency of  $\text{CH}_3\text{NH}_3\text{PbI}_3$  Perovskite upon Controlled Exposure to Humidified Air. *J. Am. Chem. Soc.* **2015**, *137*, 1530–1538.
- (169) Hong, X.; Ishihara, T.; Nurmiikko, A. V. Photoconductivity and Electroluminescence in Lead Iodide Based Natural Quantum Well Structures. *Solid State Commun.* **1992**, *84*, 657–661.
- (170) Sichert, J. A.; Tong, Y.; Mutz, N.; Vollmer, M.; Fischer, S.; Milowska, K. Z.; García Cortadella, R.; Nickel, B.; Cardenas-Daw, C.; Stolarczyk, J. K.; et al. Quantum Size Effect in Organometal Halide Perovskite Nanoplatelets. *Nano Lett.* **2015**, *15*, 6521–6527.
- (171) Papavassiliou, G. C. Three- and Low-Dimensional Inorganic Semiconductors. *Prog. Solid State Chem.* **1997**, *25*, 125–270.
- (172) Kikuchi, K.; Takeoka, Y.; Rikukawa, M.; Sanui, K. Structure and Optical Properties of Lead Iodide Based Two-Dimensional Perovskite Compounds Containing Fluorophenethylamines. *Curr. Appl. Phys.* **2004**, *4*, 599–602.
- (173) Dammak, T.; Koubaa, M.; Boukhechdaden, K.; Bougzhala, H.; Mlayah, A.; Abid, Y. Two-Dimensional Excitons and Photoluminescence Properties of the Organic/Inorganic ( $4\text{-FC}_6\text{H}_4\text{C}_2\text{H}_4\text{NH}_3\right)_2[\text{PbI}_4]$ ) Nanomaterial. *J. Phys. Chem. C* **2009**, *113*, 19305–19309.
- (174) Wulfberg, G. *Inorganic Chemistry*; University Science Books: Sausalito, 2000.
- (175) Ehrenreich, H. Band Structure and Transport Properties of Some 3–5 Compounds. *J. Appl. Phys.* **1961**, *32*, 2155–2166.
- (176) Tanaka, K.; Takahashi, T.; Ban, T.; Kondo, T.; Uchida, K.; Miura, N. Comparative Study on the Excitons in Lead-Halide-Based Perovskite-Type Crystals  $\text{CH}_3\text{NH}_3\text{PbBr}_3$   $\text{CH}_3\text{NH}_3\text{PbI}_3$ . *Solid State Commun.* **2003**, *127*, 619–623.
- (177) Even, J.; Pedesseau, L.; Jancu, J.-M.; Katan, C. Importance of Spin-orbit Coupling in Hybrid Organic/inorganic Perovskites for Photovoltaic Applications. *J. Phys. Chem. Lett.* **2013**, *4*, 2999–3005.
- (178) Galkowski, K.; Mitigölu, A.; Miyata, A.; Plochocka, P.; Portugall, O.; Eperon, G. E.; Wang, J. T.-W.; Stergiopoulos, T.; Stranks, S. D.; Snaith, H. J.; et al. Determination of the Exciton Binding Energy and Effective Masses for Methylammonium and Formamidinium Lead Tri-Halide Perovskite Semiconductors. *Energy Environ. Sci.* **2016**, *9*, 962–970.
- (179) Glazer, A. M. The Classification of Tilted Octahedra in Perovskites. *Acta Crystallogr., Sect. B: Struct. Crystallogr. Cryst. Chem.* **1972**, *28*, 3384–3392.
- (180) Weller, M. T.; Weber, O. J.; Henry, P. F.; Di Pumbo, A. M.; Hansen, T. C. Complete Structure and Cation Orientation in the Perovskite Photovoltaic Methylammonium Lead Iodide between 100 and 352 K. *Chem. Commun.* **2015**, *51*, 4180–4183.
- (181) Onoda-Yamamoto, N.; Matsuo, T.; Suga, H. Dielectric Study of  $\text{CH}_3\text{NH}_3\text{PbX}_3$  ( $X = \text{Cl}, \text{Br}, \text{I}$ ). *J. Phys. Chem. Solids* **1992**, *53*, 935–939.
- (182) Wehrenfennig, C.; Liu, M.; Snaith, H. J.; Johnston, M. B.; Herz, L. M. Charge Carrier Recombination Channels in the Low-Temperature Phase of Organic-Inorganic Lead Halide Perovskite Thin Films. *APL Mater.* **2014**, *2*, 081513.
- (183) D’Innocenzo, V.; Grancini, G.; Alcocer, M. J. P.; Kandada, A. R. S.; Stranks, S. D.; Lee, M. M.; Lanzani, G.; Snaith, H. J.; Petrozza, A. Excitons versus Free Charges in Organo-Lead Tri-Halide Perovskites. *Nat. Commun.* **2014**, *5*, 3586.
- (184) Sestu, N.; Cadelano, M.; Sarritzu, V.; Chen, F.; Marongiu, D.; Piras, R.; Mainas, M.; Quochi, F.; Saba, M.; Mura, A.; et al. Absorption F-Sum Rule for the Exciton Binding Energy in Methylammonium Lead Halide Perovskites. *J. Phys. Chem. Lett.* **2015**, *6*, 4566–4572.
- (185) Onoda-Yamamoto, N.; Matsuo, T.; Suga, H. Calorimetric and IR Spectroscopic Studies of Phase Transitions in Methylammonium Trihalogenoplumbates (II). *J. Phys. Chem. Solids* **1990**, *51*, 1383–1395.
- (186) Leguy, A. M. A.; Frost, J. M.; McMahon, A. P.; Sakai, V. G.; Kochelmann, W.; Law, C.; Li, X.; Foglia, F.; Walsh, A.; O'Regan, B. C.; et al. The Dynamics of Methylammonium Ions in Hybrid organic-Inorganic Perovskite Solar Cells. *Nat. Commun.* **2015**, *6*, 7124.
- (187) Poglitsch, A.; Weber, D. Dynamic Disorder in Methylammoniumtrihalogenoplumbates (II) Observed by Millimeter-Wave Spectroscopy. *J. Chem. Phys.* **1987**, *87*, 6373–6378.
- (188) Bakulin, A. A.; Selig, O.; Bakker, H. J.; Rezus, Y. L. A.; Müller, C.; Glaser, T.; Lovrincic, R.; Sun, Z.; Chen, Z.; Walsh, A.; et al. Real-Time Observation of Organic Cation Reorientation in Methylammonium Lead Iodide Perovskites. *J. Phys. Chem. Lett.* **2015**, *6*, 3663–3669.
- (189) Even, J.; Pedesseau, L.; Katan, C. Analysis of Multivalley and Multibandgap Absorption and Enhancement of Free Carriers Related to Exciton Screening in Hybrid Perovskites. *J. Phys. Chem. C* **2014**, *118*, 11566–11572.
- (190) Kim, H.-S.; Im, S. H.; Park, N. Organolead Halide Perovskite: New Horizons in Solar Cell Research. *J. Phys. Chem. C* **2014**, *118*, 5615–5625.
- (191) Hirasawa, M.; Ishihara, T.; Goto, T.; Uchida, K.; Miura, N. Magnetoabsorption of the Lowest Exciton in Perovskite-Type Compound  $(\text{CH}_3\text{NH}_3)\text{PbI}_3$ . *Phys. B* **1994**, *201*, 427–430.
- (192) Yin, W.-J.; Shi, T.; Yan, Y. Unique Properties of Halide Perovskites as Possible Origins of the Superior Solar Cell Performance. *Adv. Mater.* **2014**, *26*, 4653–4658.
- (193) Shirayama, M.; Kadokami, H.; Miyadera, T.; Sugita, T.; Tamakoshi, M.; Kato, M.; Fujiseki, T.; Murata, D.; Hara, S.; Murakami, T. N.; et al. Optical Transitions in Hybrid Perovskite Solar Cells: Ellipsometry, Density Functional Theory, and Quantum Efficiency Analyses for  $\text{CH}_3\text{NH}_3\text{PbI}_3$ . *Phys. Rev. Appl.* **2016**, *5*, 014012.
- (194) Sun, S.; Salim, T.; Mathews, N.; Duchamp, M.; Boothroyd, C.; Xing, G.; Sum, T. C.; Lam, Y. M. The Origin of High Efficiency in Low-Temperature Solution-Processable Bilayer Organometal Halide Hybrid Solar Cells. *Energy Environ. Sci.* **2014**, *7*, 399–407.
- (195) Ball, J. M.; Stranks, S. D.; Hörrnertner, M. T.; Hüttner, S.; Zhang, W.; Crossland, E. J. W.; Ramirez, I.; Riede, M.; Johnston, M. B.; Friend, R. H.; et al. Optical Properties and Limiting Photocurrent of Thin-Film Perovskite Solar Cells. *Energy Environ. Sci.* **2015**, *8*, 602–609.
- (196) Looper, P.; Stuckelberger, M.; Niesen, B.; Werner, J.; Filipic, M.; Moon, S.-J.; Yum, J.-H.; Topic, M.; De Wolf, S.; Ballif, C. Complex Refractive Index Spectra of  $\text{CH}_3\text{NH}_3\text{PbI}_3$  Perovskite Thin Films Determined by Spectroscopic Ellipsometry and Spectrophotometry. *J. Phys. Chem. Lett.* **2015**, *6*, 66–71.
- (197) Lin, Q.; Armin, A.; Nagiri, R. C. R.; Burn, P. L.; Meredith, P. Electro-Optics of Perovskite Solar Cells. *Nat. Photonics* **2014**, *9*, 106–112.
- (198) Park, J.-S.; Choi, S.; Yan, Y.; Yang, Y.; Luther, J. M.; Wei, S.-H.; Parilla, P.; Zhu, K. Electronic Structure and Optical Properties of  $\alpha\text{-CH}_3\text{NH}_3\text{PbBr}_3$  Perovskite Single Crystal. *J. Phys. Chem. Lett.* **2015**, *6*, 4304–4308.

- (199) Casey, H. C.; Sell, D. D.; Wecht, K. W. Concentration Dependence of the Absorption Coefficient for n- and p-type GaAs between 1.3 and 1.6 eV. *J. Appl. Phys.* **1975**, *46*, 250.
- (200) Leguy, A.; Hu, Y.; Campoy-Quiles, M.; Alonso, M. I.; Weber, O. J.; Azarhoosh, P.; van Schilfgaarde, M.; Weller, M. T.; Bein, T.; Nelson, J.; et al. The Reversible Hydration of  $\text{CH}_3\text{NH}_3\text{PbI}_3$  in Films, Single Crystals and Solar Cells. *Chem. Mater.* **2015**, *27*, 3397–3407.
- (201) Manser, J. S.; Saidaminov, M. I.; Christians, J. A.; Bakr, O. M.; Kamat, P. V. Making and Breaking of Lead Halide Perovskites. *Acc. Chem. Res.* **2016**, *49*, 330–338.
- (202) Mosconi, E.; Azpiroz, J. M.; De Angelis, F. Ab Initio Molecular Dynamics Simulations of Methylammonium Lead Iodide Perovskite Degradation by Water. *Chem. Mater.* **2015**, *27*, 4885–4892.
- (203) Urbach, F. The Long-Wavelength Edge of Photographic Sensitivity and of the Electronic Absorption of Solids. *Phys. Rev.* **1953**, *92*, 1324.
- (204) Sadhanala, A.; Deschler, F.; Thomas, T. H.; Dutton, S. E.; Goedel, K. C.; Hanusch, F. C.; Lai, M. L.; Steiner, U.; Bein, T.; Docampo, P.; et al. Preparation of Single-Phase Films of  $\text{CH}_3\text{NH}_3\text{Pb}(\text{I}_{1-x}\text{Br}_x)_3$  with Sharp Optical Band Edges. *J. Phys. Chem. Lett.* **2014**, *5*, 2501–2505.
- (205) De Wolf, S.; Holovsky, J.; Moon, S.-J.; Löper, P.; Niesen, B.; Ledinsky, M.; Haug, F.-J.; Yum, J.-H.; Ballif, C. Organometallic Halide Perovskites: Sharp Optical Absorption Edge and Its Relation to Photovoltaic Performance. *J. Phys. Chem. Lett.* **2014**, *5*, 1035–1039.
- (206) Eperon, G. E.; Stranks, S. D.; Menelaou, C.; Johnston, M. B.; Herz, L. M.; Snaith, H. J. Formamidinium Lead Trihalide: A Broadly Tunable Perovskite for Efficient Planar Heterojunction Solar Cells. *Energy Environ. Sci.* **2014**, *7*, 982–988.
- (207) Rau, U. Reciprocity Relation between Photovoltaic Quantum Efficiency and Electroluminescent Emission of Solar Cells. *Phys. Rev. B: Condens. Matter Mater. Phys.* **2007**, *76*, 085303.
- (208) Tvingstedt, K.; Malinkiewicz, O.; Baumann, A.; Deibel, C.; Snaith, H. J.; Dyakonov, V.; Bolink, H. J. Radiative Efficiency of Lead Iodide Based Perovskite Solar Cells. *Sci. Rep.* **2014**, *4*, 6071.
- (209) Sutter-Fella, C. M.; Li, Y.; Amani, M.; Ager, J. W.; Toma, F. M.; Yablonovitch, E.; Sharp, I. D.; Javey, A. High Photoluminescence Quantum Yield in Band Gap Tunable Bromide Containing Mixed Halide Perovskites. *Nano Lett.* **2016**, *16*, 800–806.
- (210) Miller, O. D.; Yablonovitch, E.; Kurtz, S. R. Strong Internal and External Luminescence as Solar Cells Approach the Shockley-Queisser Limit. *IEEE J. Photovoltaics* **2012**, *2*, 303–311.
- (211) Coutts, T. J.; Emery, K. A.; Ward, J. S. Modeled Performance of Polycrystalline Thin-Film Tandem Solar Cells. *Prog. Photovoltaics* **2002**, *10*, 195–203.
- (212) Hoke, E. T.; Slotcavage, D. J.; Dohner, E. R.; Bowring, A. R.; Karunadasa, H. I.; McGehee, M. D. Reversible Photo-Induced Trap Formation in Mixed-Halide Hybrid Perovskites for Photovoltaics. *Chem. Sci.* **2015**, *6*, 613–617.
- (213) Rehman, W.; Milot, R. L.; Eperon, G. E.; Wehrenfennig, C.; Boland, J. L.; Snaith, H. J.; Johnston, M. B.; Herz, L. M. Charge-Carrier Dynamics and Mobilities in Formamidinium Lead Mixed-Halide Perovskites. *Adv. Mater.* **2015**, *27*, 7938–7944.
- (214) Shimizu, M.; Fujisawa, J.-I.; Ishii-Hayase, J. Influence of Dielectric Confinement on Excitonic Nonlinearity in Inorganic-Organic Layered Semiconductors. *Phys. Rev. B: Condens. Matter Mater. Phys.* **2005**, *71*, 205306.
- (215) Kitazawa, N.; Watanabe, Y. Optical Properties of Natural Quantum-Well Compounds  $(\text{C}_6\text{H}_5\text{C}_n\text{H}_{2n}-\text{NH}_3)_2\text{PbBr}_4$  ( $n = 1-4$ ). *J. Phys. Chem. Solids* **2010**, *71*, 797–802.
- (216) Kitazawa, N.; Yaemponga, D.; Aono, M.; Watanabe, Y. Optical Properties of Organic-Inorganic Hybrid Films Prepared by the Two-Step Growth Process. *J. Lumin.* **2009**, *129*, 1036–1041.
- (217) Tanaka, K.; Takahashi, T.; Kondo, T.; Umeda, K.; Ema, K.; Umebayashi, T.; Asai, K.; Uchida, K.; Miura, N. Electronic and Excitonic Structures of Inorganic-Organic Perovskite-Type Quantum-Well Crystal  $(\text{C}_4\text{H}_9\text{NH}_3)_2\text{PbBr}_4$ . *Japanese J. Appl. Physics, Part 1 Regul. Pap. Short Notes Rev. Pap.* **2005**, *44*, 5923–5932.
- (218) Goto, T.; Makino, H.; Yao, T.; Chia, C. H.; Makino, T.; Segawa, Y.; Mousdis, G. A.; Papavassiliou, G. C. Localization of Triplet Excitons and Biexcitons in the Two-Dimensional Semiconductor  $(\text{CH}_3\text{C}_6\text{H}_4\text{CH}_2\text{NH}_3)_2\text{PbBr}_4$ . *Phys. Rev. B: Condens. Matter Mater. Phys.* **2006**, *73*, 115206.
- (219) Kitazawa, N.; Aono, M.; Watanabe, Y. Synthesis and Luminescence Properties of Lead-Halide Based Organic-inorganic Layered Perovskite Compounds  $(\text{C}_n\text{H}_{2n+1}\text{NH}_3)_2\text{PbI}_4$  ( $n = 4, 5, 7, 8$  and  $9$ ). *J. Phys. Chem. Solids* **2011**, *72*, 1467–1471.
- (220) Gauthron, K.; Lauret, J.-S.; Doyennette, L.; Lanty, G.; Al Choueiry, A.; Zhang, S. J.; Brehier, A.; Largeau, L.; Mauguin, O.; Bloch, J.; et al. Optical Spectroscopy of Two-Dimensional Layered  $(\text{C}_6\text{H}_5\text{C}_2\text{H}_4-\text{NH}_3)_2\text{PbI}_4$  Perovskite. *Opt. Express* **2010**, *18*, 5912–5919.
- (221) Dou, L.; Wong, A. B.; Yu, Y.; Lai, M.; Kornienko, N.; Ginsberg, N. S.; Wang, L.; Alivisatos, A. P.; Yang, P.; Eaton, S. W.; et al. Atomically Thin Two-Dimensional Organic-Inorganic Hybrid Perovskites. *Science* **2015**, *349*, 1518–1521.
- (222) Kondo, T.; Azuma, T.; Yuasa, T.; Ito, R. Biexciton Lasing in the Layered Perovskite-Type Material  $(\text{C}_6\text{H}_{13}\text{NH}_3)_2\text{PbI}_4$ . *Solid State Commun.* **1998**, *105*, 253–255.
- (223) Tanaka, K.; Kondo, T. Bandgap and Exciton Binding Energies in Lead-Iodide-Based Natural Quantum-Well Crystals. *Sci. Technol. Adv. Mater.* **2003**, *4*, 599–604.
- (224) Weisbuch, C.; Benisty, H. Microcavities in Ecole Polytechnique Fédérale de Lausanne, Ecole Polytechnique (France) and Elsewhere: Past, Present and Future. *Phys. Status Solidi B* **2005**, *242*, 2345–2356.
- (225) Saba, M.; Cadelano, M.; Marongiu, D.; Chen, F.; Sarritzu, V.; Sestu, N.; Figus, C.; Aresti, M.; Piras, R.; Geddo Lehmann, A.; et al. Correlated Electron-hole Plasma in Organometal Perovskites. *Nat. Commun.* **2014**, *5*, 5049.
- (226) Draguta, S.; Thakur, S.; Morozov, Y. V.; Wang, Y.; Manser, J. S.; Kamat, P. V.; Kuno, M. Spatially Non-Uniform Trap State Densities in Solution-Processed Hybrid Perovskite Thin Films. *J. Phys. Chem. Lett.* **2016**, *7*, 715–721.
- (227) Tian, Y.; Merdasa, A.; Unger, E.; Abdellah, M.; Zheng, K.; McKibbin, S.; Mikkelsen, A.; Pullerits, T.; Yartsev, A.; Sundström, V.; et al. Enhanced Organo-Metal Halide Perovskite Photoluminescence from Nanosized Defect-Free Crystallites and Emitting Sites. *J. Phys. Chem. Lett.* **2015**, *6*, 4171–4177.
- (228) Yamada, Y.; Nakamura, T.; Endo, M.; Wakamiya, A.; Kanemitsu, Y. Photocarrier Recombination Dynamics in Perovskite  $\text{CH}_3\text{NH}_3\text{PbI}_3$  for Solar Cell Applications. *J. Am. Chem. Soc.* **2014**, *136*, 11610–11613.
- (229) Chung, I.; Song, J. H.; Im, J.; Androulakis, J.; Malliakas, C. D.; Li, H.; Freeman, A. J.; Kenney, J. T.; Kanatzidis, M. G.  $\text{CsSnI}_3$ : Semiconductor or Metal? High Electrical Conductivity and Strong Near-Infrared Photoluminescence from a Single Material. High Hole Mobility and Phase-Transitions. *J. Am. Chem. Soc.* **2012**, *134*, 8579–8587.
- (230) Milot, R. L.; Eperon, G. E.; Snaith, H. J.; Johnston, M. B.; Herz, L. M. Temperature-Dependent Charge-Carrier Dynamics in  $\text{CH}_3\text{NH}_3\text{PbI}_3$  Perovskite Thin Films. *Adv. Funct. Mater.* **2015**, *25*, 6218–6227.
- (231) Wu, X.; Trinh, M. T.; Niesner, D.; Zhu, H.; Norman, Z.; Owen, J. S.; Yaffe, O.; Kudisch, B. J.; Zhu, X.-Y. Trap States in Lead Iodide Perovskites. *J. Am. Chem. Soc.* **2015**, *137*, 2089–2096.
- (232) Fang, H.-H.; Raissa, R.; Abdu-Agueye, M.; Adjokatse, S.; Blake, G. R.; Even, J.; Loi, M. A. Photophysics of Organic-Inorganic Hybrid Lead Iodide Perovskite Single Crystals. *Adv. Funct. Mater.* **2015**, *25*, 2378–2385.
- (233) Saba, M.; Quochi, F.; Mura, A.; Bongiovanni, G. Excited State Properties of Hybrid Perovskites. *Acc. Chem. Res.* **2016**, *49*, 166–173.
- (234) Elliott, R. J. Intensity of Optical Absorption by Excitons. *Phys. Rev.* **1957**, *108*, 1384–1389.
- (235) Sturge, M. D. Optical Absorption of Gallium Arsenide between 0.6 and 2.75 eV. *Phys. Rev.* **1962**, *127*, 768–773.
- (236) Wehrenfennig, C.; Liu, M.; Snaith, H. J.; Johnston, M. B.; Herz, L. M. Homogeneous Emission Line Broadening in the Organo

- Lead Halide Perovskite  $\text{CH}_3\text{NH}_3\text{PbI}_{3-x}\text{Cl}_x$ . *J. Phys. Chem. Lett.* **2014**, *5*, 1300–1306.
- (237) Manser, J. S.; Kamat, P. V. Band Filling with Free Charge Carriers in Organometal Halide Perovskites. *Nat. Photonics* **2014**, *8*, 737–743.
- (238) Kira, M.; Jahnke, F.; Koch, S. Microscopic Theory of Excitonic Signatures in Semiconductor Photoluminescence. *Phys. Rev. Lett.* **1998**, *81*, 3263–3266.
- (239) Koch, S. W.; Kira, M.; Khitrova, G.; Gibbs, H. M. Semiconductor Excitons in New Light. *Nat. Mater.* **2006**, *5*, 523–531.
- (240) Hirasawa, M.; Ishihara, T.; Goto, T. Exciton Features in 0-, 2-, and 3-Dimensional Networks of  $[\text{PbI}_6]^{4-}$  Octahedra. *J. Phys. Soc. Jpn.* **1994**, *63*, 3870–3879.
- (241) Ishihara, T. Optical Properties of PbI-Based Perovskite Structures. *J. Lumin.* **1994**, *60–61*, 269–274.
- (242) Liu, M.; Johnston, M. B.; Snaith, H. J. Efficient Planar Heterojunction Perovskite Solar Cells by Vapour Deposition. *Nature* **2013**, *501*, 395–398.
- (243) Wannier, G. H. The Structure of Electronic Excitation Levels in Insulating Crystals. *Phys. Rev.* **1937**, *52*, 191–197.
- (244) Yang, W.; Yao, Y.; Wu, C.-Q. Origin of the High Open Circuit Voltage in Planar Heterojunction Perovskite Solar Cells: Role of the Reduced Bimolecular Recombination. *J. Appl. Phys.* **2015**, *117*, 095502.
- (245) Johnston, M. B.; Herz, L. M. Hybrid Perovskites for Photovoltaics: Charge-Carrier Recombination, Diffusion, and Radiative Efficiencies. *Acc. Chem. Res.* **2016**, *49*, 146–154.
- (246) Yamada, Y.; Nakamura, T.; Endo, M.; Wakamiya, A.; Kanemitsu, Y. Photoelectronic Responses in Solution-Processed Perovskite  $\text{CH}_3\text{NH}_3\text{PbI}_3$  Solar Cells Studied by Photoluminescence and Photoabsorption Spectroscopy. *IEEE J. Photovoltaics* **2015**, *5*, 401–405.
- (247) Wu, K.; Bera, A.; Ma, C.; Du, Y.; Yang, Y.; Li, L.; Wu, T. Temperature-Dependent Excitonic Photoluminescence of Hybrid Organometal Halide Perovskite Films. *Phys. Chem. Chem. Phys.* **2014**, *16*, 22476–22481.
- (248) Chen, Z.; Yu, C.; Shum, K.; Wang, J. J.; Pfenninger, W.; Vockic, N.; Midgley, J.; Kenney, J. T. Photoluminescence Study of Polycrystalline  $\text{CsSnI}_3$  Thin Films: Determination of Exciton Binding Energy. *J. Lumin.* **2012**, *132*, 345–349.
- (249) Menéndez-Proupin, E.; Beltrán Ríos, C. L. B.; Wahnón, P. Nonhydrogenic Exciton Spectrum in Perovskite  $\text{CH}_3\text{NH}_3\text{PbI}_3$ . *Phys. Status Solidi RRL* **2015**, *9*, 559–563.
- (250) Zhu, X.-Y.; Podzorov, V. Charge Carriers in Hybrid Organic–Inorganic Lead Halide Perovskites Might Be Protected as Large Polarons. *J. Phys. Chem. Lett.* **2015**, *6*, 4758–4761.
- (251) Beilsten-Edmands, J.; Eperon, G. E.; Johnson, R. D.; Snaith, H. J.; Radaelli, P. G. Non-Ferroelectric Nature of the Conductance Hysteresis in  $\text{CH}_3\text{NH}_3\text{PbI}_3$  Perovskite-Based Photovoltaic Devices. *Appl. Phys. Lett.* **2015**, *106*, 173502.
- (252) Schmitt-Rink, S.; Chmela, D. S.; Miller, D. A. B. Theory of Transient Excitonic Optical Nonlinearities in Semiconductor Quantum-Well Structures. *Phys. Rev. B: Condens. Matter Mater. Phys.* **1985**, *32*, 6601–6609.
- (253) Quarti, C.; Grancini, G.; Mosconi, E.; Bruno, P.; Ball, J. M.; Lee, M. M.; Snaith, H. J.; Petrozza, A.; Angelis, F. De. The Raman Spectrum of the  $\text{CH}_3\text{NH}_3\text{PbI}_3$  Hybrid Perovskite: Interplay of Theory and Experiment. *J. Phys. Chem. Lett.* **2014**, *5*, 279–284.
- (254) Tanaka, K.; Takahashi, T.; Kondo, T.; Umebayashi, T.; Asai, K.; Ema, K. Image Charge Effect on Two-Dimensional Excitons in an Inorganic–Organic Quantum-Well Crystal. *Phys. Rev. B: Condens. Matter Mater. Phys.* **2005**, *71*, 045312.
- (255) Saha, M. N. On a Physical Theory of Stellar Spectra. *Proc. R. Soc. London, Ser. A* **1921**, *99*, 135–153.
- (256) Grancini, G.; Srimath Kandada, A. R.; Frost, J. M.; Barker, A. J.; De Bastiani, M.; Gandini, M.; Marras, S.; Lanzani, G.; Walsh, A.; Petrozza, A. Role of Microstructure in the Electron–Hole Interaction of Hybrid Lead Halide Perovskites. *Nat. Photonics* **2015**, *9*, 695–701.
- (257) Valverde-Chávez, D. A.; Ponseca, C. S.; Stoumpos, C. C.; Yartsev, A.; Kanatzidis, M. G.; Sundström, V.; Cooke, D. G. Intrinsic Femtosecond Charge Generation Dynamics in Single Crystal  $\text{CH}_3\text{NH}_3\text{PbI}_3$ . *Energy Environ. Sci.* **2015**, *8*, 3700–3707.
- (258) Stranks, S. D.; Burlakov, V. M.; Leijtens, T.; Ball, J. M.; Goriely, A.; Snaith, H. J. Recombination Kinetics in Organic–Inorganic Perovskites: Excitons, Free Charge, and Subgap States. *Phys. Rev. Appl.* **2014**, *2*, 034007.
- (259) de Quilettes, D. W.; Vorpahl, S. M.; Stranks, S. D.; Nagaoka, H.; Eperon, G. E.; Ziffer, M. E.; Snaith, H. J.; Ginger, D. S. Impact of Microstructure on Local Carrier Lifetime in Perovskite Solar Cells. *Science* **2015**, *348*, 683–686.
- (260) Cingolani, R.; Calcagnile, L.; Colí, G.; Rinaldi, R.; Lomoscolo, M.; Di Dio, M.; Franciosi, A.; Vanzetti, L.; La Rocca, G. C.; Campi, D. Radiative Recombination Processes in Wide-Band-Gap II–VI Quantum Wells: The Interplay between Excitons and Free Carriers. *J. Opt. Soc. Am. B* **1996**, *13*, 1268.
- (261) Price, M. B.; Butkus, J.; Jellico, T. C.; Sadhanala, A.; Briane, A.; Halpert, J. E.; Broch, K.; Hodgkiss, J. M.; Friend, R. H.; Deschler, F. Hot-Carrier Cooling and Photoinduced Refractive Index Changes in Organic–inorganic Lead Halide Perovskites. *Nat. Commun.* **2015**, *6*, 8420.
- (262) Zimmermann, R. Nonlinear Optics and the Mott Transition in Semiconductors. *Phys. Status Solidi B* **1988**, *146*, 371–384.
- (263) Mott, N. F. Metal-Insulator Transition. *Rev. Mod. Phys.* **1968**, *40*, 677–683.
- (264) Schweizer, H.; Forchel, A.; Hangleiter, A.; Schmitt-Rink, S.; Löwenau, J.; Haug, H. Ionization of the Direct-Gap Exciton in Photoexcited Germanium. *Phys. Rev. Lett.* **1983**, *51*, 698–701.
- (265) Haug, H.; Schmitt-Rink, S. Basic Mechanisms of the Optical Nonlinearities of Semiconductors Near the Band Edge. *J. Opt. Soc. Am. B* **1985**, *2*, 1135–1142.
- (266) Thomas, G. A.; Rice, T. M. Trions, Molecules and Excitons above the Mott Density in Ge. *Solid State Commun.* **1977**, *23*, 359–363.
- (267) Shah, J.; Leheny, R. F.; Lin, C. Dynamic Burstein Shift in GaAs. *Solid State Commun.* **1976**, *18*, 1035–1037.
- (268) Shah, J.; Combescot, M.; Dayem, A. H. Investigation of Exciton-Plasma Mott Transition in Si. *Phys. Rev. Lett.* **1977**, *38*, 1497–1500.
- (269) Hoyer, W.; Kira, M.; Koch, S. W. Influence of Coulomb and Phonon Interaction on the Exciton Formation Dynamics in Semiconductor Heterostructures. *Phys. Rev. B: Condens. Matter Mater. Phys.* **2003**, *67*, 155113.
- (270) Sum, T. C.; Mathews, N.; Xing, G.; Lim, S. S.; Chong, W. K.; Giovanni, D.; Dewi, H. A. Spectral Features and Charge Dynamics of Lead Halide Perovskites: Origins and Interpretations. *Acc. Chem. Res.* **2016**, *49*, 294–302.
- (271) Srimath Kandada, A. R.; Petrozza, A. Photophysics of Hybrid Lead Halide Perovskites: The Role of Microstructure. *Acc. Chem. Res.* **2016**, *49*, 536–544.
- (272) Christians, J. A.; Manser, J. S.; Kamat, P. V. Multifaceted Excited State of  $\text{CH}_3\text{NH}_3\text{PbI}_3$ . Charge Separation, Recombination, and Trapping. *J. Phys. Chem. Lett.* **2015**, *6*, 2086–2095.
- (273) Sheng, C.; Zhang, C.; Zhai, Y.; Mielczarek, K.; Wang, W.; Ma, W.; Zakhidov, A.; Vardeny, Z. V. Exciton versus Free Carrier Photogeneration in Organometal Trihalide Perovskites Probed by Broadband Ultrafast Polarization Memory Dynamics. *Phys. Rev. Lett.* **2015**, *114*, 116601.
- (274) Wang, L.; McCleese, C.; Kovalsky, A.; Zhao, Y.; Burda, C. Femtosecond Time-Resolved Transient Absorption Spectroscopy of  $\text{CH}_3\text{NH}_3\text{PbI}_3$  Perovskite Films: Evidence for Passivation Effect of  $\text{PbI}_2$ . *J. Am. Chem. Soc.* **2014**, *136*, 12205–12208.
- (275) Stamplecoskie, K. G.; Manser, J. S.; Kamat, P. V. Dual Nature of the Excited State in Organic–Inorganic Lead Halide Perovskites. *Energy Environ. Sci.* **2015**, *8*, 208–215.
- (276) Manser, J. S.; Reid, B.; Kamat, P. V. Evolution of Organic–Inorganic Lead Halide Perovskite from Solid-State Iodoplumbate Complexes. *J. Phys. Chem. C* **2015**, *119*, 17065–17073.

- (277) Zhai, Y.; Sheng, C. X.; Zhang, C.; Vardeny, Z. V. Ultrafast Spectroscopy of Photoexcitations in Organometal Trihalide Perovskites. *Adv. Funct. Mater.* **2016**, *26*, 1617–1627.
- (278) Burstein, E. Anomalous Optical Absorption Limit in InSb. *Phys. Rev.* **1954**, *93*, 632–633.
- (279) Moss, T. S. The Interpretation of the Properties of Indium Antimonide. *Proc. Phys. Soc., London, Sect. B* **1954**, *67*, 775–782.
- (280) Miller, A.; Miller, D. A. B.; Smith, S. D. Dynamic Non-Linear Optical Processes in Semiconductors. *Adv. Phys.* **1981**, *30*, 697–800.
- (281) Kamat, P. V.; Dimitrijevic, N. M.; Nozik, A. J. Dynamic Burstein-Moss Shift in Semiconductor Colloids. *J. Phys. Chem.* **1989**, *93*, 2873–2875.
- (282) Puthusseriy, J.; Lan, A.; Kosel, T. H.; Kuno, M. Band-Filling of Solution-Synthesized CdS Nanowires. *ACS Nano* **2008**, *2*, 357–367.
- (283) Zimmermann, R.; Kilimann, K.; Kraeft, W. D.; Kremp, D.; Röpke, G. Dynamical Screening and Self-Energy of Excitons in the electron–Hole Plasma. *Phys. Status Solidi B* **1978**, *90*, 175–187.
- (284) Chen, K.; Barker, A. J.; Morgan, F. L. C.; Halpert, J. E.; Hodgkiss, J. M. Effect of Carrier Thermalization Dynamics on Light Emission and Amplification in Organometal Halide Perovskites. *J. Phys. Chem. Lett.* **2015**, *6*, 153–158.
- (285) Trinh, M. T.; Wu, X.; Niesner, D.; Zhu, X. Many-Body Interactions in Photo-Excited Lead Iodide Perovskite. *J. Mater. Chem. A* **2015**, *3*, 9285–9290.
- (286) Huang, D.; Chyi, J.-I.; Morkoç, H. Carrier Effects on the Excitonic Absorption in GaAs Quantum-Well Structures: Phase-Space Filling. *Phys. Rev. B: Condens. Matter Mater. Phys.* **1990**, *42*, 5147–5153.
- (287) Je, K.-C.; Choi, M.; Yim, S.-Y.; Ahn, J.; Park, S.-H. Separation of Screened Coulomb Interaction and Phase-Space Filling in Exciton Bleaching of Multiple Quantum Wells. *Phys. Rev. B: Condens. Matter Mater. Phys.* **2002**, *66*, 155312.
- (288) Meier, T.; Koch, S. Excitons versus Unbound Electron-Hole Pairs and Their Influence on Exciton Bleaching: A Model Study. *Phys. Rev. B: Condens. Matter Mater. Phys.* **1999**, *59*, 13202–13208.
- (289) Ulbricht, R.; Hendry, E.; Shan, J.; Heinz, T. F.; Bonn, M. Carrier Dynamics in Semiconductors Studied with Time-Resolved Terahertz Spectroscopy. *Rev. Mod. Phys.* **2011**, *83*, 543–586.
- (290) Poncea, C. S., Jr.; Sundström, V. Revealing the Ultrafast Charge Carrier Dynamics in Organo Metal Halide Perovskite Solar Cell Materials Using Time Resolved THz Spectroscopy. *Nanoscale* **2016**, *8*, 6249–6257.
- (291) La-o-vorakiat, C.; Salim, T.; Kadro, J.; Khuc, M.-T.; Haselsberger, R.; Cheng, L.; Xia, H.; Gurzadyan, G. G.; Su, H.; Lam, Y. M.; et al. Elucidating the Role of Disorder and Free-Carrier Recombination Kinetics in  $\text{CH}_3\text{NH}_3\text{PbI}_3$  Perovskite Films. *Nat. Commun.* **2015**, *6*, 7903.
- (292) Saeki, A.; Yasutani, Y.; Oga, H.; Seki, S. Frequency-Modulated Gigahertz Complex Conductivity of  $\text{TiO}_2$  Nanoparticles: Interplay of Free and Shallowly Trapped Electrons. *J. Phys. Chem. C* **2014**, *118*, 22561–22572.
- (293) Ulbricht, R.; Hendry, E.; Shan, J.; Heinz, T. F.; Bonn, M. Carrier Dynamics in Semiconductors Studied with Time-Resolved Terahertz Spectroscopy. *Rev. Mod. Phys.* **2011**, *83*, 543–586.
- (294) Poncea, C. S.; Savenije, T. J.; Abdellah, M.; Zheng, K.; Yartsev, A.; Pascher, T.; Harlang, T.; Chabera, P.; Pullerits, T.; Stepanov, A.; et al. Organometal Halide Perovskite Solar Cell Materials Rationalized: Ultrafast Charge Generation, High and Microsecond-Long Balanced Mobilities, and Slow Recombination. *J. Am. Chem. Soc.* **2014**, *136*, 5189–5192.
- (295) Wehrenfennig, C.; Liu, M.; Snaith, H. J.; Johnston, M. B.; Herz, L. M. Charge-Carrier Dynamics in Vapour-Deposited Films of the Organolead Halide Perovskite  $\text{CH}_3\text{NH}_3\text{PbI}_{3-x}\text{Cl}_x$ . *Energy Environ. Sci.* **2014**, *7*, 2269–2275.
- (296) Guo, Z.; Manser, J. S.; Wan, Y.; Kamat, P. V.; Huang, L. Spatial and Temporal Imaging of Long-Range Charge Transport in Perovskite Thin Films by Ultrafast Microscopy. *Nat. Commun.* **2015**, *6*, 7471.
- (297) Simpson, M. J.; Doughty, B.; Yang, B.; Xiao, K.; Ma, Y.-Z. Spatial Localization of Excitons and Charge Carriers in Hybrid Perovskite Thin Films. *J. Phys. Chem. Lett.* **2015**, *6*, 3041–3047.
- (298) Yang, Y.; Yang, M.; Li, Z.; Crisp, R.; Zhu, K.; Beard, M. C. Comparison of Recombination Dynamics in  $\text{CH}_3\text{NH}_3\text{PbBr}_3$  and  $\text{CH}_3\text{NH}_3\text{PbI}_3$  Perovskite Films: Influence of Exciton Binding Energy. *J. Phys. Chem. Lett.* **2015**, *6*, 4688–4692.
- (299) Zhang, M.; Yu, H.; Lyu, M.; Wang, Q.; Yun, J.-H.; Wang, L. Composition-Dependent Photoluminescence Intensity and Prolonged Recombination Lifetime of Perovskite  $\text{CH}_3\text{NH}_3\text{PbBr}_{3-x}\text{Cl}_x$  Films. *Chem. Commun.* **2014**, *50*, 11727–11730.
- (300) De Bastiani, M.; D’Innocenzo, V.; Stranks, S. D.; Snaith, H. J.; Petrozza, A.; Bastiani, M. De; Innocenzo, V. D. Role of the Crystallization Substrate on the Photoluminescence Properties of Organo-Lead Mixed Halides Perovskites. *APL Mater.* **2014**, *2*, 081509.
- (301) Wehrenfennig, C.; Eperon, G. E.; Johnston, M. B.; Snaith, H. J.; Herz, L. M. High Charge Carrier Mobilities and Lifetimes in Organolead Trihalide Perovskites. *Adv. Mater.* **2014**, *26*, 1584–1589.
- (302) Noel, N. K.; Abate, A.; Stranks, S. D.; Parrott, E. S.; Burlakov, V. M.; Goriely, A.; Snaith, H. J. Enhanced Photoluminescence and Solar Cell Performance via Lewis Base Passivation of Organic-Inorganic Lead Halide Perovskites. *ACS Nano* **2014**, *8*, 9815–9821.
- (303) You, J.; Hong, Z.; Yang, Y. M.; Chen, Q.; Cai, M.; Song, T.; Chen, C.; Lu, S.; Liu, Y.; Zhou, H.; et al. Low-Temperature Solution-Processed Perovskite Solar Cells with High Efficiency and Flexibility. *ACS Nano* **2014**, *8*, 1674–1680.
- (304) Liang, P. W.; Liao, C. Y.; Chueh, C. C.; Zuo, F.; Williams, S. T.; Xin, X. K.; Lin, J.; Jen, A. K. Y. Additive Enhanced Crystallization of Solution-Processed Perovskite for Highly Efficient Planar-Heterojunction Solar Cells. *Adv. Mater.* **2014**, *26*, 3748–3754.
- (305) Poncea, C. S.; Hutter, E. M.; Piatkowski, P.; Cohen, B.; Pascher, T.; Douhal, A.; Yartsev, A.; Sundström, V.; Savenije, T. J. Mechanism of Charge Transfer and Recombination Dynamics in Organo Metal Halide Perovskites and Organic Electrodes, PCBM, and Spiro-OMeTAD: Role of Dark Carriers. *J. Am. Chem. Soc.* **2015**, *137*, 16043–16048.
- (306) Noel, N. K.; Stranks, S. D.; Abate, A.; Wehrenfennig, C.; Guarnera, S.; Haghaghirad, A.-A.; Sadhanala, A.; Eperon, G. E.; Pathak, S. K.; Johnston, M. B.; et al. Lead-Free Organic-Inorganic Tin Halide Perovskites for Photovoltaic Applications. *Energy Environ. Sci.* **2014**, *7*, 3061–3068.
- (307) Savenije, T. J.; Poncea, C. S.; Kunneman, L.; Abdellah, M.; Zheng, K.; Tian, Y.; Zhu, Q.; Canton, S. E.; Scheblykin, I. G.; Pullerits, T.; et al. Thermally Activated Exciton Dissociation and Recombination Control the Carrier Dynamics in Organometal Halide Perovskite. *J. Phys. Chem. Lett.* **2014**, *5*, 2189–2194.
- (308) Tauc, J.; Menth, A. States in the Gap. *J. Non-Cryst. Solids* **1972**, *8–10*, 569–585.
- (309) Lasher, G.; Stern, F. Spontaneous and Stimulated Recombination Radiation in Semiconductors. *Phys. Rev.* **1964**, *133*, A553–A563.
- (310) Beard, M. C.; Ellingson, R. J. Multiple Exciton Generation in Semiconductor Nanocrystals: Toward Efficient Solar Energy Conversion. *Laser Photonics Rev.* **2008**, *2*, 377–399.
- (311) Robel, I.; Gresback, R.; Kortshagen, U.; Schaller, R. D.; Klimov, V. I. Universal Size-Dependent Trend in Auger Recombination in Direct-Gap and Indirect-Gap Semiconductor Nanocrystals. *Phys. Rev. Lett.* **2009**, *102*, 177404.
- (312) Hangleiter, A.; Häcker, R. Enhancement of Band-to-Band Auger Recombination by Electron-Hole Correlations. *Phys. Rev. Lett.* **1990**, *65*, 215–218.
- (313) Christians, J. A.; Leighton, D. T., Jr.; Kamat, P. V. Rate Limiting Interfacial Hole Transfer in  $\text{Sb}_2\text{S}_3$  Solid-State Solar Cells. *Energy Environ. Sci.* **2014**, *7*, 1148–1158.
- (314) Robel, I.; Bunker, B. A.; Kamat, P. V.; Kuno, M. Exciton Recombination Dynamics in CdSe Nanowires: Bimolecular to Three-Carrier Auger Kinetics. *Nano Lett.* **2006**, *6*, 1344–1349.
- (315) Langevin, P. The Recombination and Mobilities of Ions in Gases. *Ann. Chim. Phys.* **1903**, *28*, 433–530.

- (316) Yamada, K.; Kawaguchi, H.; Matsui, T.; Okuda, T.; Ichiba, S. Structural Phase Transition and Electrical Conductivity of the Perovskite  $\text{CH}_3\text{NH}_3\text{Sn}_{1-x}\text{Pb}_x\text{Br}_3$  and  $\text{CsSnBr}_3$ . *Bull. Chem. Soc. Jpn.* **1990**, *63*, 2521–2525.
- (317) Yamada, K.; Matsui, T.; Tsuritani, T.; Okuda, T.; Ichiba, S.  $^{127}\text{I}$ -NQR,  $^{119}\text{Sn}$  Mössbauer Effect, and Electrical Conductivity of  $\text{MSnI}_3$  ( $M = \text{K}, \text{NH}_4, \text{Rb}, \text{Cs}$ , and  $\text{CH}_3\text{NH}_3$ ). *Z. Naturforsch., A: Phys. Sci.* **1990**, *45*, 307–312.
- (318) Adriaenssens, G. J.; Arkhipov, V. I. Non-Langevin Recombination in Disordered Materials with Random Potential Distributions. *Solid State Commun.* **1997**, *103*, 541–543.
- (319) Pivrikas, A.; Juška, G.; Mozer, A. J.; Scharber, M.; Arlauskas, K.; Sariciftci, N. S.; Stubb, H.; Österbacka, R. Bimolecular Recombination Coefficient as a Sensitive Testing Parameter for Low-Mobility Solar-Cell Materials. *Phys. Rev. Lett.* **2005**, *94*, 176806.
- (320) Ma, J.; Wang, L. Nanoscale Charge Localization Induced by Random Orientations of Organic Molecules in Hybrid Perovskite  $\text{CH}_3\text{NH}_3\text{PbI}_3$ . *Nano Lett.* **2015**, *15*, 248–253.
- (321) Choi, J. J.; Yang, X.; Norman, Z. M.; Billinge, S. J. L.; Owen, J. S. Structure of Methylammonium Lead Iodide Within Mesoporous Titanium Dioxide: Active Material in High-Performance Perovskite Solar Cells. *Nano Lett.* **2014**, *14*, 127–133.
- (322) Vietmeyer, F.; Frantsuzov, P. A.; Janko, B.; Kuno, M. Carrier Recombination Dynamics in Individual CdSe Nanowires. *Phys. Rev. B: Condens. Matter Mater. Phys.* **2011**, *83*, 115319.
- (323) Brandt, O.; Kanamoto, K.; Gotoda, M.; Isu, T.; Tsukada, N. Recombination Processes and Photoluminescence Intensity in Quantum Wells under Steady-State and Transient Conditions. *Phys. Rev. B: Condens. Matter Mater. Phys.* **1995**, *51*, 7029–7037.
- (324) Vrućinić, M.; Matthiesen, C.; Sadhanala, A.; Divitini, G.; Cacovich, S.; Dutton, S. E.; Ducati, C.; Atatüre, M.; Snaith, H.; Friend, R. H.; et al. Local Versus Long-Range Diffusion Effects of Photoexcited States on Radiative Recombination in Organic-Inorganic Lead Halide Perovskites. *Adv. Sci.* **2015**, *2*, 1500136.
- (325) Wang, C.; Li, C.-Y.; Hasselbeck, M. P.; Imangholi, B.; Sheik-Bahae, M. Precision, All-Optical Measurement of External Quantum Efficiency in Semiconductors. *J. Appl. Phys.* **2011**, *109*, 093108.
- (326) Bisquert, J.; Mora-Seró, I. Simulation of Steady-State Characteristics of Dye-Sensitized Solar Cells and the Interpretation of the Diffusion Length. *J. Phys. Chem. Lett.* **2010**, *1*, 450–456.
- (327) Masetti, G.; Severi, M.; Solmi, S. Modeling of Carrier Mobility against Carrier Concentration in Arsenic-, Phosphorus-, and Boron-Doped Silicon. *IEEE Trans. Electron Devices* **1983**, *30*, 764–769.
- (328) Pearson, G. L.; Haynes, J. R.; Shockley, W. Comment on Mobility Anomalies in Germanium. *Phys. Rev.* **1950**, *78*, 295–296.
- (329) Gonzalez-Pedro, V.; Juarez-Perez, E. J.; Arsyad, W.-S.; Barea, E. M.; Fabregat-Santiago, F.; Mora-Sero, I.; Bisquert, J. General Working Principles of  $\text{CH}_3\text{NH}_3\text{PbX}_3$  Perovskite Solar Cells. *Nano Lett.* **2014**, *14*, 888–893.
- (330) Saidaminov, M. I.; Abdelhady, A. L.; Murali, B.; Alarousu, E.; Burlakov, V. M.; Peng, W.; Dursun, I.; Wang, L.; He, Y.; Maculan, G.; et al. High-Quality Bulk Hybrid Perovskite Single Crystals within Minutes by Inverse Temperature Crystallization. *Nat. Commun.* **2015**, *6*, 7586.
- (331) Dong, Q.; Fang, Y.; Shao, Y.; Mulligan, P.; Qiu, J.; Cao, L.; Huang, J. Electron-Hole Diffusion Lengths  $> 175$  Micrometers in Solution-Grown  $\text{CH}_3\text{NH}_3\text{PbI}_3$  Single Crystals. *Science* **2015**, *347*, 967–970.
- (332) Kedem, N.; Brenner, T. M.; Kulbak, M.; Schaefer, N.; Levchenko, S.; Levine, I.; Abou-Ras, D.; Hodes, G.; Cahen, D. Light-Induced Increase of Electron Diffusion Length in a p-n Junction Type  $\text{CH}_3\text{NH}_3\text{PbBr}_3$  Perovskite Solar Cell. *J. Phys. Chem. Lett.* **2015**, *6*, 2469–2476.
- (333) Sheng, R.; Ho-Baillie, A.; Huang, S.; Chen, S.; Wen, X.; Hao, X.; Green, M. A. Methylammonium Lead Bromide Perovskite-Based Solar Cells by Vapor-Assisted Deposition. *J. Phys. Chem. C* **2015**, *119*, 3545–3549.
- (334) Chung, I.; Lee, B.; He, J.; Chang, R. P. H.; Kanatzidis, M. G. All-Solid-State Dye-Sensitized Solar Cells with High Efficiency. *Nature* **2012**, *485*, 486–489.
- (335) Pool, V. L.; Gold-Parker, A.; McGehee, M. D.; Toney, M. F. Chlorine in  $\text{PbCl}_2$ -Derived Hybrid-Perovskite Solar Absorbers. *Chem. Mater.* **2015**, *27*, 7240–7243.
- (336) Buin, A.; Pietsch, P.; Xu, J.; Voznyy, O.; Ip, A. H.; Comin, R.; Sargent, E. H. Materials Processing Routes to Trap-Free Halide Perovskites. *Nano Lett.* **2014**, *14*, 6281–6286.
- (337) Liu, J.; Prezhdov, O. V. Chlorine Doping Reduces Electron–Hole Recombination in Lead Iodide Perovskites: Time-Domain Ab Initio Analysis. *J. Phys. Chem. Lett.* **2015**, *6*, 4463–4469.
- (338) Hodes, G.; Kamat, P. V. Understanding the Implication of Carrier Diffusion Length in Photovoltaic Cells. *J. Phys. Chem. Lett.* **2015**, *6*, 4090–4092.
- (339) Frost, J. M.; Walsh, A. What Is Moving in Hybrid Halide Perovskite Solar Cells? *Acc. Chem. Res.* **2016**, *49*, 528–535.
- (340) Pisula, W.; Feng, X.; Müllen, K. Charge-Carrier Transporting Graphene-Type Molecules. *Chem. Mater.* **2011**, *23*, 554–567.
- (341) Tamai, Y.; Ohkita, H.; Benten, H.; Ito, S. Exciton Diffusion in Conjugated Polymers: From Fundamental Understanding to Improvement in Photovoltaic Conversion Efficiency. *J. Phys. Chem. Lett.* **2015**, *6*, 3417–3428.
- (342) Jiang, C.-S.; Yang, M.; Zhou, Y.; To, B.; Nanayakkara, S. U.; Luther, J. M.; Zhou, W.; Berry, J. J.; van de Lagemaat, J.; Padture, N. P.; et al. Carrier Separation and Transport in Perovskite Solar Cells Studied by Nanometre-Scale Profiling of Electrical Potential. *Nat. Commun.* **2015**, *6*, 8397.
- (343) Baumann, A.; Väth, S.; Rieder, P.; Heiber, M. C.; Tvingstedt, K.; Dyakonov, V. Identification of Trap States in Perovskite Solar Cells. *J. Phys. Chem. Lett.* **2015**, *6*, 2350–2354.
- (344) Gundel, P.; Schubert, M. C.; Warta, W. Origin of Trapping in Multicrystalline Silicon. *J. Appl. Phys.* **2008**, *104*, 073716.
- (345) Oga, H.; Saeki, A.; Ogomi, Y.; Hayase, S.; Seki, S. Improved Understanding of the Electronic and Energetic Landscapes of Perovskite Solar Cells: High Local Charge Carrier Mobility, Reduced Recombination, and Extremely Shallow Traps. *J. Am. Chem. Soc.* **2014**, *136*, 13818–13825.
- (346) Kim, J.; Lee, S.-H.; Lee, J. H.; Hong, K.-H. The Role of Intrinsic Defects in Methylammonium Lead Iodide Perovskite. *J. Phys. Chem. Lett.* **2014**, *5*, 1312–1317.
- (347) Yin, W.-J.; Shi, T.; Yan, Y. Unusual Defect Physics in  $\text{CH}_3\text{NH}_3\text{PbI}_3$  Perovskite Solar Cell Absorber. *Appl. Phys. Lett.* **2014**, *104*, 063903.
- (348) Garcia-Fernandez, P.; Aramburu, J. a.; Barriuso, M. T.; Moreno, M. Key Role of Covalent Bonding in Octahedral Tilting in Perovskites. *J. Phys. Chem. Lett.* **2010**, *1*, 647–651.
- (349) Kulbak, M.; Cahen, D.; Hodes, G. How Important Is the Organic Part of Lead Halide Perovskite Photovoltaic Cells? Efficient  $\text{CsPbBr}_3$  Cells. *J. Phys. Chem. Lett.* **2015**, *6*, 2452–2456.
- (350) Soufiani, A. M.; Huang, F.; Reece, P.; Sheng, R.; Ho-Baillie, A.; Green, M. A. Polaronic Exciton Binding Energy in Iodide and Bromide Organic-Inorganic Lead Halide Perovskites. *Appl. Phys. Lett.* **2015**, *107*, 231902.
- (351) Miller, E. M.; Zhao, Y.; Mercado, C. C.; Saha, S. K.; Luther, J. M.; Zhu, K.; Stevanović, V.; Perkins, C. L.; van de Lagemaat, J. Substrate-Controlled Band Positions in  $\text{CH}_3\text{NH}_3\text{PbI}_3$  Perovskite Films. *Phys. Chem. Chem. Phys.* **2014**, *16*, 22122–22130.
- (352) Busmundrud, O.; Feder, J. Electrical Conduction and Phase Transitions in  $\text{CsPbCl}_3$ . *Solid State Commun.* **1971**, *9*, 1575–1577.
- (353) Mizusaki, J.; Arai, K.; Fueki, K. Ionic Conduction of the Perovskite-Type Halides. *Solid State Ionics* **1983**, *11*, 203–211.
- (354) Snaith, H. J.; Abate, A.; Ball, J. M.; Eperon, G. E.; Leijtens, T.; Noel, N. K.; Stranks, S. D.; Wang, J. T. W.; Wojciechowski, K.; Zhang, W. Anomalous Hysteresis in Perovskite Solar Cells. *J. Phys. Chem. Lett.* **2014**, *5*, 1511–1515.
- (355) Yuan, Y.; Huang, J. Ion Migration in Organometal Trihalide Perovskite and Its Impact on Photovoltaic Efficiency and Stability. *Acc. Chem. Res.* **2016**, *49*, 286–293.

- (356) Eperon, G. E.; Paternò, G. M.; Sutton, R. J.; Zampetti, A.; Haghghirad, A. A.; Cacialli, F.; Snaith, H. J. Inorganic Caesium Lead Iodide Perovskite Solar Cells. *J. Mater. Chem. A* **2015**, *3*, 19688–19695.
- (357) Zhang, Y.; Liu, M.; Eperon, G. E.; Leijtens, T. C.; McMeekin, D.; Saliba, M.; Zhang, W.; de Bastiani, M.; Petrozza, A.; Herz, L. M.; et al. Charge Selective Contacts, Mobile Ions and Anomalous Hysteresis in organic–Inorganic Perovskite Solar Cells. *Mater. Horiz.* **2015**, *2*, 315–322.
- (358) van Reenen, S.; Kemerink, M.; Snaith, H. J. Modeling Anomalous Hysteresis in Perovskite Solar Cells. *J. Phys. Chem. Lett.* **2015**, *6*, 3808–3814.
- (359) Unger, E. L.; Hoke, E. T.; Bailie, C. D.; Nguyen, W. H.; Bowring, A. R.; Heumuller, T.; Christoforo, M. G.; McGehee, M. D. Hysteresis and Transient Behavior in Current-Voltage Measurements of Hybrid-Perovskite Absorber Solar Cells. *Energy Environ. Sci.* **2014**, *7*, 3690–3698.
- (360) Chen, B.; Yang, M.; Zheng, X.; Wu, C.; Li, W.; Yan, Y.; Bisquert, J.; Garcia-Belmonte, G.; Zhu, K.; Priya, S. Impact of Capacitive Effect and Ion Migration on the Hysteretic Behavior of Perovskite Solar Cells. *J. Phys. Chem. Lett.* **2015**, *6*, 4693–4700.
- (361) Kim, H. S.; Park, N. Parameters Affecting I–V Hysteresis of  $\text{CH}_3\text{NH}_3\text{PbI}_3$  Perovskite Solar Cells: Effects of Perovskite Crystal Size and Mesoporous  $\text{TiO}_2$  Layer. *J. Phys. Chem. Lett.* **2014**, *5*, 2927–2934.
- (362) Xu, J.; Buin, A.; Ip, A. H.; Li, W.; Voznyy, O.; Comin, R.; Yuan, M.; Jeon, S.; Ning, Z.; McDowell, J. J.; et al. Perovskite–Fullerene Hybrid Materials Suppress Hysteresis in Planar Diodes. *Nat. Commun.* **2015**, *6*, 7081.
- (363) Eames, C.; Frost, J. M.; Barnes, P. R. F.; O'Regan, B. C.; Walsh, A.; Islam, M. S. Ionic Transport in Hybrid Lead Iodide Perovskite Solar Cells. *Nat. Commun.* **2015**, *6*, 7497.
- (364) Azpiroz, J. M.; Mosconi, E.; Bisquert, J.; De Angelis, F. Defect Migration in Methylammonium Lead Iodide and Its Role in Perovskite Solar Cell Operation. *Energy Environ. Sci.* **2015**, *8*, 2118–2127.
- (365) Haruyama, J.; Sodeyama, K.; Han, L.; Tateyama, Y. First-Principles Study of Ion Diffusion in Perovskite Solar Cell Sensitizers. *J. Am. Chem. Soc.* **2015**, *137*, 10048–10051.
- (366) Egger, D. A.; Kronik, L.; Rappe, A. M. Theory of Hydrogen Migration in Organic-Inorganic Halide Perovskites. *Angew. Chem., Int. Ed.* **2015**, *54*, 12437–12441.
- (367) Xiao, Z.; Yuan, Y.; Shao, Y.; Wang, Q.; Dong, Q.; Bi, C.; Sharma, P.; Gruverman, A.; Huang, J. Giant Switchable Photovoltaic Effect in Organometal Trihalide Perovskite Devices. *Nat. Mater.* **2014**, *14*, 193–198.
- (368) Yuan, Y.; Chae, J.; Shao, Y.; Wang, Q.; Xiao, Z.; Centrone, A.; Huang, J. Photovoltaic Switching Mechanism in Lateral Structure Hybrid Perovskite Solar Cells. *Adv. Energy Mater.* **2015**, *5*, 1500615.
- (369) Li, C.; Tscheuschner, S.; Paulus, F.; Hopkinson, P. E.; Kießling, J.; Köhler, A.; Vaynzof, Y.; Huettner, S. Iodine Migration and Its Effect on Hysteresis in Perovskite Solar Cells. *Adv. Mater.* **2016**, *28*, 2446–2454.
- (370) Bag, M.; Renna, L. A.; Adhikari, R. Y.; Karak, S.; Liu, F.; Lahti, P. M.; Russell, T. P.; Tuominen, M. T.; Venkataraman, D. Kinetics of Ion Transport in Perovskite Active Layers and Its Implications for Active Layer Stability. *J. Am. Chem. Soc.* **2015**, *137*, 13130–13137.
- (371) Tress, W.; Marinova, N.; Moehl, T.; Zakeeruddin, S. M.; Nazeeruddin, M. K.; Grätzel, M. Understanding the Rate-Dependent J–V Hysteresis, Slow Time Component, and Aging in  $\text{CH}_3\text{NH}_3\text{PbI}_3$  Perovskite Solar Cells: The Role of a Compensated Electric Field. *Energy Environ. Sci.* **2015**, *8*, 995–1004.
- (372) Bischak, C. G.; Sanehira, E. M.; Precht, J. T.; Luther, J. M.; Ginsberg, N. S. Heterogeneous Charge Carrier Dynamics in Organic–Inorganic Hybrid Materials: Nanoscale Lateral and Depth-Dependent Variation of Recombination Rates in Methylammonium Lead Halide Perovskite Thin Films. *Nano Lett.* **2015**, *15*, 4799–4807.
- (373) Shao, Y.; Fang, Y.; Li, T.; Wang, Q.; Dong, Q.; Deng, Y.; Yuan, Y.; Wei, H.; Wang, M.; Gruverman, A.; et al. Grain Boundary Dominated Ion Migration in Polycrystalline Organic–inorganic Halide Perovskite Films. *Energy Environ. Sci.* **2016**, *9*, 1752–1759.
- (374) Huang, W.; Manser, J. S.; Kamat, P. V.; Ptasińska, S. Evolution of Chemical Composition, Morphology, and Photovoltaic Efficiency of  $\text{CH}_3\text{NH}_3\text{PbI}_3$  Perovskite under Ambient Conditions. *Chem. Mater.* **2016**, *28*, 303–311.
- (375) Kadro, J. M.; Nonomura, K.; Gachet, D.; Grätzel, M.; Hagfeldt, A. Facile Route to Freestanding  $\text{CH}_3\text{NH}_3\text{PbI}_3$  Crystals Using Inverse Solubility. *Sci. Rep.* **2015**, *5*, 11654.
- (376) Zhu, F.; Men, L.; Guo, Y.; Zhu, Q.; Bhattacharjee, U.; Goodwin, P. M.; Petrich, J. W.; Smith, E. A.; Vela, J. Shape Evolution and Single Particle Luminescence of Organometal Halide Perovskite Nanocrystals. *ACS Nano* **2015**, *9*, 2948–2959.
- (377) Park, Y.-S.; Guo, S.; Makarov, N.; Klimov, V. I. Room Temperature Single-Photon Emission from Individual Perovskite Quantum Dots. *ACS Nano* **2015**, *9*, 10386–10393.